

BULGARIAN CHEMICAL COMMUNICATIONS

2019 Volume 51 / Issue 4

*Journal of the Chemical Institutes
of the Bulgarian Academy of Sciences
and of the Union of Chemists in Bulgaria*

ONE HUNDRED YEARS OF THE FOUNDER OF CHEMICAL ENGINEERING IN BULGARIA – Prof. Dimiter G. Elenkov, DSc



November 4th this year marks the 100th anniversary of the birth of Prof. D.Sc. Eng. Dimiter G. Elenkov, Corresponding Member of the Bulgarian Academy of Sciences (BAS). He was the founder of chemical engineering in Bulgaria.

Prof. D. Elenkov created the discipline "Basic Processes and Apparatuses in the Chemical Industry" (now called "Chemical Engineering") at the Institute of Chemical Technology (later High Institute of Chemical Technology and now University of Chemical Technology and Metallurgy

Under his guidance and at his initiative, a Central Laboratory for Theoretical Foundations of Chemical Engineering (CLATOCHT) was established at BAS. Again at his initiative, this Central Laboratory grew into the Institute of Chemical Engineering in 1986, as it has been until now.

Prof. D. Elenkov's scientific activity was oriented towards the practical realization of the chemical and mass exchange processes taking place in the chemical technology. Together with the traditional heat and mass transfer processes in multiphase systems under his leadership, in CLATOCHT, the modern branches of chemical engineering science were developed, namely: chemical reactor engineering, chemical systems engineering and biochemical reactors. The latter is currently one of the leading research fields at the Institute of Chemical Engineering and in the country. All of them, equipped with modern mathematical apparatus and modern research methodologies, have contributed not only to the scientific growth of young scientists, but also to solving practical problems in chemical industry and in environment protection from pollution caused by chemical production in Bulgaria.

Examples are the installation for capturing sulfur dioxide, combined with the capture of lead and zinc at the State Mining Company at Eliseyna and the Lead-Zinc Plant- Kardzhali; the intensification of aniline production in Neochim - Dimitrovgrad; the capture of hydrogen sulphide in industrial gases and the optimization of the regeneration of carbon sulphide at Svilosa -Svishtov; the catalytic oxidation of sulfur dioxide and the production of sulfuric acid in a heterogeneous reactor (KCM-Plovdiv) and others.

Under his guidance, 17 doctoral theses were defended, and the scientists with habilitation who have grown with his support are sixteen.

He was elected Corresponding Member of BAS in 1977. He was Professor Emeritus and Doctor of Leningrad Institute of Technology (1982), now in St. Petersburg, Russia.

Prof. Dimiter Elenkov is the winner of twelve different awards of Bulgarian state bodies and institutions.

The contribution of Prof. Dimiter Elenkov to the training and development of thousands of highly qualified chemists and chemical engineers is remarkable. It can be affirmed that there are no Bulgarian scientists and specialists working in the field of chemical engineering who were not strongly impacted by his example in teaching and scientific guidance.

The Bulgarian chemical engineering community remembers him with gratitude and respect.

Prof. Venko Beschkov, 2019

Aspartic acid as an efficient and green catalyst for the one-pot synthesis of 2-amino-4*H*-chromene derivatives under thermal, solvent free conditions

M. Abreshteh, K. Khandan-Barani*, A. Hassanabadi

Department of Chemistry, Zahedan Branch, Islamic Azad University, Zahedan, Iran

Received June 22, 2018; Revised April 12, 2019,

A high-yielding synthesis of 2-amino-4*H*-chromenes is described involving the reaction of 1-naphthol or 2-naphthol, with aryl aldehydes and malononitrile in the presence of a catalytic amount of aspartic acid under thermal, solvent-free conditions. The salient features of this protocol are: aerobic conditions, non-hazardous, green catalyst, short reaction times and mild reaction conditions.

Keywords: Aspartic acid, 2-Amino-4*H*-chromenes, Solvent-free, Green catalyst, Malononitrile, Multi-component reactions

INTRODUCTION

The discovery of novel synthetic methodologies to facilitate the preparation of compound libraries is a focal point of research activity in the field of modern medicinal and combinatorial chemistry [1]. One approach to address this challenge involves the development of multicomponent reactions (MCRs), in which three or more reactants are combined together in a single reaction flask to generate a product with the most of the atoms contained in the starting materials [2]. The rapid assembly of molecular diversity utilizing MCRs has received a great deal of attention, especially for the design and construction of elaborate heterocyclic frameworks possessing enhanced “drug-like” properties [3-5].

The chromene derivatives are widely present in natural alkaloids, flavonoids, tocopherols, and anthocyanins [6]. Moreover, functionalized chromenes have played an ever-increasing role in the synthetic approaches to promising compounds in the field of medicinal chemistry [7]. Among the different types of chromene systems, 2-amino-4*H*-chromenes are of particular utility as they belong to preferential medicinal scaffolds serving for generation of small-molecule ligands with highly pronounced anticoagulant, diuretic, spasmolytic and antianaphylactic activities [8-10]. 2-Amino-4*H*-chromenes are generally produced by refluxing active methylene compounds (e.g., malononitrile and cyanoacetic acid esters), with an aldehyde and an activated phenol in organic solvents such as ethanol and acetonitrile, and in the presence of catalyst for several hours [11-13]. Various modified catalysts were used such as cetyltrimethyl ammonium chloride [14], cetyltrimethyl ammonium bromide under ultrasound irradiation [15], KSF clay [16], KF/Al₂O₃ [17], TiCl₄ [18], triethylamine [19], basic γ -alumina [10],

MgO [9], heteropolyacids [20], basic ionic liquids [21], iodine/K₂CO₃ [22]. The methods reported previously for the synthesis of chromene derivatives suffer from severe disadvantages such as long reaction times, hazardous organic solvents, complex work-up and purification, strongly acidic conditions, high temperatures and inadequate yields. Based on the above information and due to our interest in developing synthetic strategies for the construction of heterocyclic compounds, we have now used aspartic acid-catalyzed condensation as a new rapid method affording excellent yields for the synthesis of 2-amino-4*H*-chromenes under thermal solvent-free conditions.

EXPERIMENTAL

Instruments

Melting points were determined with an Electrothermal 9100 apparatus. Elemental analyses were performed using a Heraeus CHN-O-Rapid analyzer. Mass spectra were recorded on a FINNIGAN-MAT 8430 mass spectrometer operating at an ionization potential of 70 eV. IR spectra were recorded on a FT-IR-JASCO-460 plus spectrometer.

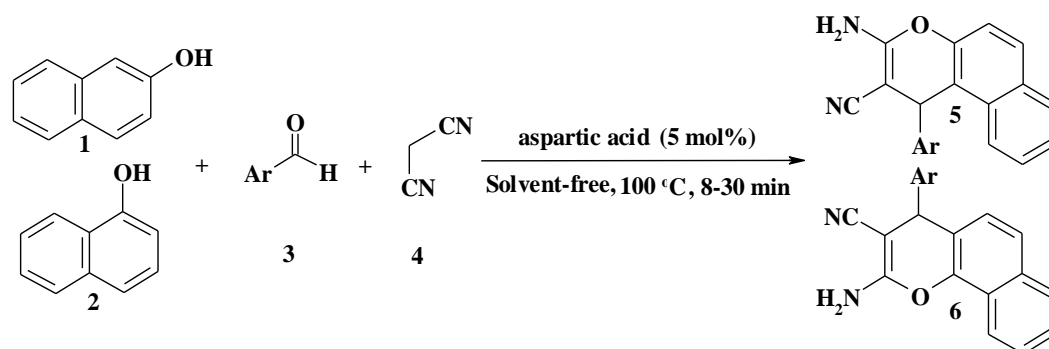
The NMR spectra were obtained on a Bruker Avance DRX-400 FT spectrometer (¹H NMR at 400 Hz, ¹³C NMR at 100 Hz) using DMSO-d₆ as solvent with TMS as internal standard.

General experimental procedure

Aspartic acid (5 mol%) was added to a mixture of 1-naphthol or 2-naphthol (1 mmol), aryl aldehyde (1 mmol), and malononitrile (1 mmol), the reaction mixture was heated to 100°C and maintained for the appropriate time (Table 2). The progress of the reaction was followed by TLC (hexane:ethylacetate).

* To whom all correspondence should be sent:

E-mail: kh_khandan_barani@yahoo.com



Scheme 1. Synthesis of 2-amino-4H-chromenes in the presence of aspartic acid under thermal, solvent-free conditions.

Table 1. Evaluation of the activity of different catalysts for synthesis of 2-amino-4H-chromene derivatives

Entry	Catalyst	Conditions	Yield ^a /%
1	Tetrabutyl ammonium chloride	H ₂ O/reflux	95
2	Tetrabutyl ammonium fluoride	H ₂ O/reflux	88
3	Fe(HSO ₄) ₃	CH ₃ CN/reflux	86
4	H ₁₄ [NaP ₃ W ₃₀ O ₁₁₀]	H ₂ O/reflux	93
5	Methanesulfonic acid	CH ₃ CN/reflux	90
6	Aspartic acid	Solvent-free/ 100°C	85-97 [This work]

^a Yields of the isolated products

Table 2. Optimization of the reaction conditions for synthesis of **5a**

Entry	Catalyst (amount, mol%)	T(°C)	Time (h)	Yield (%)
1	Aspartic acid (0)	50	24	-
2	Aspartic acid (0)	100	24	Trace
3	Aspartic acid (2.5)	30	12	10
4	Aspartic acid (2.5)	65	5	45
5	Aspartic acid (2.5)	80	3	65
6	Aspartic acid (2.5)	100	1	75
7	Aspartic acid (2.5)	125	1	75
8	Aspartic acid (5)	100	½ (30 min)	92
9	Aspartic acid (10)	100	½ (30 min)	92
10	Aspartic acid (15)	100	½ (30 min)	85

After the completion of the reaction, the mixture was washed with H₂O (3×10 mL) and filtered to remove the catalyst. The crude product was recrystallized from hot ethanol to obtain the pure compound.

RESULTS AND DISCUSSION

In continuation of our studies on MCRs [23-27] we report here the reaction between 2-naphthol **1** or 1-naphthol **2**, aryl aldehydes **3**, and malononitrile **4** in the presence of a catalytic amount of aspartic acid under thermal, solvent-free conditions. (Scheme 1). Aspartic acid was used for preparation of 2-amino-4H-chromenes. In order to establish the better catalytic activity of aspartic acid, we have compared the reaction using other catalysts. The results are listed in Table 1.

Initially, we began with the condensation of 2-naphthol (1 mmol), benzaldehyde (1 mmol) and

malononitrile (1 mmol) in solvent-free conditions at 50°C for 24 h in the absence of catalyst, which led to very poor yield of 3-amino-1-phenyl-1H-benzo[*f*]chromene-2-carbonitrile. To enhance the yield of the desired product the temperature of the reaction was increased to 100°C but no appreciable increment in the product yield was observed. Then, it was thought worthwhile to carry out the reaction in the presence of organocatalyst aspartic acid. We also evaluated the amount of catalyst required for this transformation and it was found that using 2.5 mol%, 5 mol%, 10 and 15 mol% catalyst, the maximum yield (92%) was obtained when the reaction mixture was loaded with 5 mol% of the catalyst (Table 2). Further increasing of the amount of catalyst loading affects the yield and slightly slows down the reaction. The detailed results obtained are given in Table 2.

Table 3. Reaction between 1-naphthol or 2-naphthol, aryl aldehydes and malononitrile in the presence of a catalytic amount of aspartic acid under thermal, solvent-free conditions.

Product	Naphthol	Ar	Time (min)	Yield (%) ^a	m.p. (° C)
6a	1-naphthol	C ₆ H ₅	20	93	212-214
6b	1-naphthol	4-Cl-C ₆ H ₄	8	97	230-232
6c	1-naphthol	3,4-(CH ₃ O) ₂ C ₆ H ₃	25	89	211-213
6d	1-naphthol	2-Cl-C ₆ H ₄	10	95	237-239
6e	1-naphthol	4-NO ₂ -C ₆ H ₄	8	96	190-192
5a	2-naphthol	C ₆ H ₅	30	92	279-281
5b	2-naphthol	4-Cl-C ₆ H ₄	10	95	208-210
5c	2-naphthol	2-Cl-C ₆ H ₄	10	94	262-264
5d	2-naphthol	2,4-(Cl) ₂ C ₆ H ₃	8	95	241-243
5e	2-naphthol	4-Br-C ₆ H ₄	8	97	243-245
5f	2-naphthol	4-CH ₃ -C ₆ H ₄	15	90	181-183
5g	2-naphthol	3,4-(CH ₃ O) ₂ C ₆ H ₃	30	85	143-145
5h	2-naphthol	4-CH ₃ O-C ₆ H	15	87	181-183
5i	2-naphthol	4-NO ₂ -C ₆ H ₄	10	95	186-188
5j	2-naphthol	3-CH ₃ O-C ₆ H ₄	20	93	259-261
5k	2-naphthol	3-HO-C ₆ H ₄	25	91	282-284
5l	2-naphthol	2-HO-4-NO ₂ -C ₆ H ₃	15	88	225-227

^a Yields refer to the pure isolated products

To study the scope of the reaction, a series of aromatic aldehydes, malononitrile and 1-naphthol or 2-naphthol catalyzed by aspartic acid under thermal, solvent-free conditions were examined. The results are shown in Table 3. In all cases, the aromatic aldehyde substituted with either electron-donating or electron-withdrawing groups underwent the reaction smoothly and gave products in excellent yields. Compound **5l** is new and its composition and structure were deduced by elemental and spectral analysis. The mass spectrum of compound **5l** showed a molecular ion peak at m/z 359. The ¹H-NMR spectrum of compound **5l** exhibited a methine proton signal at 5.36 ppm. The OH proton was observed at 11.01 ppm and a singlet signal at δ 9.23 ppm for the NH₂ hydrogen atoms, which disappears after addition of some D₂O. Also

observed were multiplets between 7.26 and 8.16 ppm which are related to aromatic protons. The ¹³C-NMR spectrum of compound **5l** showed 20 signals in agreement with the proposed structure, the IR spectrum also supported the suggested structure.

In summary, we have shown that aspartic acid has advantages in the preparation of 2-amino-4*H*-chromenes such as short reaction times, simple work-up, aerobic conditions, non-hazardous, green catalyst and affords excellent yield. The present method does not involve any hazardous organic solvent. Therefore, this procedure could be classified as green chemistry.

3-Amino-1-(2-hydroxy-4-nitrophenyl)-1H-benzof[f]chromene-2-carbonitrile (5l). Yellow solid; FTIR (ν_{\max} , cm⁻¹): 3422, 3346, 2197 1657 and

1590; ¹H NMR (DMSO-d₆), δ: 11.01 (s, 1H, OH), 9.23 (s, 2H, NH₂), 7.26-8.16 (m, 9H, Ar-H), 5.36 (s, 1H, CH) ppm; ¹³C NMR (DMSO-d₆), δ: 58.4, 97.6, 106.5, 113.0, 119.4, 121.8, 122.1, 122.3, 122.6, 124.1, 126.6, 130.1, 131.3, 131.7, 133.9, 143.9, 149.3, 158.9 ppm; MS (m/z, %): 359 (7); Analyses: Calcd. for C₂₀H₁₃N₃O₄: C, 66.85; H, 3.65; N, 11.69. Found: C, 66.98; H, 3.80; N, 11.85%.

REFERENCES

1. A. Nefzi, J.M. Ostresh, R.A. Houghten, *Chem. Rev.*, **97**, 449 (1997).
2. L. Weber, *Drug Dis. Today*, **7**, 143 (2002).
3. R.V.A. Orru, M. de Greef, *Synthesis*, 1471 (2003).
4. S. Bräse, C. Gil, K. Knepper, *Bioorg. Med. Chem.*, **10**, 2415 (2002).
5. C.O. Kappe, *QSAR Comb. Sci.*, **22**, 630 (2003).
6. J.B. Harborne, T.J. Mabry (eds.), *The Flavanoids - Advances in Research*, Chapman & Hall, London, 1982.
7. W. Sun, L.J. Cama, E. T. Birzin, S. Warriar, L. Locco, R. Mosley, M.L. Hammond, S.P. Rohrer, *Bioorg. Med. Chem. Lett.*, **16**, 1468 (2006).
8. L. Bonsignore, G. Loy, D. Secci, A. Calignano, *Eur. J. Med. Chem.*, **28**, 517 (1993).
9. D. Kumar, V.B. Reddy, B.K. Mishra, G.R. Rana, N. Mallikarjuna, R. Nadagouda, S. Varma, *Tetrahedron*, **63**, 3093 (2007).
10. R. Maggi, R. Ballini, G. Sartori, *Tetrahedron Lett.*, **45**, 2297 (2004).
11. D.R. Anderson, S. Hegde, E. Reinhard, L. Gomez, W.F. Vernier, L. Lee, S. Liu, A. Sambandam, P. A. Snider, L. Masih, *Bioorg. Med. Chem. Lett.*, **15**, 1587 (2005).
12. W. Kemnitzer, S. Kasibhatla, S. Jiang, H. Zhang, J. Zhao, S. Jia, L. Xu, C. Crogan-Grundy, R. Denis, N. Barriault, L. Vaillancourt, S. Charron, J. Dodd, G. Attardo, D. Labrecque, S. Lamothe, H. Gourdeau, B. Tseng, J. Drewe, S.X. Cai, *Bioorg. Med. Chem. Lett.*, **15**, 4745 (2005).
13. W. Kemnitzer, J. Drewe, S. Jiang, H. Zhang, Y. Wang, J. Zhao, S. Jia, J. Herich, D. Labrecque, R. Storer, K. Meerovitch, D. Bouffard, R. Rej, R. Denis, C. Blais, S. Lamothe, G. Attardo, H. Gourdeau, B. Tseng, S. Kasibhatla, S.X. Cai, *J. Med. Chem.*, **47**, 6299 (2004).
14. R. Ballini, G. Bosica, M.L. Conforti, R. Maggi, A. Mazzacanni, P. Righi, G. Sartori, *Tetrahedron*, **57**, 1395 (2001).
15. T. S. Jin, J.C. Xiao, S.J. Wang, T.S. Li, *Ultrason. Sonochem.*, **11**, 393 (2004).
16. R. Ballini, F. Bigi, M.L. Conforti, *Catal. Today*, **60**, 305 (2000).
17. X. Wang, D. Shi, S. Tu, *Synth. Commun.*, **34**, 509 (2004).
18. B. Sunil Kumar, N. Srinivasulu, R. Udipi, B. Rajitha, Y. Thirupathi Reddy, P. Narsimha Reddy, P. Kumar, *Russ. J. Org. Chem.*, **4**, 1813 (2006).
19. A.M. Shestopalov, Y.M. Emelianova, *Russ. Chem. Bull.*, **51**, 2238 (2002).
20. M.M. Heravi, Kh. Bakhtiari, V. Zadsirjan, F.F. Bamoharram, M.O. Heravi, *Bioorg. Med. Chem. Lett.*, **17**, 4262 (2007).
21. K. Gong, H.L. Wang, Z-L. Fang Liu, *Catal. Commun.*, **9**, 650 (2008).
22. Y. M. Ren, Ch. Cai, *Catal. Commun.*, **9**, 1017 (2008).
23. K. Khandan-Barani, M. Kangani, M. Mirbaluchzahi, Z. Siroos, *Inorg. Nano-Metal Chem.*, **5**, 751 (2017).
24. K. Khandan-Barani, M. T. Maghsoodlou, A. Hassanabadi, M.R. Hosseini-Tabatabaei, J. Saffari, M. Kangani, *Res. Chem. Intermed.*, **41**, 3011 (2015).
25. A. Motamedi-Asl, K. Khandan-Barani, *Iran. J. Catal.*, **5**, 339 (2015).
26. M.T. Maghsoodlou, K. Khandan-Barani, N. Hazeri, S.M. Habibi-Khorassani, A.C. Willis, *Res. Chem. Intermed.*, **40**, 779 (2014).
27. M. T. Maghsoodlou, N. Hazeri, K. Khandan-Barani, S. M. Habibi-Khorassani, A. Abedi, *J. Heterocycl. Chem.*, **51**, E152 (2014).

Reduction of nitro compounds using copper as catalyst in dioxolane medium

Vinaya, Sumana Y. Kotian, K. M. Lokanatha Rai

Department of Studies in Chemistry, University of Mysore, Manasagangotri, Mysuru, Karnataka, India

Received July, 4, 2018; Revised April 13, 2019

Reduction of aromatic nitro compounds using copper as catalyst is reported in this paper. This novel method is simple, ecofriendly and does not make use of any acidic/basic medium for the reduction. Water is added along with dioxalane solvent making it more suitable and versatile.

Keywords: Aromatic nitro compounds, copper, dioxolane, nitrophthalic acid.

INTRODUCTION

Reduction of aromatic nitro compounds into their respective amines is of great interest as they are being used as important scaffolds for the synthesis of biologically potent molecules [1]. They have also found applications in the preparation of agricultural chemicals and dyes. Various procedures have been reported in the literature; selective reduction is an extremely demanding task as the reduction sometimes stops at the formation of intermediate azoarenes, hydrazines and hydroxylamines [2]. Of late, few methods are reported involving metal nanoparticles of Ag in NaBH_4 [3], using coinage metal nanoparticles - Au, Ag, Cu/aqueous NaBH_4 [4], copper/cobalt phthalocyanines were used as catalysts for the reduction [5], gold nanoparticles supported on TiO_2 or $\text{Fe}_2\text{O}_3/\text{H}_2$ [6], carbon nanofiber held on platinum and palladium nanoparticles [7], bimetallic Pt-Ni nanoparticles [8], polymer-supported nanostructured platinum carbonyl clusters [9], copper nanoparticles along with ammonium formate in ethylene glycol [10], Ir, Pt, and Pd supported on carbon as catalysts [11], Pt/ CaCO_3 or Pt/C- H_3PO_4 [12]. There have been reports for the use of copper for conjugate reduction [13], cationic copper/pybox catalyst for the reduction of secondary amides [14] using tetramethyldisiloxane (TMDS) in the presence of copper complexes [15], copper carbene complex for the conjugate reduction of α,β -unsaturated carbonyl compounds [16], nickel chloride supported on natural phosphate [17], copper nanoparticles under ultrasound and microwave irradiation [18].

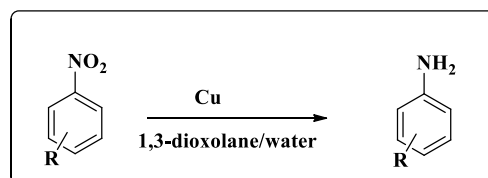
The earlier reports of the aromatic nitro compounds using zinc and tin indicate that the reaction is dependent on pH of the reaction medium. Our research group has reported the use of iron [19] and zinc [20] in previous reports. Herein, we report a novel method for the reduction of

aromatic nitro compounds using copper powder in 1,3-dioxolane in presence of water. The reaction is accomplished in neutral medium and proceeds with excellent chemoselectivity and yield. This reaction avoids the use of acids/acidic medium for the reduction of nitro compounds.

MATERIALS AND METHODS

All the reaction precursors, aromatic nitro compounds, copper turnings and solvents were obtained from SRL, India and were used without any further purification. The completion of reaction and formation of the products were monitored by thin layer chromatography (TLC) carried out on aluminium sheets coated in Merck Kieselgel silica gel 60, procured from Merck India. The boiling points and melting points of the formed products were determined by the boiling and melting point apparatus (Campbell Electronics, Mumbai, India). All the products formed are known and reported and their authenticity was confirmed and compared to authentic compounds obtained from Sigma-Aldrich, Mumbai. Purification was done by column chromatography carried out using silica gel (60–120 mesh) as the stationary phase.

And the temperatures which are mentioned in the procedure refer to the temperature of the oil bath used for heating.



Scheme 1. General procedure for reduction of aromatic nitro compounds to aromatic amines.

Aromatic nitro compound (1.0 g, 0.08 moles) was refluxed with copper (5.0 g, 0.08 moles) in dioxalane (7 mL) in the presence of catalytic amount of water (0.5 mL) for 15- 40h with different

* To whom all correspondence should be sent:
E-mail: kmlrai@yahoo.com

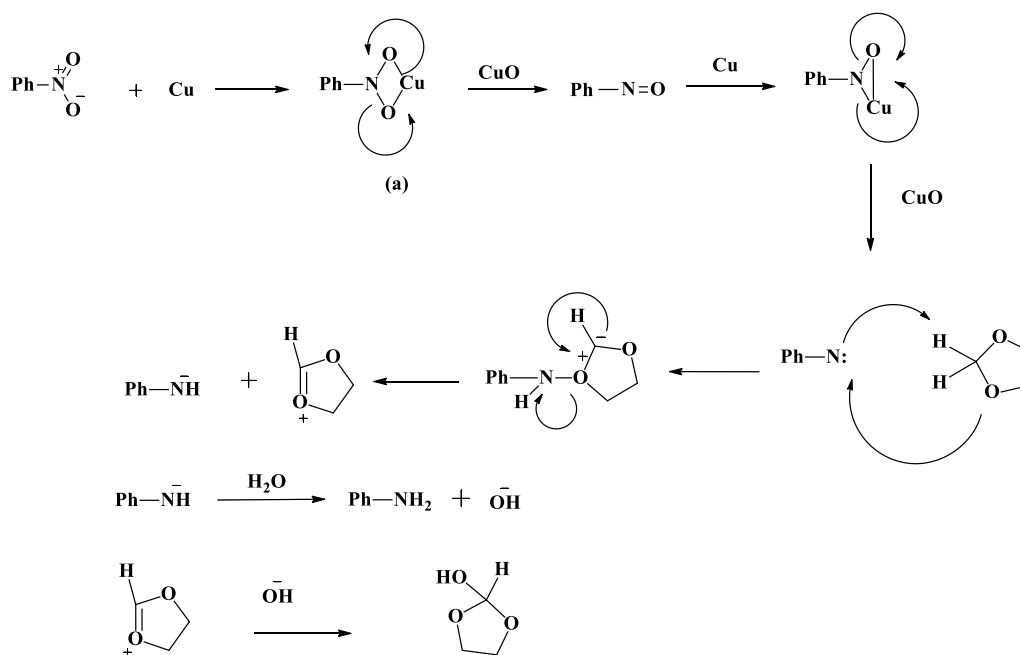
Vinaya, Sumana Y. Kotian, K. M. Lokanatha Rai: Reduction of nitro compounds using copper as catalyst in dioxolane... nitro compounds. The completion of the reaction was monitored using TLC. After the reaction was completed, the reaction mixture was filtered off to remove the residue (formed from catalyst). The filtrate was extracted with ether and acidified with 5% HCl and the aqueous layer was separated and neutralized with 5% NaOH. The reduced compound was then re-extracted with ether and was concentrated under reduced pressure using a rotary evaporator. The crude product was purified by column chromatography. The pure product obtained was identified by TLC and was compared with the reported products.

RESULTS AND DISCUSSION

Reduction was carried out by reacting a mixture of aromatic nitro compound (1 mole) and copper (0.05-0.08 moles) in presence of 1,3-dioxolane-water, as a solvent under reflux temperature for 15 to 40 h. Copper (II) oxide which was formed as a valuable byproduct was separated by filtration. 1,3-dioxolane/water mixture was easily recovered by vacuum distillation and reused. In general, our desired product aromatic amines were obtained in 75-90% yield. We further observed that the reaction did not proceed in the absence of water. We also observed that, when 1,3-dioxolane was replaced by other water-miscible solvents like DMSO, acetonitrile, methanol, etc., the reaction was not activated. This method has several advantages like:

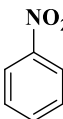
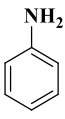
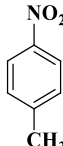
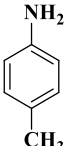
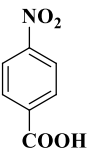
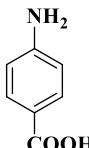
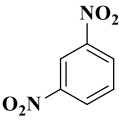
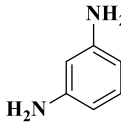
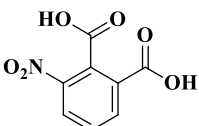
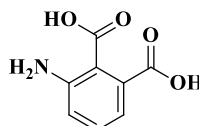
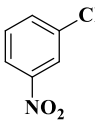
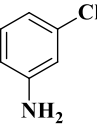
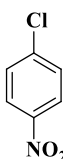
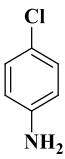
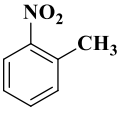
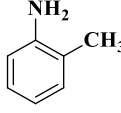
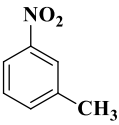
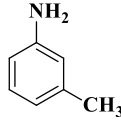
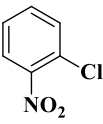
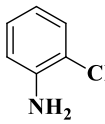
the reduction avoids corrosive media, it makes use of an environmentally friendly solvent, and the most important benefit is, it selectively reduces nitro group in the presence of other reducible groups and it avoids the use of hydrogen under pressure and expensive catalysts. Recycling of solvents and easy work up makes it an ideal method for the reduction of aromatic nitro compounds. During the reduction, functional groups like methoxy, cyano, ester, chloro, amide, alkene and keto groups are tolerated.

Proposed mechanism for the reduction of nitro compounds to amines is given below in Scheme 2. First step involves the oxidative addition of metal to nitro compound leading to the formation of intermediate (a), which undergoes retrocycloaddition to form a nitroso derivative and one molecule of CuO. Further, another Cu atom adds to the nitroso derivative which eliminates a molecule of CuO to form the unstable nitrene intermediate. In presence of dioxolane, nitrene pulls out a proton as depicted in the scheme. The driving force for the reaction could be the coordination of 1,3-dioxolane with copper in oxidative addition intermediate (a). The formation of intermediate nitroso compound was detected by GC. GC also showed the formation of a minor amount of azoxy compounds probably by the reaction of nitrene with the nitroso derivative.



Scheme 2. Probable mechanism.

Table 1. Reduction of aromatic nitro compounds to corresponding amines

Entry	Nitro compound	Time (h)	Product	Yield %	B.p. (lit.) °C	B.p. (obs) °C	M.p. (lit.) °C	M.p. (obs.) °C
1		38		70	184.1	184	-	-
2		20		80	200	199.5	-	-
3		23		75	-	-	187	187
4		15		85	282	282	-	-
5		40		78	-	-	180	178
6		14		73	96	95.5	-	-
7		15		75	232	232.2	-	-
8		18		72	201	201.5	-	-
9		20		74	203	202.5	-	-
10		21		71	209	208.9	-	-

CONCLUSION

In conclusion, we have reported a novel method for the reduction of aromatic nitro compounds. The reported method has several advantages like: the reduction avoids corrosive media, it makes use of an environmentally friendly solvent, and the most important benefit is that, it selectively reduces nitro group in the presence of other reducible groups. The method avoids the use of hydrogen under pressure and expensive catalysts. Recycling of solvents and easy work up makes it an ideal method for the reduction of aromatic nitro compounds.

Acknowledgement: The authors would like to express their gratitude to the University of Mysore for providing the laboratory facility to carry out this work.

REFERENCES

1. H. I. Subbagh, *European Journal of Medicinal Chemistry, Karnataka*, 4324 (2011).
2. C. Yu, B. Liu, L. Hu, *J. Org. Chem.*, **66**, 919 (2001).
3. N. Pradhan, A. Pal, T. Pal, *Colloids and Surfaces A, Physicochemical and Engineering Aspects*, **196**, 247 (2002).
4. N. Pradhan, A. Pal, T. Pal, *Langmuir*, **17**, 1800 (2001).
5. U. Sharma, P. Kumar, N. Kumar, V. Kumar, B. Singh, *Adv. Synth. Catal.*, **352**, 1834 (2010).
6. A. Corma, P. Serna, *Science*, **313**, 332 (2006).
7. M. Takasaki, Y. Motoyama, K. Higashi, S.H. Yoon, I. Mochida, H. Nagashima, *Org. Lett.*, **10**, 1601 (2008).
8. S. K. Ghosh, M. Mandal, S. Kundu, S. Nath, T. Pal, *Applied Catalysis A: General*, **268**, 61 (2004).
9. P. Maity, S. Basu, S. Bhaduri, G. K. Lahiri, *Adv. Synth. Catal.*, **349**, 1955 (2007).
10. A. Saha, B. Ranu, *J. Org. Chem.* **73**, 6867 (2008).
11. I. A. Makaryan, V. I. Savchenko, *Stud. Surf. Sci. Catal.*, **75**, 2439 (1993).
12. U. Siegrist, P. Baumeister, H.U. Blaser, *Chem. Ind.* **75**, 207 (1998).
13. Y. Moritani, D. H. Appella, V. Jurkauskas, S. L. Buchwald, *J. Am. Chem. Soc.* **122**, 6797 (2000).
14. Sh. Das, B. Join, K. Junge, M. Beller, *Chem. Commun.*, **48**, 2683 (2012).
15. Y. Li, Sh. Das, Sh. Zhou, K. Junge, M. Beller, *J. Am. Chem. Soc.* **134**, 9727 (2012).
16. V. Jurkauskas, J. P. Sadighi, S. L. Buchwald, *Org. Lett.*, **5**, 14 (2003).
17. A. Baba, H. Ouahbi, A. Hassine, J. Sebti, L. Laasri, S. Sebti, *Mediterranean Journal of Chemistry*, **7**(5), 317 (2018).
18. H. Feng, Y. Li, Sh. Lin, E. Van der Eycken, G. Song, *Sustainable Chemical Processes*, **2**, 14 (2014).
19. M. Vishwanath S, Sumana Y. Kotian, K. M. Lokanatha Rai, *Journal of Chemistry and Chemical Sciences*, **8**(5), 904 (2018).
20. P. Sunil Kumar, K. M. Lokanatha Rai, *Chemical Papers*, **66**, 772 (2012).

Proximate (lipid, moisture, ash) levels and fatty acid profiles in edible parts of common cuttlefish (*Sepia officinalis*, L., 1758) from different geographical areas

A. Ozyilmaz^{1*}, O. Duysak², D. Bozdogan Konuskan³

¹Iskenderun Technical University, Faculty of Marine Science and Technology, Department of Marine Technologies, Iskenderun/Hatay, Turkey

²Iskenderun Technical University, Faculty of Marine Science and Technology, Department of Basic Science, Iskenderun/Hatay, Turkey

³Mustafa Kemal University, Faculty of Agriculture, Department of Food Science Engineering, Hatay, Turkey

Received June 19, 2018; Revised June 17, 2019

Proximate (lipid, moisture, ash) levels and fatty acid compositions of common cuttlefish (*Sepia officinalis*) from different geographical areas along the Eastern Mediterranean coasts of Turkey (Fethiye, Antalya, Gazipasa, Anamur, and Iskenderun) were evaluated. The average total saturated fatty acids (SFA) ranged from 30.5% to 33.2%. The major SFA components were C16:0 (ranging from 18.2 to 20.74%) and C18:0 (ranging from 7.46 to 8.70%) for all sampling points. The average levels of mono unsaturated fatty acids (MUFA) of specimens from Iskenderun, Fethiye, Antalya, Gazipasa, and Anamur were calculated to be 12.17%, 12.05%, 10.75%, 10.32%, and 10.05%, respectively. Among major fatty acids of the MUFA, the highest and lowest levels of C18:1n9 were calculated to be 4.26% in Fethiye and Anamur, respectively. Polyunsaturated fatty acids (PUFA) level from all of the mantle part of common cuttlefish was calculated to be higher than 55%. The highest amounts of arachidonic acid (ARA, C20:4n6), eicosapentaenoic acid (EPA, C20:5n3), and docosahexaenoic acid (DHA, C22:6n3) were observed in Anamur, Fethiye, Gazipasa with the values of 6.76%, 16.57%, and 29.69%, respectively. It was concluded that the proximate (lipid, moisture, ash) levels and fatty acid components of the cuttlefish had been affected from different geographical areas and have high quality unsaturated fatty acids (e.g., PUFA, DHA, EPA) which are described as essential fatty acids required for a healthy life.

Keywords: *Sepia officinalis*, Mediterranean, fatty acid, DHA, EPA

INTRODUCTION

European common cuttlefish is the best known cephalopod native in all European and Mediterranean waters [1]. Cephalopods are not only very valuable food items for human beings but also very important nutritional source for the predators in the sea. Common cuttlefish is the mainly fished cephalopod in the Mediterranean [2,3].

Compared to other sea creatures, common cuttlefish has a relatively short life span around two years. They have the ability to grow fast because of their carnivore diet and metabolic activity [4]. Mature common cuttlefish die after spawning, generally in spring (Boletzky 1983; Dunn 1999 cited in [14]).

Of marine invertebrates, common cuttlefish is considered to be one of the commercially important fish with high prices in Turkish coastal waters, as well as all around the world. According to reports of Fisheries statistics [5], approximately 1.163, 1.396, and 1.244 tons of cuttlefish were captured in Turkey in 2011, 2012, and 2013, respectively.

Nowadays, because common cuttlefish contain the omega 3 fatty acids such as C20:5n3 (EPA) and

C22:6n3 (DHA), they are appreciated for their many beneficial health effects.

Fish lipids are constituents of different lipid classes such as phospholipids, partial glycerides, free fatty acids, and esters. They are found in fish and in other sea products including shrimp, octopus, squids, and cuttlefish. Previous research has pointed out that cuttlefish is low in fat. Major part of the lipids is a valuable source of essential fatty acids. Although there are a few research studies on cuttlefish [6-10], there exists very limited information about the biochemical characteristics of cuttlefish from different geographical areas along coasts of the Mediterranean. The objective of the present study is to investigate the possible effects of different geographical areas along the coasts of eastern Mediterranean on lipid contents, moisture amounts, ash levels, and fatty acid compositions of common cuttlefish (*Sepia officinalis*).

EXPERIMENTAL

Sample collection

Five different coasts which are also important bays (Fethiye, Antalya, Gazipasa, Anamur, and Iskenderun) along Eastern Mediterranean in Turkey (Figure 1) were selected to obtain cuttlefish for the present study.

* To whom all correspondence should be sent:

E-mail: ayse.ozyilmaz@iste.edu.tr,

ozyilam@yahoo.com

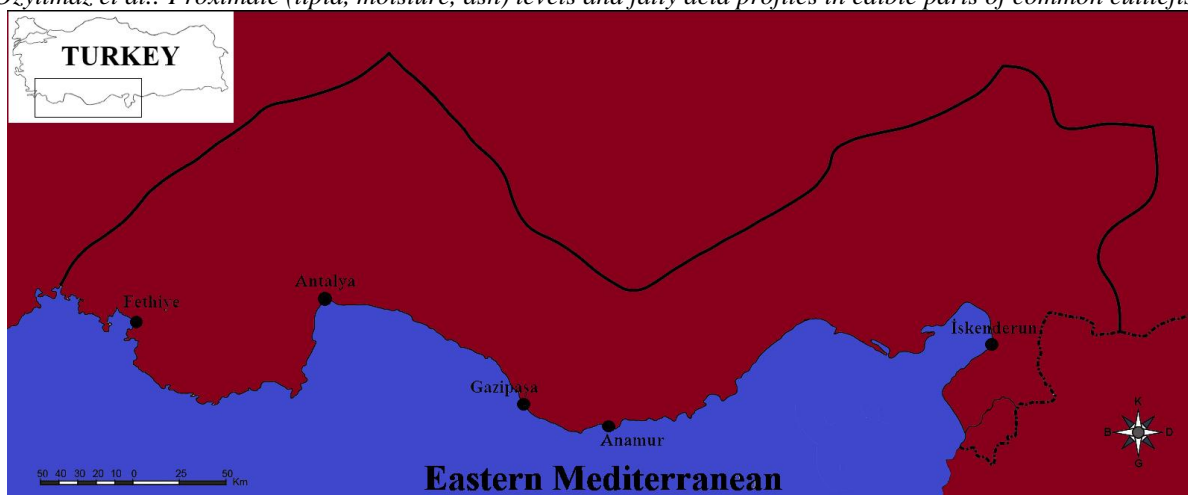


Figure 1. Sampling area (Fethiye, Antalya, Gazipaşa, Anamur, and Iskenderun) along the Eastern Mediterranean.

Of a total of 50 samples used in the present study, only five randomly selected samples from each coast were measured morphometrically, the measurements of which are shown in Table 1. The common cuttlefish are highly captured and the most frequently consumed fish in the selected areas. The fish were bought from fish markets in April 2014 on the same day when they were caught, placed on ice, and immediately transferred to the laboratory. The mantle parts (the main edible portion) were removed for the analyses right after body measurements. The mantle length (ML) was measured with a digital Caliper (0.01mm, Mitutoyo/Japan). The body weights were determined with a precision close to 0.01.

Moisture and ash contents

Moisture and ash contents of the cuttlefish were determined according to the recommended method (Commission of European Communities) ISOR 1442 (CEC, 1979) [20] and AOAC 35.1.14 (2003) [21] method no 938.08, respectively.

Lipid extraction, fatty acid methyl esters (FAME) preparation and column conditions

Lipid extraction was carried out according to the modified Bligh and Dyer method [11]. A detailed information about lipid extraction is given in Özyılmaz and Öksüz (2015) [19]. The conversion and separation of FAMES was performed as described in Ozyilmaz (2016) [12]. Fatty acid profiles of cuttlefish from Fethiye, Antalya, Gazipaşa, Anamur, and Iskenderun were determined by GC-MS (gas chromatography-mass spectrometry) using a Hewlett Packard GC (model 6890) and coupled with Hewlett Packard (model 5972A, HP 6890 system) MS detector. Separations

of fatty acids were achieved with an HP-INNOWAX. Polyethylene glycol capillary column model number: HP 19091N-136, nominal length: 60.0 m, nominal diameter: 250 μm , nominal film thickness: 0.25 μm) was used in this experiment. Split flow was maintained at 9.9 ml/min; total flow: 13.9 ml/min helium. The separation was performed using helium as carrier gas. The injector was maintained at 270°C with an injection volume of 1 μL in splitless mode with a total injection volume of 1 μl . The injector was washed three times with iso-octane post-injection, the injector program was also set to triple-wash before next injection. The initial column temperature was set at 120°C and held for 3 min, and then increased to 180°C with a 10°C per min ramp rate and held at this temperature for ten min. Then the temperature was increased again to 250°C with a 10°C per min ramp rate and held at this temperature for 17 min. The separation of the total fatty acids took a total of 43 min.

Statistical analysis

Data were subjected to analysis of variance (ANOVA) and mean comparison was carried out using Duncan's test. Significance was established at $P < 0.05$.

RESULTS AND DISCUSSION

The results of the morphological measurements and lipid analyses are presented in Table 1. The average mantle weight of cuttlefish from Fethiye, Antalya, Gazipaşa, Anamur, and Iskenderun which are along the coasts of Eastern Mediterranean varied from 258.80 to 72.40 g. The average mantle length of cuttlefish from Fethiye, Antalya, Gazipaşa, Anamur, and Iskenderun was 14.10, 12.02, 8.10, 11.38, and 12.00 cm, respectively.

Table 1. Morphological measurements and proximate contents of the cuttlefish

Locations	Mantle Length (cm)	Body Weight (g)	Lipid (%)	Ash(%)	Moisture(%)
Fethiye	14.10±1.56	258.80±71.02	1.38±0.01 ^a	1.60±0.06 ^a	75.42±0.72 ^a
Antalya	12.02±3.12	204.60±78.85	1.82±0.07 ^b	1.50±0.04 ^a	76.18±1.66 ^{b,c}
Gazipaşa	8.10±1.60	72.40±49.80	1.80±0.14 ^b	1.56±0.07 ^a	75.23±1.53 ^{b,c}
Anamur	11.38±2.21	169.00±49.95	1.70±0.05 ^b	1.76±0.08 ^a	77.28±1.02 ^c
İskenderun	12.00±0.80	178.00±27.43	0.89±0.09 ^c	1.64±0.06 ^a	75.82±0.34 ^{a,b}

Data represent means± standard deviation (n=5 for mantle length and body weight; n=3 for lipid, moisture, and ash) Means followed by different letters within the same row are significantly different (P<0.05).

Previous research set a standard on the age of cuttlefish. For example, 8.7 cm and 10.0 cm male and female cuttlefish from Antalya can be considered as adult cuttlefish [13, 14]. The standard sexual maturity lengths were calculated to be 12.04 cm for females and 10.30 cm for males in Iskenderun. Based on these standards set in previous studies, all cuttlefish collected from all sampling points in this study can be considered as adults.

The average moisture and ash contents of all sampling points (cuttlefish from Fethiye, Antalya, Gazipaşa, Anamur, and Iskenderun) were measured to be between 75.42±0.72% and 77.28±1.02% and between 1.50±0.04% and 1.76±0.08%, respectively (Table 1). The differences in the moisture contents of the cuttlefish were found to be statistically significant (P<0.05), except for ash contents (P>0.05). Similar findings regarding moisture and ash contents were reported by Ayas *et al.* (2012) [15] for male and female cuttlefish from Mersin in winter and spring.

Even though there seem to be slight differences among lipid levels, these differences were found to be statistically significant for cuttlefish collected from all five sampling points in terms of lipid levels regarding sampling points differences (P<0.05) in the present study. The mean total lipid contents of the cuttlefish's mantle from five different sampling points ranged from 1.82% to 0.89%. According to Ackman (1989) [16], fish having lipid lower than 2% can be classified as lean fish. Accordingly, all cuttlefish caught from 5 different sampling points in the current study can be considered as lean fish. On the other hand, Tir *et al.* (2015) [10] reported higher lipid levels for the same species from a different part of the Mediterranean (Rades, located in northern Tunisia). Fatty acid profiles (% of total fatty acids) of cuttlefish from the five sampling points are presented in Table 2. The fatty acids of cuttlefish from each sampling point were in the range of 30.48-33.21% for saturated fatty acids (SFA), 10.05-12.17% for monounsaturated fatty acids (MUFA), and 55.23-58.14% for polyunsaturated fatty acids (PUFA). The percentages of PUFA in cuttlefish from all sampling points were calculated to be higher

than the sum of the average levels of SFA and MUFA.

In all cuttlefish's fatty acid total amount, the highest proportions of two fatty acids were palmitic acid (C16:0, 18.20-20.74%), stearic acid (C18:0, 7.46-8.70%) in SFA, oleic acid, and 20:1n9 in MUFA. Additionally, the highest amounts of three fatty acids in cuttlefish were ARA, EPA, and DHA in PUFA. Regarding the highest levels of fatty acids in SFA, MUFA, and PUFA, the results in this study are in agreement with previously reported studies on cuttlefish fatty acids of cephalopods [6-10].

The cuttlefish from all sampling points were found to be rich in PUFA, which is in accordance with the previously reported values of PUFA [6-10]. Although the sums of PUFA contents of cuttlefish from five different sampling points differed from each other, especially the percentages of arachidonic acid (ARA, C20:4n6), eicosapentaenoic acid (EPA, C20:5n3), and docosahexaenoic acid (DHA, C22:6n3) were found to be very close to each other. The DHA levels of cuttlefish from Gazipasa and the EPA levels of cuttlefish from Gazipasa and Anamur statistically differed from all other sampling points (P<0.05). The levels of ARA in cuttlefish from all sampling points significantly differed from each other (P<0.05).

Ozogul *et al.* (2008) [8] studied cuttlefish from eastern Mediterranean in an area close to the sampling area of the present study in Iskenderun. Accordingly, seasonal changes of fatty acid compositions of cuttlefish along with other cephalopods data regarding levels of DHA were reported to be higher than those of DHA in the current study. Additionally, fatty acid level (in spring 29.5%, DHA) of cuttlefish reported by Ozyurt *et al.* (2006) [7] was higher than that of cuttlefish reported in the present study, except for cuttlefish from Gazipasa which was very close to the findings presented here. DHA levels of cuttlefish from all sampling points were calculated to be higher than 27%. Ozogul *et al.* (2009) [17] investigated fatty acid profiles of 34 marine water fish species from northeast Mediterranean.

Table 2. Fatty acids profiles (% of total fatty acids) of cuttlefish from five locations (Fethiye, Antalya, Gazipaşa, Anamur, and Iskenderun)

Fatty Acids	Locations				
	Fethiye	Antalya	Gazipaşa	Anamur	İskenderun
C14:0	1.72±0.01 ^a	1.68±0.05 ^a	1.43±0.03 ^b	1.15±0.00 ^c	1.17±0.02 ^c
C15:0	0.89±0.02 ^a	1.08±0.01 ^b	0.66±0.01 ^c	0.53±0.01 ^d	0.70±0.00 ^e
C16:0	19.92±0.67 ^{ab}	20.62±0.51 ^b	20.74±0.18 ^c	19.41±0.12 ^d	18.20±0.05 ^c
C17:0	1.57±0.01 ^a	1.71±0.04 ^b	1.37±0.01 ^c	1.16±0.02 ^a	1.71±0.06 ^b
C18:0	7.46±0.19 ^a	7.75±0.11 ^b	8.59±0.07 ^c	7.92±0.02 ^b	8.70±0.09 ^c
C20:0	0.42±0.10 ^a	0.36±0.01 ^{ab}	0.22±0.11 ^b	0.33±0.02 ^{ab}	0.49±0.08 ^a
Total SFA	31.98	33.21	33.00	30.48	30.97
C15:1	ND	0.22±0.01 ^a	0.08±0.11 ^b	0.21±0.04 ^a	0.20±0.05 ^a
C16:1n9	0.75±0.01 ^{ac}	0.77±0.02 ^b	0.27±0.27 ^b	0.56±0.00 ^a	0.69±0.06 ^c
C16:1n7	0.24±0.01 ^{ac}	0.21±0.01 ^{ac}	0.06±0.08 ^b	0.17±0.02 ^a	0.28±0.01 ^c
C17:1	0.42±0.20 ^a	0.42±0.23 ^a	0.25±0.04 ^a	0.45±0.08 ^a	0.65±0.14 ^a
C18:1n9	4.26±0.12 ^a	3.66±0.14 ^{c}	3.49±0.03 ^c	3.05±0.08 ^d	3.75±0.06 ^b
C18:1n7	2.12±0.24 ^{ab}	1.92±0.14 ^{ac}	1.62±0.01 ^c	1.81±0.05 ^{ac}	2.34±0.00 ^a
C20:1n9	3.52±0.09 ^a	2.97±0.00 ^b	4.21±0.04 ^c	3.17±0.02 ^d	3.48±0.03 ^a
C22:1n9	0.69±0.04 ^a	0.48±0.08 ^b	ND	0.34±0.11 ^b	0.78±0.10 ^a
C24:1n9	0.06±0.08 ^a	0.08±0.12 ^{ab}	0.36±0.06 ^a	0.32±0.13 ^b	ND
Total MUFA	12.05	10.75	10.32	10.05	12.17
C16:2n4	0.24±0.01 ^b ^a	0.26±0.06 ^b ^a	0.14±0.00 ^b	0.19±0.01 ^{bc}	0.28±0.00 ^a
C16:3n4	0.28±0.13 ^{ab}	0.31±0.01 ^b	0.15±0.01 ^a	0.14±0.01 ^a	0.24±0.03 ^{ab}
C16:4n1	1.21±0.18 ^a	1.79±0.02 ^b	1.33±0.08 ^{ac}	2.14±0.03 ^a	1.60±0.16 ^{cb}
C18:2n6	0.67±0.21 ^{ab}	0.66±0.16 ^{ab}	0.35±0.01 ^c	0.52±0.11 ^c	0.84±0.24 ^b
C18:3n6	0.46±0.29 ^a	0.38±0.13 ^a	0.25±0.01 ^a	0.22±0.01 ^a	0.52±0.19 ^a
C20:3n6	0.53±0.08 ^a	0.52±0.05 ^a	0.50±0.01 ^a	0.55±0.06 ^a	0.58±0.05 ^a
C20:4n6	3.94±0.19 ^a	3.67±0.06 ^b	5.66±0.08 ^c	6.76±0.05 ^d	4.78±0.06 ^e
C22:2n6	ND	0.14±0.21 ^a	0.12±0.16 ^a	0.32±0.01 ^a	ND
C22:4n6	0.32±0.01 ^a	0.40±0.07 ^a	0.61±0.04 ^b	0.55±0.03 ^b	0.40±0.03 ^a
C22:5n6	0.78±0.03 ^a	0.87±0.01 ^b	1.06±0.12 ^b	1.60±0.02 ^c	0.81±0.01 ^b
C18:3n3	0.21±0.01 ^a	0.22±0.01 ^a	0.19±0.01 ^a	0.17±0.08 ^a	0.20±0.02 ^a
C18:4n3	0.19±0.27 ^a	0.08±0.11 ^a	ND	0.20±0.01 ^a	ND
C20:3n3	0.56±0.01 ^a	0.64±0.03 ^a	0.54±0.05 ^a	0.52±0.06 ^a	0.57±0.00 ^a
C20:5n3	16.57±0.68 ^a	16.13±0.41 ^a	13.42±0.25 ^b	14.25±0.21 ^b	15.61±0.10 ^a
C22:5n3	1.38±0.03 ^a	1.46±0.06 ^a	1.63±0.04 ^b	1.85±0.05 ^c	1.23±0.01 ^d
C22:6n3	27.90±0.17 ^a	27.70±0.47 ^a	29.69±0.84 ^b	28.20±0.18 ^a	27.62±0.40 ^a
Total PUFA	55.23	55.25	55.59	58.14	55.28
Total n6	6.70	6.65	8.53	10.50	7.94
Total n3	46.80	46.23	45.45	45.17	45.22
n6/n3	0.14	0.14	0.19	0.23	0.18
DHA/EPA	1,69	1,72	2,21	1,98	1,77
PUFA/SFA	1.73	1.66	1.68	1.91	1.78

Data represent means ± standard deviation (n=2). ND not detected.

Means followed by different letters within the same row are significantly different (P<0.05).

They found out that DHA levels of the fish were in the range of 3.31 to 31.03%. Only 2 fish species exceeded 27% and few ones were close to that level.

Comparing this previous information with the ones of the present study, one can say that cuttlefish from Fethiye, Antalya, Gazipaşa, Anamur, and

Iskenderun have higher DHA levels than many marine fish species. Based on the results of the present study and previous studies on fatty acid profiles of cuttlefish, lower lipid levels and higher DHA levels are distinctive characteristics for common cuttlefish. The average levels of EPA in cuttlefish from Fethiye (16.57%), Antalya (16.13%), and Iskenderun (15.61%) were close to each other ($P>0.05$) and higher than those of EPA in cuttlefish from Gazipaşa (13.42%) and Anamur (14.25%). EPA was the second-highest fatty acid in PUFA for the cuttlefish from all sampling points in this study. Similar results regarding EPA levels were observed in previously reported studies [7-10].

Additionally, the total MUFA levels of cuttlefish from all sampling points were calculated to be the lowest ones compared to the SFA and PUFA levels. In MUFA, oleic acid is the most widely distributed fatty acid and generally the highest fatty acid and supposed to be the deterministic fatty acid level of MUFA, especially, in muscle and liver oils of bony and cartilaginous fish [12,17-19].

The levels of 20:1n9 in MUFA were found to be slightly higher than those of oleic acid in lipids of all cuttlefish from two sampling points (Gazipaşa and Anamur). The levels of oleic acid found in lipids of all cuttlefish from three sampling points (Fethiye, Antalya, and Iskenderun) are still the highest fatty acid levels found in MUFA. However, the levels of oleic acid in cuttlefish are exceptionally low compared to bony fish oil. Similar results were observed in some cephalopods especially in cuttlefish [7,8]. Having low oleic acid compared to that of fish lipid could be a distinctive characteristic for cuttlefish. Additionally, the levels of stearic acid in cuttlefish from all sampling points were found to be higher than those of oleic acid. However, the levels of oleic acid are generally higher in bony fish oil. Similar results were observed in some cephalopods, especially in cuttlefish [7,8]. Having higher stearic acid compared to oleic acid level could be another distinctive characteristic for cuttlefish.

Moreover, the major fatty acids in SFA of cuttlefish from all sampling points were C16:0 (palmitic acid), C18:0 (stearic acid), C17:0 (heptadecanoic acid), and C14:0 (myristic acid). These results are in agreement with the results of previous studies on fatty acid composition of common cuttlefish [7,9]. Total average SFA and PUFA levels of all cuttlefish from all sampling points were also found to be higher than 30% and 55%, respectively. The ratio of PUFA/SFA was calculated to be 1.66-1.91, which is higher than the recommended minimum PUFA/SFA ratio by HMSO (1994) but in agreement with the previously reported study of Ozogul *et al.* (2008) [8].

In conclusion, lipid, moisture, ash levels, and fatty acid compositions of the cuttlefish from all sampling points diverged. Almost all sampling points in the current study affected the tested biochemical characteristics. These are probably the results of the biological and geographical conditions, e.g., environmental conditions, food availability and life stages. Stearic acid level in cuttlefish is considerably higher than that of oleic acid compared to bony fish. In general, the cuttlefish from eastern Mediterranean have low fat and rich unsaturated fatty acids, especially EPA and DHA. Different geographical areas seem to have an effect on proximate and fatty acids contents. Even if some individual fatty acids of cuttlefish were different or very close to each other, they are all good for health.

REFERENCES

1. C.F.E. Roper, M.J. Sweeney, C.E., Nauen, *FAO Spec. Catal. 3, FAO Fish. Syn.*, **125**, 277 (1984).
2. M.R. Dunn, *Fisheries Research*, **40**, 277 (1999).
3. J. Royer, G.J. Pierce, E. Foucher, J.P. Robin, *Fisheries Research*, **78**, 96 (2006).
4. P.G. Lee, *Marine and Freshwater Behav. Phys.*, **25**, 35 (1994).
5. TURKSTAT Fishery Statistics, Turkish Statistical Institute, Ankara, Turkey 2015.
6. S. Zlatanov, K. Laskaridis, C. Feist, A. Sagredos, *Molecular Nutri. Food Res.*, **50**, 967 (2006).
7. G. Ozyurt, O. Duysak, A. Akamca, C. Tureli, *Food Chem.*, **95**, 382 (2006).
8. Y. Ozogul, O. Duysak, F. Ozogul, A.S. Ozkutuk, C. Tureli, *Food Chem.*, **108**, 847 (2008).
9. Y. Özogul, *J. of Fisheries Sciences*, **6**, 99 (2012).
10. M. Tir, I. Rebeh, K. Telahigue, T. Hajji, H. Mejri, M. El Cafi, *J. Am. Oil Chem. Soc.*, **92**, 1643 (2015).
11. S.W.F. Hanson, J. Olley, *Proc. Biochem. Soc.*, **89**, 101 (1963).
12. A. Özyılmaz, *J. Appl. Ichthyol.*, **32**, 564 (2016).
13. R. Erdilal, M. Ünlüsayın, H. Gülyavuz, *Aegean J. Fish. and Aqua. Sci.*, **24**, 247 (2007).
14. Ö. Duysak, G. Özcan, Ş. Çek, C. Tureli, *Ind. J. Geo-Mar. Sci.*, **43**, 1689 (2014).
15. D. Ayas, Y. Ozogul, İ. Ozogul, Y. Uçar, *Int. J. of Food Sci. Nutr.*, **63**, 440 (2012).
16. R.G. Ackman, *Food and Nutr. Sci.*, **13**, 161 (1989).
17. Y. Özogul, F. Özogul, E. Çiçek, A. Polat, E. Kuley, *Int. J. Food Sci. Nutr.*, **60**, 464 (2009).
18. A. Özyılmaz, B. Palalı, *Yunus Research Bulletin*, **3**, 29 (2014).
19. A. Özyılmaz, A. Öksüz, *J. Ani. Plant Sci.* **25**, 160 (2015).
20. (CEC, 1979) EEC Recommended Oven Drying Method ISOR 1442, Commission of European Communities.
21. AOAC, 35.1.14 (2003 Official Methods of Analysis of the Association of Analytical Chemists), Washington, DC, edn. 15.

Adsorption of cobalt onto activated charcoal and its utilization for decolorization of bromocresol green dye

I. Khan^{1,2*}, N. Ur Rahman¹, A. Ali¹, K. Saeed^{1,2}

¹Department of Chemistry, University of Malakand, Chakdara, Dir (Lower), Khyber Pakhtunkhwa, Pakistan

²Department of Chemistry, Bacha Khan University, Charsadda, Khyber Pakhtunkhwa, Pakistan

Received July 27, 2018; Revised March 29, 2019

Activated charcoal was prepared from pine tree cones and was treated with 5M HNO₃ and HCl solutions. The acid-treated charcoals (ATC) were used for the adsorption of cobalt ions from aqueous solution and then utilized for the decolorization of bromocresol green (BG) dye in aqueous medium. The adsorption study revealed that ATC adsorbed 9.063 mg/g of cobalt within 2 h. The ATC and cobalt-adsorbed ATC (Co-ATC) were characterized by scanning electron microscopy (SEM), and energy dispersive X-ray spectroscopy (EDX). The SEM images showed that Co nanoparticles are adsorbed and dispersed on the surface of ATC. The presence of Co nanoparticles was also confirmed by EDX. The decolorization study was carried out using UV/Vis spectrophotometry and the results revealed that ATC decolorized 16.85% of the dye while Co-ATC decolorized about 40.5% of the dye within 12 h.

Key words: Adsorption, Activated carbon, Decolorization, Cobalt, Bromocresol green

INTRODUCTION

The presence of heavy metals in surface waters and wastewaters is a major source of aquatic pollution and is becoming a severe environmental and public health problem due to various industrial waste water discharges. Heavy metals have attained relatively more significance due to their persistence, bio-magnification and toxicity. Heavy metal-contaminated effluents come from various industries like mining, radiator manufacturing, alloy industries, metal electroplating, and storage batteries manufacturing industry [1, 2]. Various physical and chemical methods were proposed for the removal of these contaminants, such as membrane filtration, chemical precipitation, ion exchange and adsorption [3]. Among these methods, adsorption is the most suitable method because of profitability, low-cost adsorbents, ease of operation and efficiency [4]. Several adsorbents have been synthesized in the past in order to find out a sustainable and cost-effective way of removal of metals from the environment [5]. Activated carbons are the most potential adsorbents for heavy metal adsorption due to their high surface area, high adsorption capacity, micro porous character, chemical nature of their surface and can be prepared from various feedstocks' [6, 7].

Similarly, dyes are widely applied for various purposes in different industries because of their durability and effectiveness [8]. Dyes and pigments are discharged into waste water effluents from various industries like paper, food, leather, textile

and dye manufacturing industries. Due to their large size and complex structure, these coloring effluents are toxic and resistant to destruction [9]. The dye-containing waste waters are toxic to aquatic organisms, human beings and cause biological magnification, eutrophication, toxicity, non-aesthetic pollution and perturbation in aquatic life [10]. The treatment of wastewater containing dyes is a challenging task as most of the dyes are non-degradable and persist for a very long time [11]. If these pollutants are not removed from the effluents then the color and toxicity of dyestuffs may cause objectionable impact on the ecosystem [12].

Various physical, chemical, and biological methods such as adsorption, ozonation, precipitation, reverse osmosis, flocculation, precipitation and ultra filtration are used for the purification and removal of color from waste water [13]. Presently advanced oxidation processes (AOPs) such as H₂O₂/UV, O₃/UV and heterogeneous photocatalysis are widely used for waste water purification. Among these processes, heterogeneous photocatalysis is an effective method for the degradation of organic pollutants (such as dyes present in wastewater), which is based on UV-light irradiation [14]. For example Tolia *et al.* studied the photocatalytic degradation of malachite green dyes using doped and undoped ZnS nanoparticles [15].

In the present study, first Co was adsorbed onto ATC from aqueous solution and then it was utilized for the decolorization of bromocresol green (BG) dye in aqueous medium. BG is an anionic triphenylmethane dye, highly water-soluble and

* To whom all correspondence should be sent:
E-mail: idreeschem_uom@yahoo.com

hardly biodegradable [16]. Various approaches have been introduced for the removal of BG dye from waste water, for example Fassi *et al.* removed BG dye by various photochemical processes such as direct UV photolysis, acetone/UV and advanced oxidation processes ($\text{H}_2\text{O}_2/\text{UV}$ and $\text{S}_2\text{O}_8^{2-}/\text{UV}$) [17]. Similarly, Chaleshtori *et al.* photocatalytically degraded BG dye by using porous titanium–niobium oxide as a photocatalyst under UV light irradiation [18]. In this study the effect of several parameters such as irradiation time, catalyst dosage and recycled catalyst on dye removal was studied. The main aim of the present study is to remove both heavy metal and dye from water using a low-cost adsorbent. Firstly, the AC was used for the adsorption of Co from aqueous medium and then Co-ATC was utilized for the decolorization of BG dye in aqueous medium.

MATERIALS AND METHODS

Materials

Pine cones were collected around the University of Malakand. $\text{CoCl}_2 \cdot 6\text{H}_2\text{O}$ was supplied by Merck, Darmstadt, Germany and used as such without any further purification. HNO_3 was purchased from Sigma Aldrich. HCl (37%) was supplied by Riedel-de Haen. BG dye was purchased from Peking Chemical Works, Peking, China.

Charcoal synthesis and its activation

The pine cones were grinded into small pieces and then heated in a pressure cooker for 1 h. The obtained charcoal was grinded and sieved through a screener having 100 μm mesh size. 5 g of charcoal, 100 mL of HNO_3 (5M) and 100 mL of HCl (5M) were put in a reaction vessel and refluxed at 70 °C for 2 h. The sample was filtered and the obtained acid treated charcoal (ATC) was washed several times with deionized water in order to remove acids from charcoal.

Adsorption of Co onto acid-treated activated charcoal

15 mL of cobalt chloride solutions of different concentrations (100, 200, 300 and 400 ppm) were taken separately in vials and then 0.2 g of ATC were added in each vial and shaken on a mechanical shaker for 2 h. The adsorption was performed at neutral pH, room temperature with a shaking speed of 60 Hz. The Co-ATC was separated by centrifugation and maximum adsorption capacity was determined by atomic adsorption spectrometry.

10 mL of BG (250 ppm) and 0.02 g of Co-ATC were put in a 50 mL beaker and kept under UV-light irradiation (254 nm, 15 W) under constant stirring. After a specific irradiation time, the catalyst was separated from the irradiated dye through centrifugation at a speed of 1200 rpm for 10 min. The catalyst was recycled by washing several times with distilled water through sonication and then dried in an oven at 80 °C. The recycled catalyst was reused for the decolorization of BG in order to compare its efficiency with that of the original catalyst. The dye removal study of dye was performed by UV-Vis spectrophotometry. The percent removal of BG dye in aqueous medium was calculated by the following equations [13]:

$$\text{Degradation rate (\%)} = \left(\frac{C_0 - C}{C_0} \right) \times 100$$

$$\text{Degradation rate (\%)} = \left(\frac{A_0 - A}{A_0} \right) \times 100$$

where C_0 and C stand for initial dye concentration and dye concentration after UV irradiation, respectively. A_0 and A show initial absorbance and dye absorbance after UV irradiation, respectively.

Instrumentation

The morphological study of ATC and Co-ATC was carried out on JEOL, JSM-5910 SEM. The EDX spectrometric analysis of Co-ATC was performed on Model INCA 200/Oxford Instruments, UK, company Oxford, in order to determine the elemental composition of the sample. The photodegradation study of BG was performed on a UV-Vis spectrophotometer (UV-1800, Shimadzu, Japan).

RESULTS AND DISCUSSION

Adsorption study

The adsorption technique is commonly used for the removal of pollutants like dyes, heavy metals, etc., but after adsorption the adsorbents are commonly discarded. In our study, we used ATC for the removal of Co from aqueous solution and then utilized the Co-adsorbed ATC for dye decoloration. Table 1 show that the adsorption of Co increases as its concentration increases. The results revealed that ATC adsorption capacity increases as Co concentration increases up to a certain limit (300 ppm) and then levels off. It was also found that the adsorption capacity is almost constant after 300 ppm, which might be due to the saturation of active sites present on the surface of ATC.

Table 1. Adsorption of Co by ATC

Solution Concentration (ppm)	Adsorption of Cobalt (mg/g)
100	5.709
200	6.602
300	9.063
400	9.165

Morphological study

Figure 1 shows the surface morphology of ATC and Co-ATC. Figure 1a reveals that the surface of charcoal is not damaged by treating with strong nitric acid. Figure 1b clearly shows that Co is adsorbed on the surface of charcoal. The size of Co was below 600 nm. The micrographs also illustrated that Co particles were dispersed on the surface of activated charcoal.

EDX Study

Figure 2 shows the EDX spectrum of Co-ATC. The EDX study reveals that carbon is present in large quantity as compared to other elements. The spectrum also shows the presence of an oxygen peak, which indicates that carboxylic functional groups were introduced during the functionalization of charcoal by treating with concentrated HNO₃ and

HCl. Figure 2 also shows that Co is adsorbed in high quantity on the surface of Co-ATC. The adsorption of Co was also confirmed by atomic absorption spectrometry and the results are shown in table 1.

BG dye decolorization study

The ATC and Co-ATC were used for the decolorization of BG under UV-light irradiation. Figure 3a shows the UV/Vis spectra of BG before and after UV irradiation in aqueous medium in the presence of ATC. The removal of BG was measured by the relative intensity of the UV/Vis spectra, which gave maximum absorbance peak at 438 nm. Figure 3a also shows that the decolorization of BG increased slowly as irradiation time increased. The decrease in peak intensity illustrated that BG decolorization occurred in the presence of ATC.

The UV/Vis spectra of BG before and after UV irradiation in aqueous solution in the presence of Co-ATC are shown in figure 3b. The spectra revealed that the photodegradation of BG gradually increased as the irradiation time increased. The results also illustrated that the dye was significantly removed in the presence of Co-ATC as compared to ATC.

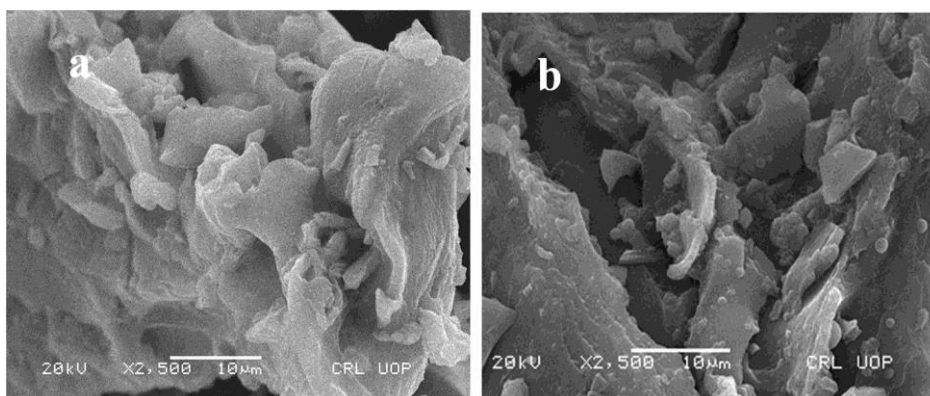


Fig. 1. SEM images of (a) ATC and (b) Co-ATC

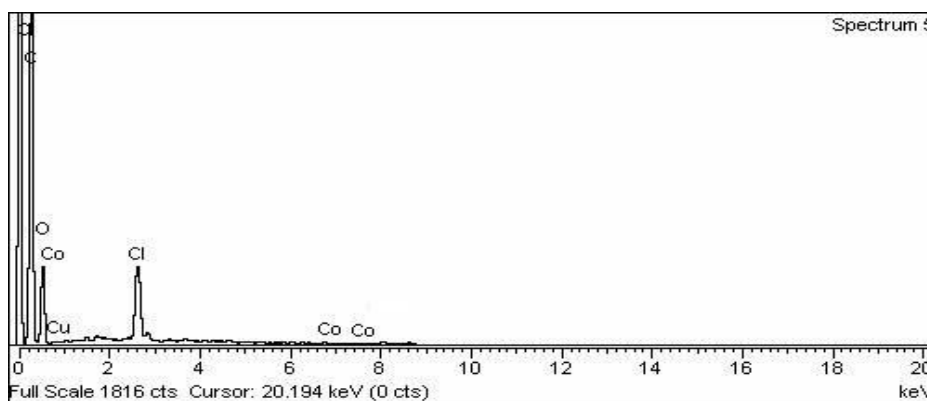


Fig. 2. EDX spectrum of Co-ATC

Figure 3c shows the difference in % removal of BG dye in the presence of ATC and Co-ATC. The results showed that only 16.85 % of the dye was removed in the presence of ATC, while Co-ATC removed 40.5 % of the dye within 12 h. The increase in the catalytic efficiency of Co-ATC was due to the presence of Co on the surface of charcoal. Chaleshtori photocatalytically degraded

BG dye under UV light in aqueous medium using non-porous and porous titanium–niobium oxides derived from KTiNbO_5 but their photocatalysts are not economical [19]. Figure 4 shows the kinetic study of the photodegradation reaction of BG dye in the presence of ATC and Co-ATC. The correlation coefficients (R^2) values are also shown in the graph (Figure 4).

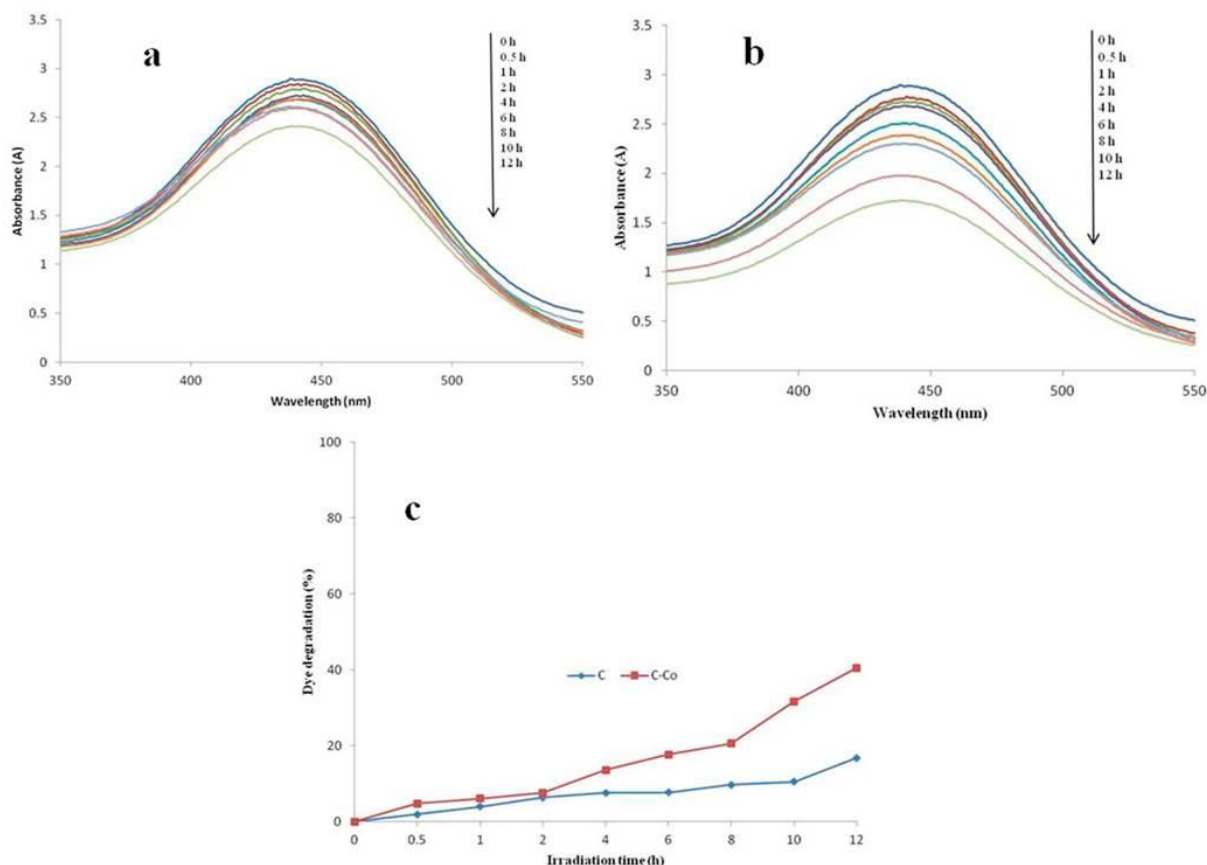


Fig. 3. UV–Vis absorbance spectra of BG decolorization by (a) ATC, (b) Co-ATC under UV-light irradiation vs. time, and (c) % removal of BG with ATC and Co-ATC.

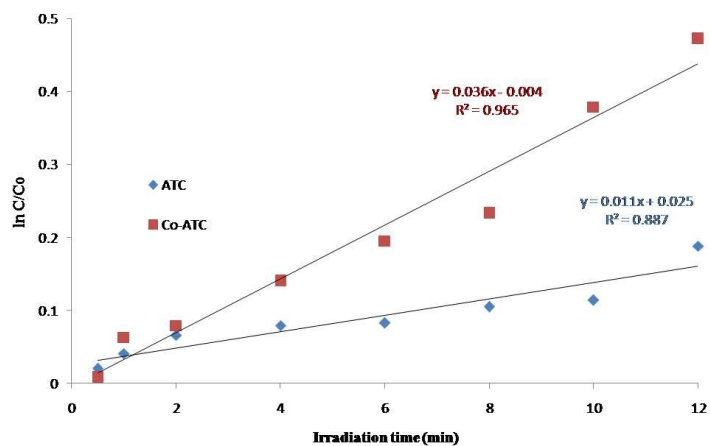


Fig. 4. Kinetic study of BG dye decolorization reaction in the presence of ATC and Co-ATC

The effect of catalyst amount on the decolorization of BG dye was also studied by applying different amounts of catalyst. Different amounts of ATC and Co-ATC such as 0.010, 0.015, 0.020, 0.025 and 0.030 g were added to each 10 mL of dye and their effects were studied under the same experimental conditions at a constant time of 4 h. Figure 5 shows the UV/Vis spectra of BG in aqueous solution before and after UV-light irradiation using different amounts of ATC. The results clearly demonstrated that the removal of dye increased as the amount of ATC increased. Figure 6 shows the UV/VIS spectra of BG before and after UV-light irradiation using different amounts of Co-ATC photocatalyst. The spectra show that the rate of decolorization increased as the amount of Co-ATC increased.

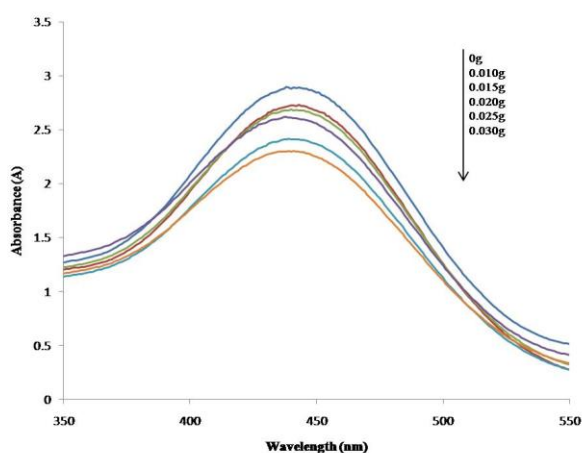


Fig. 5. UV-Vis absorbance spectra of BG photodegraded by ATC under UV irradiation vs. catalyst dosage.

Figure 7 shows the difference in % removal of BG dye using different quantities of ATC and Co-ATC under UV-light irradiation. The results illustrated that at every dosage Co-ATC decolorized more dye as compared to ATC. The results show that 0.010 g of ATC decolorized about 6.46 % of dye while 0.030 g of charcoal decolorized 20.62 % of dye. Similarly, 0.01g of Co-ATC decolorized 7.6 % while 0.030 g decolorized 41.86 % of dye within 4 h as is clear from table 2. The same results are also reported by Fassi *et al.*

Table 2. % Removal of BG vs. catalyst dosage

Catalyst dosage (g)	% Removal by ATC	% Removal by CO-ATC
0.010	6.46	7.6
0.015	7.6	13.57
0.020	9.67	20.62
0.025	16.85	32.5
0.030	20.62	41.86

[20] using TiO₂/UV for photodegradation of BG dye, who found that dye degradation/removal rate increased with an increase in the amount of catalyst.

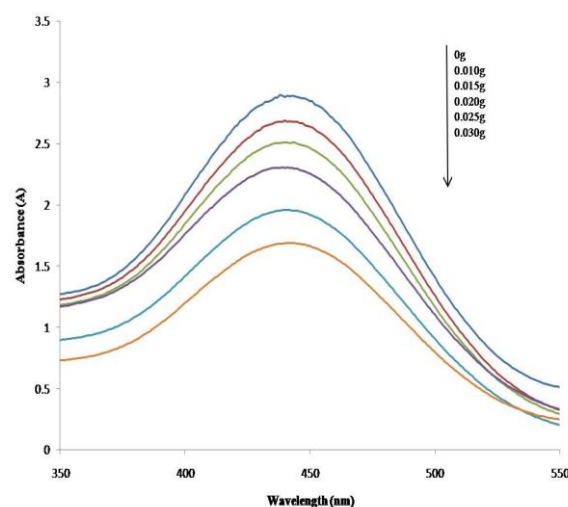


Fig. 6. UV-Vis absorbance spectra of BG decolorized by Co-ATC under UV irradiation vs. catalyst dosage

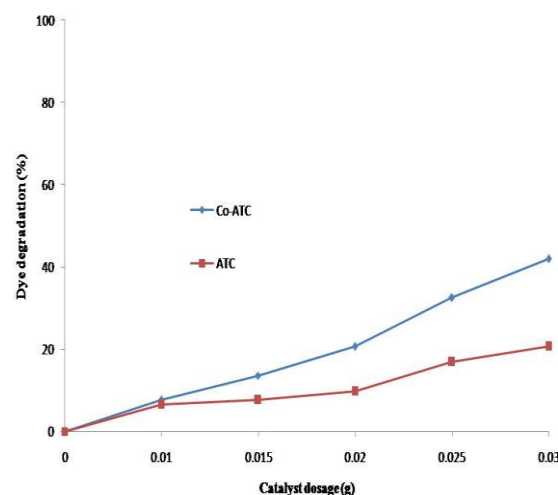


Fig. 7. Difference in % removal of BG in aqueous medium by different dosages of ATC and Co-ATC

CONCLUSION

Cobalt ions were adsorbed on AC and utilized for the decolorization of BG dye in aqueous medium. The SEM images showed that the acid treatment did not affect the surface morphology of charcoal. The SEM study illustrated that Co ions gets agglomerated on the surface of ATC. The dye decolorization study revealed that Co-ATC decolorized a larger quantity of BG than the ATC. The high removal efficiency of Co-ATC is attributed to the catalytic effect of Co present on the surface of ATC. Both ATC and Co-ATC can be easily removed after reaction but Co-ATC can be more efficiently separated due to the additional mass of adsorbed cobalt. The Co-ATC decolorized about 40 % of dye while ATC decolorized about 16 % of dye within 12 h. The % removal of dye increases by increasing catalyst dosage and 0.030 g of Co-ATC decolorized 41.86 % of dye within 4 h.

REFERENCES

1. A. Seco, P. Marzal, C. Gabaldon, J. Ferrer, *J. Chem. Technol. Biotechnol.*, **68**, 23 (1997).
2. K. Kadirvelu, K. Thamaraiselvi, C. Namasivayam, *Bioresour. Technol.*, **76**, 63 (2001).
3. M. O. Corapcioglu, C. P. Haung, *Water Res.*, **21**, 1031 (1987).
4. A. Demirbas, *J. Hazard. Mater.*, **157**, 220 (2008).
5. S. Ahmad, A. Ahmad, S. Khan, S. Ahmad, I. Khan, S. Zada, P. Fu, *J. Ind. Eng. Chem.* **72**, 117 (2019).
6. M. Kobya, E. Demirbas, E. Senturk, M. Ince, *Bioresour. Technol.*, **96**, 1518 (2005).
7. M. Ishaq, K. Saeed, A. Shoukat, I. Ahmad, A. R. Khan, *International Journal of Science Inventions Today*, **3**, 705 (2014).
8. A. Khan, S. J. Shah, K. Mehmood, Awais, N. Ali, H. Khan, *J. Mater. Sci.: Mater. Electron.*, doi.org/10.1007/s10854-018-0305-5.
9. K. Saeed, G. Ali, I. Khan, H. Khan, *J. Chem. Eng. Chem. Res.*, **2**, 671 (2015).
10. J. Santhanalakshmi, R. Komalavalli, *Chem. Sci. Trans.*, **1**, 522 (2012).
11. H. Khan, A. K. Khalil, A. Khan, K. Saeed, N. Ali, *Korean J. Chem. Eng.*, **33**, 2802 (2016).
12. H. L. Wang, D. Y. Zhao, W. F. Jiang, *Desalin. Water Treat.*, **51**, 2826 (2013).
13. K. Saeed, I. Khan, S. Y. Park, *Desalin. Water Treat.*, **54**, 3146 (2015).
14. C. Sahoo, A. K. Gupta, I. M. S. Pillai, *J. Environ. Sci. Health A* ., **47**, 1428 (2012).
15. J. V. Tolia, M. Chakraborty, Z. V. P. Chakraborty, *Pol. J. Chem. Technol.*, **14**, 16 (2012).
16. S. Fassi, K. Djebbar, I. Bousnoubra, H. Chenini, T. Sehili, *Desalin. Water Treat.*, (2013), doi: 10.1080/19443994.2013.809971.
17. S. Fassi, I. Bousnoubra, T. Sehili, K. Djebbar, *Journal of Materials and Environmental Science*, **3**, 732 (2012).
18. M. Z. Chaleshtori, M. Hosseini, R. Edalatpour, S. M. S. Masud, R. R. Chianelli, *Mater. Res. Bull.*, **48**, 3961 (2013).
19. M. Z. Chaleshtori, M. Hosseini, R. Edalatpour, S. M. S. Masud, R. R. Chianelli, *Mater. Res. Bull.*, **48**, 3961(2013).
20. S. Fassi, K. Djebbar, T. Sehili, *J. Mater. Environ. Sci.*, **5**, 1093 (2014).

Kinetics of oxidation of $[\text{Fe}(\text{phen})_3]^{2+}$ by persulphate: catalysis in the water pools of CTAB reverse micelles

K.V. Nagalakshmi^{1*}, P. Shyamala²

¹Department of Chemistry, Gayatri Vidya Parishad College of Engineering (Autonomous), Madhurawada, Visakhapatnam-530048, India

²Department of PNCO, School of Chemistry, Andhra University, Visakhapatnam-530017, India

Received August 15, 2018; Revised April 21, 2019

The kinetics of oxidation of $[\text{Fe}(\text{phen})_3]^{2+}$ by persulphate was carried out in water pools of CTAB/chloroform/hexane reverse micelles. The reaction obeys first-order kinetics with respect to each of the reactants. In the reverse micellar medium, the reaction was found to be around fifty times faster compared to aqueous medium under identical experimental conditions. The pronounced acceleration is accounted for by the lower micropolarity of the reverse micelles, which facilitates the ion-pair formation between oppositely charged ions. The effect of variation of W ($W = [\text{H}_2\text{O}] / [\text{CTAB}]$) at constant $[\text{CTAB}]$ and variation of $[\text{CTAB}]$ at fixed W was studied. At a fixed concentration of CTAB, the second-order rate constant of the reaction increases with increasing value of W and is independent of the concentration of CTAB at constant W .

Keywords: Kinetics, Oxidation, Ferrous, Persulphate, Reverse micelles, Water pools.

INTRODUCTION

The reverse micelles formed spontaneously in organic solvents are thermodynamically stable and have been characterized by various techniques. The solubilized water present in the polar cavity of reverse micelles is called "water pool". This water pool has unique properties like lower dielectric constant, i.e. micropolarity, higher viscosity, lower thermodynamic activity of water, higher ionic strength (in the case of reverse micelles made of ionic surfactants) and altered nucleophilicity compared to water in the conventional aqueous media [1-5]. These anomalous properties of the water pool are dependent on the W parameter, $W = ([\text{H}_2\text{O}]/[\text{surfactant}])$ and as the value of W increases, the properties approach that of ordinary water. Since the water pool has different properties compared to ordinary water, the rates of reactions and mechanisms can be expected to be different [6-10]. Another advantage of reverse micelles is that they are good solvents for both hydrophobic and hydrophilic reactants and therefore, appear to be useful media for studying reactions involving different types of reactants [11,12].

Earlier we have reported reactions taking place in the presence of reverse micelles and have given a quantitative assessment for the change in special properties with change in W and the observed kinetic results were quantitatively explained using Berezin pseudo phase model [13-15]. It has been reported that the lower dielectric constant of the water pool enhances the ion-pair formation and

reactions involving formation of ion pairs between reactants may provide a basis for understanding the nature of bound water in the reverse micelles [16,17]. With this objective, oxidation of $[\text{Fe}(\text{phen})_3]^{2+}$ by persulphate was chosen, which is very well known in aqueous and in various solvent mixtures [18,19].

EXPERIMENTAL

All solutions were prepared in double distilled water. Chemicals used were of analytical grade. Tris (1,10-phenanthroline) iron(II) complex (0.02 mol dm^{-3}) was prepared by mixing stoichiometric amounts (1:3) of ferrous ammonium sulphate (Merck, India) and 1,10-phenanthroline (Merck, India) in water. A stock solution of sodium persulphate (0.2 mol dm^{-3}) was freshly prepared by using sodium persulphate (Merck, India)

Chloroform and hexane were double distilled before use. CTAB (cetyltrimethylammonium bromide) purchased from Sigma was used without further purification. Reverse micellar solutions of CTAB (0.1 mol dm^{-3} , 0.2 mol dm^{-3} and 0.3 mol dm^{-3}) were prepared by dissolving requisite amounts of CTAB in chloroform-hexane (3:2 v/v) mixtures.

Preparation of reverse micellar medium and initiation of the reaction

$[\text{Fe}(\text{phen})_3]^{2+}$ (0.02 ml , 0.02 mol dm^{-3}) was injected into 10 ml of 0.1 mol dm^{-3} CTAB solution using a micropipette. Persulphate solution (0.02 ml , 0.2 mol dm^{-3}) was then added to initiate the reaction.

The reaction mixture was shaken vigorously to obtain a transparent and homogeneous solution that

* To whom all correspondence should be sent:
E-mail: kvnlpc15@gmail.com

can be regarded as a reverse micellar system. The molar ratio of [water] to [CTAB], i.e. W , was varied in the range from 2.22 to 16.6.

Kinetic measurement

The kinetic study of the oxidation of $[Fe(phen)_3]^{2+}$ by persulphate was carried out using a Shimadzu UV-1800 double beam spectrophotometer by measuring the decrease in absorbance of $[Fe(phen)_3]^{2+}$ at a wavelength of 510 nm. The reaction was carried out under pseudo first-order conditions, $[S_2O_8^{2-}] \gg [[Fe(phen)_3]^{2+}]$. The concentration of $[Fe(phen)_3]^{2+}$ was 4×10^{-5} mol dm^{-3} . Persulphate was varied from 4.0×10^{-4} to 36.0×10^{-4} mol dm^{-3} . In all cases good linear plots were obtained for \log (absorbance) *versus* time indicating first-order kinetics with respect to $[Fe(phen)_3]^{2+}$. The kinetic data are the averages from duplicate runs with reproducibility better than $\pm 3\%$.

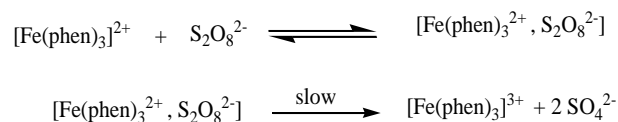
Calculation of effective concentration

When reactants are in the water pool they are confined to a small volume leading to a concentration effect. In the case of unimolecular reactions taking place in the water pools of the reverse micelles, the measured first-order rate constants can be compared directly with the rate constant of a reaction in aqueous medium. However, in the case of bimolecular reactions taking place in the water pools of the reverse micelles, the calculation of second-order rate constant involves the consideration of the effective concentration of the reactants. The effective concentration of a reactant in the water pool is calculated by dividing the overall concentration by the volume fraction of solubilized water. Volume fraction, f , is the volume of aqueous phase in the water pool divided by the total volume of the solution [20]. The volume fractions lie in the range from 4.00 to 36.0×10^{-3} for 0.1 mol dm^{-3} CTAB. For example, if the concentration of CTAB is 0.1 mol dm^{-3} and $W = 3.33$, then $f = (0.06/10.0)$. If $[S_2O_8^{2-}]_{overall} = 4.0 \times 10^{-4}$, then $[S_2O_8^{2-}]_{effective} = [S_2O_8^{2-}]_{overall} / f = \{4.0 \times 10^{-4} / 0.006\} = 0.066$ mol dm^{-3} . From now onwards, the subscript 'o' is used to represent overall concentration and subscript 'e' to represent effective concentrations.

RESULTS AND DISCUSSION

The kinetics of the reaction was investigated in CTAB reverse micelles under pseudo first-order conditions, varying the overall concentration of persulphate in the range from 4.0×10^{-4} to 36.0×10^{-4} mol dm^{-3} and keeping the $\{Fe(phen)_3\}^{2+}$ complex at 4.0×10^{-5} mol dm^{-3} , thus isolating the complex. The

reaction obeys first-order kinetics with respect to $\{Fe(phen)_3\}^{2+}$ as shown by the linear plots of \log (A_t) *versus* time (Fig. 1). A plot of pseudo first-order rate constant, k' *versus* $[S_2O_8^{2-}]_o$ was found to be linear passing through the origin indicating first-order kinetics with respect to $S_2O_8^{2-}$ (Fig. 2). Based on the observed results in the CTAB reverse micellar medium, the following mechanism (Scheme 1) is proposed in CTAB reverse micelles:



Scheme 1.

The reaction was markedly catalyzed in the presence of CTAB reverse micelles and the second-order rate constant was found to be greater than that in aqueous medium by around fifty times under identical experimental conditions (Table 1).

Table 1. Comparison of rate constants in the aqueous medium and in the presence of reverse micelles (0.1 mol dm^{-3} CTAB) at the same ionic strength (μ). $[Fe(phen)_3]_o^{2+} = 4 \times 10^{-5}$ mol dm^{-3} ; $[S_2O_8^{2-}]_o = 4 \times 10^{-4}$ mol dm^{-3} ; $T = 304$ K

μ (mol dm^{-3})	$k_{2aq,med} \times 10^3$ (mol $^{-1}$ dm^3 sec $^{-1}$)	$k_{2(rev mic)} \times 10^3$ (mol $^{-1}$ dm^3 sec $^{-1}$)
3.33	7.06	52.4
12.5	0.621	28.0

The acceleration in reverse micelles is due to the fact that the water pool of a reverse micelle is distinctly less polar [21,22] than the aqueous medium and favours ion-pair formation of the complex with persulphate and facilitates the reaction between opposite charges.

Effect of variation of W on rate

The second-order rate constant increases with increasing W at constant CTAB concentration and is independent of CTAB concentration at constant W (Table 2). At constant CTAB concentration, an increase in W results in an increase in dielectric constant and a decrease in ionic strength of the medium. These two have opposing effects on the reaction. If there is only the effect of the dielectric constant, then the rate should decrease with W . If the ionic strength effect alone exists, there should be an increase in rate with increase in W since low ionic strength favours cation-anion reaction. Therefore, the rate constant is a resultant effect of these two factors. The increase in second-order rate constant k_2 with W implies that the effect of decrease in ionic strength on the rate is more pronounced than the increase in dielectric constant of the medium. Therefore, the increase in the rate of

K.V. Nagalakshmi, P. Shyamala: Kinetics of oxidation of $[Fe(phen)_3]^{2+}$ by persulphate: catalysis in the water pools of CTAB ... reaction with W is due to decrease in ionic strength. Hence, the effect of W was assessed in terms of ionic strength relating the rate constant k_2 .

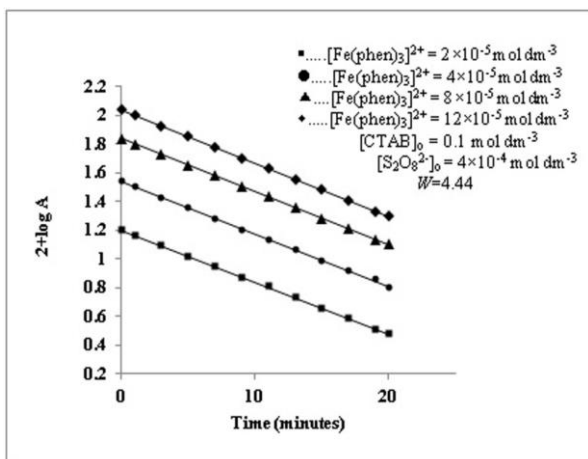


Fig. 1. Plots of $\log(A_t)$ vs time at different concentrations of $[Fe(phen)_3]^{2+}$; $[CTAB] = 0.1 \text{ mol dm}^{-3}$, $[S_2O_8^{2-}] = 4.0 \times 10^{-4} \text{ mol dm}^{-3}$, $W = 4.44$; $T = 304 \pm 0.1 \text{ K}$. $[Fe(phen)_3]^{2+} = 2.0 \times 10^{-5} \text{ mol dm}^{-3}$; $[Fe(phen)_3]^{2+} = 4.0 \times 10^{-5} \text{ mol dm}^{-3}$; $[Fe(phen)_3]^{2+} = 8.0 \times 10^{-5} \text{ mol dm}^{-3}$; $[Fe(phen)_3]^{2+} = 12.0 \times 10^{-5} \text{ mol dm}^{-3}$

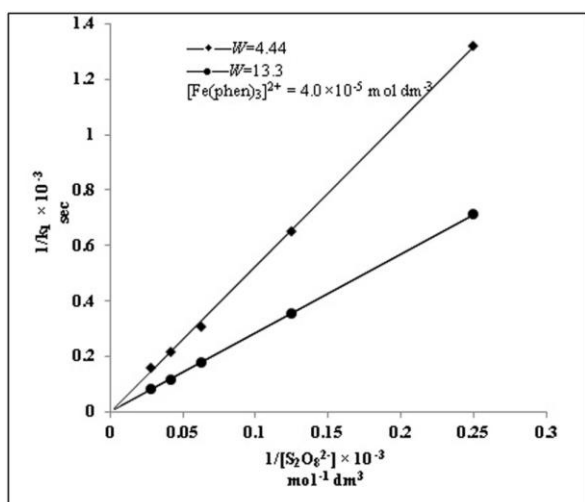


Fig. 2. Plots of $1/k_2$ vs $1/[S_2O_8^{2-}]$; $[Fe(phen)_3]^{2+} = 4.0 \times 10^{-5} \text{ mol dm}^{-3}$; $[CTAB] = 0.1 \text{ mol dm}^{-3}$; $T = 304 \pm 0.1 \text{ K}$; $W = 4.44$, $W = 13.3$.

The ionic strength, μ , at each W was equated to the effective concentration of bromide ion $[Br^-]_e$ in the water pool.

$$\log k_2 = \log k_2^0 + \frac{2A Z_A Z_B \sqrt{\mu}}{1 + \sqrt{\mu}} + B' \mu \dots \dots (1)$$

$$\log k_2 = \log k_2^0 - \frac{4 \sqrt{\mu}}{1 + \sqrt{\mu}} + B' [Br^-]_e \dots \dots (2)$$

where A is equal to 0.503, Z_A & Z_B are +2 and -2, the charges of the respective ions. B' is interaction parameter. In the present case, the specific interactions are between the positively

charged micellar surface, CTA^+ and $S_2O_8^{2-}$ & $[Fe(phen)_3]^{2+}$ and Br^- , represented by the specific interaction terms B_{CTA^+} , $S_{2O_8^{2-}}$ and $B_{[Fe(Phen)_3]^{2+} Br^-}$, respectively.

The effect of ionic strength on the rate of reaction can be examined using Guggenheim equation [23]. In the case of ionic surfactants, the value of W controls the concentration of polar heads of surfactants (CTA^+) and its counter ions (Br^-) in the aqueous water pool [24].

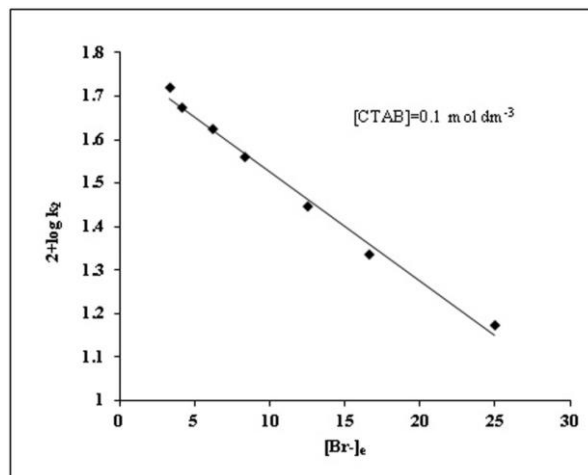


Fig. 3. Plots of $\log k_2$ vs $[Br^-]_e$ at different values of W; $[Fe(phen)_3]^{2+} = 4.0 \times 10^{-5} \text{ mol dm}^{-3}$; $[S_2O_8^{2-}] = 4.0 \times 10^{-4} \text{ mol dm}^{-3}$; $[CTAB] = 0.1 \text{ mol dm}^{-3}$, $T = 304 \pm 0.1 \text{ K}$.

At high ionic strength the variation of the second term in Eqn. (2) with $\mu \{=[Br^-]_e\}$ can be neglected in comparison with the third term. If this is true, plots of $\log k_2$ vs. $\mu \{=[Br^-]_e\}$ should be linear. Interestingly, the plot of $\log k_2$ versus $\mu \{=[Br^-]_e\}$ was found to be linear for all concentrations of CTAB (Fig. 3) and the interaction parameter B' was obtained from the slope of the plot. The value of B' was found to be -0.0252, -0.0256, and -0.0254 for 0.1, 0.2 and 0.3 mol dm^{-3} CTAB, respectively.

Effect of variation of [CTAB] on rate

The effect of variation of the concentration of CTAB on the rate of reaction was studied and Table 2 shows that the variation of the concentration of CTAB (0.1-0.3 mol dm^{-3}) at all W values does not have any significant effect on the rate. Since the increase in CTAB concentration at constant W increases the interfacial area, this shows that the reaction is taking place mainly in the water pool and not on the micellar surface, so there is no significant change in rate with the change in CTAB concentration. If reaction occurred at the interface of the reverse micelle, the rate constant would change with variation of CTAB concentration.

K.V. Nagalakshmi, P. Shyamala: Kinetics of oxidation of $[Fe(phen)_3]^{2+}$ by persulphate: catalysis in the water pools of CTAB ...
Table 2. Effect of W and [CTAB] on rate constant (k_2). $[Fe(phen)_3]^{2+} = 4 \times 10^{-5} \text{ mol dm}^{-3}$; $[S_2O_8^{2-}]_0 = 4 \times 10^{-4} \text{ mol dm}^{-3}$;
 $T = 304 \text{ K}$

CTAB (mol dm^{-3})	W	$\mu \{[Br]_e\}$	$k_1 \times 10^3 (\text{s}^{-1})$	$k_2 \times 10^3$ ($\text{mol}^{-1} \text{dm}^3 \text{s}^{-1}$)
0.1	2.22	25.0	1.49	14.9
	3.33	16.6	1.45	21.6
	4.44	12.5	1.40	28.0
	6.66	8.33	1.20	36.3
	8.88	6.25	1.05	42.0
	13.3	4.16	0.756	47.2
	16.6	3.33	0.682	52.4
0.2	2.22	25.0	0.735	14.7
	3.33	16.6	0.725	21.9
	4.44	12.5	0.706	28.2
	6.66	8.33	0.616	38.5
	8.88	6.25	0.529	42.3
	13.3	4.16	0.436	47.9
	16.6	3.33	0.343	51.9
0.3	2.22	25.0	0.481	14.5
	3.33	16.6	0.482	21.9
	4.44	12.5	0.461	27.7
	6.66	8.33	0.403	36.6
	8.88	6.25	0.351	42.1
	13.3	4.16	0.258	46.9
	16.6	3.33	0.227	51.5

CONCLUSIONS

1. The reaction between $[Fe(phen)_3]^{2+}$ and $S_2O_8^{2-}$ obeys first-order kinetics with respect to each of the reactants in the CTAB reverse micellar medium.

2. The reaction was found to be accelerated fifty times in the presence of CTAB reverse micelles. The significant increase of rate in the CTAB reverse micellar medium is due to the low dielectric constant of the bound water, which favours ion-pair formation of the complex with persulphate ion and facilitates the reaction between opposite charges.

3. The increase in second-order rate constant (k_2) of the reaction with W was assessed in terms of ionic strength using Guggenheim equation.

4. The second-order rate constant (k_2) of the reaction is almost the same at all concentrations of CTAB, indicating that the reaction completely takes place in the water pool.

Acknowledgement: Two of us (KVNL and PS) thank UGC, India under the minor research project MRP-4552(14) (SERO/UGC) and DST, India under the project SERB/F/5725/2013-14, respectively, for financial support.

REFERENCES

1. F.M. Menger, J.A. Donohue, R.F. Williams, *J. Am. Chem. Soc.*, **95**(1), 286 (1973).
2. A. Goto, H. Kishimoto, *Bull. Chem. Soc. Jpn.*, **62**,

- 2854 (1989).
3. B.K. Mishra, B.S. Valandikar, J.J. Knujappu, C. Manomar, *J. Colloid Interface Sci.*, **127**, 373 (1989).
4. J. Burgess, *J. Colloid Surf.* **48**, 185 (1990).
5. N.J. Bridge, P.D.I. Fletcher, *J. Chem. Soc. Faraday Trans.*, **79**, 2161 (1983).
6. J. Sunamoto, T. Hamada, *Bull. Chem. Soc. Jpn.*, **51**, 3130 (1978).
7. N.J. Bridge, P.D.I. Fletcher, *J. Chem. Soc. Faraday Trans.*, **79**(9) 2161 (1983).
8. K.M. Harasit, T. Majumdar, M. Ambikesh, *Int. J. Chem. Kinet.*, **43**(10), 579 (2011).
9. M.D. Johnson, B.B. Lorenz, P.C. Wilkins, B.G. Lemons, B. Baruah, N. Lamborn, M. Stahla, P.B. Chatterjee, D.T. Richens, D.C. Crans, *Inorg. Chem.*, **51**(5), 2757 (2012).
10. K.J.S. Jamil, *J. Dispersion Sci. Technol.*, **27**(6), 795 (2006).
11. R. Schomacker, K. Stickdorn, W. Knoche, *J. Chem. Soc., Faraday Trans.*, **87**, 847 (1991).
12. Y. Miyake, T. Owari, F. Shiga, M. Teramoto, *J. Chem. Soc., Faraday Trans.*, **90**, 979 (1994).
13. M.Padma, P. Shyamala, A.Sathyanarayana, P.V. Subba Rao, *Ind. J. Chem.*, **52**(A), 221 (2013).
14. P. Shyamala, P.V. Subba Rao, *Kinet. Catal.*, **51**(2), 207 (2010).
15. K.V. Nagalakshmi, P. Shyamala, P.V. Subba Rao, *Ind. J. Chem.*, **54**(A), 351 (2015).
16. K.V. Nagalakshmi, M. Padma, V.Srikanth, P.Shyamala, P.V. Subba Rao, *Transition Met. Chem.*, **38**, 523 (2013).

K.V. Nagalakshmi, P. Shyamala: Kinetics of oxidation of $[Fe(phen)_3]^{+2}$ by persulphate: catalysis in the water pools of CTAB ...

17. D. Sarkar, K.C. Khilar, G. Begum, P.V. Subba Rao, *Colloids and Surfaces A: Physico Chemical and Engineering Aspects*, **268(1)**, 73 (2005).
18. S. Raman, C. H. Brubaker, *J. Inorg. Nucl. Chem.*, **31**, 1091 (1969).
19. M.J. Blandamer, B. John, P. P. Duce, R.I. Haines, *J. Chem. Soc., Dalton. Trans.*, **12**, 2442 (1980).
20. P.L. Luisi, B.E. Straub, *Reverse Micelles*, Plenum Press, New York, 1984.
21. J.H. Fendler, *Acc. Chem. Res.*, **9(4)**, 153 (1976).
22. L. Yang, K. Zhao, *Langmuir*, **23**, 8732 (2007).
23. E. A. Guggenheim, *Phil. Mag.*, **19**, 588 (1935).
24. E. Munoz, C. Gomez-Herrera, M. Garciani, M.L. Moya, F. Sanchez, *J. Chem. Soc., Faraday Trans.*, **87(1)**, 129 (1991).

Mass spectroscopic and biological activity investigations of bis(triorganotin(IV)) carboxylates with acetylene dicarboxylic acid

Sh. Hussain^{1*}, Gh. Abbas¹, Mu. Shahid²

¹Department of Chemistry, Lahore Garrison University, DHA Phase VI, Lahore, Pakistan

²Department of Chemistry and Biochemistry, University of Agriculture, Faisalabad, Pakistan

Received September 11, 2018; Revised April 1, 2019

Three bis(triorganotin(IV)) dicarboxylates of the general formulae $R_3SnOOCLCOOSnR_3$ (Where $L = C\equiv C$; $R = Me$ (**1**), Bu (**2**), Ph (**3**)) were subjected to mass spectroscopic and biological activity studies. The investigated complexes demonstrated the common mass fragmentation modes due to their structural similarities. Each product was primarily degraded into a trialkyl/triaryltin(IV) cation. The free ligand precursor was biologically inactive against all the tested microbes while the product complexes **1-3** were proved to be potent inhibitors of bacteria and fungi. The complexes were also screened for their minimum inhibitory concentration (MIC) evaluation. *In vitro* hemolytic activity studies were also performed on human red blood cells. The organotin(IV) complexes displayed lower cytotoxic effects (12.98-18.85%) as compared to the free ligand (19.68%). The triphenyltin(IV) product **3** showed interaction with salmon sperm DNA and was found to be the most active antimicrobial agent having the lowest hemolytic effects. Its antibacterial/antifungal potential was even higher than that of the standard antimicrobial drugs streptomycin and fluconazole in some cases.

Key words: EIMS, salmon sperm, antibacterial, antifungal, hemolytic

INTRODUCTION

Infectious diseases are the major causes of disability, morbidity and mortality in the world. The death rate of humans due to the infectious diseases is in millions especially in developing countries [1]. The control of bacterial infections has been remarkably effective since the discovery of antimicrobial drugs. However, some of the pathogens are rapidly becoming resistant to many of the first discovered and available drugs. The increasing prevalence of multidrug resistance in pathogenic microorganisms, as well as undesirable side effects of certain antibiotics has triggered immense interest in the search for new antimicrobial drugs [2]. In recent years there are numerous studies on organotin(IV) complexes to evaluate their biological potential against fungal and bacterial strains [3]. They are toxic against a variety of microorganisms and are used as active components in various biocidal formulations, finding applications in such diverse areas as fungicides, miticides, mollucides, marine antifouling paints, surface disinfectants, and wood preservatives [4,5]. A large number of organotin compounds are used as pharmaceuticals and pesticides, the activities mainly depends upon the number and nature of organic groups [6,7] as well as the structure of the molecule and coordination number of tin moiety [8,9]. Furthermore the activity will decrease from tetra alkyl substituted tin(IV)

compounds to mono alkyl substituted tin(IV) compounds [10]. The biological activity is usually associated with the nature of organic ligand, since the organic ligand assists in the transportation of the complexes across the cell membrane [11]. Several organotin compounds exhibit promising *in vitro* antitumor activities against human tumor cell lines [12]. Currently attempts have been made to search for organometallic compounds as a new alternative drug in combating human cancers. Some organotin derivatives are reported to be even more active than the standard anticancer drug *cis*-platin [13]. It has well been established that organotin(IV) compounds are very important in cancer chemotherapy because of their apoptosis inducing character and received considerable attention as antiproliferative and anticancer drugs [11]. There are also reports on the use of organotin carboxylates as potential antineoplastic and antituberculosis agents [14].

The current study focuses on the mass spectroscopic investigations of bis(triorganotin(IV)) complexes with acetylene dicarboxylic acid. The products were also tested for their DNA binding, antibacterial and antifungal activities. These were also investigated to find their toxic hemolytic effects.

* To whom all correspondence should be sent:

E-mail: shabbirhussain@lgu.edu.pk
shabchem786@gmail.com

EXPERIMENTAL

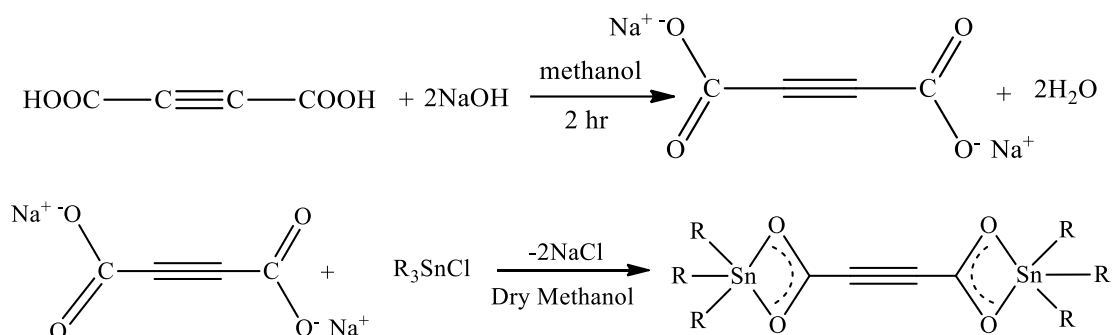
Materials and Methods

Triorganotin chloride precursors (Me_3SnCl , Bu_3SnCl & Ph_3SnCl) and sodium hydroxide (NaOH) were purchased from Aldrich (Germany). Acetylene dicarboxylic acid (HLH) and solvents (methanol, petroleum ether & DMSO) were of Merck (Germany) origin. The methanol was dried before use by a standard procedure [15]. Melting points were noted by taking the compound in a capillary tube and using the electrochemical melting point apparatus model MP-D Mitamura Rikero Kogyo (Japan) and are uncorrected. Elemental analyses were performed on the CHN-932 elemental analyzer Leco Corporation USA. Infrared spectra were recorded in the range of $4000\text{--}400\text{ cm}^{-1}$ on a Perkin-Elmer-1000 FTIR spectrophotometer. The ^1H and ^{13}C NMR spectral measurements were performed on a Bruker ARC 300 MHz-FT-NMR spectrometer. The electron ionization mass spectra (EIMS) were recorded using a Thermo Fisher Exactive Orbitrap instrument.

The complexes were investigated for their interaction with salmon sperm DNA [16,17]. The pure pathogenic (bacterial and fungal) cultures

were obtained from the Biochemistry Department of the University of Agriculture, Faisalabad. The origin and identification of these microorganisms is given below: *E. coli* (ATCC 25922), *B. subtilis* (JS-2004); *S. aureus* (API Staph TAC-6736152); *P. multocida* (Local isolate); *A. alternate* (ATCC-19575); *G. lucidum* (Local isolate); *P. notatum* (FCBP-PTF0111); *T. harzianum* (E-58).

The ligand and the products were compared for their antimicrobial activities against various bacterial (*Escherichia coli*, *Bacillus subtilis*, *Staphylococcus aureus* and *Pasturella multocida*) and fungal (*Alternaria alternata*, *Ganoderma lucidum*, *Penicillium notatum*, *Trichoderma harzianum* and *Aspergillus niger*) strains by the disc diffusion method [18]. The complexes were also evaluated for their minimum inhibitory concentrations (MIC) [19]. Fluconazole and streptomycin were used as standard drugs for antibacterial and antifungal screening tests, respectively. The *in vitro* hemolytic bioassays [20] of the products were investigated with respect to Triton X-100 as a positive control and PBS as a negative control. The complexes **1-3** were synthesized by using a two-step reported procedure (Scheme 1) [21].



Scheme 1. Synthesis of complexes **1-3** where R = Me (**1**), *n*-Bu (**2**), Ph (**3**)

RESULTS AND DISCUSSION

The products have shown sharp melting points and are soluble in common organic solvents, i.e., DMSO, MeOH and CHCl_3 . The synthesized products were characterized by microanalysis, IR and NMR (^1H & ^{13}C) and EIMS.

IR and NMR Spectroscopy

The data obtained by IR, ^1H NMR and ^{13}C NMR spectroscopic analyses were found identical to those reported elsewhere [21] for the same complexes.

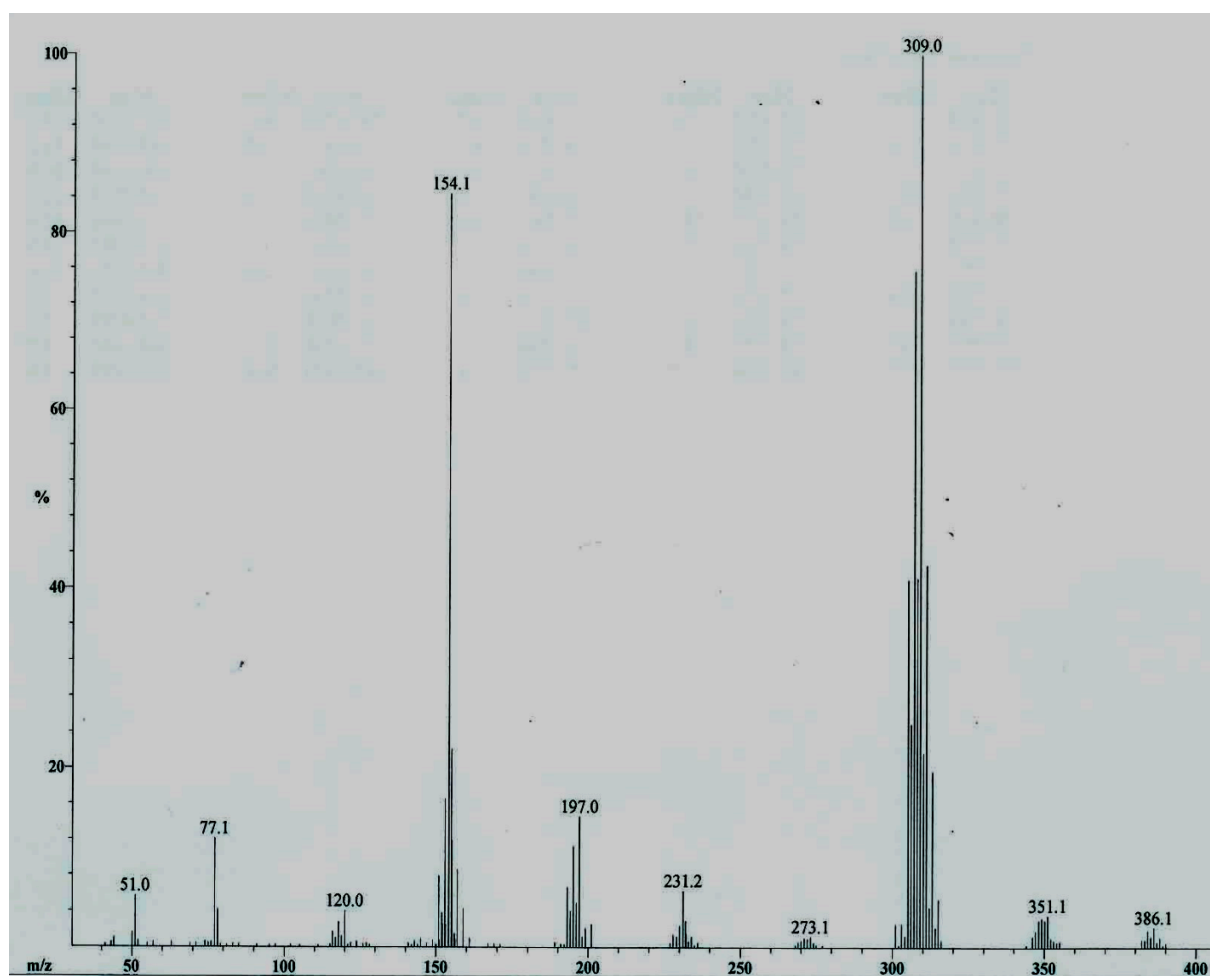
Mass Spectrometry

The electron ionization mass spectra (EI-MS) were recorded for the investigated complexes. The fragment ions are shown in Table 1. The degradation pattern of the products is shown in Scheme 2. The mass spectroscopic patterns verified the structural similarities between the three products **1-3**. The EI-mass spectrum of a representative complex **3** is shown in Figure 1.

Table 1. Mass spectral data[#] of the complexes

Compound No.	MS, m/z (%)
1	[C ₁₀ H ₁₈ O ₄ Sn ₂] ⁺ 442 (n.o.) [#] , [C ₁₀ H ₁₈ O ₃ Sn ₂] ⁺ 423 (5), [C ₉ H ₁₅ OSn ₂] ⁺ 379 (25), [C ₆ H ₉ OSn ₂] ⁺ 337 (100), [C ₅ H ₅ Sn ₂] ⁺ 305 (16), [C ₇ H ₉ O ₄ Sn] ⁺ 277 (10), [C ₆ H ₆ O ₄ Sn] ⁺ 262 (1), [C ₄ O ₄ Sn] ⁺ 232 (2), [C ₇ H ₉ OSn] ⁺ 229 (4), [C ₅ H ₆ O ₂ Sn] ⁺ 218 (12), [C ₃ H ₉ Sn] ⁺ 165 (68), [C ₂ H ₆ Sn] ⁺ 150 (21), [CH ₃ Sn] ⁺ 135 (61), [Sn] ⁺ 120 (35), [C ₄ H ₂ O ₂] ⁺ 82 (10).
2	[C ₄₀ H ₃₀ O ₄ Sn ₂] ⁺ 814 (n.o.) [#] , [C ₂₂ H ₁₅ O ₄ Sn] ⁺ 463 (1), [C ₁₆ H ₁₀ O ₄ Sn] ⁺ 386 (3), [C ₁₈ H ₁₅ Sn] ⁺ 351 (4), [C ₁₀ H ₅ O ₄ Sn] ⁺ 309 (100), [C ₁₂ H ₁₀ Sn] ⁺ 273 (2), [C ₄ O ₄ Sn] ⁺ 231 (7), [C ₆ H ₅ Sn] ⁺ 197 (16), [C ₁₂ H ₁₀] ⁺ 154 (86), [Sn] ⁺ 120 (5), [C ₆ H ₅] ⁺ 77 (12), [C ₄ H ₃] ⁺ 51(7).
3	[C ₂₈ H ₅₄ O ₄ Sn ₂] ⁺ 694 (n.o.) [#] , [C ₁₆ H ₂₇ O ₄ Sn] ⁺ 403 (2), [C ₁₂ H ₁₈ O ₄ Sn] ⁺ 346 (18), [C ₁₂ H ₂₇ Sn] ⁺ 291 (100), [C ₈ H ₁₈ Sn] ⁺ 234 (44), [C ₄ O ₄ Sn] ⁺ 232 (43), [C ₄ H ₉ Sn] ⁺ 177 (19), [Sn] ⁺ 120 (7), [C ₄ H ₉] ⁺ 57 (81)

[#] Molecular ion peak (M⁺); n.o. = not observed.

**Figure 1.** EI-mass spectrum of complex 3

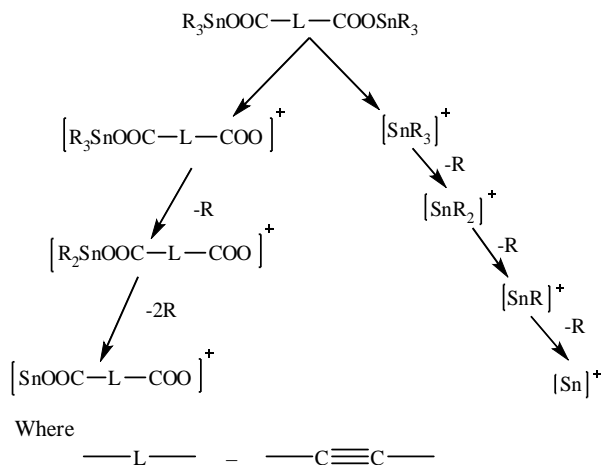
Mass-spectral data showed the rich distribution of ions but the fragments containing the tin are particularly important in structural characterization of organotin(IV) complexes. Such fragments are easily identified from the characteristic isotopic peak patterns for tin. The mass spectra displayed a series of peaks very close to each other due to

isotopic effects of Sn, i.e., tin has 10 naturally occurring isotopes. The most intense peak in each group of ions corresponds to the most abundant isotope of tin (Sn-120). The spectra showed no molecular ion (M⁺) peak; the absence of molecular ion peak in the mass spectra is a common observation in most organometallic complexes

Sh. Hussain et al.: Mass spectroscopic and biological activity investigations of bis(triorganotin(IV)) carboxylates ... [22]. Owing to their large sizes, the coordination products underwent an extensive fragmentation so a complex mass spectral pattern was observed. The metal complexes have shown many common features (Scheme 2) in their fragmentation patterns, due to the close structural similarities between the products. Each of these bimetallic complexes was split into a triorganotin cation (R_3Sn^+) and $[R_3SnOOC-L-COO]^+$ (where $R = Me, Bu, Ph; L = CC$); these fragment ions lost the methyl, butyl or phenyl radicals and degraded into $[Sn]^+$ and $[SnOOC-L-COO]^+$ ions in the former and the latter case, respectively.

DNA Interaction Studies

DNA is generally considered as the target agent for most of the anticancer compounds. So the investigated complexes **1-3** were also studied for their binding with DNA using absorption spectroscopy in the wavelength range of 250-400 cm^{-1} .



Scheme 2. Common EIMS pattern of **1** ($R = Me$), **2** ($R = Ph$) and **3** ($R = Bu$)

The absorbance and shifts were noted in the presence and absence of SS-DNA. Each measurement was performed at the same concentration of the complex (2 mM) while varying the concentration of DNA (Figure 2) [14].

It was found that the alkyltin(IV) derivatives **1** and **2** did not show any affinity for DNA; only the triphenyltin(IV) derivative **3** expressed its binding with DNA. These results are in complete agreement with the earlier findings [23, 24] that only the phenyltin(IV) complexes exhibit interaction with DNA. Actually, the phenyl group in an organotin(IV) species facilitates its interaction with the double stranded DNA [14].

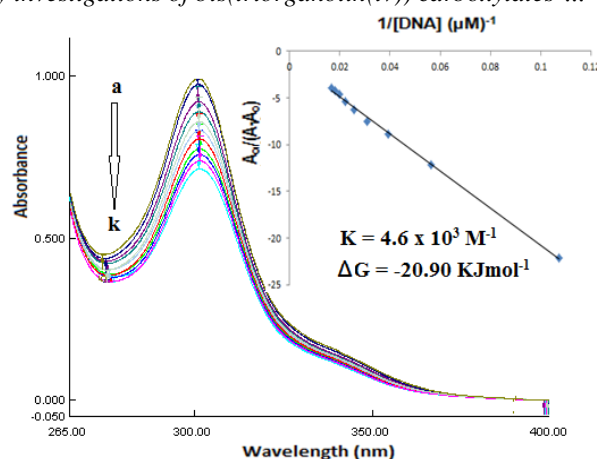


Figure 2. Absorption spectra of the complex **3** (2 mM) in the absence (a) and presence of 10 μM (b), 19 μM (c), 27 μM (d), 35 μM (e), 42 μM (f), 48 μM (g), 54 μM (h), 59 μM (i), 64 μM (j) and 69 μM (k) DNA. The direction of the arrow demonstrates increasing concentrations of DNA. Inset graph is the plot of $A_0/(A-A_0)$ vs. $1/[DNA]$ to find the Gibbs free energy and the binding constant of the DNA-complex adduct.

The pure complex (2 mM) displayed very strong absorption at 302 nm which may be attributed to the $\pi-\pi^*$ transitions of the phenyl ring. After the addition of DNA and then increasing its concentration during each successive measurement, the absorption was lowered (hypsochromism) with a minor red shift (Fig. 1). The extent of hypsochromism demonstrates the strength of intercalative binding between complex and DNA [14, 23]. After intercalation, the π^* orbital of the intercalated ligand could couple with the π orbital of the base pairs of DNA, which results in a decrease of the $\pi-\pi^*$ transition energy. The bathochromism (red shift) may be observed when the DNA duplex is stabilized [25].

After 24 h, the experiment was repeated to produce again the visible spectra which displayed the identical results thus verifying the stability of the drug-DNA adduct.

The intrinsic binding constant 'K' was calculated for the investigated DNA active product **3** by using Benesi-Hildebrand equation 1 [26]:

$$\frac{A_0}{A - A_0} = \frac{\epsilon_G}{\epsilon_{H-G} - \epsilon_0} + \frac{\epsilon_G}{\epsilon_{H-G} - \epsilon_G} \times \frac{1}{K[DNA]} \quad (\text{Eqn. 1})$$

where A = absorbance of the drug and its adduct with DNA; A_0 = absorbance of the drug; ϵ_{H-G} = absorption coefficient of the drug-DNA adduct; ϵ_G = absorption coefficient of the drug.

The association constant was obtained from the intercept-to-slope ratios of $A_0/(A-A_0)$ vs. $1/[DNA]$ plot. The binding constant (K) was found to be $4.6 \times 10^3 M^{-1}$.

The Gibbs free energy (ΔG) was calculated by using equation 2:

$$\Delta G = -RT \ln K \quad (\text{Eqn. 2})$$

where T is the temperature (298 K) and R is general gas constant (8.314 J K⁻¹mol⁻¹). The Gibbs free energy was found to be -20.9 kJ mol⁻¹. The negative value of ΔG suggests that the interaction of the compounds with DNA is a spontaneous process.

Biological Activity Studies

The free ligand and the investigated bis(triorganotin(IV)) dicarboxylates were evaluated for their antimicrobial activities by the disc diffusion method [18]. The samples were tested against various strains of fungi (*Alternaria alternata*, *Ganoderma lucidum*, *Penicillium notatum* and *Trichoderma harzianum*) and bacteria (*Escherichia coli*, *Bacillus subtilis*, *Staphylococcus aureus* and *Pasturella multocida*). Fluconazole and streptomycin were used as standard drugs for antifungal and antibacterial screening tests. One mg of a test sample was dissolved in 1 ml of the solvent (water for the ligand/reference drug and DMSO for the complex) and 100 μ L of this solution was applied to soak 9 mm filter paper discs. The zones of inhibition of the discs were measured in mm. The compounds were also tested to find their minimum inhibitory concentration (MIC) using a standard procedure [19]. The wells exhibiting MICs were visually noted. The data are summarized in Tables 2-5.

The organotin(IV) products were found to be biologically active against the tested microbes. The coordination of the ligand with trialkyltin(IV) or triphenyltin(IV) moieties has appreciably induced antimicrobial activities in the product complexes **1-3**. Thus, the homobimetallic complexes of tin displayed considerably higher inhibitory effects as compared to the free ligand HLH. The antifungal/antibacterial activities of some complexes were even higher than those of the standard drugs (Tables 2 and 3). The minimum inhibitory concentration values of the complexes are given in Tables 4 and 5. The biological activities varied according to the nature of the substituent at tin [27]. The inhibitory action of organotin(IV) compounds is mainly due to their ability to interact with DNA and proteins. They can also damage mitochondria, thus causing the death of microorganisms [28].

Hemolytic Activities of Complexes

The disodium salt of the free ligand (**Na₂L**) and the complexes **1-3** were evaluated for their toxic hemolytic effects by a reported procedure [20]. Human red blood cells were obtained from volunteers and the average lysis was reported with respect to Triton X-100 and PBS as a positive (100% lysis) and PBS as negative (0% lysis) controls, respectively. The results obtained are summarized in Table 6.

Table 2. Antibacterial activity data^a of the ligand (HLH) and the complexes 1-3

Compound No.	Bacterial inhibition zone (mm)			
	<i>E. coli</i>	<i>B. subtilis</i>	<i>S. aureus</i>	<i>P. multocida</i>
HLH	--	--	--	-
1	30 ^a ±0.14	26 ^{ab} ±0.37	30 ^c ±0.28	22 ^c ±0.21
2	30 ^a ±0.19	22 ^{bc} ±0.32	32 ^a ±0.14	30 ^{ab} ±0.46
3	28 ^c ±0.28	18 ^c ±0.51	31 ^b ±0.42	34 ^a ±0.38
Streptomycin	30 ^a ±0.17	31 ^a ±0.28	31 ^b ±0.31	29 ^{ab} ±0.28

^a Concentration = 1 mg/ml in DMSO; Data are expressed as the mean \pm standard deviation of samples analyzed individually in triplicate at p<0.1. Values having same letters in superscripts of the same column do not differ significantly; 0 = No activity, 5-10 = Activity present, 11-25 = Moderate activity, 26-40 = Strong activity; Streptomycin is standard antibacterial drug.

Table 3. Antifungal activity data^a of the ligand (HLH) and the complexes 1-3

Compound No.	<i>A. alternata</i>	<i>G. lucidum</i>	<i>P. notatum</i>	<i>T. harzianum</i>
HLH	-	-	-	20 ^c ±0.19
1	41 ^{ab} ±0.21	28 ^{bc} ±0.13	26 ^c ±0.11	24 ^{bc} ±0.14
2	30 ^c ±0.22	25 ^c ±0.12	30 ^{bc} ±0.23	26 ^{bc} ±0.19
3	42 ^a ±0.18	32 ^{bc} ±0.25	34 ^{bc} ±0.12	33 ^a ±0.21
Fluconazole	38 ^{ab} ±0.29	41 ^a ±0.21	45 ^a ±0.31	-

^a Concentration = 1 mg/ml in DMSO. Data are expressed as the mean ± standard deviation of samples analyzed individually in triplicate at p<0.1. Values having same letters in superscripts of the same column do not differ significantly; 0 = No activity, 5-10 = Activity present, 11-25 = Moderate activity, 26-40 = Strong activity; Fluconazole is standard antifungal drug.

Table 4. MIC (bacterial) of the ligand (HLH) and the complexes 1-3 (mg/well)

Compound No.	<i>E. coli</i>	<i>B. subtilis</i>	<i>S. aureus</i>	<i>P. multocida</i>
HLH	3.12	25	25	25
1	3.90×10 ⁻¹	7.81×10 ⁻¹	3.90×10 ⁻¹	3.12
2	3.90×10 ⁻¹	6.25	3.12	6.25
3	7.81×10 ⁻¹	7.81×10 ⁻¹	3.12	6.25
Streptomycin	9.7×10 ⁻²	1.95×10 ⁻¹	6.25	3.12

Table 5. MIC (fungal) data of the ligand (HLH) and the complexes 1-3 (mg/well)

Compound No.	<i>A. alternata</i>	<i>G. lucidum</i>	<i>P. notatum</i>	<i>T. harzianum</i>
HLH	-	-	-	6.25
1	3.90×10 ⁻¹	1.95×10 ⁻¹	1.95×10 ⁻¹	1.95×10 ⁻¹
2	3.90×10 ⁻¹	1.95×10 ⁻¹	>2.44×10 ⁻²	>2.44×10 ⁻²
3	1.95×10 ⁻¹	9.76×10 ⁻²	1.95×10 ⁻¹	>2.44×10 ⁻²
Fluconazole	1.56	1.56	>2.44×10 ⁻²	25

Table 6. Hemolytic activities of the disodium salt of the ligand (Na₂L) and the complexes 1-3

Compound No.	Na ₂ L	1	2	3	Triton-X 100	PBS
% of Hemolysis	19.68±0.05	17.31±0.06	18.85±0.03	12.98±0.06	99.53±0.00	0.00±0.00

All the coordinated products possessed lower hemolytic activity as compared to Na₂L, thus coordination with the metal ion has reduced the cytotoxic hemolytic effects of the resultant species. The lowest activity (12.98%) was reported for the complex **3** and the highest value (18.85%) was recorded for the complex **2**. All other compounds presented their hemolytic activities within this

range of minimum and maximum values. The synthesized complexes possessed hemolytic activities much lower as compared to Triton X-100 and much closer to PBS.

CONCLUSIONS

Bis(triorganotin(IV)) derivatives of acetylene dicarboxylic acid demonstrate the common mass fragmentation mode due to their structural similarities. The free ligand precursor was biologically inactive against all the tested microbes but a proficient antimicrobial potential was developed after its coordination with tin. The complexes were also screened for their minimum inhibitory concentration (MIC) evaluations. The *in vitro* hemolytic activity studies were also performed on human red blood cells. All the tin(IV) coordinated products displayed lower cytotoxic effects (12.98-18.85%) as compared to the free ligand (19.68%). The triphenyltin(IV) derivative **3** was unique in the sense that (i) it was the most active biological agent (ii) it showed interaction with salmon sperm DNA (iii) it possesses less toxic hemolytic effects compared to all three complexes. Its antibacterial/antifungal potential was even higher than those of the standard antimicrobial drugs streptomycin and fluconazole.

REFERENCES

1. C.J. Murray, A.D. Lopez, *The Lancet*, **349**, 1498 (1997).
2. M.S. Ali, M.S. Islam, M.M. Rahman, M.R. Islam, M.A., Sayeed, M.R. Islam, *J. Basic. Clin. Pharm.*, **2**, 103 (2011).
3. S. Mariam, S. Hussain, S. Ali, S. Shahzadi, S. Ramzan, M. Shahid. *Iran. J. Sci. Technol., A*, **42**, 1277 (2018).
4. M. Jain, V. Singh, R.V. Singh, *J. Iran. Chem. Soc.*, **1**, 20 (2004).
5. A. Mukhtar, F. Mohamat-Yusuff, S.Z. Zulkifli, H. Harino, A. Ismail, K. Inoue. *Environments*, **6**, 26 (2019).
6. S.K. Shukla, V.K. Tiwari, S. Rani, K. Ravi, I.C. Tewari, *Int. J. Agr. Sci.*, **2**, 5 (2010).
7. S.K. Dubey, U. Roy, *Appl. Organomet. Chem.*, **17**, 3 (2003).
8. S. Hussain, S. Ali, S. Shahzadi, M. Shahid, A.A. Tahir, S.M. Abbas, M. Riaz, I. Ahmad, I. Hussain, *J. Coord. Chem.*, **70**, 4070 (2017).
9. S. Hussain, S. Ali, S. Shahzadi, S.K. Sharma, K. Qanungo, M. Shahid. *Bioinorg. Chem. Appl.*, **11** (2014), Article ID 959203. doi:10.1155/2014/959203.
10. W. Lou, M. Chen, X. Wang W, Liu, *Size Phys. Chem. C.*, **111**, 9658 (2007).
11. C. Pellerito, P.D. Agati, T. Fiore, C. Mansueto, V. Mansueto, G. Stocco, L. Nagy, *J. Inorg. Biochem.*, **99**, 1294 (2005).
12. M. Kashif, S.Z. Khan, Zia-ur-Rehman, A, Shah, I. Butler, *Inorg. Chim. Acta*, **423**, 14 (2014).
13. F. Shaheen, S. Ali, S. Shahzadi, *Der. Chemica Sinica*, **8**, 494 (2017).
14. X. Zhang, H. Yan, Q. Song, X. Liu, L. Tang, *Polyhedron*, **26**, 3743 (2007).
15. W.L.F. Armarego, C.L.L. Chai, *Purification of Laboratory Chemicals*, 5th edn., Butterworth Heinemann, London, 2003.
16. C.V. Sastri, D. Eswaramoorthy, L. Giribabu, B.G. Maiya, *J. Inorg. Biochem.*, **94**, 138 (2003).
17. S. Hussain, S. Ali, S. Shahzadi, M.N. Tahir, M. Shahid. *J. Coord. Chem.*, **68**, 2369 (2015).
18. CLSI (The Clinical Laboratory Standards Institute), *J. Clin. Microbiol.*, **45**, 2758 (2007).
19. S.D. Sarker, L. Nahar, Y. Kumarasamy, *Methods*, **42**, 321 (2007).
20. P. Sharma, J.D. Sharma, *J. Ethnopharmacol.*, **74**, 239 (2001).
21. S. Hussain, S. Ali, S. Shahzadi, S.K. Sharma, K. Qanungo, I.H. Bukhari, *J. Coord. Chem.*, **65**, 278 (2012).
22. S.M. Abbas, M. Sirajuddin, S. Ali, S.T. Hussain, F.A. Shah, A. Meetsma, *J. Chem. Soc. Pak.*, **35**, 861 (2013).
23. F. Javed, S. Ali, M.W. Shah, K.S. Munawar, S. Shahzadi, Hameedullah, H. Fatima, M. Ahmed, S.K. Sharma, K. Qanungo, *J. Coord. Chem.*, **67**, 2795 (2014).
24. S. Hussain, I.H. Bukhari, S. Ali, S. Shahzadi, M. Shahid, K.S. Munawar, *J. Coord. Chem.*, **68**, 662 (2015).
25. M. Sirajuddin, S. Ali, V. McKee, S. Zaib, J. Iqbal, *RSC Adv.*, **4**, 57505 (2014).
26. M.S. Ahmad, M. Hussain, M. Hanif, S. Ali, B. Mirza, *Molecules*, **12**, 2348 (2007).
27. P. Chaudhary, M. Swami, D.K. Sharma, R.V. Singh, *Appl. Organomet. Chem.*, **23**, 140 (2009).
28. M. Carcelli, A. Fochi, P. Pelagatti, G. Pelizzi, U. Russo, *J. Organomet. Chem.*, **626**, 161 (2001).

Antibiocorrosive coatings based on antimicrobial polymer hybrid composites

N. Lekishvili^{1*}, Kh. Barbakadze^{1,2,3}, B. Arziani², G. Lekishvili², W. Brostow³

¹*Ivane Javakhishvili Tbilisi State University, Institute of Inorganic-Organic Hybrid Compounds and Non-traditional Materials, 3, I. Chavchavadze Ave., 0179 Tbilisi, Georgia*

²*Tbilisi State Medical University, 33, V. Pshavela Ave., 0186 Tbilisi, Georgia*

³*University of North Texas, Laboratory of Advanced Polymers & Optimized Materials, Department of Materials Science and Engineering and Department of Physics, University of North Texas, 3940 North Elm Street, Denton, TX 76207, US*

Received August 29, 2018; Accepted June 5, 2019,

Antimicrobial composites and coatings with specific properties based on polyurethane and nano sized arsenic trioxide (As_2O_3) obtained by transformation of secondary resources were created and studied. Thermo-physical characteristics, basic tribological (scratch resistance, wear, dynamic friction) and surface properties of the obtained composites and materials were studied. The addition of silicon-organic oligomers into polyurethane matrix modifies thermal, tribological and operational properties of corresponding materials in the desired direction. Strong intermolecular interactions and compatibility between materials components were verified by performed tests and reflected in the morphology of the hybrids as well. The elaborated antimicrobial hybrid coatings are characterized with good fixation on various samples and wares, good strength, elasticity; they do not change the colour during photo- and isothermal aging and have a number of applications.

Keywords: arsenic trioxide, secondary resources, antimicrobial, coating, properties

INTRODUCTION

Increased concern to the antimicrobial safety in the various spheres is an issue of global importance. In response to the deterioration of ecological conditions, the increasing bacterial and fungal population on various surfaces stimulates a series of biocorrosive processes that cause significant economic losses to industry and pose serious threats to cultural heritage (historic buildings and monuments, archaeological patterns, museum exhibits, etc.) as well [1].

Bacterial corrosion is a result of synergistic interactions between the various materials surfaces, abiotic corrosion products, microbial cells and their metabolites [2]. Pathogenic microorganisms are placed on the surfaces of various natural and synthetic materials (leather, wood, plastics), polymers, and stimulate irreversible deterioration of their physical and mechanical properties, biodegradation and finally, damaging. That affects many fields of technique and industry and causes losses annually amounting to billions of dollars [3, 4].

The development of new type inorganic-organic multifunctional hybrid materials has the real prospect to solve this problem [5]. Antimicrobial covering/protecting of various natural and synthetic materials and wares will also achieve the protection of humans in case of their direct contact with the

surfaces of aforementioned materials and will solve a number of environmental problems.

During the last two decades the design of polyfunctional inorganic-organic antimicrobial hybrid materials has attracted considerable research interest. The wide range of possible hybrids may include innovative combinations, starting from organic and organometallic molecules to inorganic compounds, biogenic transition metals complex compounds or clusters, dispersed in a polymer matrix [6].

Hence, the exploration of new antimicrobial compounds and materials has a great actuality and needs further development for effective prevention and/or inhibition of the growth of detrimental microorganisms and control of biocorrosion processes [6].

Arsenic and its compounds have long been identified for their bactericidal effects and thus they are mainly used in the production of pesticides, anthelmiths, wood preservatives, etc. In addition, arsenic compounds have a long history of use in medicine. Since arsenic trioxide (As_2O_3) was first approved by the FDA as the front line therapy for acute promyelocytic leukemia 25 years ago, its anti-cancer properties for various malignancies have been under intense investigation [7, 8].

It is very important to search a cheap base for creating the materials mentioned above on a wide scale, especially from natural and industrial secondary resources. Caucasus region (Georgia) is

* To whom all correspondence should be sent:
E-mail: nodar@lekishvili.info

rich in natural resources. Among them arsenic takes a special place [9, 10].

Arsenic deposits are basically situated in the north region of Georgia in the form of occurrences. It is very important that these ores do not contain impurity elements, and the best chance is given to produce highly pure metal arsenic and As₂O₃.

Nanotechnology is currently growing as a multidisciplinary field of science and has proved its potential by fetching benefits in modern functional coatings development. The coatings containing nano-particles offer much better material and processing properties than conventional coatings (e.g. increased indentation resistance, high elasticity, fast drying, and no expansion after contact with water, high water vapour permeability).

Thus, a number of environmental benefits are to be expected from nanotechnology-based coatings including: a) thinner coating layers; b) minimization or substitution of solvents and toxic compounds used in coating materials; c) less consumption of energy and cleaning agents; d) extended life span of the coated objects, etc.

EXPERIMENTAL

Polyurethane was obtained by interaction of 4,4-dimethylmethanediisocyanate with oligobutylene glycol adipinate in an equimolar ratio. Silicon organic oligomers – α,ω -dihydroxydimethyl-(methylvinyl)oligoorganosiloxane ($\eta=2.7$ Pa·s; $M_{\text{ebu}} \approx 2.95 \cdot 10^4$), bis(hydroxyalkyl)oligodimethylsiloxane ($M_n \approx 5.600$) and oligo[dimethylsiloxane-co-(3-aminopropyl)methyl]siloxane were obtained from Aldrich Chemicals.

Antimicrobial coating - sample preparation: to the cyclohexanone solution (155°C) of the PU matrix a definite amount (3, 7, 10 wt.%) of the selected silicon-organic modifiers and bioactive component were gradually added and were stirred for 30-40 min (25°C) until formation of light coloured homogenous mass. Obtained materials were deposited as thin layers on the surface of the various substrates (wood, Teflon) and were left in the air during 48-72 h (25°C) to produce homogenous and smooth protective layers.

Differential scanning calorimetric measurements were performed with DSC 200 (Netzsch, Germany). All tests (10 mg of each sample) were conducted under dry nitrogen; temperature range from -100°C to +300°C; heating rate 5°C/min.

Thermogravimetric analysis was carried out using Perkin Elmer TGA-7; 10-20 mg of each dry sample was tested [11]. Temperature range 30-700°C; heating rate 10°C/min.

Hydrophobicity was studied by a gravimetric method [12].

Tribological characterization: Scratch and sliding wear tests were performed on a Micro-Scratch Tester (MST) applying linearly increasing force in the range of 0.03-30.0 N or else a constant force (25°C) [13]. The sliding wear (SWD) results were obtained by multiple scratching with a diamond tip along the same groove. Both in single scratching or in SWD, one obtains the penetration depth R_p and the residual (healing) depth R_h determined two minutes later. Both R_p and R_h values were taken at the midpoint. The viscoelastic recovery φ was defined by equation (1) which applies to the single scratch resistance tests, as well as to the sliding wear:

$$\varphi = \frac{R_p - R_h}{R_p} \times 100\% \quad (1)$$

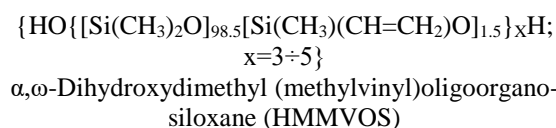
Dynamic friction was measured using Nanovea pin-on-disk tribometer. 440 steel balls made by Salem Specialty Balls with 3.2 mm diameter were used. Temperature 20±2°C, speed 100 rpm, sliding distance 40 m, radius 2.0 mm, load 2.0 N, 2000 revolutions, test duration 20 min.

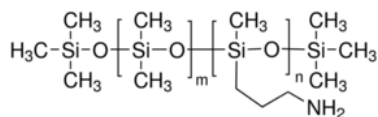
The scanning electron microscope (Eclipse ME 600, Nikon) was used to observe the changes in the wear tracks after testing and to study the possible modes of failure or deformation.

RESULTS AND DISCUSSION

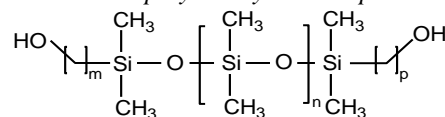
For creation of antimicrobial hybrid coatings nano-sized As₂O₃ (3 and 5 wt.%) obtained by transformation of arsenic secondary resources were used as the bioactive component (BC) [14-17]. By using non-realized secondary resources it is possible to elaborate relatively cheap bioactive components and inorganic-organic hybrid antimicrobial coatings based on them for protection of the rich cultural heritage in this region.

As polymeric matrix polyurethane (PU) was selected considering its mechanical and tribological properties [18,19]. For modification of some characteristics (elasticity, formation of homogeneous films on various substrates, hydrolytic and thermal stability) of the basic polyurethane matrix polyoligoorganosiloxanes with functional groups (hydroxy-, amino-) at the silicon atom were used:





Oligo[dimethylsiloxane-co-(3-aminopropyl)methyl]siloxane (ODMAPMS)



Bis(hydroxyalkyl)oligodimethylsiloxane (BHODMS)

Table 1. Polyurethane composites for antimicrobial coatings

Polymer matrices and hybrid composites	
1. PU	8. PU/10 wt.% ODMAPMS
2. PU/3 wt.% HMMVOS	9. PU/7 wt.% BHODMS
3. PU/3 wt.% As ₂ O ₃	10. PU/10 wt.% BHODMS
4. PU/5 wt.% As ₂ O ₃	11. PU/7 wt.% ODMAPMS/3 wt.% As ₂ O ₃
5. PU/3 wt.% HMMVOS/3wt.% As ₂ O ₃	12. PU/10 wt.% ODMAPMS/3 wt.% As ₂ O ₃
6. PU/3 wt.% BHODMS	13. PU/7 wt.% BHODMS/3 wt.% As ₂ O ₃
7. PU/7 wt.% ODMAPMS	14. PU/10 wt.% BHODMS/3 wt.% As ₂ O ₃

Differential scanning calorimetric (DSC) method was used to locate the crystalline phases, glass and phase transition temperature regions of the modified matrices and the hybrid polymer composites obtained on their basis.

DSC studies showed that all tested materials are amorphous (no exothermic peak characteristic for crystallization is displayed on the DSC diagrams) and no melting transitions are visible. Endothermic peaks on the obtained DSC diagrams correspond to glass transition regions (T_g). It was shown that tested hybrids have glass transition in the range from +38.8°C to +59.7°C. This is important for the use of the obtained coatings for protection of museum exhibits since optical clarity at room temperature or in a wider temperature range is assured. Doping of nano sized arsenic trioxide as bioactive component into the basic polymer has no significant influence on the value of T_g . Glass transition temperature regions are more sensitive towards siloxane modifiers. In particular, by incorporation of oligoorganosiloxanes into the researched composites provokes a decrease of T_g from 58.7-56°C to 38.8-44.3°C.

DSC study also showed phase transition in the glassy state, so called β -transitions (T_β) [20]. It was established that addition of bioactive component into modified polymer composites reduces the absolute value of T_β from -56°C to -(48-51)°C. Thus, adding 3 wt.% of As₂O₃ to PU results in lowering of the β -transition temperature T_β centered around the regions from -43.6°C to -37°C correspondingly (Table 1, comp. 1, 2, 5, 13, 14). Thus, addition of BCs enhances the stability of the low-temperature amorphous phase.

Decomposition behaviour and thermal stability parameters of pure and modified hybrid composites were determined by thermogravimetric analysis as follows: initial degradation temperature ($T_{In.dec.}$), decomposition temperature ($T_{dec.}$) with corresponding weight loss (wt.%) and temperature of the maximum rate of degradation ($T_{max.}$), - temperature after which no changes are observed.

Intensive destruction process of the pure PU matrix takes place in the temperature range of 290-460°C with a large weight loss of 81.3% of the original weight. In the 460-570°C range weight drop of the remaining weight is seen (Table 2).

Table 2. TGA data of the PU hybrids

Hybrid	$T_{st.dec.}$, °C	$T_{In.dec.}$, °C	Weight loss, %	$T_{max.}$, °C
1	280	290-460	81.3	570
2	285	320-480	36.0	590
4	290	420-532	62.7	685
5	330	410-538	31.4	670
6	300	355-548	27.1	630
7	315	360-390	78.8	580
8	320	360-400	80.0	590
9	320	360-420	77.1	590
10	290	330-480	78.3	580
12	340	360-490	74.3	590
14	340	380-530	75.1	600

PU-composites modified by polyoligoorganosiloxanes are quite stable up to 290-340°C and weight loss does not exceed 5-6 wt.% (Table 2).

Intensive destruction process of modified samples takes place in the range of about 320-548°C. As is seen in Table 2, both $T_{st.dec}$ and T_{max} of the modified polymer hybrids increased with respect to pure PU. Further addition of BC shifts $T_{In.dec.}$ to the higher temperatures with reduced weight loss. The full thermal degradation of modified hybrid composites is observed in the range of 580-685°C.

Tribological characterization of materials deals with friction, wear, scratch resistance and design of interactive surfaces in relative motion [21]. The basic tribological and surface properties (morphology, outward appearance, optical stability) of the obtained non-modified and modified PU composites and materials were studied.

Penetration depth (R_p) diagrams of the examined composites at constant load as a function of the number of scratch tests were obtained. Analysis of results showed an improvement of resistance towards instantaneous deformation of the corresponding composites obtained *via* modification of basic polyurethane by siloxane modifiers (Fig. 1; composites 1, 7-10, Table 1). Penetration depths of composites 7-10 are in the range of 200-245 μm while for pure PU $R_p \approx 298 \mu\text{m}$. Increasing of wt.% of the used modifier lowers R_p with respect to the pure PU. Namely, the maximum reductions in R_p were shown for composites obtained by modification with 10 wt.% of siloxane modifiers - R_p ranging around 200-206 μm (Fig. 1; comp. 8, 10, Table 1). Herewith the best result showed the modified composite by 10 wt.% BHODMS (Fig. 1; comp. 10, Table 1). Further incorporation of BC slightly lowers R_p with respect to the pure PU and hybrids (Fig. 1; comp. 11-14, Table 1).

Modifications with silicon-organic oligomers caused a decrease in residual depth (R_h) after healing (determined after 2 min) by about 80-90 μm (Fig. 2; comp. 7-10, Table 1). The maximum reduction of R_h was shown by the composite modified with 10 wt.% BHODMS (Fig. 2; comp. 10, Table 1). For corresponding hybrids a further slight decrease in R_h was observed as well (Fig. 2; comp. 11-14, Table 1).

The values of viscoelastic recovery (φ) of modified composites calculated from eqn. (1) are in the range of 60-70%. A slightly higher viscoelastic recovery was registered for PU materials modified with 10 wt.% BHODMS (Fig. 3, comp. 10, 13, Table 1). Thus, improvements in penetration and residual depths, as well of viscoelastic recovery of the examined hybrids with respect to basic PU are manifested.

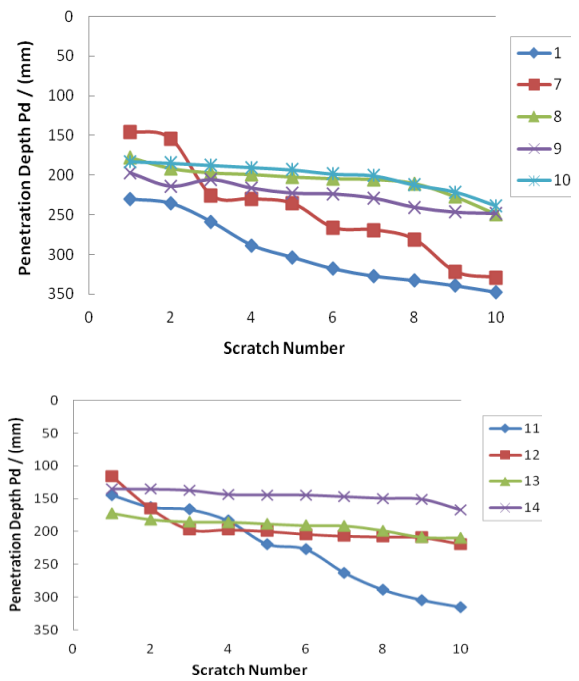


Figure 1. Penetration depths of pure and modified PU composites and antimicrobial coatings (Table 1).

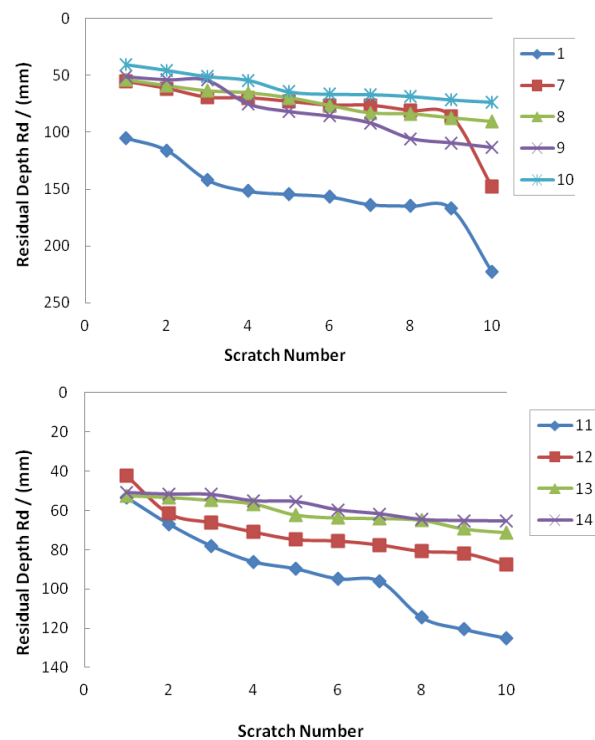


Figure 2. Residual depths of pure and modified PU composites and antimicrobial coatings (Table 1).

By dynamic friction tests it was shown that modification with ODMAPMS and BHODMS lowers the coefficient of dynamic friction (f) of the corresponding composites in respect to pure PU (Fig. 4; comp. 7-10, Table 1). Herewith the increase in modifier's quantity causes an improvement of wear resistance. Accordingly, lower values of the average dynamic friction were

shown by the composite modified with 10 wt.% silicon-organic oligomers with respect to pure PU (Fig. 4; comp. 8, 10, Table 1). Subsequent incorporation of BC shows a further decrease of the values of average friction as a function of composition (Fig. 4; comp. 11-14, Table 1). The hybrid coating obtained by modification with 10 wt.% BHODMS and BC is characterized with the best wear resistance among the tested composites (Fig. 4; comp. 14, Table 1).

The analysis of the dependence of the dynamic friction on the sliding distance mostly shows a steady behaviour of the values of dynamic friction during the tests (Fig. 5).

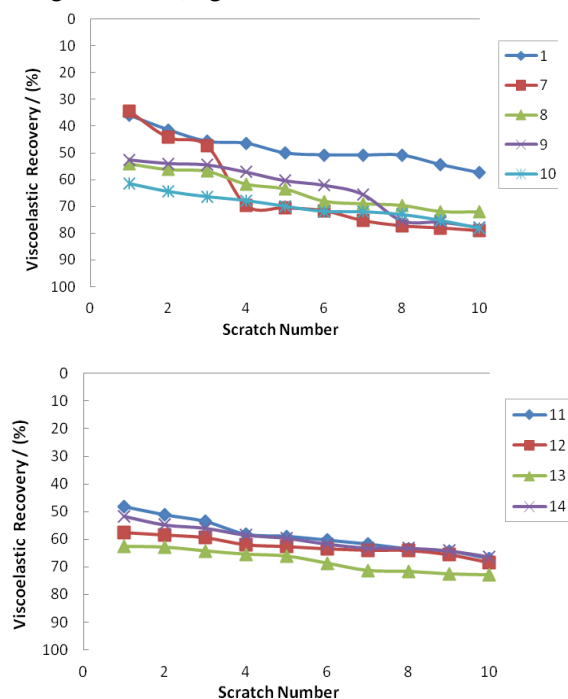


Figure 3. Viscoelastic recovery of pure and modified PU composites and antimicrobial coatings (Table 1)

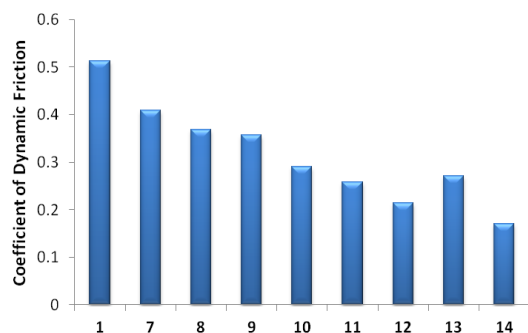


Figure 4. Comparison of the values of the average coefficient of dynamic friction for polymer matrices and antimicrobial coatings based on them (Table 1).

The decrease in the coefficient of dynamic friction for PU matrices modified by oligo organosiloxanes is caused by the plasticizer effect of the flexible chains of siloxane modifiers. By

doping of bioactive components into basic PU the coefficient of dynamic friction of the tested coatings slightly increases (Fig. 5; comp. 3, 4, Table 1). Further addition of bioactive component with higher quantities increases the hardness of the formed coatings (Fig. 5; comp. 4, Table 1). Herewith, doping the optimal amount of bioactive component into PU modified with HMMVOS gives satisfying results of wear resistance (Fig. 5; comp. 5, Table 1). Thus, modified polyurethane matrices and corresponding antimicrobial coatings are characterized with lower friction than pure PU. It was established that the wear resistance of the tested composites mainly depends on their composition, on the nature and quantity of modifiers and on the experimental conditions.

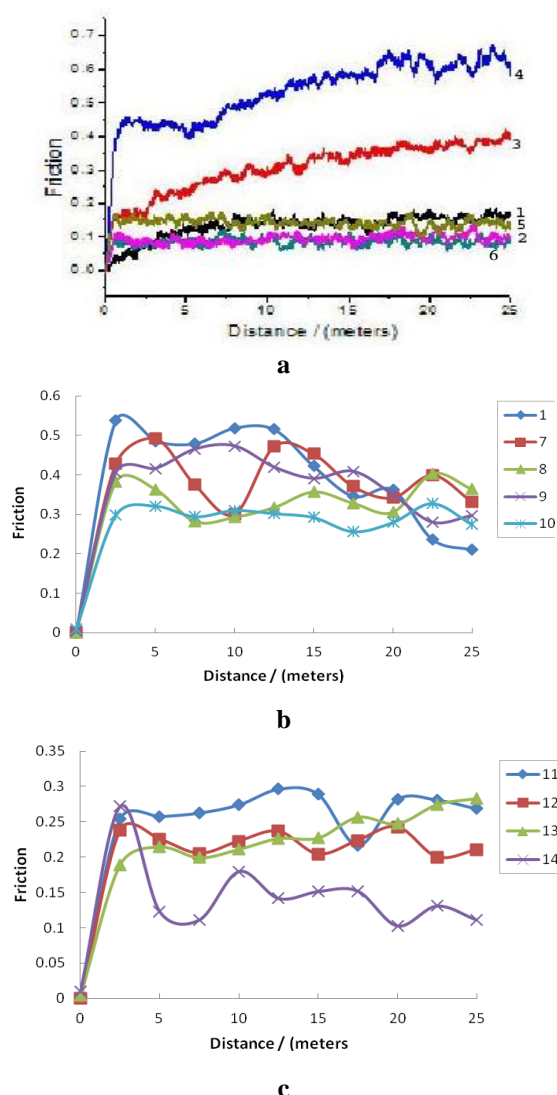


Figure 5. Dependence of the dynamic friction on the sliding distance for pure and modified PU matrices and corresponding antimicrobial coatings (Table 1).

The obtained results were also confirmed by studying the surface morphology (SEM) of the polymeric matrices and antimicrobial coatings (Fig.

6). Plastic deformation behavior of modified PU films is characterized with less crack nucleation in comparison with non-modified one. Namely, plastic deformation of corresponding films under 2N constant load showed that a split behavior of PU matrix modified by 3 wt.% α,ω -dihydroxymethylvinyloligoorganosiloxane is characterized with less crack nucleation in comparison with pure

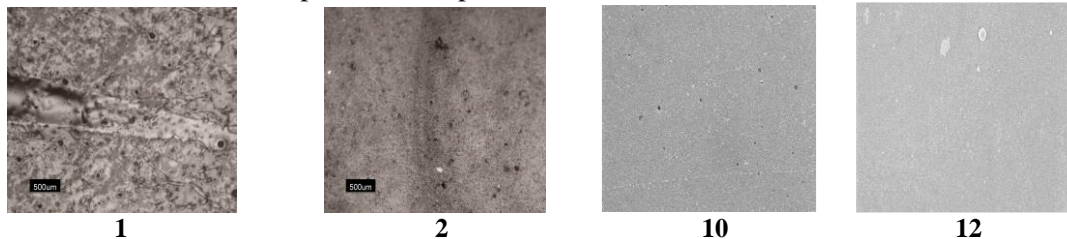


Figure 6. Surface morphology of the PU matrices and antimicrobial coatings (Table 1)

Table 3. Hydrophobicity of the PU matrices and corresponding antimicrobial hybrids

N _o	W _{H₂O} , wt.%	N _o	W _{H₂O} , wt.%	N _o	W _{H₂O} , wt.%
1	0.046	6	0.027	11	0.027
2	0.025	7	0.028	12	0.026
3	0.016	8	0.027	13	0.024
4	0.012	9	0.026	14	0.025
5	0.010	10	0.024		

This effect is caused by the plasticizing behaviour of siloxane modifiers.

Hydrophobic properties of coatings play a significant role in the process of adhesion of microorganisms on various surfaces. Water absorption ability (W_{H₂O}, wt.%) of the obtained antimicrobial coatings was determined by a gravimetric method [11]. As performed tests showed, silicon-organic and bioactive inorganic modifiers act as a barrier in the polyurethane matrix, hindering the effective path for the water molecules to travel, and accordingly lead to an increase in water absorption resistance. Thus, W_{H₂O} did not exceed 0.03 wt.% during 720 h in all cases (Table 3). It was established that during three months, under conditions of isothermal aging (40-60°C) and “light-weather” (complex action of air oxygen, carbon dioxide, visible light, moisture) the initial appearance, color, optical transparency and mechanical properties (surface homogeneity without splits formation) of the created anti-biocorrosive coatings were not deteriorated.

Based on the research carried out it was shown that the mechanical, tribological and operational properties of antimicrobial composite and materials were improved by the proper combination of the structure, bioactivity and ratio of basic components. The elaborated antimicrobial coatings are characterized with good fixation on various samples and wares, sufficient strength, elasticity and good tribological properties; they do not

PU. It **should** be noted that composites obtained by modification of PU with 10 wt.% bis(hydroxyalkyl)polydimethylsiloxane and BC, have smoother surfaces, without brittleness and porous regions and demonstrated the least crack nucleation among the tested polymeric matrices (Fig. 6; comp. 1, 2, 10, 12, Table 1).

scratch easily; do not change the relief of the surface and the colour during photo- and isothermal aging (40-60°C); are relatively cheap, available and safe for human. Bioactive components conferred to the antimicrobial coatings completely new properties. Accordingly, not only covering and antimicrobial protection of various natural and synthetic materials, wares and museum exhibits can be achieved, but meanwhile, the coatings provide removal and annihilation of harmful effects of microorganisms, fungi and bacteria, which also presupposes solving of a number of environmental problems.

CONCLUSIONS

New generation multifunctional polymer coatings with specific properties were developed by using siloxane oligomers as modifiers of a selected polyurethane matrix. As bioactive component nano-sized arsenic trioxide was used, which is non-volatile, non-flammable, biocompatible with the used polymer matrix and dimensionally stable, obtained by transformation of cheap secondary resources of arsenic production. It was established that the addition of silicon-organic oligomers into the polyurethane matrix modifies the thermal, tribological and operational properties of the corresponding materials in the desired direction. The coatings are characterized with good fixation on various surfaces, strength and elasticity, thermal stability, hydrophobicity and their features and

colour are not worsened during photo- and isothermal aging.

Acknowledgements: Authors would like to thank Shota Rustaveli National Science Foundation of Georgia (RNSF) for financial support (Kh.Barbakadze; Grant project #YS/33/11-811/15).

REFERENCES

1. B. Tribollet, *Mater. & Corros.*, **54**, 7, 527 (2003).
2. G.T. Howard, *Int. Bieterior. & Biodegr.*, **49**, 4, 242 (2002).
3. Gu Ji-Dong, *Int. Bieterior. & Biodegr.*, **52**, 1, 69 (2003).
4. H.A. Videla, *Int. Biodeterior. & Biodegr.*, **49**, 259 (2002).
5. N. Lekishvili, R. Gigauri, M. Rusia, M. Kezherashvili, Kh. Barbakadze, G. Lekishvili, B. Arziani, 2nd International Caucasian Symposium on Polymers and Advanced Materials, 21, Tbilisi, Georgia, 2010.
6. P. Gomez-Romero, C. Sanchez, Functional Hybrid Materials, Wiley-VCH, Weinheim, 2006.
7. W. H. Miller, Jr., H. M. Schipper, J. S. Lee, J. Singer, S. Waxman, *J. Cancer Res.*, **62**, 14, 3893 (2002).
8. N. Lekishvili, M. Rusia, Rus. Gigauri, L. Arabuli, Kh. Barbakadze, I. Didbaridze, M. Samkharadze, Arsenic and Stibium Advanced Compounds with Specific Properties, Universali Press, Tbilisi, Georgia, 2014.
9. R. Gigauri, G. Chachava, M. Gverdtseteli, I. Laperashvili, Proceedings of the Academy of Sciences of Georgia, Chemistry Series, **33**(4), 395 (2007).
10. W. Brostow, M. Gakhutishvili, Rus. Gigauri, Sh. Japaridze, N. Lekishvili, *Chem. Eng. J. (US)*, **159**, 24 (2010).
11. K.P. Menard, Performance of Plastics, Ch. 6, (W. Brostow, ed.), Hanser, Munich - Cincinnati, 2000.
12. Kh. Barbakadze, W. Brostow, T. Datashvili, N. Hnatchuk, N. Lekishvili, *Wear*, **394-395**, 228 (2018).
13. W. Brostow, V. Kovacevic, D. Vrsaljko, J. Whitworth, *J. Mater. Educ.*, **32**(5-6), 273 (2010).
14. J.L. Hobman, L.C. Crossman, *J. Med. Microbiol.*, **64**, 471 (2014).
15. A. Pal, S. Saha, S.K. Maji, M. Kundu, A. Kundu, *Adv. Mat. Lett.*, **3**, 177 (2012).
16. V. Jadhav, S. Sachar, S. Chandra, D. Bahadur, P. Bhatt, *J. Nanosci. Nanotechnol.*, **16**, 1 (2016).
17. A. Subastri, V. Arun, P. Sharma, E. Preedia babu, A. Suyavaran, S. Nithyananthan, G.M. Alshammari, B. Aristatile, V. Dharuman, Ch. Thirunavukkarasu, *Chemico-Biological Interactions*, vol. 295, p. 73-83, (2018), <https://doi.org/10.1016/j.cbi.2017.12.025>
18. Yu. Savelyev, A. Grekov, V. Veselov, Ukraine Patent 14952A (1997).
19. Yu. Savelyev, Handbook of Condensation Thermoplastic Elastomers, Willey-VCH Verlag GmbH & Co., KgaA, 2005.
20. VC 2007 Wiley Periodicals, Inc. *J. Polym. Sci. Part B: Polym. Phys.*, **45**, 627 (2007).
21. W. Brostow, J.-L. Deborde, M. Jaklewicz, P. Olszynski, *J. Mater. Educ.*, **24**(4-6), 119 (2003).

Modelling the interaction and prediction of microtubule assembly inhibition of podophyllotoxin and its derivatives by molecular docking

M. D. Atanasova^{1*}, P. Sasheva², I. M. Yonkova², I. A. Doytchinova¹

¹Department of Chemistry, Faculty of Pharmacy, Medical University – Sofia, Bulgaria

²Department of Pharmacognosy, Faculty of Pharmacy, Medical University – Sofia, Bulgaria

Received October 17, 2018; Accepted June 1, 2019

The interactions of 15 podophyllotoxin derivatives (synthetic and naturally occurring) within the colchicine binding site of β -tubulin were modelled by molecular docking. The docking protocol was optimized in terms of scoring function, radius of binding site and number of flexible amino acids within the binding site. Each docking run was repeated three times and the average fitness score was correlated with the pID_{50} . The Pearson's correlation coefficient r was 0.655. The derived model was validated by cross-validation in 5 groups. The differences between pID_{50exp} and pID_{50pred} of the studied compounds were less than one log unit for 93% of the compounds. The inhibitory activities of three new natural compounds were predicted. One of them, 4'-demethyl-6-methoxypodophyllotoxin, showed predicted ID_{50} value of 0.36 μ M, placing this compound as one of most active inhibitors. This is in agreement with its known cytotoxicity which is 2 to 3.5 times higher than the cytotoxicity of etoposide in the different cell lines. The tubulin inhibition was suggested as a probable mechanism of the cytotoxicity of this compound.

Keywords: podophyllotoxin, molecular docking, modelling, colchicine binding site, microtubule inhibition, quantitative relationships

INTRODUCTION

Microtubules (MTs) are hollow, cylindrical organelles that play critical roles in diverse cellular processes. One of their essential functions is the participation in cell division as the main structure units of mitotic spindle, thus being responsible for the arranged segregation of replicated chromosomes into daughter cells [1, 2]. MTs of cytoskeleton together with actin filaments and intermediate filaments play a major role in determining and retaining the dynamic spatial organization of cytoplasm, as well as in specifying the characteristic cell shape [3]. Additionally, microtubules are the main structural components of eucariotic cilia and flagella [4]. They are involved in the elongated neuronal processes and in the intracellular transport [5,6].

As the microtubules are essential for the cell growth and division, they are target for a wide variety of substances, which mostly bind the protein tubulin [7-9]. Tubulin, the building block of microtubules, is a 100 kDa heterodimer formed by α - and β -polypeptides, that are equivalent in size and structure [10, 11]. Each tubulin subunit is a product of multiple genes, called isotypes [12]. Additional posttranslational modifications can be accomplished to both subunits, as polyglutamylation, polyglycylation, reversible tyrosination, phosphorylation and acetylation [12, 13]. Apart from the acetylation of Lys40, the main site for posttranslational modifications is the

specific for each isotype C-terminal region, which is highly acidic and unstructured and is lying as a flexible arm at the MT lattice surface [11, 13]. Nevertheless, the major tubulin isotypes are highly conserved and typically containing only 2-8 % amino acid sequence divergence [14]. There are many specific binding sites on a tubulin heterodimer. The β -tubulin is much more known, as it is the main target of multiple ligands that hinder microtubule dynamics, several of which are anticancer drugs [15, 16]. The suppression of microtubule dynamics is a casual link in mitosis [17] and is realized by microtubule detachment (vinblastine, colchicine) or by hyperstabilisation of microtubule organizing centres (paclitaxel) [12]. Usually, the inhibitors bind to one of the three distinct sites – the colchicine, vinblastine and taxol sites [18, 19]. Despite the high degree of conservation between the isoforms, the geometry of the ligand binding site is specific for each of the β -tubulin isotypes, possibly rendering differences in binding affinities [20]. Interestingly, the majority of differences between the isoforms are found outside the ligand binding sites and concentrated in lateral and longitudinal surfaces, changing the overall kinetics of microtubule assembly and disassembly [21, 22].

Podophyllotoxin (Fig. 1) is a naturally occurring lignan [23] that destabilises the microtubules, causing arrest in the cell division [24]. The molecule competes for a colchicine-binding site of a soluble tubulin dimer.

* To whom all correspondence should be sent:
E-mail: matanasova@ddg-pharmfac.net

The presence of ligand in the tubulin dimer disturbs the interaction between the helices of α - and β -tubulin, which are involved in adopting straight conformation. Failure to lock straight conformation results in loss of lateral contact thus preventing microtubule assembly [19, 25]. Podophyllotoxin, like most of the microtubule-binding agents is needed only in small concentrations to inhibit the microtubule growth [26]. There are several characteristics of the podophyllotoxin interaction with the β -tubulin: podophyllotoxin binds to β -tubulin faster than the colchicine, does not activate GTP hydrolysis, and does not interact with the α -subunit T5 loop [25, 27]. These properties make podophyllotoxin a potential chemotherapeutic agent and trials for anticancer activity were done in humans [28, 29]. Although the adverse effects, as high gastrointestinal toxicity, have restricted its application as antineoplastic agent [30, 31], it is widely used for the local treatment of genital warts [32]. The remarkable biological activity makes podophyllotoxin an important source for developing of less toxic analogues. Thus the semi-synthetic anticancer drugs etoposide, teniposide and etopophos were developed. Despite of the structural similarity to podophyllotoxin, they act as topoisomerase II inhibitors [32-35]. Nowadays they are used for the treatment of Hodgkin's disease, small cell anaplastic lung cancer, testicular cancer and other malignancies [33, 36, 37]. The success of podophyllotoxin-based drugs made podophyllotoxin skeleton an attractive lead in the synthesis and isolation of novel active analogues [38].

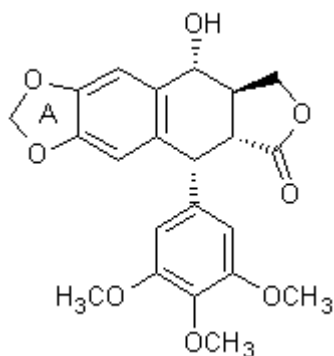


Figure 1. Structure of podophyllotoxin

In the present study, we applied molecular docking to model the binding of podophyllotoxin derivatives (synthetic and naturally occurring) within the colchicine binding site of β -tubulin in

order to derive a quantitative relationship between the docking-based scores of the complexes and the microtubule inhibition. The derived relationship was validated by cross-validation in 5 groups. The lowest-energy pose of the most active microtubule inhibitor in the study was used to analyse the interactions between β -tubulin and inhibitor. The derived relationship was used to predict the activities of novel podophyllotoxin derivatives.

MATERIALS AND METHODS

Homology modelling

In the present study, the inhibition of microtubule assembly by podophyllotoxin and its congeners was conducted on chicken brain tubulin [39]. As X-ray data for chicken tubulins are absent, the X-ray structure of cattle brain tubulin-podophyllotoxin complex (pdb code 1SA1) [19] was used as a template for homology modelling of the binding site. The binding site consists of 38 residues identified within a distance of 8Å from podophyllotoxin in the colchicine-binding site (Fig. 2).

There are seven isotypes of chicken β -tubulin, as isotypes β -II and β -III are dominant in brain [40, 41]. They were compared with the X-ray structure of cattle tubulin by sequence alignment (Figure 2). The binding site is highly conserved and only single mutations are available at positions 200, 239, 316, 330 and 351. The chicken isoforms IIa (given as P09203 TBB1_CHICK in Figure 2) and IIb (given as P32882 TBB2_CHICK in Figure 2) have one single mutation V316I. The substitution of Val with the bulkier Ile narrows the binding site [14]. Single point mutation of the X-ray bovine β -tubulin was performed to generate the V316I isoform, followed by MM optimization with AMBER03 force field. No water molecules are present in the binding site. The V316I isoform was used as a target in the subsequent docking simulations.

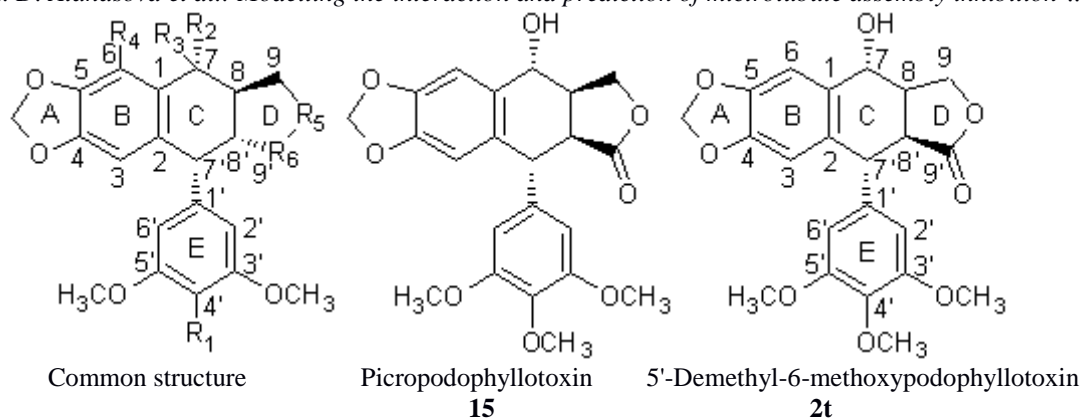
Data set and microtubule inhibition

The structures of the studied compounds and their inhibition on the microtubule assembly are given in Scheme 1. Compounds **1-8**, **15** and **1t-3t** have natural origin [39, 42], while compounds **9-14** are synthetic congeners of podophyllotoxin.

The inhibitory activity is measured as ID₅₀ and it ranges from 0.2 μ M to 30 μ M.

1SA1:B PDBID CHAIN SEQUENCE	mreivhiqagqcgngigakfwevisdehgidptgsyhgdsdlqlerinvyvneaagnkyv	60
SP P09203 TBB1_CHICK	mreivhiqagqcgngigakfwevisdehgidptgsyhgdsdlqlerinvyvneaagnkyv	60
SP P32882 TBB2_CHICK	mreivhiqagqcgngigakfwevisdehgidptgsyhgdsdlqlerinvyvneaagnkyv	60
SP P09206 TBB3_CHICK	mreivhiqagqcgngigakfwevisdehgidptgsyhgdsdlqlerinvyvneaagnkyv	60
SP P09652 TBB4_CHICK	mreivhiqagqcgngigakfwevisdehgidpsgnyvgdsdlqlerinvyvneaagnkyv	60
SP P09653 TBB5_CHICK	mreivhiqagqcgngigtkfwevisdehgidpaggyvgdsalqlerinvyvneaagnkyv	60
SP P09207 TBB6_CHICK	mreivhiqagqcgngigakfwevisdehgidpagnycnaslqlerinvyvneaagnkyv	60
SP P09244 TBB7_CHICK	mreivhiqagqcgngigakfwevisdehgidptgtyhgdsdlqlerinvyvneaagnkyv	60
1SA1:B PDBID CHAIN SEQUENCE	prailvdlepgtmdevsvrsgpfgqifrdpndfvfgqsgagnnwakghytegaelvdsldvv	120
SP P09203 TBB1_CHICK	prailvdlepgtmdevsvrsgpfgqifrdpndfvfgqsgagnnwakghytegaelvdsldvv	120
SP P32882 TBB2_CHICK	prailvdlepgtmdevsvrsgpfgqifrdpndfvfgqsgagnnwakghytegaelvdsldvv	120
SP P09206 TBB3_CHICK	prailvdlepgtmdevsvrsgpfgqifrdpndfvfgqsgagnnwakghytegaelvdsldvv	120
SP P09652 TBB4_CHICK	prailvdlepgtmdevsvrsgafghlfrpdnfvfgqsgagnnwakghytegaelvdsldvv	120
SP P09653 TBB5_CHICK	prailvdlepgtmdevsvrsgpfgqifrdpndfvfgqsgagnnwakghytegaelvdsldvv	120
SP P09207 TBB6_CHICK	prailvdlepgtmdevsvrsgkigplfrpdnfvfgqsgagnnwakghytegaelvdsldvv	120
SP P09244 TBB7_CHICK	prailvdlepgtmdevsvrsgpfgqifrdpndfvfgqsgagnnwakghytegaelvdsldvv	120
1SA1:B PDBID CHAIN SEQUENCE	rkesescdclqgflthslgggtgsgmgtlliskireeyprdimntfsvmpspkvsdtvv	180
SP P09203 TBB1_CHICK	rkesescdclqgflthslgggtgsgmgtlliskireeyprdimntfsvmpspkvsdtvv	180
SP P32882 TBB2_CHICK	rkesescdclqgflthslgggtgsgmgtlliskireeyprdimntfsvmpspkvsdtvv	180
SP P09206 TBB3_CHICK	rkesescdclqgflthslgggtgsgmgtlliskireeyprdimntfsvmpspkvsdtvv	180
SP P09652 TBB4_CHICK	rkesescdclqgflthslgggtgsgmgtlliskireeyprdimntfsvmpspkvsdtvv	180
SP P09653 TBB5_CHICK	rkesescdclqgflthslgggtgsgmgtlliskireeyprdimntfsvmpspkvsdtvv	180
SP P09207 TBB6_CHICK	rkesescdclqgflthslgggtgsgmgtlliskireeyprdimntfsvmpspkvsdtvv	180
SP P09244 TBB7_CHICK	rkesescdclqgflthslgggtgsgmgtlliskireeyprdimntfsvmpspkvsdtvv	180
1SA1:B PDBID CHAIN SEQUENCE	epynatlsvhqlventdEtYcidnealydicfrtlklttptygdlnhlvsatmsgvTTCL	240
SP P09203 TBB1_CHICK	epynatlsvhqlventdEtYcidnealydicfrtlklttptygdlnhlvsatmsgvTTCL	240
SP P32882 TBB2_CHICK	epynatlsvhqlventdEtYcidnealydicfrtlklttptygdlnhlvsatmsgvTTCL	240
SP P09206 TBB3_CHICK	epynatlsvhqlventdEtYcidnealydicfrtlklttptygdlnhlvsatmsgvTTCL	240
SP P09652 TBB4_CHICK	epynatlsvhqlventdEtYcidnealydicfrtlklatptygdlnhlvsatmsgvTTCL	240
SP P09653 TBB5_CHICK	epynatlsvhqlventdEtYcidnealydicfrtlklttptygdlnhlvsatmsgvTTCL	240
SP P09207 TBB6_CHICK	epynatlsvhqlventdEtYcidnealydicfrtlklttptygdlnhlvsatmsgvTTCL	240
SP P09244 TBB7_CHICK	epynatlsvhqlventdEtYcidnealydicfrtlklttptygdlnhlvsatmsgvTTCL	240
1SA1:B PDBID CHAIN SEQUENCE	RFpgQLNaDLRKLAVNMVpfrlhfFmpgfpaltsrsgqqyraltvpeltqqmfdaknm	300
SP P09203 TBB1_CHICK	RFpgQLNaDLRKLAVNMVpfrlhfFmpgfpaltsrsgqqyraltvpeltqqmfdaknm	300
SP P32882 TBB2_CHICK	RFpgQLNaDLRKLAVNMVpfrlhfFmpgfpaltsrsgqqyraltvpeltqqmfdaknm	300
SP P09206 TBB3_CHICK	RFpgQLNaDLRKLAVNMVpfrlhfFmpgfpaltsrsgqqyraltvpeltqqmfdaknm	300
SP P09652 TBB4_CHICK	RFpgQLNaDLRKLAVNMVpfrlhfFmpgfpaltsrsgqqyraltvpeltqqmfdaknm	300
SP P09653 TBB5_CHICK	RFpgQLNaDLRKLAVNMVpfrlhfFmpgfpaltsrsgqqyraltvpeltqqmfdaknm	300
SP P09207 TBB6_CHICK	RFpgQLNaDLRKLAVNMVpfrlhfFmpgfpaltsrsgqqyraltvpeltqqmfdaknm	300
SP P09244 TBB7_CHICK	RFpgQLNaDLRKLAVNMVpfrlhfFmpgfpaltsrsgqqyraltvpeltqqmfdaknm	300
1SA1:B PDBID CHAIN SEQUENCE	aacdprhgryLTVaVFRgrmsmkevdeqMlnvqknssyfvevIpNNVKTaVCDipprg	360
SP P09203 TBB1_CHICK	aacdprhgryLTVaVFRgrmsmkevdeqMlnvqknssyfvevIpNNVKTaVCDipprg	360
SP P32882 TBB2_CHICK	aacdprhgryLTVaVFRgrmsmkevdeqMlnvqknssyfvevIpNNVKTaVCDipprg	360
SP P09206 TBB3_CHICK	aacdprhgryLTVaVFRgrmsmkevdeqMlnvqknssyfvevIpNNVKTaVCDipprg	360
SP P09652 TBB4_CHICK	aacdprhgryLTVaVFRgrmsmkevdeqMlnvqknssyfvevIpNNVKTaVCDipprg	360
SP P09653 TBB5_CHICK	aacdprhgryLTVaVFRgrmsmkevdeqMlnvqknssyfvevIpNNVKTaVCDipprg	360
SP P09207 TBB6_CHICK	aacdprhgryLTVaVFRgrmsmkevdeqMlnvqknssyfvevIpNNVKTaVCDipprg	360
SP P09244 TBB7_CHICK	aacdprhgryLTVaVFRgrmsmkevdeqMlnvqknssyfvevIpNNVKTaVCDipprg	360
1SA1:B PDBID CHAIN SEQUENCE	lkmsaTfIgNstaiqelfkrireqftamfrrkafhlhwtgegmdemefteaesnmndlvs	420
SP P09203 TBB1_CHICK	lkmsaTfIgNstaiqelfkrireqftamfrrkafhlhwtgegmdemefteaesnmndlvs	420
SP P32882 TBB2_CHICK	lkmsaTfIgNstaiqelfkrireqftamfrrkafhlhwtgegmdemefteaesnmndlvs	420
SP P09206 TBB3_CHICK	lkmsaTfIgNstaiqelfkrireqftamfrrkafhlhwtgegmdemefteaesnmndlvs	420
SP P09652 TBB4_CHICK	lkmsaTfIgNstaiqelfkrireqftamfrrkafhlhwtgegmdemefteaesnmndlvs	420
SP P09653 TBB5_CHICK	lkmsaTfIgNstaiqelfkrireqftamfrrkafhlhwtgegmdemefteaesnmndlvs	420
SP P09207 TBB6_CHICK	lkmsaTfIgNstaiqelfkrireqftamfrrkafhlhwtgegmdemefteaesnmndlvs	420
SP P09244 TBB7_CHICK	lkmsaTfIgNstaiqelfkrireqftamfrrkafhlhwtgegmdemefteaesnmndlvs	420
1SA1:B PDBID CHAIN SEQUENCE	eyqqyqdatadeqqefeegeedeadea---- 445	
SP P09203 TBB1_CHICK	eyqqyqdatadeqqefeegeedeadea---- 445	
SP P32882 TBB2_CHICK	eyqqyqdatadeqqefeegeedeadea---- 445	
SP P09206 TBB3_CHICK	eyqqyqdatadeqqefeegeedeadea---- 445	
SP P09652 TBB4_CHICK	eyqqyqdatadeqqefeegeedeadea---- 445	
SP P09653 TBB5_CHICK	eyqqyqdatadeqqefeegeedeadea---- 445	
SP P09207 TBB6_CHICK	eyqqyqdatadeqqefeegeedeadea---- 445	
SP P09244 TBB7_CHICK	eyqqyqdatadeqqefeegeedeadea---- 445	

Figure 2. Sequence alignment of the X-ray structure of cattle brain tubulin and the seven isotopes of chicken β -tubulin. The residues of the colchicine-binding site are given by capital letters.



No	Compound	R ₁	R ₂	R ₃	R ₄	R ₅	R ₆	ID ₅₀ (μ M)
1	Podophyllotoxin	OCH ₃	OH	H	H	O	C=O	0.6
2	Epipodophyllotoxin	OCH ₃	H	OH	H	O	C=O	5
3	Deoxypodophyllotoxin	OCH ₃	H	H	H	O	C=O	0.5
4	β -Peltatin	OCH ₃	H	H	OH	O	C=O	0.7
5	4'-Demethylpodophyllotoxin	OH	OH	H	H	O	C=O	0.5
6	4'-Demethylepipodophyllotoxin	OH	H	OH	H	O	C=O	2
7	4'-Demethyldeoxypodophyllotoxin	OH	H	H	H	O	C=O	0.2
8	α -Peltatin	OH	H	H	OH	O	C=O	0.5
9	Podophyllotoxin-cyclic ether	OCH ₃	OH	H	H	O	CH ₂	1
10	Deoxypodophyllotoxin-cyclic ether	OCH ₃	H	H	H	O	CH ₂	0.8
11	Deoxypodophyllotoxin-cyclopentane	OCH ₃	H	H	H	H ₂	CH ₂	5
12	Deoxypodophyllotoxin-cyclopentanone	OCH ₃	H	H	H	C=O	CH ₂	5
13	Podophyllotoxin-cyclic sulfide	OCH ₃	OH	H	H	S	CH ₂	10
14	Deoxypodophyllotoxin-cyclic sulfide	OCH ₃	H	H	H	S	CH ₂	10
15	Picropodophyllotoxin							30
1t	4'-Demethyl-6-methoxypodophyllotoxin	OH	OH	H	OCH ₃	O	C=O	
2t	5'-Demethyl-6-methoxypodophyllotoxin							
3t	6-Methoxypodophyllotoxin	OCH ₃	OH	H	OCH ₃	O	C=O	

Scheme 1. Structures and inhibition of microtubule assembly of podophyllotoxin and its derivatives. Compounds **1** – **15** compose the training set; compounds **1t** – **3t** are newly isolated compounds [42], not tested.

The effects of different concentrations of podophyllotoxin and its derivatives on microtubule assembly were determined spectrophotometrically at 350 nm on a Gilford spectrophotometer equipped with an automatic recorder and Haake RK2 thermostatically regulated liquid circulator to maintain constant temperature [39]. The changes in turbidity occurred when unassembled tubulin in the presence of GTP in MES buffer at 37° *in vitro*

polymerizes to form microtubules. The absorption of each drug at 350 nm was initially measured. There are no changes in turbidity when inhibition of microtubule assembly occurs.

Docking Protocol

The docking simulations in the present study were performed by GOLD v.5.2.2 software [43]. The protocol was optimized in terms of scoring

function, radius of the binding site and flexible residue side chains within the binding site in order to correlate best with pID_{50} ($-\log ID_{50}$). Four scoring functions, available in GOLD (ChemPLP, GoldScore, ChemScore and ASP), were compared at the following settings: flexible ligands, fixed protein and radius of the binding site 6Å. Four radiuses of the binding site were tested: 5Å, 6Å, 7Å and 8Å at fixed protein and flexible ligands. Up to 10 flexible residues in the binding site were selected stepwise in order to improve the correlation score/ pID_{50} . Each run included 10 poses. The poses were ranked by two criteria: 1) rmsd (root mean square deviation) lower than 1.5Å and 2) highest fitness score. Only the highest-scored pose with $rmsd < 1.5Å$ was considered. Each docking run was repeated three times and the average fitness score was used for correlation with the pID_{50} . The correlation was evaluated by the Pearson's correlation coefficient r and evaluated by leave-group-out cross-validation coefficient q^2 .

RESULTS AND DISCUSSION

Optimization of the Docking Protocol

The molecular docking procedure was optimized stepwise in terms of scoring function, radius and side-chain flexibility of the binding site.

Selection of scoring functions. GOLD v.5.2.2 [43] provides four scoring functions (SFs): ChemPLP, ChemScore, GoldScore and ASP. They were applied on the training set at the following settings: rigid protein, flexible ligand and radius of the binding site 6Å (Table 1). GoldScore had the highest correlation coefficient r with the pID_{50} (0.467) and it was selected as a SF used further in the study.

Radius of the binding site. The radius of the binding site was changed from 5Å to 8Å. The docking simulations were run with GoldScore, fixed protein and flexible ligands. The best correlation between docking score and inhibition of microtubule assembly was at 7Å ($r = 0.509$).

Table 1. Optimization of the docking protocol. Selected settings are given in bold.

Steps	r	Settings
1. Selection of SF		Rigid protein, flexible ligand, radius of the binding site 6Å
ChemScore	0.224	
ChemPLP	-0.114	
GoldScore	0.467	
APS	0.210	
2. Radius of the binding site		Gold Score, rigid protein, flexible ligand
5Å	0.392	
6Å	0.476	
7Å	0.509	
8Å	0.470	
3. Flexibility of the binding site		Gold Score, flexible ligand, radius of the binding site 7Å
200Tyr	0.532	
236Val	0.576	
240Leu	0.597	
241Arg	0.555	
247Asn	0.599	
250Leu	0.602	
255Val	0.514	
313Val	0.521	
317Phe	0.512	
347Asn	0.570	
349Val	0.583	
247Asn and 200Tyr	0.643	
247Asn and 256Asn	0.643	
250Leu and 237Thr	0.655	

Flexibility of the binding site. Each residue within the radius of 7 Å was set flexible and the effect was rendered by the GoldScore/pIC₅₀ correlation coefficient. The residues 240Leu, 247Asn and 250Leu showed the highest correlations. A second flexible residue was added to each of them and all combinations were screened. The best combinations are given in Table 1. The addition of a third flexible residue does not increase the correlation.

The optimized docking protocol includes the following settings: GoldScore, flexible ligand, radius of the binding site 7 Å and two flexible residues (250Leu and 237Thr).

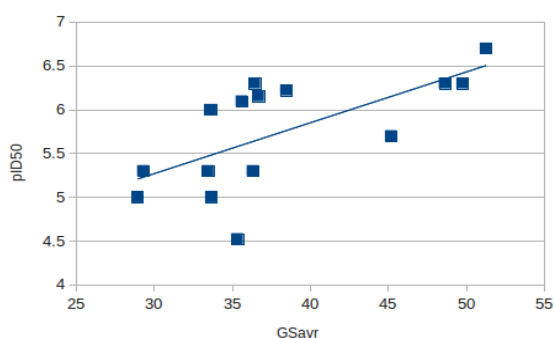


Figure 3. Linear relationship between pID₅₀ and GoldScore.

Linear Relationship between GoldScore and pID₅₀.

Between pID₅₀ and the GoldScore values derived by the optimized docking protocol exists a moderate linear relationship (Fig. 3) given by the following equation:

$$pID_{50} = 0.0581 * GoldScore + 3.5297$$

$$n = 15, r = 0.655$$

The relationship was validated by leave-group-out cross-validation and the derived q^2 was 0.371. The differences between the experimental and predicted pID₅₀ values were below 1 log unit, with the exception of picropodophyllotoxin (Table 2).

The microtubule inhibition of the three newly isolated compounds (**1t** – **3t**) was predicted by the derived relationship (Table 3). The activities of 5'-demethyl-6-methoxypodophyllotoxin (**2t**) and 6-podophyllotoxin (**3t**) are expected to be moderate with ID₅₀ values of 3.79 and 4.47, respectively. However, the inhibitory activity of 4'-demethyl-6-methoxypodophyllotoxin (**1t**) is very high with predicted ID₅₀ value of 0.36 μM placing the compound among the most active microtubule inhibitors. This prediction is in a good agreement with the high cytotoxicity of **1t** which is 2 to 3.5 times higher than that of etoposide in different human leukemic cell lines [44]. The present study suggests that the probable mechanism of action of 4'-demethyl-6-methoxypodophyllotoxin is inhibition of microtubule assembly.

Table 2. Experimental and predicted by cross-validation pID₅₀ values.

No	Compound	pID ₅₀ exp.	pID ₅₀ pred.	pID ₅₀ exp - pID ₅₀ pred.
1	Podophyllotoxin	6.22	5.83	0.39
2	Epipodophyllotoxin	5.30	5.63	-0.33
3	Deoxypodophyllotoxin	6.30	5.64	0.66
4	β-Peltatin	6.15	5.60	0.55
5	4'-Demethylpodophyllotoxin	6.30	6.46	-0.16
6	4'-Demethylepipodophyllotoxin	5.70	6.18	-0.48
7	4'-Demethyldeoxypodophyllotoxin	6.70	6.40	0.29
8	α-Peltatin	6.30	6.37	-0.07
9	Podophyllotoxin-cyclic ether	6.00	5.48	0.52
10	Deoxypodophyllotoxin-cyclic ether	6.10	5.59	0.51
11	Deoxypodophyllotoxin-cyclopentane	5.30	5.57	-0.27
12	Deoxypodophyllotoxin-cyclopentanone	5.30	5.19	0.11
13	Podophyllotoxin-cyclic sulfide	5.00	5.17	-0.17
14	Deoxypodophyllotoxin-cyclic sulfide	5.00	5.48	-0.48
15	Picropodophyllotoxin	4.52	5.67	-1.15

Table 3. Predicted ID₅₀ values for the newly isolated podophyllotoxin derivatives.

No	Compound	ID _{50pred} (μM)
1t	4'-Demethyl-6-methoxypodophyllotoxin	0.36
2t	5'-Demethyl-6-methoxypodophyllotoxin	3.79
3t	6-Methoxypodophyllotoxin	4.47

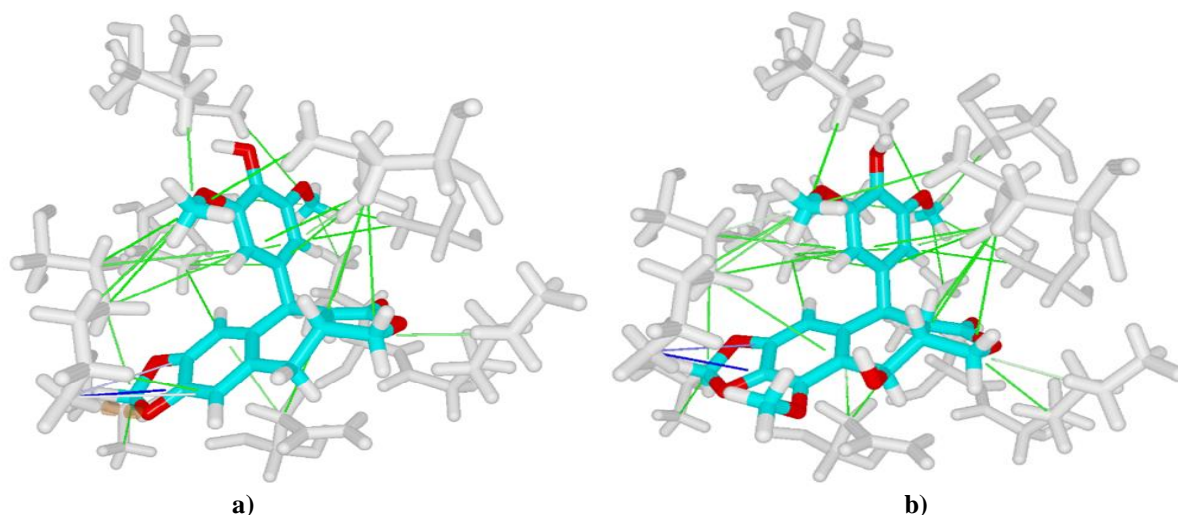


Figure 4. Interactions between **a)** the most active compound **7** and tubulin, and **b)** the test compound **1t** and tubulin. Cation – π interaction is shown in blue, hydrophobic interactions – in green, and hydrogen bond – in dashed orange.

Interactions between Inhibitors and Tubulin

The interactions between the inhibitor **7** and tubulin within the colchicine binding site are given in Fig. 4a. Cation- π interaction exists between 350Lys and ring A from the ligand. A hydrogen bond is detected between 350Lys and O-atom in ring A. Many hydrophobic interactions occur between 4'-demethyldeoxypodophyllotoxin (compound **7**) and the residues from the binding site. Very similar are the interactions between the newly isolated derivative **1t** and tubulin (Fig. 4b).

CONCLUSION

In the present study the interaction of podophyllotoxin derivatives and colchicine binding site in chicken β II-tubulin isotypes IIa and IIb was modelled by molecular docking. The docking protocol was optimized in terms of scoring function, binding site radius and flexible residues within the binding site in order to correlate with the inhibitory activity of the compounds. The linear relationship between pID₅₀ and GoldScore was validated by cross-validation in 5 groups. It was used to predict the inhibition of three newly isolated derivatives of podophyllotoxin. One of them, 4'-demethyl-6-methoxy-podophyllotoxin, was predicted to be among the most active inhibitors of tubulin. Tubulin inhibition is a

probable mechanism of the observed cytotoxicity of this compound.

REFERENCES

1. S. Inoue, *J. Cell Biol.*, **91**, 131 (1981).
2. J. D. Pickett-Heaps, D. H. Tippit, K. R. Porter, *Cell*, **29**, 729 (1982).
4. J. E. Heuser, M. W. Kirschner, *J. Cell Biol.*, **86** (1), 212 (1980).
5. I. R. Gibbons, in: *Molecules and cell movement*, S. Inoue, R. E. Stephens (eds.), Raven Press, New York, 1975, p. 207.
6. J. H. Hayden, R. D. Allen, *J. Cell Biol.*, **99**, 1785 (1984).
7. R. D. Vale, B. J. Schnapp, T. S. Reese, M. Sheetz, *Cell*, **40**, 449 (1985).
8. L. C. Morejohn, D. E. Fosket, *Pharmacol. Ther.*, **51**, 217 (1991).
9. P. Kohler, *Int. J. Parasitol.*, **31**, 336 (2001).
10. A. Jordan, J. A. Hadfield, N. J. Lawrence, A. T. McGown, *Med. Res. Rev.*, **18**, 259 (1998).
11. R. F. Luduena, E. M. Shooter, L. Wilson, *J. Biol. Chem.*, **252**, 7006 (1977).
12. E. Nogales, *Annu. Rev. Biophys. Biomol. Struct.*, **30**, 397 (2001).
13. R. F. Ludueña, in: *International Review of Cytology - a Survey of Cell Biology*, K. W. Jeon, (ed.), vol. 178, Academic Press, San Diego, 1998, p. 207.
14. P. Verdier-Pinard, E. Pasquier, H. Xiao, B. Burd, C. Villard, D. Lafitte, L. M. Miller, R. H. Angeletti, S. B. Horwitz, D. Braguer, *Anal. Biochem.*, **384**, 197 (2009).

15. S. Sharma, B. Poliks, C. Chiauzzi, R. Ravindra, A. R. Blanden, S. Bane, *Biochem.*, **49** (13), 2932 (2010).
16. J. Huzil, R. F. Ludueña, J. Tuszynski, *Nanotechnology*, **17**, S90 (2006).
17. M. A. Jordan, L. Wilson, *Curr. Opin. Cell. Biol.*, **10**, 123 (1998).
18. T. Mitchison, M. Kirschner, *Nature*, **312**, 237 (1984).
19. M. Jordan, L. Wilson, *Nat. Rev. Canc.*, **4**, 253 (2004).
20. R. B. G. Ravelli, B. Gigant, P. A. Curmi, I. Jourdain, S. Lachkar, A. Sobel, M. Knossow, *Nature*, **428**, 198 (2004).
21. J. Huzil, P. Winter, L. Johnson, A. Weis, T. Bakos, A. Banerjee, R. F. Ludueña, S. Damaraju, J. Tuszynski, *Chem. Biol. Drug Des.*, **75**, 541 (2010).
22. J. T. Huzil, K. Chen, L. Kurgan, J. A. Tuszynski, *Cancer Inform.*, **3**, 159 (2007).
23. C. A. Burkhardt, M. Kavallaris, B. S. Horwitz, *Biochim. Biophys. Acta*, **1471**, O1 (2001).
24. I. Ionkova, *Pharmacog. Rev.*, **1** (1), 57 (2007).
25. A. L. Parker, M. Kavallaris, J. A. McCarroll, *Front. Oncol.*, **4**, 153 (2014).
26. A. Dorleans, B. Gigant, R. B. G. Ravelli, P. Mailliet, V. Mikol, M. Knossow, *Proc. Natl. Acad. Sci.*, **106** (33), 13775 (2009).
27. R. A. Stanton, K. M. Gernet, J. H. Nettles, R. Aneja, *Med. Res. Rev.*, **31** (3), 443 (2011).
28. C. Wang, A. Cormier, B. Gigant, M. Knossow, *Biochem.*, **46**, 10595 (2007).
29. J. L. Hartwell, A. W. Shrecker, *Fortschr. Chem. Org. Naturstoffe*, **15**, 106 (1958).
30. M. G. Kelly, J. L. Hartwell, *J. Nat. Cancer Inst.*, **14**, 967 (1954).
31. H. Savel, *Proc. Am. Assoc. Cancer Res.*, **5**, 56 (1964).
32. H. Savel, *Progr. Exptl. Tumor Res.*, **8**, 189 (1966).
33. A. Koulman, W. J. Quax, N. Pras, in: *Biotechnology of medicinal plants: vitalizer and therapeutic*, K. G. Ramawat (ed.), Science Publishers Inc., Enfield (USA), Plymouth (UK), 2004, p. 225.
34. K. R. Hande, *Eur. J. Cancer*, **34**, 1514 (1998).
35. W. Ross, T. Rowe, B. Glisson, J. Yalowich, L. Liu, *Cancer Res.*, **44**, 5857 (1984).
36. A. J. Wozniak, W. E. Ross, *Cancer Res.*, **43**, 120 (1983).
37. H. L. McLeod, W. E. Evans, in: *Cancer Medicine 4th Edition*, J. F. Holland, R. C. Bast, D. L. Morton, E. III Frei, D. W. Kufe, R. R. Weichselbaum, (eds.), Williams & Wilkins: Baltimore, 1997, p. 259.
38. H. J. Wichers, G. G. Versluis-De Haan, J. W. Marsman, M. P. Harkes, *Phytochemistry*, **11**, 3601 (1991).
39. H. Saito, Y. Nishimura, S. Kondo, T. Takeuchi, H. Umezawa, *Bull. Chem. Soc. Jpn.*, **61**, 1259 (1988).
40. J. D. Loike, C. F. Brewer, H. Sternlicht, W. J. Gensler, S. B. Horwitz, *Cancer Res.*, **38**, 2688 (1978).
41. J. C. Havercroft, D. W. Cleveland, *J. Cell Biol.*, **99**, 1927 (1984).
42. R. F. Ludueña, *Mol. Biol. of the Cell*, **4**, 445 (1993).
43. P. Sasheva, I. Ionkova, N. Stoilova, *Nat. Prod. Commun.*, **10** (7), 1225 (2015).
44. G. Jones, P. Willett, R. C. Glen, A. R. Leach, R. Taylor, *J. Mol. Biol.*, **267**, 727 (1997).
45. N. Vasilev, G. Momekov, M. Zaharieva, S. Konstantinov, P. Bremner, M. Heinrich, I. Ionkova, *Neoplasma*, **52** (5), 425 (2005).

Adsorption of polyacrylamide on activated carbon

D. Chamovska^{1,2*}, A. Porjazoska Kujundziski³

¹Ss. Cyril and Methodius University, Faculty of Technology and Metallurgy, "Rugjer Boshkovic" 16, Skopje, R. North Macedonia

²Research Center for Environment and Materials, Macedonian Academy of Sciences and Arts, Skopje, R. North Macedonia

³International Balkan University, Faculty of Engineering, "Makedonsko-Kosovska brigada" bb, Skopje, R. North Macedonia

Received October 29, 2018; Revised April 23, 2019

The authors (D.Chamoska and A.Porjazoska Kujundziski) dedicate this paper to Prof. Dr. Toma Grchev.

The adsorption behavior of polyacrylamide (PAA) with different molecular weights ($\overline{M}_n = 5\ 000 - 1\ 350\ 000\ \text{g mol}^{-1}$) on activated carbon (AC) (0.05 – 2.0 g), from aqueous solutions of 0.5 mol dm⁻³ H₂SO₄, was studied. An effort was made to find a dependence of the quantity of adsorbed PAA, m_a^m (mol g⁻¹ or mg g⁻¹), on the polymer equilibrium concentration in the solution, as well as on the molecular weight of the polymer. The viscosimetric study of PAA adsorption on activated carbon from 0.5 mol dm⁻³ H₂SO₄ at room temperature shows a typical Langmuir behavior following the relation: $m_a^m = 70.6 \cdot \overline{M}_n^{-1.38}$ (mol g⁻¹), where m_a^m is the monomolecular capacity.

Keywords: Adsorption, polyacrylamide, activated carbon, Langmuir isotherm, viscosimetry.

INTRODUCTION

Adsorption of polymers onto solid surfaces has attracted big attention, regarding its practical importance in many areas of application, such as: processes of corrosion inhibition [1-3], mechanical and thermal processing of metals and alloys, surface finish in metal processing, improvement of energy efficiency in fluids transportation, stabilization of colloidal suspensions, preparation of paints, coatings, printing inks, but also in biology, medicine and pharmacology [2, 4].

The features of the polymer/substrate boundary mainly depend on the properties of solid surfaces, type of the solvents used, but in the large extent, on the polymer characteristics, especially the possible changes of the polymer chains conformation in a process of adsorption [5].

Some of the studies of the adsorption behavior of polyacrylamide (PAA) on gold and mild steel from sulfuric and hydrochloric acid, applying cyclic voltammetry, indicated a strong dependence of the adsorption process on polymer molecular weight, electrode potential, as well as temperature [6].

Frumkin's isotherm has been shown to be the best fit to the experimentally obtained values. It has been noticed that, at very low polymer concentration in the solution, polymer adsorption occurs as a result of direct attachment of polymer segments to a metal surface, leading to an almost complete coverage, creating an average thickness of

the adsorbed layer of around 0.8 nm, and a flat orientation of polymer molecules [6].

As far as the electrode potential is concerned, an endothermic process of adsorption of PAA on gold substrate occurs at high anodic potentials, including a simultaneous process of desorption of water molecules and adsorption of PAA macromolecules [6].

Analysis of the effect of temperature on the adsorption mechanism of PAA on silica proposed a decrease of the polymer adsorption on the solid surface, as far as the temperature of the system rises from 15° to 35 °C. Namely, increased temperature leads to conformational changes of the polymer coils into linear forms, disrupting their attachment to solid substrates [7].

Adsorption of polymers has been studied using pure metallic [8, 9] or metal oxide substrates [10, 11]. However, adsorbents based on activated carbon, which is an inert solid material with high porosity and large surface area, attract big attention.

Adsorption of pollutants includes surface interactions between contaminants and activated carbon surfaces *via* van der Waals forces and induced dipole interactions.

Adsorption capacity of activated carbon depends on the size of the inner surface, as well as on the shape and distribution of pore size [12, 13]. Compared to larger carbon particles, μm-sized activated carbon particles enable faster reaction and a greater capacity of contaminant removal. In

* To whom all correspondence should be sent:
E-mail: dragica@tmf.ukim.edu.mk;
dragica.camovska@gmail.com

addition to this, modification of surface chemistry has been considered as a convenient technique for improvement of the adsorption capacity of activated carbon [13-16]. Characteristics such as: type, quantity, and concentration of oxygen-containing functional groups, have been considered as crucial in determination of surface features of activated carbon [15].

The aim of this study is to find a correlation between molecular characteristics of polyacrylamide and its adsorption behavior on solid adsorbents, mainly, activated carbon substrate. The adsorption parameters for the best fit of the experimentally obtained data were determined.

EXPERIMENTAL

The adsorption process of polyacrylamide (PAA), with different molecular weights, ($\overline{M}_n = 5\,000 - 1\,350\,000 \text{ g mol}^{-1}$), onto activated carbon (AC) (Merck, p.a. art. 2186) used as adsorbent, from 0.5 mol dm^{-3} solutions of H_2SO_4 , at a temperature of 293 K, was studied using viscosimetry. Different quantities of activated carbon, from 0.05 to 2 g, were added to 100 cm^3 of 0.5 mol dm^{-3} aqueous solution of H_2SO_4 , with constant concentration of polymer, 50 - 150 mg (100 cm^3)⁻¹ with a given molecular weight.

After intensive stirring for at least 6 h, when equilibrium was attained, the suspension was filtered and the equilibrium concentration of PAA in solution was determined viscosimetrically.

The specific surface area of activated carbon was determined by the adsorption of methylene blue from aqueous solution, whose equilibrium concentration was found spectrophotometrically ($\lambda=570 \text{ nm}$).

RESULTS AND DISCUSSION

The previous studies of the adsorption of polyacrylamide (PAA) on gold surfaces, by simultaneous monitoring of the double-layer capacity using cyclic voltammetry, showed that the coverage (θ) of the metal surface with polymer molecules depends on the molar concentration of PAA, as well as on its molecular weight, and the size of the statistical polymer coil in the solution ($R_G = 7.49 \cdot 10^{-3} \cdot \overline{M}_n^{0.64}$) [17]. The results related to the adsorption of PAA on activated carbon, presented in this study, would indicate dependences of the quantity of adsorbed polymer on its equilibrium concentration in the solution and its molecular weight.

The specific area of activated carbon was determined by adsorption of a relatively big organic molecule, such as methylene blue (MB), with a known value of molecule area σ [18, 19] that can only enter in mesopores and larger micropores of the substrate [19, 20]. It is known that the dimensions of methylene blue molecule are $1.43 \text{ nm} \times 0.61 \text{ nm} \times 0.4 \text{ nm}$ [21], thus, each adsorbed molecule of methylene blue takes 0.9 nm^2 of the adsorbent surface.

Equilibrium concentration of methylene blue on activated carbon from aqueous suspensions of AC (20 to 200 mg in 100 cm^3 solution), containing $10^{-3} \text{ mol dm}^{-3}$ of methylene blue, has been determined by spectrophotometry at $\lambda=570 \text{ nm}$. These results are presented in Table 1 and Fig. 1.

Table 1. Experimental data of methylene blue adsorption (319.5 g mol^{-1}) on activated carbon from aqueous solutions at 293 K.

C_{AJ} mg (100 cm^3) ⁻¹	$C \cdot 10^4$ mol dm^{-3}	$m_a^* \cdot 10^5$ mol	$m_a \cdot 10^4$ mol g^{-1}
0	10.0	0	0
20	7.78	2.215	11.07
40	6.34	3.66	9.149
60	4.43	5.57	9.28
80	3.69	7.314	9.143
100	1.47	8.53	8.53
120	0.86	9.14	7.62
160	0.255	9.79	6.094
200	0.202	9.80	4.90

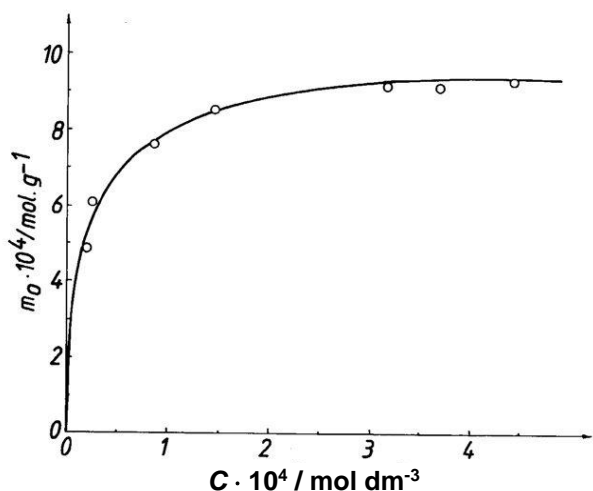


Figure 1. Dependence of the quantity of adsorbed methylene blue on activated carbon on the equilibrium concentration of methylene blue in the solution.

Experimental data show a typical Langmuir behavior of the chemisorption of methylene blue on activated carbon and formation of a monolayer of adsorbed molecules. Monomolecular capacity, m_a^m (mol g⁻¹), as well as adsorption coefficient K_L , were determined using experimental data (Table 1) and Langmuir equation:

$$C/m_a = 1/K_L \cdot m_a^m + C/m_a^m \quad (1)$$

where, C is the equilibrium concentration of methylene blue after adsorption (mol dm⁻³), m_a is adsorbed quantity of methylene blue (mol g⁻¹), K_L is adsorption coefficient (dm³ mol⁻¹), and m_a^m (mol g⁻¹) is monomolecular capacity ($\theta = 1$).

Very good linear relationship was determined by regression analysis of the experimental data (C/m_a)/ C ($R \geq 0.99$), while calculated monomolecular capacity, m_a^m , and adsorption coefficient, K_L , took values of $1.06 \cdot 10^{-3}$ mol g⁻¹ and $2.54 \cdot 10^4$ mol⁻¹ ($\Delta G^\circ = 35.08$ kJ mol⁻¹), respectively. The specific area of activated carbon, 575 m² g⁻¹, was calculated using the equation:

$$A_{AC} = m_a^m \cdot N_A \cdot \sigma_{MB} \cdot 1 \cdot 10^{-18}, \text{ m}^2 \text{ g}^{-1} \quad (2)$$

According to the general pores' classification, micropores in activated carbon are characterized by diameters, d_p , of maximum 2 nm, diameters of mesopores are ranged between 2 and 50 nm, while sizes of macropores are bigger than 50 nm in diameter [22].

As far as the adsorption of PAA is concerned, the dimensions of polyacrylamide coil, given in Table 2, designate that undeformed polymer coil with number average molecular weight $\bar{M}_n = 200$

000 g mol⁻¹ enters into part of the mesopores, $d_p > 40$ nm, and coils with $\bar{M}_n = 600\,000$ and $1\,350\,000$ g mol⁻¹ penetrate just in the macropores of activated carbon. So, the determination of the area of adsorbed macromolecule, σ_{PAA} , requires awareness of the pore distribution in wide ranges, from $d_p = 1$ to $d_p = 200$ nm.

Adsorption of PAA on activated carbon from 0.5 mol dm⁻³ H₂SO₄ was studied viscosimetrically, at a temperature of 293 K. Adsorbent quantities from 0.05 to 2 g were added to 100 cm³ of an aqueous solution of 0.5 M H₂SO₄, and a constant concentration of polymer with a given molecular weight (Table 3).

After rigorous mixing for at least 6 h, the suspension was filtered, and the polymer concentration remaining in the solution was defined by viscosity measurements.

It is known that for a specified solvent at a constant temperature, the viscosity of dilute polymer solutions depends on the polymer concentration in the solution, and its molecular weight. The relationship between intrinsic viscosity and polymer molecular weight is presented by the Mark-Houwink equation, Eqn. 3 [23]:

$$[\eta] = k \bar{M}_n^\alpha \quad (3)$$

where for very dilute solutions:

$$[\eta] = 1/C [2(\eta_{sp} - \ln \eta_{rel})]^{1/2} \quad (4)$$

$$\eta_{sp} = \eta_{rel} - 1 = t/t_0 - 1 \quad (5)$$

Constants k and α depend on the nature of both, solvents and polymers, and also on the temperature.

Viscosimetry measurements of PAA solutions, in 0.5 mol dm⁻³ H₂SO₄, showed linear dependences of viscosity on polymer concentration, Eqns. 6-9 and Fig. 2.

$$\eta_{rel} = 1.902 \cdot 10^{-4} \cdot C + 1.00434 \quad (6)$$

(for $\bar{M}_n = 5\,000$ g mol⁻¹)

$$\eta_{rel} = 2.302 \cdot 10^{-3} \cdot C + 1.00136 \quad (7)$$

(for $\bar{M}_n = 200\,000$ g mol⁻¹)

$$\eta_{rel} = 4.544 \cdot 10^{-3} \cdot C + 0.9812 \quad (8)$$

(for $\bar{M}_n = 600\,000$ g mol⁻¹)

$$\eta_{rel} = 5.434 \cdot 10^{-3} \cdot C + 0.9893 \quad (9)$$

(for $\bar{M}_n = 1\,350\,000$ g mol⁻¹)

These relations clearly indicate that the specific viscosity for dilute polymer solutions in 0.5 mol dm⁻³ H₂SO₄ follows the equation:

$$\eta_{sp} = k \cdot C \quad (10)$$

where the regression analyses directed to the relationship between the constant, k , and polymer's

molecular weight:

$$k = 1.106 \cdot 10^{-6} \cdot \bar{M}_n^{0.623} \quad (11)$$

Table 2. Basic parameters for the size of the statistical polymer coil depending on the molecular weight of PAA.

\bar{M}_n g mol ⁻¹	R_G nm	σ nm ²	$C_s (\theta=1)$ mol m ⁻²	$C_s (\theta=1)$ mg m ⁻²
5 000	1.75	9.6	$1.74 \cdot 10^{-7}$	0.870
200 000	18.50	1075	$1.55 \cdot 10^{-9}$	0.300
600 000	37.40	4385.7	$3.78 \cdot 10^{-10}$	0.227
1 350 000	62.80	12 383	$1.34 \cdot 10^{-10}$	0.181

Table 3. Experimental data of PAA adsorption on activated carbon from aqueous solutions of 0.5 mol dm⁻³ H₂SO₄, obtained viscosimetrically.

\bar{M}_n^{PAA} g mol ⁻¹	C^{PAA} mol dm ⁻³	C_{AJ} mg(100 cm ³) ⁻¹	η_{rel} ($t = 6h$)	m_a^{PAA} mg (100 cm ³) ⁻¹	$C_e^{\text{PAA}} \cdot 10^6$ mol dm ⁻³	$m_a \cdot 10^6$ mol g ⁻¹
200 000	$7,5 \cdot 10^{-6}$ [150 mg(100 cm ³) ⁻¹]	0	1.3467	150	7.50	0.000
		40	1.289	125	6.25	3.125
		50	1.271	117	5.85	3.300
		80	1.222	96	4.80	3.375
		180	1.0796	34	1.685	3.222
		300	1.0543	23	1.145	2.120
		500	1.0416	17.5	0.875	1.325
600 000	$1,67 \cdot 10^{-6}$ [100 mg(100 cm ³) ⁻¹]	700	1.0382	16	0.820	0.957
		0	1.4353	100	1.670	0.000
		60	1.3195	74.5	1.244	0.708
		90	1.2537	60	1.002	0.741
		160	1.0990	26	0.434	0.771
		250	1.0312	11	0.184	0.593
1 350 000	$3,7 \cdot 10^{-7}$ [50 mg(100 cm ³) ⁻¹]	500	1.0085	~6	0.100	0.313
		0	1.2611	50	0.370	0.000
		30	1.2067	~40	0.296	0.247
		50	1.1741	34	0.252	0.237
		80	1.1252	25	0.185	0.185
		180	1.049	11	0.082	0.161
300	1.014	~4.5	0.033	0.112		
500	1.011	~4.0	0.0296	0.068		

Table 4. Thermodynamic parameters for adsorption of PAA on activated carbon from aqueous solutions of 0.5 mol dm⁻³ H₂SO₄, at 293 K.

\bar{M}_n^{PAA} g mol ⁻¹	m_a^m mol g ⁻¹ (mg g ⁻¹)	K_L dm ³ mol ⁻¹	$-\Delta G^0$ kJ mol ⁻¹
5 000	$3.854 \cdot 10^{-5}$ (~193)	$5.575 \cdot 10^4$	36.41
200 000	$3.48 \cdot 10^{-6}$ (696)	$2.45 \cdot 10^6$	45.62
600 000	$7.755 \cdot 10^{-7}$ (465)	$1.343 \cdot 10^7$	49.77
1 350 000	$2.523 \cdot 10^{-7}$ (340)	$3.668 \cdot 10^7$	52.21
Methylene blue (319.5)	$1.06 \cdot 10^{-3}$ (339)	$2.54 \cdot 10^4$	35.08

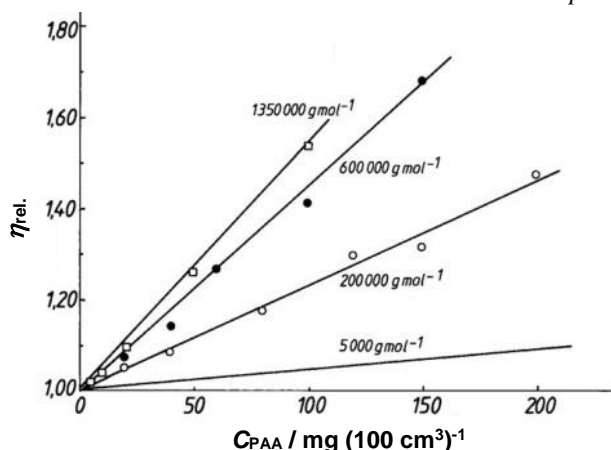


Figure 2. Dependences of relative viscosity on PAA concentration in aqueous solution of $0.5 \text{ mol dm}^{-3} \text{ H}_2\text{SO}_4$ at 293 K.

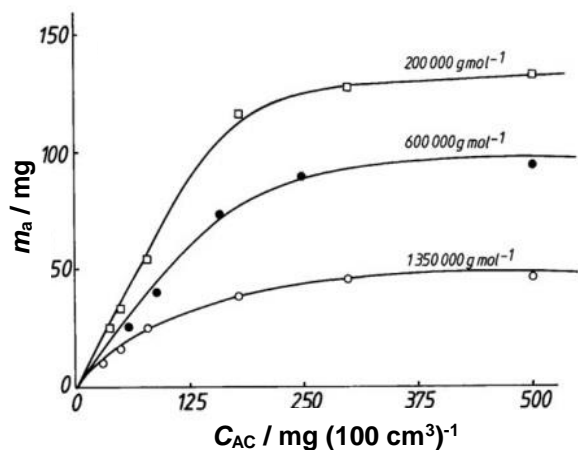


Figure 3. Dependences of adsorbed PAA quantity on AC concentration in 0.5 mol dm^{-3} aqueous solution of H_2SO_4 at 293 K.

Thus,

$$\eta_{sp} / C = 1.106 \cdot 10^{-6} \cdot \bar{M}_n^{0.623} \quad (12)$$

where C is the PAA concentration in the solution ($\text{mg} / 100 \text{ cm}^3$ solution).

Direct correlation of the hydrodynamic volume of the polymer coil ($4/3R_G^3\pi$) on polymer viscosity and molecular weight is given by Eqn. 13 [24]:

$$v = 100 [\eta] M / N_A = 4/3 R_G^3\pi \quad (13)$$

where, R_G is the radius of giration (cm), M is molecular weight of the polymer (g mol^{-1}), and $[\eta]$ is characteristic viscosity of polymer solution.

Dependences of adsorbed quantity of PAA on the concentration of activated carbon for different molecular weights are given in Figure 3.

Equilibrium concentration of PAA in the solution, i.e., adsorbed polymer quantity on activated carbon, was calculated using experimental data of the relative viscosity of the filtrate.

Experimentally obtained values, Table 3, were fitted to the Langmuir equation, and the values of the basic adsorption parameters are presented in Table 4.

Adsorption coefficient, K_L , as well as Gibbs energy of adsorption process, clearly depend on PAA molecular weight, as it was previously shown for PAA adsorption on gold substrates [17].

It is obvious that an increase in polymer molecular weight influences a decrease of the monomolecular capacity of the adsorbed polymer, which is in accordance with the results related to the adsorption of poly(methyl methacrylate) on carbon black or Al_2O_3 [24].

The relations of the monomolecular adsorption capacity, m_a^m , on the molecular weight are presented by Eqn. 14:

$$m_a^m = k \cdot \bar{M}_n^\alpha \quad (14)$$

So that:

$$m_a^m = 70.6 \cdot \bar{M}_n^{-1.38} \quad (\text{mol g}^{-1}) \quad (15)$$

or

$$m_a^m = 7.04 \cdot 10^4 \cdot \bar{M}_n^{-0.382} \quad (\text{mg g}^{-1}) \quad (16)$$

Similar relations were determined for the adsorption model of undistorted polymer coil on a solid surface (Table 2):

$$m_a^m = 9.47 \cdot 10^{-3} \cdot \bar{M}_n^{-1.28} \quad (\text{mol m}^{-2}) \quad (17)$$

or

$$m_a^m = 9.43 \cdot \bar{M}_n^{-0.28} \quad (\text{mg m}^{-2}) \quad (18)$$

Experimentally obtained data for monomolecular capacity, m_a^m (mg g^{-1} , Table 4), as well as those for C_s (mg m^{-2} , Table 2), indicate a significant deformation of the polymer coil during the process of adsorption on activated carbon.

CONCLUSIONS

The adsorption process of polyacrylamide (PAA) with different molecular weights ($\bar{M}_n = 5\,000 - 1\,350\,000 \text{ g mol}^{-1}$) on activated carbon, studied by viscosimetry, showed a typical Langmuir behavior. A clear dependence of the monomolecular capacity of PAA on the polymer molecular weight, $m_a^m = 70.6 \cdot \bar{M}_n^{-1.38} \text{ (mol g}^{-1}\text{)}$, was shown. The comparison of this equation with the relation $m_a^m = k \cdot \bar{M}_n^{-1.38}$, obtained for undistorted polymer coil, indicates a significant deformation of PAA at the time of the adsorption process on activated carbon.

REFERENCES

1. T. Shimura, K. Aramaki, *Corros. Sci.*, **49**, 1378 (2007).
2. M. R. Porter, *Recent Developments in the Technology of Surfactants*, Elsevier, New York, 1990.
3. T. Grchev, M. Cvetkovska, J. W. Schultze, *Corros. Sci.*, **32**, 103 (1991).
4. A. K. Chakraborty, M. Tirrell, *MRS Bulletin*, **21**, 28 (1996).
5. G.B. Kaggwa, S. Froebe, L. Huynh, J. Ralston, K. Bremmell, *Langmuir*, **21**, 4695 (2005).
6. T. Grchev, M. Cvetkovska, T. Stafilov, J. W. Schultze, *Electrochim. Acta*, **36**, 1315 (1991).
7. M. Wiśniewska, *Appl. Surface Sci.*, **258**, 3094 (2012).
8. K. David, N. Dan, R. Tannenbaum, *Surf. Sci.*, **601**, 1781 (2007).
9. L. S. Spinelli, A. S. Aquino, E. Lucas, A. R. d'Almeida, R. Leal, A. L. Martins, *Polym. Eng. Sci.*, **48**, (2008).
10. A. I. Chervanyov, G. Heinrich, *J. Chem. Phys.*, **131**, 104905 (2009).
11. E. Hershkovits, A. Tannenbaum, R. Tannenbaum, *J. Phys. Chem. C Nanomater. Interfaces.*, **111**, 12369 (2007).
12. S. K. W. Sing, *Carbon*, **27**, 5 (1989).
13. M.A. Rahman, M. Asadullah, M. M. Haque, M.A. Motin, M.B. Sultan, M.A.K. Azad, *J. Surface Sci. Technol.*, **22**, 133 (2006).
14. R.T. Yang, *Gas Separation by Adsorption Processes*, Elsevier Science, New York, Rev. edn., 2013.
15. V. A. Garten, D. E. Weiss, *Aust. J. Chem.*, **10**, 309 (1957).
16. Y. Kawabuchi, S. K. Kawano, I. Mochida, *Carbon*, **34**, 711 (1996).
17. D.B. Chamovska, T. P. Grchev, M. V. Cvetkovska, *Turk. J. Chem.* **30**, 653 (2006).
18. M. N. Alaya, M. A. Hourieh, A. M. Youssef, F. El-Sejarah, *Adsorpt. Sci. Technol.*, **18**, 27 (2000).
19. C. A. Nunes, M. C. Guerreiro, *Quím. Nova*, **34**, 472 (2011).
20. A. Baçaoui, A. Yaacoubi, A. Dahbi, C. Bennouna, R. P. T. Luu, F. J. Maldonado-Hodar, J. Rivera-Utrilla, C. Moreno-Castilla, *Carbon*, **39**, 425 (2001).
21. P.F.R. Ortega, J.P.C. Trigueiro, M.R. Santos, Â M.L. Denadai, L.C.A. Oliveira, A.P.C. Teixeira, G.G. Silva, R.L. Lavall, *J. Chem. Eng. Data*, **62**, 729 (2017).
22. H. Shi, *Electrochim. Acta*, **41**, 1633 (1996).
23. P C.Hiemenz, L.P. Timothy. *Polymer Chemistry*. Second edn., Boca Raton, CRC P, (2007) 336, 338.
24. Y. S. Lipatov, L. M. Sergeeva, *Adsorption of Polymers*, John Wiley & Sons, New York, 1974.

Investigating the influence of *p*-substituents upon spectral, thermal, kinetic, molecular modeling and molecular docking characteristics of new synthesized arylazobithiazolyhydrazones

N.M. El-Metwaly^{1,2*}, S. Bondock^{2,3}, I.I. Althagafi¹, A.M. Khedr^{1,4*}, A.A. El-Zahhar^{3,5}, F. A. Saad¹

¹ Department of Chemistry, Faculty of Applied Science, Umm Al-Qura University, Makkah, Saudi Arabia

² Chemistry Department, Faculty of Science, Mansoura University, Mansoura, Egypt

³ Chemistry Department, Faculty of Science, King Khalid University, Abha, Saudi Arabia

⁴ Chemistry Department, Faculty of Science, Tanta University, Tanta, Egypt

⁵ Nuclear Chemistry Department, Atomic Energy Authority, Cairo-13759, Egypt

Received January 7, 2019; Revised May 31, 2019

A series of novel arylazobithiazolyhydrazones (**A-E**) were efficiently synthesized *via* the reaction of thiazolythiosemicarbazone **3** with hydrazonoyl chlorides **4a-c** in boiling ethanol containing triethylamine as catalyst. The synthesized thiazoleazodye derivatives were characterized by microanalyses and spectral data (IR, ¹H-NMR and ¹³C-NMR), as well as thermal analysis. Moreover, theoretical implementations for compounds (modeling and docking) were taken in consideration. The molecular and structural formulae were established on the basis of analyses and compared altogether in their general features. The influence of substituents on thermal, kinetic, biological activity and reactivity was investigated. The decomposition pathway is completely affected by substituents type. The kinetic parameters estimated have direct relation with the heating rate as well, deeply affected by the inductive effect of substituents. Variable essential parameters were computed upon optimized structures applying Gaussian 09 and Hyper Chem 8.1 programs. In between, the indices attributed to reactivity and biological features point to the priority of compound E in coinciding with the presence of sulfur atom in the substituent group. Also, docking study differentiates between tested derivatives; their behavior in docking efficiency was varied in coinciding with various substituents, as expected. The best docking efficiency was recorded with derivative E, which includes a highly inductive functional group (SO₂NH₂) as *p*-substituent.

Keywords: kinetic study, bithiazolyhydrazones, Gaussian 09 software, molecular docking

INTRODUCTION

The synthesis of heterocyclic compounds has been thoroughly investigated over decades as raising significant interest to their great therapeutic effects and various heterocyclic compounds containing nitrogen and sulfur display elastic structures for drugs improvement [1]. Thiazoles are considered as a heavily studied class of aromatic five-membered heterocyclics which are found in many powerful biologically active drugs such as Sulfathiazol (antimicrobial drug), Ritonavir (antiretroviral drug), Abafungin (antifungal drug) and Tiazofurin (antineoplastic drug) [2]. Thus, thiazole or thiazolyl moiety if it is present in any compound will show numerous biological activities such as anti-inflammatory [3], antimicrobial & antifungal [4], antihypertensive [5], anticancer [6], anti-HIV [7], antidiabetic [8], and anticonvulsant [9] activities. Hydrazone-based compounds represent a very important class of derivatives with a broad spectrum of strong pharmacological influences [10]. A variety of hydrazones were

synthesized with potential pharmacological activities like antibacterial, anti-inflammatory, analgesic, anti-hypertensive, antifungal, antiplatelet, antimalarial, anticonvulsant, antidepressant, antiviral, and anticancer [11]. Beside their extensive biological characteristics they also integrate with other active functional groups to display pharmacologically active molecules [12, 13]. For example, thiazolyhydrazones displayed an excellent ability to effectively inhibit leukemic tumor cell growth and to decrease the concentrations of deoxyribonucleoside triphosphate [14]. Furthermore, excessive accumulation of metal ions in brain leads to neurodegeneration. Metal-promotion neurotoxicity is proposed to be attached with various neurological diseases [15]. Recently, chelation therapy has become a significant handling for the symptoms associated with the central nervous system [16]. Different classes of sulfur- and nitrogen-containing compounds are capable to form complexes with metal ions interacting with biological systems [17-19]. Referring to the strong reactivity of the hydrazine nitrogen (C=N) and azo

* To whom all correspondence should be sent:

E-mail: abkhedr2010@yahoo.com

n_elmetwaly00@yahoo.com

(N=N) groups, compounds including both groups represent a versatile class which is significant in curing chemistry [20-23].

On the other hand, thermal methods of analysis are most widely used to study industrially important products such as polymers, pharmaceuticals, metals, minerals, alloys, clays, various metal complexes, etc. [24]. Panchal *et al.* [25] have reported thermo gravimetric analysis of lanthanide coordination polymers with the Schiff base N,N'-di(o-hydroxy phenyl) terephthalaldehyde and determined final decomposition products. Aghera and Parsania [26] have reported thermo gravimetric analysis of symmetric double Schiff bases containing cardo group to understand the effect of different substituents on thermal stability, kinetic parameters of Schiff bases. Recently, Gangani and Parsania [27] have reported thermo acoustical studies of various substituted symmetric double Schiff bases. From researches reported, this work aims to start synthesis of new arylazobithiazolylhydrazone derivatives with various *p*-substituents over one side, and to investigate their influence on the kinetic parameters upon thermal study. The effect of aromatic substituents on the homolysis of organic compounds suffers an observable shortage in literature review. The formulae will be established based on elemental, spectral and conformational optimization software. The docking towards DNA was taken in consideration, to give a comparative view about their inhibition efficiency, which points to their expected efficiency with infected cell DNA.

EXPERIMENTAL

All reagents and solvents used were purchased from Sigma-Aldrich and used without any further treatments.

Techniques of analyses

Using a digital Gallen-Kamp MFB-595 instrument with open capillary tubes, the melting points were recorded and are uncorrected. On Shimadzu FTIR 440 spectrometer using KBr pellets, the IR spectra were determined over range of 400-4000 cm^{-1} . Using a Bruker model 400 MHz Ultra Shield NMR spectrometer through DMSO- d_6 using tetramethylsilane (TMS) (internal standard), the $^1\text{H-NMR}$ and $^{13}\text{C-NMR}$ spectra were recorded. Chemical shifts were reported as δ_{ppm} units. The elemental analyses were performed using Perkin-Elmer 2400 CHN Elemental Analyzer. Shimadzu Thermal Analyzer was used to obtain the TGA curves of the complexes applying variable heating rates; 5-25 $\text{K}\cdot\text{min}^{-1}$, under pure N_2 atmosphere, over the range of 20-900 $^\circ\text{C}$. Conformational analysis

was executed by Gaussian 09 program and molecular docking by Autodock 4.2 tools. 1-(2-Allylamino-4-methylthiazol-5-yl)ethanone (**1**) and hydrazoneyl chlorides **4a-e** were prepared according to previously reported procedures [28, 29].

Synthesis of 2-(1-(2-allylamino-4-methylthiazol-5-yl)ethylidene)-N-phenylhydrazine-1-thiocarboxamide (3)

A solution of 0.01 mol (1.96 g) of 1-(2-allylamino-4-methylthiazol-5-yl)ethanone **1** was dissolved in 30 mL of ethanol and then 0.01 mol (1.67 g) of 4-phenylthiosemicarbazide was added in presence of 0.5 mL of conc. HCL. The solution was heated under reflux for 4 h, then allowed to cool down to room temperature. The precipitate (compound **3**) was isolated by filtration, washed with ethanol, dried and recrystallized from MeOH:DMF (1:1) mixture (Scheme 1). Pale yellow powder, Yield (87%), mp 202-203 $^\circ\text{C}$; IR (KBr) $\nu_{\text{max}}/\text{cm}^{-1}$: 3310 (NH), 3187 (NH), 3036 (NH), 3015 (CH- sp^2), 2930 (CH- sp^3), 1622 (C=C), 1598 (C=N), 1261 (C=S); $^1\text{H-NMR}$ (400 MHz, DMSO- d_6): δ_{ppm} = 2.38 (s, 3H, CH_3), 2.52 (s, 3H, CH_3), 4.19 (s, 2H, NCH_2), 5.24 (dd, $J_{AB} = 1.2$, $J_{AC} = 10.4$ Hz, 1H, =C- H_A), 5.33 (dd, $J_{AB} = 1.2$, $J_{BC} = 16.8$ Hz, 1H, =C- H_B), 5.85-5.94 (m, 1H, =C- H_C), 7.16-7.65 (m, 5H, Ar-H), 9.81 (bs, 1H, NH), 10.43 (bs, 1H, NH), 11.08 (bs, 1H, NH); $^{13}\text{C-NMR}$ (100 MHz, DMSO- d_6): δ_{ppm} = 14.78 (CH_3), 16.66 (CH_3), 47.93 (CH_2N), 117.93 ($\text{CH}_2=$), 120.50 (Thiazole- C_5), 125.50 (CH_{Ar}), 128.73 (2 CH_{Ar}), 129.19 (2 CH_{Ar}), 132.63 (CH=), 139.43 (C_{Ar}), 144.64 (C=N), 154.02 (Thiazole- C_4), 166.54 (Thiazole- C_2), 177.03 (C=S); Anal. Calcd. for $\text{C}_{16}\text{H}_{19}\text{N}_5\text{S}_2$ (345.11): C, 55.63; H, 5.54; N, 20.27%, Found: C, 55.59; H, 5.52; N, 20.26%.

Synthesis of 2-allylamino-4-methyl-5-(1-((4-methyl-3-phenyl-5-(arylo)thiazol-2(3H)ylidene)hydrazone)ethyl)thiazoles (A-E)

Solutions of equimolar amounts of hydrazoneyl chloride **4** (0.005 mol) and compound **3** (1.73 g, 0.005 mol) in 30 mL of ethanol were mixed in presence of 0.5 mL of triethylamine. The mixture was heated under reflux for 3 h, then cooled down to room temperature. The resulting thiazole dye was collected by filtration, washed with aqueous ethanol, dried and recrystallized from glacial acetic acid to afford the aimed compounds (**A-E**).

2-Allylamino-4-methyl-5-(1-((4-methyl-3-phenyl-5-(4-fluorophenylazo)thiazol-2(3H)ylidene)hydrazone)ethyl)thiazole (A). Red crystals, Yield (88%), mp 236-237 $^\circ\text{C}$; IR (KBr) $\nu_{\text{max}}/\text{cm}^{-1}$: 3200 (NH), 3063 (CH- sp^2), 2989 (CH- sp^3), 1619 (C=C),

1592 (C=N), 1567 (N=N); ¹H-NMR (DMSO-d₆): δ(ppm) = 2.52 (s, 3H, CH₃), 2.49 (s, 3H, CH₃), 2.56 (s, 3H, CH₃), 5.17-5.28 (m, 2H, CH₂=), 3.92 (bs, 2H, NCH₂), 5.93 (m, 1H, =C-H_C), 7.17-7.24 (m, 5H, Ar-H), 7.49 (d, *J* = 7.5 Hz, 2H, Ar-H_{2,6}), 7.31 (d, *J* = 7.5 Hz, 2H, Ar-H_{3,5}), 8.35 (bs, 1H, NH); ¹³C-NMR (DMSO-d₆): δ_{ppm} = 16.90 (CH₃), 17.36 (CH₃), 19.69 (CH₃), 46.78 (CH₂N), 113.69 (Thiazole-C₅), 116.45 (CH₂=), 116.52 (2CH_{Ar}), 119.29 (Thiazole-C₅), 121.55 (2CH_{Ar}), 123.40 (CH_{Ar}), 132.41 (2CH_{Ar}), 134.88 (2CH_{Ar}), 135.21 (CH=), 139.93 (C_{Ar}), 149.29 (C_{Ar}), 150.21 (Thiazole-C₄), 154.27 (Thiazole-C₄), 161.52 (C_{Ar}), 168.20 (Thiazole-C₂), 168.98 (Thiazole-C₂), 173.56 (C=N); Anal. Calcd. for C₂₅H₂₄FN₇S₂ (505.64): C, 59.39; H, 4.78; N, 19.39%, Found: C, 59.57; H, 4.75; N, 19.38%.

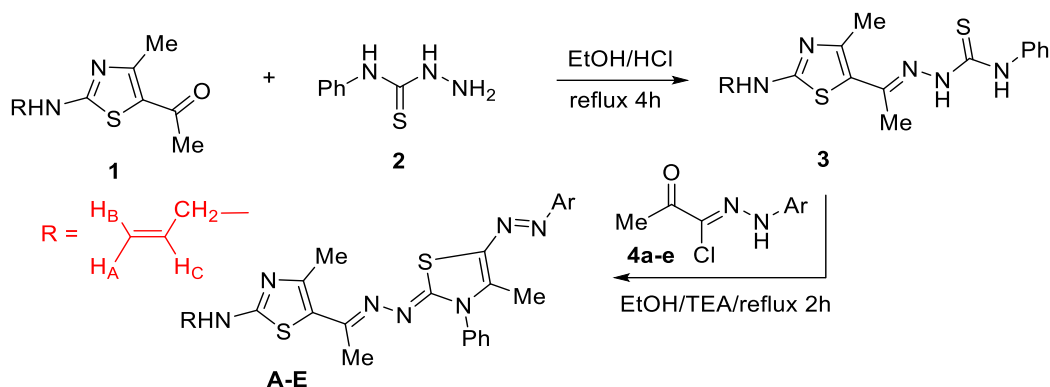
2-Allylamino-4-methyl-5-(1-((4-methyl-3-phenyl-5-(4-chlorophenylazo)thiazol-2(3H)yildene)hydrazono)ethyl)thiazole (B). Red powder, Yield (95%), mp 234-235°C; IR (KBr) ν_{max}/cm⁻¹: 3197 (NH), 3082 (CH-sp²), 2965 (CH-sp³), 1621 (C=C), 1593 (C=N), 1570 (N=N); ¹H-NMR (DMSO-d₆): δ_{ppm} = 2.11 (s, 3H, CH₃), 2.35 (s, 3H, CH₃), 2.40 (s, 3H, CH₃), 3.90 (s, 2H, NCH₂), 5.13 (dd, *J*_{AB} = 1.6, *J*_{AC} = 10.2 Hz, 1H, =C-H_A), 5.24 (dd, *J*_{AB} = 1.6, *J*_{BC} = 17.0 Hz, 1H, =C-H_B), 5.86-5.95 (m, 1H, =C-H_C), 7.10-7.39 (m, 5H, Ar-H), 7.41 (d, *J* = 7.5 Hz, 2H, Ar-H_{3,5}), 7.67 (d, *J* = 7.5 Hz, 2H, Ar-H_{2,6}), 8.05 (bs, 1H, NH), 10.59 (s, 1H, NH); ¹³C-NMR (DMSO-d₆): δ_{ppm} = 13.59 (CH₃), 16.70 (CH₃), 19.13 (CH₃), 46.55 (CH₂N), 116.24 (CH₂=), 117.32 (Thiazole-C₅), 119.54 (Thiazole-C₅), 123.91 (2CH_{Ar}), 128.70 (2CH_{Ar}), 129.81 (2CH_{Ar}), 129.81 (2CH_{Ar}), 129.98 (CH_{Ar}), 132.75 (CH=), 136.15 (C_{Ar}), 140.00 (C_{Ar}), 150.60 (C_{Ar}), 151.79 (Thiazole-C₄), 156.16 (Thiazole-C₄), 162.25 (Thiazole-C₂), 167.83 (Thiazole-C₂), 173.56 (C=N); Anal. Calcd. for C₂₅H₂₄ClN₇S₂ (522.1): C, 57.51; H, 4.63; N, 18.78%, Found: C, 57.48; H, 4.60; N, 18.75%.

2-Allylamino-4-methyl-5-(1-((4-methyl-3-phenyl-5-(4-bromophenylazo)thiazol-2(3H)yildene)hydrazono)ethyl)thiazole (C) Red crystals, Yield (90%), mp 240-241°C; IR (KBr) ν_{max}/cm⁻¹: 3191 (NH), 3082 (CH-sp²), 2935 (CH-sp³), 1620 (C=C), 1598 (C=N), 1569 (N=N); ¹H-NMR (DMSO-d₆): δ_{ppm} = 2.47 (s, 3H, CH₃), 2.48 (s, 3H, CH₃), 2.55 (s, 3H, CH₃), 3.92 (bs, 2H, NCH₂), 5.16 (dd, *J*_{AB} = 1.6, *J*_{AC} = 10.2 Hz, 1H, =C-H_A), 5.25 (dd, *J*_{AB} = 1.6, *J*_{AC} = 17.0 Hz, 1H, =C-H_B), 5.91-5.93 (m, 1H, CH=), 7.17-7.24 (m, 5H, Ar-H), 7.35 (s, 4H, Ar-H), 8.34 (s, 1H, NH); ¹³C-NMR (DMSO-d₆): δ_{ppm} = 16.87 (CH₃), 17.25 (CH₃), 19.03 (CH₃), 46.78 (CH₂N), 116.06 (2CH_{Ar}), 116.44 (CH₂=), 119.30 (Thiazole-C₅), 123.35 (Thiazole-C₅), 124.21 (CH_{Ar}), 125.81 (2CH_{Ar}), 126.51 (2CH_{Ar}), 129.51 (2CH_{Ar}), 133.31

(CH=), 134.86 (C_{Ar}), 139.81 (C_{Ar}), 143.15 (C_{Ar}), 154.21 (Thiazole-C₄), 161.47 (Thiazole-C₄), 168.29 (Thiazole-C₂), 168.96 (Thiazole-C₂), 172.75 (C=N); Anal. Calcd. for C₂₅H₂₄BrN₇S₂ (566.55): C, 53.00; H, 4.27; N, 17.31%, Found: C, 53.01; H, 4.24; N, 17.29%.

2-Allylamino-4-methyl-5-(1-((4-methyl-3-phenyl-5-(4-ethoxyphenylazo)thiazol-2(3H)yildene)hydrazono)ethyl)thiazole (D). Orange powder, Yield (86%), mp 179-180°C; IR (KBr) ν_{max}/cm⁻¹: 3198 (NH), 3068 (CH-sp²), 2970 (CH-sp³), 1622 (C=C), 1614 (C=N), 1567 (N=N); ¹H-NMR (DMSO-d₆): δ_{ppm} = 1.06 (t, *J* = 7.2 Hz, 3H, CH₃), 2.47 (s, 3H, CH₃), 2.52 (s, 3H, CH₃), 2.56 (s, 3H, CH₃), 3.92 (bs, 2H, NCH₂), 4.35 (q, *J* = 7.2 Hz, 2H, OCH₂), 5.15 (dd, *J*_{AB} = 1.5, *J*_{AC} = 10.2 Hz, 1H, =C-H_A), 5.26 (dd, *J*_{AB} = 1.5 Hz, *J*_{BC} = 16.5 Hz, 1H, =C-H_B), 5.87-5.96 (m, 1H, CH=), 6.91-7.20 (m, 5H, Ar-H), 7.44 (d, *J* = 7.8 Hz, 2H, Ar-H_{3,5}), 7.78 (d, *J* = 7.8 Hz, 2H, Ar-H_{2,6}), 8.35 (bs, 1H, NH); ¹³C-NMR (DMSO-d₆): δ_{ppm} = 16.92 (CH₃), 17.36 (CH₃), 19.02 (CH₃), 19.70 (CH₃), 46.80 (CH₂N), 56.51 (OCH₂), 114.08 (Thiazole-C₅), 116.45 (CH₂=), 119.26 (Thiazole-C₅), 123.51 (2CH_{Ar}), 126.35 (CH_{Ar}), 127.77 (2CH_{Ar}), 129.88 (2CH_{Ar}), 130.11 (2CH_{Ar}), 134.83 (CH=), 137.07 (C_{Ar}), 141.26 (C_{Ar}), 146.84 (C_{Ar}), 154.49 (Thiazole-C₄), 161.80 (Thiazole-C₄), 168.10 (Thiazole-C₂), 169.06 (Thiazole-C₂), 174.08 (C=N); Anal. Calcd. for C₂₇H₂₉N₇O₂S₂ (531.71): C, 60.99; H, 5.50; N, 18.44%, Found: C, 60.96; H, 5.48; N, 18.41%.

2-Allylamino-4-methyl-5-(1-((4-methyl-3-phenyl-5-(4-sulfonamidophenylazo)thiazol-2(3H)yildene)hydrazono)ethyl)thiazole (E). Red crystals, Yield (87%), mp 177-178°C; IR (KBr) ν_{max}/cm⁻¹: 3231, 3166 (NH₂), 3081 (NH), 3054 (CH-sp²), 2981 (CH-sp³), 1620 (C=C), 1596 (C=N), 1582 (N=N); ¹H-NMR (DMSO-d₆): δ_{ppm} = 2.47 (s, 3H, CH₃), 2.49 (s, 3H, CH₃), 2.57 (s, 3H, CH₃), 3.92 (bs, 2H, NCH₂), 5.16 (dd, *J*_{AB} = 1.5, *J*_{AC} = 10.2 Hz, 1H, =C-H_A), 5.26 (dd, *J*_{AB} = 1.5, *J*_{BC} = 17.0 Hz, 1H, =C-H_B), 5.88-5.96 (m, 1H, CH=), 6.92-7.19 (m, 5H, Ar-H), 7.22 (s, 2H, NH₂), 7.44 (d, *J* = 8.5 Hz, 2H, Ar-H_{3,5}), 7.78 (d, *J* = 8.5 Hz, 2H, Ar-H_{2,6}), 8.35 (bs, 1H, NH); ¹³C-NMR (DMSO-d₆): δ_{ppm} = 17.36 (CH₃), 19.02 (CH₃), 19.70 (CH₃), 46.81 (CH₂N), 114.08 (Thiazole-C₅), 116.45 (CH₂=), 119.26 (Thiazole-C₅), 124.51 (2CH_{Ar}), 127.77 (2CH_{Ar}), 128.55 (2CH_{Ar}), 129.12 (CH_{Ar}), 129.98 (CH_{Ar}), 134.03 (CH=), 137.07 (C_{Ar}), 141.26 (C_{Ar}), 146.84 (C_{Ar}), 154.49 (Thiazole-C₄), 161.80 (Thiazole-C₄), 168.10 (Thiazole-C₂), 169.06 (Thiazole-C₂), 176.96 (C=N); Anal. Calcd. for C₂₅H₂₆N₈O₂S₃ (566.71): C, 52.98; H, 4.62; N, 19.77%, Found: C, 52.95; H, 4.60; N, 19.75%.



A, Ar = 4-F-C₆H₄-; B, Ar = 4-Cl-C₆H₄-; C, Ar = 4-Br-C₆H₄-; D, Ar = 4-EtO-C₆H₄-; E, Ar = 4-NH₂SO₂-C₆H₄-

Scheme 1. Synthesis of 2-allylamino-4-methyl-5-(1-((4-methyl--3-phenyl-5-(arylo)thiazol-2(3H)ylidene)hydrazono)ethyl)thiazole derivatives, **A-E**.

THEORETICAL IMPLEMENTATION

Kinetics

Significant thermodynamic parameters were computed over main decomposition stage in each compound under different heating rates beside the activation energy (E) and order (n). Many researches had established mathematical equations for this purpose and clarified their scientific meaning [30-38]. The rate of decomposition (equation 1) is the yield of two separated indices (k(T) and f(α)):

$$\frac{d\alpha}{dt} = k(T)f(\alpha) \quad (1)$$

Therein, α is a fraction decomposed at time t, f(α) is a conversion function and k(T) is a temperature dependent function. The two functions are of Arrhenius type (equation 2):

$$K = A e^{-E^*/RT} \quad (2)$$

Therein, R is the gas constant (J mol⁻¹k⁻¹). Using equation 2 as a function of equation 1, equation (3) was obtained:

$$\frac{d\alpha}{dT} = \left(\frac{A}{\varphi e^{-E^*/RT}} \right) f(\alpha) \quad (3)$$

Therein, φ is the linear heating rate (dT/dt). Applying integration and approximation, equation (4) was obtained:

$$\ln g(\alpha) = \frac{-E^*}{RT} + \ln \left[\frac{AR}{\varphi E^*} \right] \quad (4)$$

g(α) function depends on the mechanism of action in the decomposition process. Implementing Coat-Redfern [32] and Horowitz-Metzger methods [37],

the temperature integral (right-hand side) and significant kinetics were evaluated.

Geometrical optimization

Applying DFT/B3LYP method using Gaussian 09 software [39], the optimized geometrical forms of arylazo-bithiazolyhydrazone derivatives were built (figure 1). 6-31G is a suitable base set for this purpose. Essential physical parameters which reflect significant features around the treated compounds were computed based on frontier energy gapes by known relations [40, 41] as follows:

- 1- $\chi = -0.5 (E_{LUMO} + E_{HOMO})$
- 2- $\mu = -\chi = 0.5 (E_{LUMO} + E_{HOMO})$
- 3- $\eta = 0.5 (E_{LUMO} - E_{HOMO})$
- 4- $S = -0.5 \eta$
- 5- $\omega = \mu^2 / 2 \eta$
- 6- $\sigma = 1/\eta$

Two considerable files (log and chk) were excreted. The files were visualized over Gauss program screen [42] to obtain essential physical data.

QSAR parameters computation

Surface area, volume, hydration energy, log P, reactivity and polarizability were the calculated QSAR parameters over optimized structures (A-E). The optimization process was executed by HyperChem (8.1) program. Semi-empirical AM1 followed by molecular mechanics (MM⁺) were the suitable setup methods before the geometrical optimization process. The optimization process was accomplished without restriction for any parameters, after which the parameters were computed separately [43].

This is a recent computational method in drug designing industry as a preliminary test of the inhibition efficiency of organic compounds towards pathogen protein. Auto Dock tool 4.2 was implemented for docking process between arylazo-bithiazolyhydrazone derivatives and calf thymus

DNA (2hio). Non-polar hydrogen atoms were added and the rotatable bonds were excluded before. Fundamental hydrogen atoms, charges (Kollman united) and solubility parameters were then added [44]. The affinity (grid) maps of $\times\times$ Å grid points and 0.375 Å spacing were obtained through Autogrid program [45].

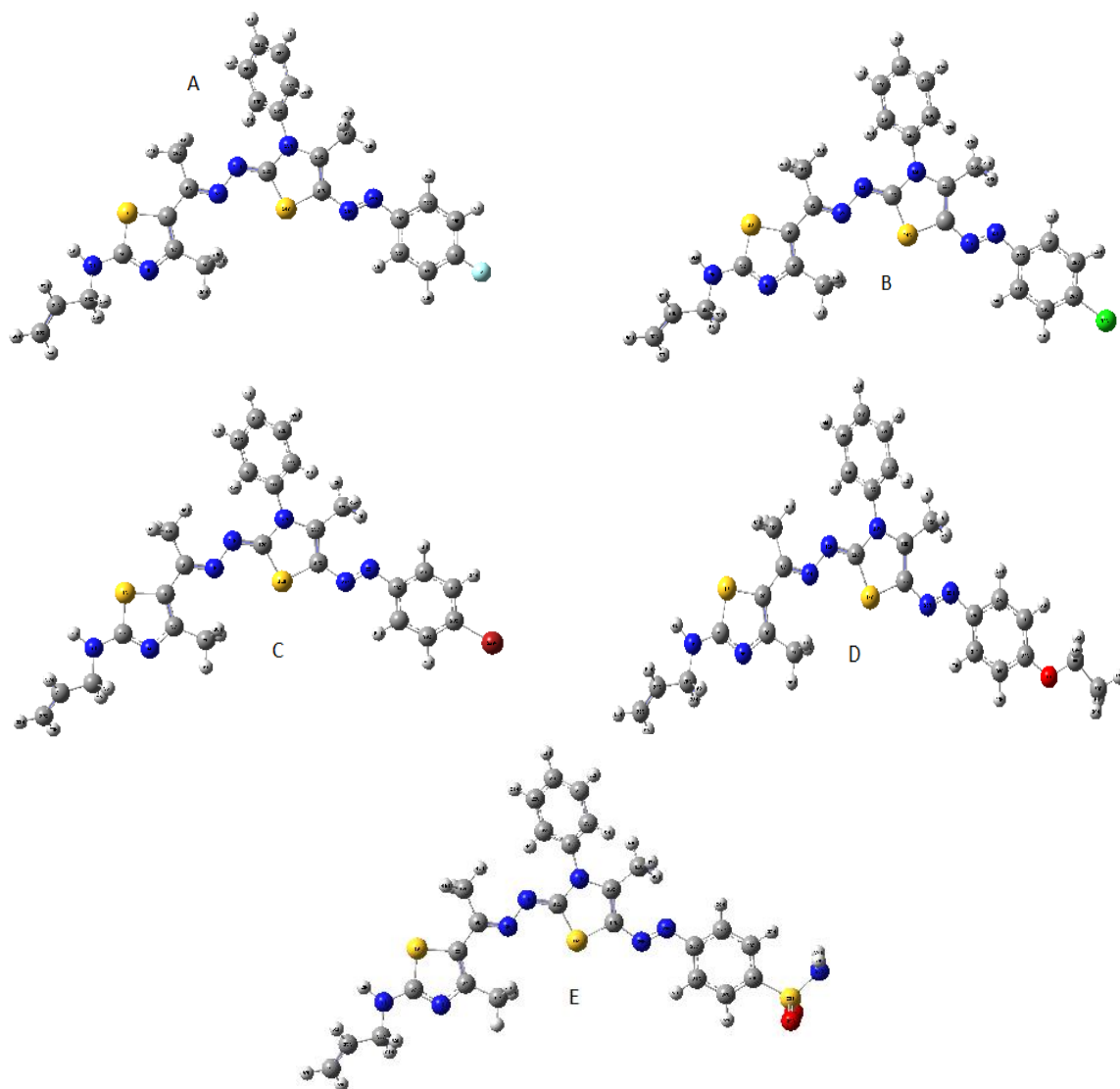


Fig. 1. The optimized structures of arylazobithiazolyhydrazone derivatives (A-E).

Electrostatic terms and van der Waals forces were estimated through dielectric function (distance-dependant) and auto dock parameter set, respectively. Docking process was executed by Solis & Wets local search method and Lamarckian genetic algorithm (LGA) [46]. The orientation, initial position and torsions of tested molecules were set incidentally. All rotatable torsions were decomposed during the docking process. Each experiment was the average value of 10 different runs which set to close after maximum of 250000

energy assessments. The used population size was 150. During the process, in the translational step (0.2 Å) quaternion and torsion steps were applied.

RESULTS AND DISCUSSION

Mechanism of action

As outlined in scheme 1, 1-(2-allylamino-4-methylthiazol-5-yl) ethanone (**1**) was condensed with 4-phenylthiosemicarbazide (**2**) in ethanol (boiling) containing HCl as a catalyst to afford thiazolythiosemicarbazone **3** in good yield. The

chemical structure of compound **3** was built based on elemental analysis, spectral data, and chemical transformations. The IR spectrum of compound **3** exhibited absorption bands at 3310, 3187, 3036, 1622, 1598, and 1261 cm^{-1} characteristic to three NH, C=C, C=N, and C=S groups, respectively. Its $^1\text{H-NMR}$ spectrum revealed, besides the expected signals of phenyl and allyl protons, two singlets at δ 2.38 and 2.52 ppm assignable to two methyl protons, and three broad singlet signals, exchangeable with D_2O , at δ 9.81, 10.43, 11.08 ppm owing to three NH protons. The $^{13}\text{C-NMR}$ spectrum of compound **3** revealed the presence of fourteen carbon signals compatible with its molecular formula ($\text{C}_{16}\text{H}_{19}\text{N}_5\text{S}_2$). The most characteristic carbon signals resonate at δ 14.78, 16.66, 47.93, 177.03 ppm owing to two methyl carbons, methylene, and thiocarbonyl group, respectively.

Next, we investigated the reactivity of the thiourea moiety in compound **3** towards hydrazonoyl chlorides with the aim to attain arylazobithiazolyhydrazones for thermal analysis investigation. Thus, reaction of compound **3** with a series of *N*-aryl hydrazonoyl chlorides **4a-e** [29] in boiling ethanol containing triethylamine as a basic catalyst gave one isolable product in each case (as evidenced by TLC analysis of the crude product), which were recognized to be products **5a-e** (Scheme 1). The structure of products **5a-e** was confirmed by elemental analyses and spectral data. The IR spectra of products **5a-e** showed in each case the disappearance of C=S absorption band and the presence of new absorption bands in the ranges 1592-1598 and 1567-1582 cm^{-1} assigned to conjugated C=N and N=N groups, respectively. The $^1\text{H-NMR}$ spectrum of compound **5d**, as an example, revealed in addition to the expected signals of the allyl amino protons, aromatic protons, and protons of three methyl groups, a triplet signal at δ 1.06 ppm and a quartet signal at 4.35 ppm assigned to ethoxy group. There is also a pair of doublet signals resonating around 7.44, 7.78 ppm with the same coupling constant value ($J = 7.8$ Hz) assigned to the four protons of *p*-substituted benzene ring residue. The $^{13}\text{C-NMR}$ spectrum of compound **5d** revealed the presence of 23 carbon signals. The sp^3 hybridized carbon atoms resonate at δ 16.92, 17.36, 19.02, 19.70, 46.80 and 56.51 ppm characteristic to four methyl carbons, CH_2N , and OCH_2 , respectively. The more downfield three carbons resonate at δ 168.10, 169.06, 174.08 ppm assigned to the carbons of thiazole- C_2 , thiazole- C_2 , and C=N, respectively (see supplementary data). The mass spectra of all products **5a-e** exhibited in each case a molecular ion peak at the correct

molecular weight for the respective compound (see Experimental). To account for the formation of products **5a-e**, it was suggested that the reaction starts *via* nucleophilic attack of the thiol group in compound **3** to the electron-deficient carbon of the hydrazone group in compounds **4a-e** and subsequent *in situ* dehydrative cyclization to give the target products **5a-e**.

TGA homolysis of arylazobithiazolyhydrazone derivatives

Although an observable shortage in researches concerning the relation between *p*-substituents and the thermal behavior of compounds, some articles exhibited essential knowledge about their pyrolysis [47-49]. All derivatives were subjected to thermal analysis (TGA and DTG) up to 800°C (figure 2). The data (Tables 1&S1-S4) show discriminate findings in mass loss for all compounds (A-E) which were recorded with heating rate variations (5-25 $\text{K} \cdot \text{min}^{-1}$) although the high similarity in homolysis pathway in various derivatives observable distinct features toward thermal stability which clearly appeared in the first stage of pyrolysis. These observations clarify the high impact of heating rate changes, as well as *p*-substituents. The substituents with high inductive effect led to difficult degradation over the whole molecule. This reflected on incomplete pyrolysis of the organic compounds. Derivative A displayed high rigidity in the pyrolysis process in agreement with the high inductive effect of the small-sized substituent (F) followed by derivative D for OC_2H_5 substituent.

Kinetic studies

This part in our research is considered the most significant, in which the study is being processed to estimate the kinetic parameters. The kinetic parameters (ΔH , ΔG and ΔS) and energy of activation were estimated by using two comparative reference equations [32, 37]. These calculated parameters serve for discrimination of the influence of changeable substituents on the degree of thermal rigidity. Moreover, the parameters were calculated under variable heating rates (5-25 $\text{K} \cdot \text{min}^{-1}$) to investigate the degree of shifts in their values in coinciding. Figure 3 displays relations for Coat-Redfern and Horowitz-Metzger methods under various conditions (heating rate and *p*-substituents). The data were computed by applying two methods (Tables 2&S5-S8) over most suitable degradation stage (second and sometimes the first). This stage accidentally the main degradation stage represents expel of a great mass.

The first view of the relations (figure 3) showed the mismatch of the resulting lines, which confirms the effect of the substituents on the behavior of thermal decomposition for compounds and also on the effect of changes in the heating rate. The data demonstrated that there are many reactions; number of reactions is increasing at low heating rates (5 and 10 K. min⁻¹) compared to high rates (15-25 K. min⁻¹). Although, only one effective reaction was taken in consideration for simplicity and the parameters are displayed in the tables reported. It is noted that all pyrolysis models are based on a single effective reaction. Moreover, there is an observable increase of kinetic parameters values with increasing heating rate. Also, the high inductive effect of the substituents leads to high values of the kinetic parameters as appeared in A, B and D compounds for F, Cl and OC₂H₅ *p*-substituents.

The best atomic distribution inside the five derivatives (figure 1) was obtained in gas phase by DFT/B3LYP method with 6-31G base set. The frontier energy gaps (E_{HOMO} - E_{LUMO}) were calculated and used for computing other significant parameters (Table 3) using reference relations [50, 51]. Electronegativity index (χ), chemical potential index (μ), global hardness index (η), global softness index (S), global electrophilicity index (ω) and absolute softness (σ) were the parameters computed. Electrophilicity parameter is indicator for the degree of reactivity and toxicity for the tested compound. Electronic chemical potential (μ) and electronegativity (χ) are two opposite faces pointing at the degree electron affinity gained from universe. Global hardness (η), global softness (S) indices are also two opposite faces pointing to the degree of flexibility of the compound which serve to distinguish the biological behavior of the compound inside the cell. All indices introduce distinguished reactivity and toxicity of compound E, which includes substituent SO₂NH₂.

Table 1. Plausible degradation process for arylazobithiazolyhydrazones (at 5 K. min⁻¹ heating rate)

Compound	Steps	Temp. range (°C)	Decomposed	Weight loss: Calcd (Found) (%)
A	1 st	50.2-81.4	CH ₄	3.17(3.17)
	2 nd	200.1-308.4	C ₇ H ₈ N ₄ S	35.64(35.67)
	3 rd	362.4-515.1	C ₅ H ₁₂ N ₃ SF	32.68(32.71)
	Residue		12C	28.50(28.45)
B	1 st	51.2-91.1	C ₇ H ₉ N ₂ S	29.35(30.00)
	2 nd	122.6-301.2	C ₉ H ₈ N ₃	30.30(30.41)
	3 rd	305.6-400.1	C ₆ H ₇ N ₂ ClS	33.45(33.61)
	Residue		3C	6.90(5.98)
C	1 st	55.1-170.2	C ₉ H ₁₁ N ₂ S	31.64(31.65)
	2 nd	221.5-452.1	C ₁₆ H ₁₁ N ₅ Br	62.34(62.33)
	3 rd	535.2-581.3	H ₂ S	6.02(6.02)
	Residue		nil	
D	1 st	122.3-305.4	C ₂₅ H ₂₅ N ₇ OS ₂	94.72(94.75)
	2 nd	350.2-403.3	C ₂ H ₄	5.28 (5.25)
	Residue		nil	
E	1 st	61.2-122.1	C ₃ H ₆ N	9.80(9.81)
	2 nd	210.1-341.2	C ₁₃ H ₁₁ N ₄ S	45.05(45.04)
	3 rd	420.3-583.2	C ₃ H ₂ N ₂ S	17.31(17.33)
	Residue		C ₆ H ₇ SO ₂ N	27.74(27.82)

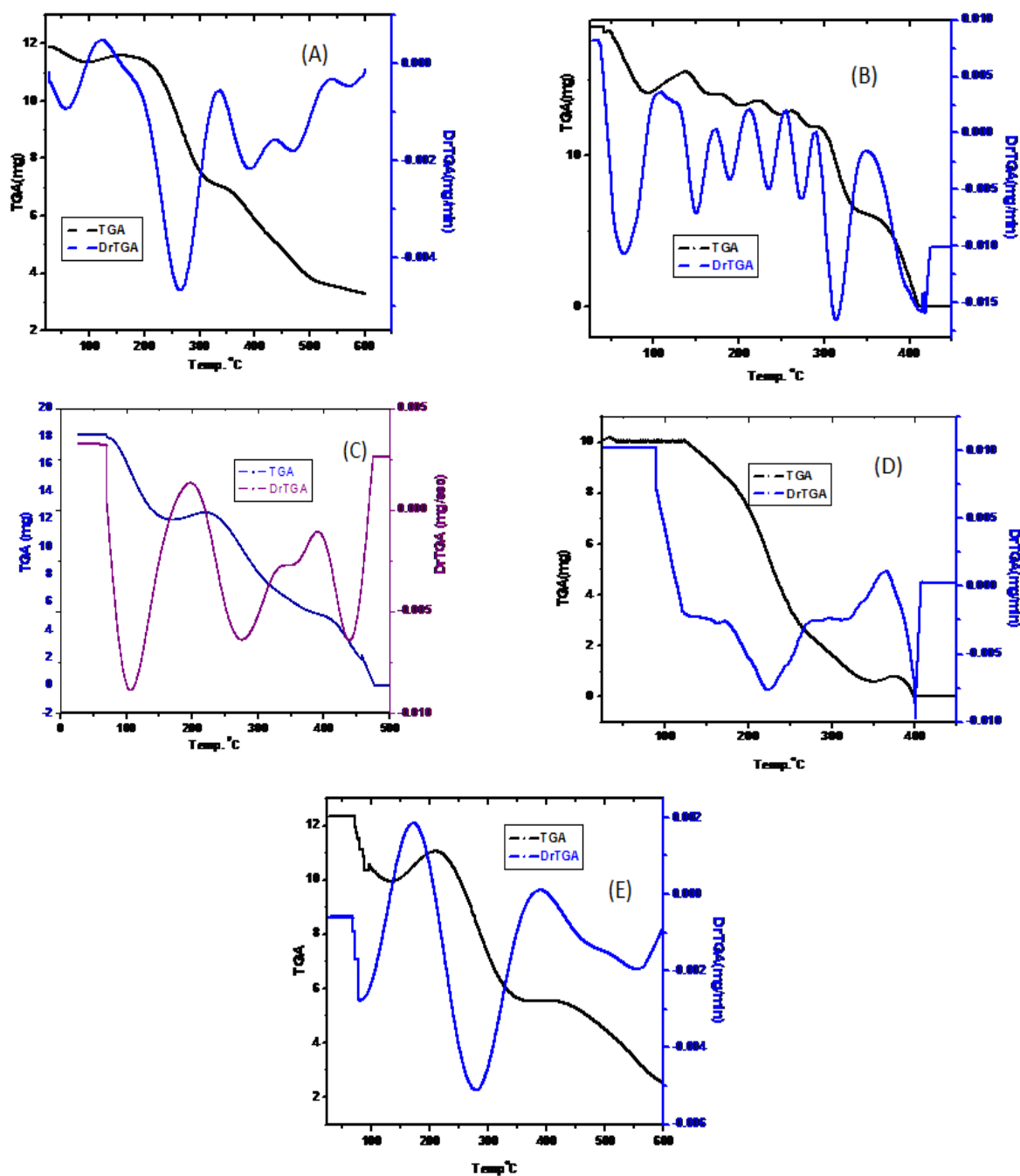


Fig. 2. TGA and DTG of compounds A-E at 5 K. min⁻¹ heating rate

Table 2. Computed kinetic parameters by Coats–Redfern (CR) and Horowitz–Metzger (HM) (for main step at 5 K min⁻¹ heating rate)

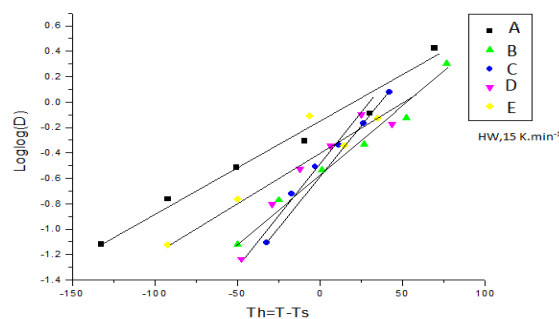
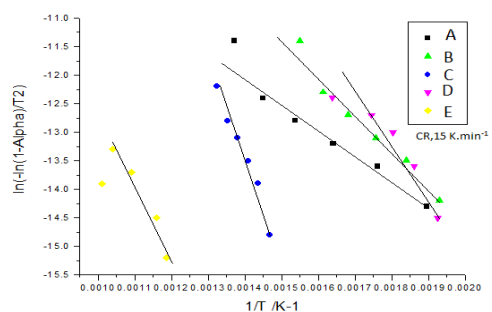
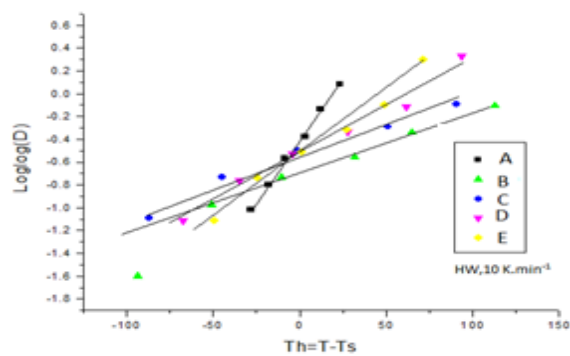
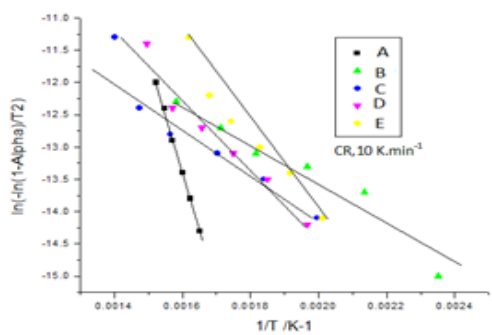
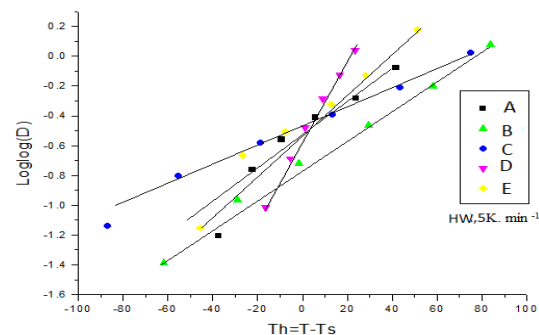
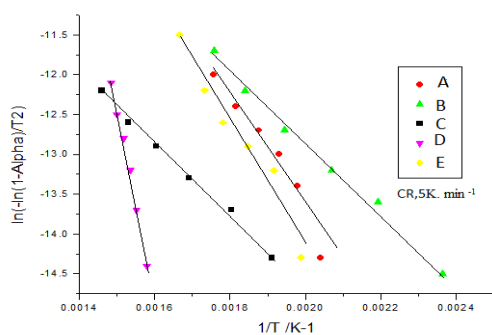
Comp.	Step	Method	Kinetic Parameters					
			E (Jmol ⁻¹)	A (S ⁻¹)	ΔS (Jmol ⁻¹ K ⁻¹)	ΔH (Jmol ⁻¹)	ΔG (Jmol ⁻¹)	r
A	2 nd	CR	4.25E+04	7.05E+03	-1.76E+02	5.82E+04	1.51E+05	0.9993
		HM	5.96E+04	5.90E+04	-1.58E+02	6.52E+04	1.49E+05	0.9991
B	2 nd	CR	2.69E+04	2.06E+01	-2.24E+02	3.29E+04	1.41E+05	0.9993
		HM	4.37E+04	2.80E+02	-2.02E+02	3.96E+04	1.38E+05	0.9991
C	2 nd	CR	3.73E+04	3.77E+00	-2.40E+02	3.22E+04	1.78E+05	0.9993
		HM	4.87E+04	5.86E+01	-2.17E+02	4.37E+04	1.76E+05	0.9991
D	2 nd	CR	4.01E+04	1.40E+04	1.94E+01	1.96E+04	1.83E+05	0.9993
		HM	4.11E+04	1.48E+4	3.90E+01	2.06E+04	1.81E+05	0.9991
E	2 nd	CR	3.51E+04	8.54E+03	-1.75E+02	6.05E+04	1.56E+05	0.9993
		HM	4.27E+04	6.06E+04	-1.58E+02	6.82E+04	1.55E+05	0.9991

Table 3. Computational parameters of arylazobithiazolyhydrazones through DFT/B3LYP method

Comp.	EH -		EH -		x (eV)	μ (eV)	η (eV)	S(eV-1)	ω (eV)	σ (eV)
	E_H (eV)	EL (eV)	EL (eV)	El-Eh						
A	-0.17306	-0.08827	-0.0848	0.08479	0.130665	-0.13067	0.042395	0.021198	0.20136	23.58768723
B	-0.17606	-0.08905	-0.087	0.08701	0.132555	-0.13256	0.043505	0.021753	0.20194	22.98586369
C	-0.17539	-0.08876	-0.0866	0.08663	0.132075	-0.13208	0.043315	0.021658	0.20136	23.08669052
D	-0.16986	-0.07713	-0.0927	0.09273	0.123495	-0.1235	0.046365	0.023183	0.164467	21.5679931
E	-0.18289	-0.10579	-0.0771	0.0771	0.14434	-0.14434	0.03855	0.019275	0.270221	25.94033722

Table 4. Estimated physical parameters extracted from log files

Comp.	Dipole moment, D (Debye)	Oscillator strength, f	Excitation energy, E (nm)	Heat of formation, E (A.U.)	Charge of <i>p</i> -substituent C^{29}
A	3.6863	0.2439	633.03	-2245.95315356	0.315047
B	4.6705	0.3433	599.73	-2606.32416645	-0.280876
C	4.3800	0.3488	603.2	-4717.72566804	-0.316959
D	3.9918	0.3666	565.56	-2300.54347509	0.318885
E	12.1981	0.3596	673.91	-2750.36357247	-0.238973



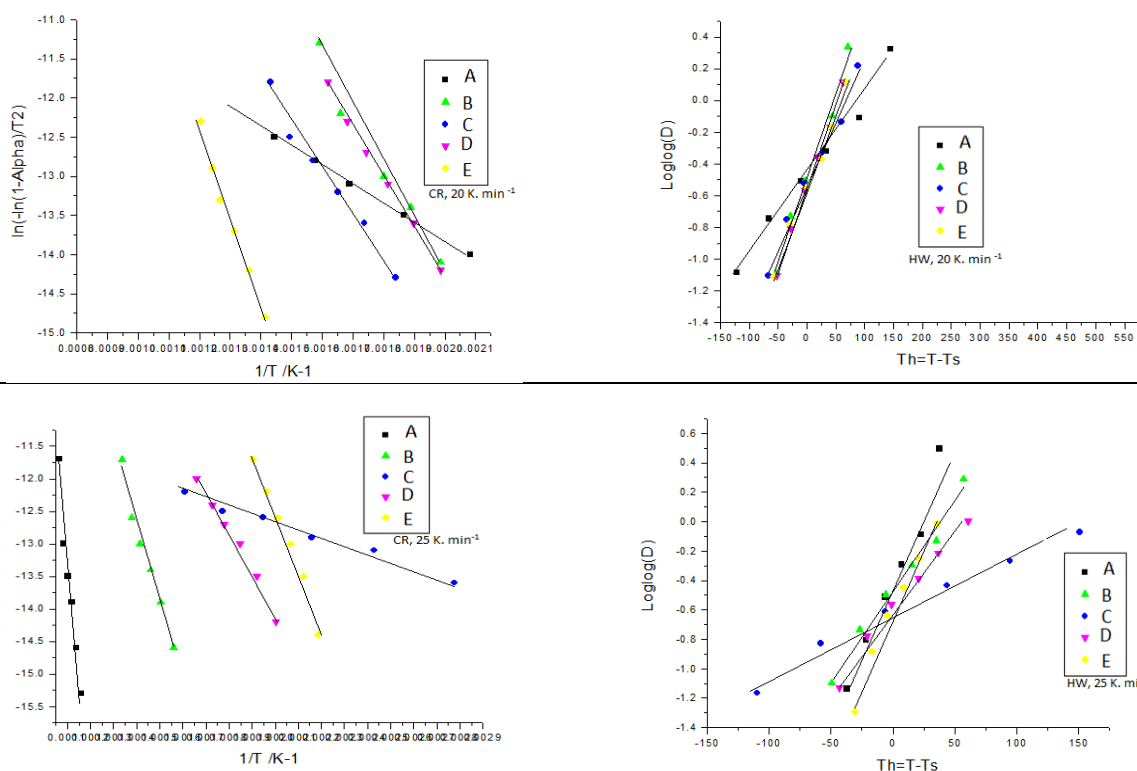


Fig. 3. The kinetic plots for Coats–Redfern (CR) and Horowitz–Metzger (HM) methods for main step in compounds (A-E) at various heating rates

Table 5. QSAR computational parameters for optimized new arylazobithiazolyhydrazone compounds

Function	A	B	C	D	E
Surface area (Approx) (\AA^2)	691.61	716.75	725.66	774.24	749.95
Surface area (Grid) (\AA^2)	793.77	823.25	835.76	882.42	871.61
Volume (\AA^3)	1384.42	1418.55	1437.20	1512.01	1499.67
Hydration energy (Kcal/mol)	-14.26	-14.21	-14.18	-15.23	-20.47
Log P	3.84	4.21	4.49	3.79	2.58
Reactivity (\AA^3)	159.32	163.91	166.73	170.32	172.45
Polarizability (\AA^3)	55.30	57.32	58.02	59.70	57.88
Mass(amu)	505.63	522.09	566.54	531.69	566.71

Oscillator strength values fall in the known range (0-1) [52], which reflects the high probability for the absorption or emission of radiations during the transition between levels. The computed values fall near to each other's and show the flexibility in absorption and emission character for all molecules. Excitation energy values coincide with heat of formation which appeared high with compound E. The computed charges over the carbon atom, which bonds to substituents, point to variable attachments from ionic to covalent.

This is another type of parameters estimated upon optimized structures applying molecular

mechanics (Table 5) of Hyper Chem (8.1) program. These parameters assert on the discrimination between derivatives under the effect of substituents. Surface area, volume, hydration energy, partition coefficient (log P has a reverse relation with biological susceptibility), reactivity and polarizability are essential parameters which give a clear insight about such influence. A marked difference between estimated values coincides with the effect of substituents. Estimated values of compound E showed its best qualities as regards reactivity and biological susceptibility [53].

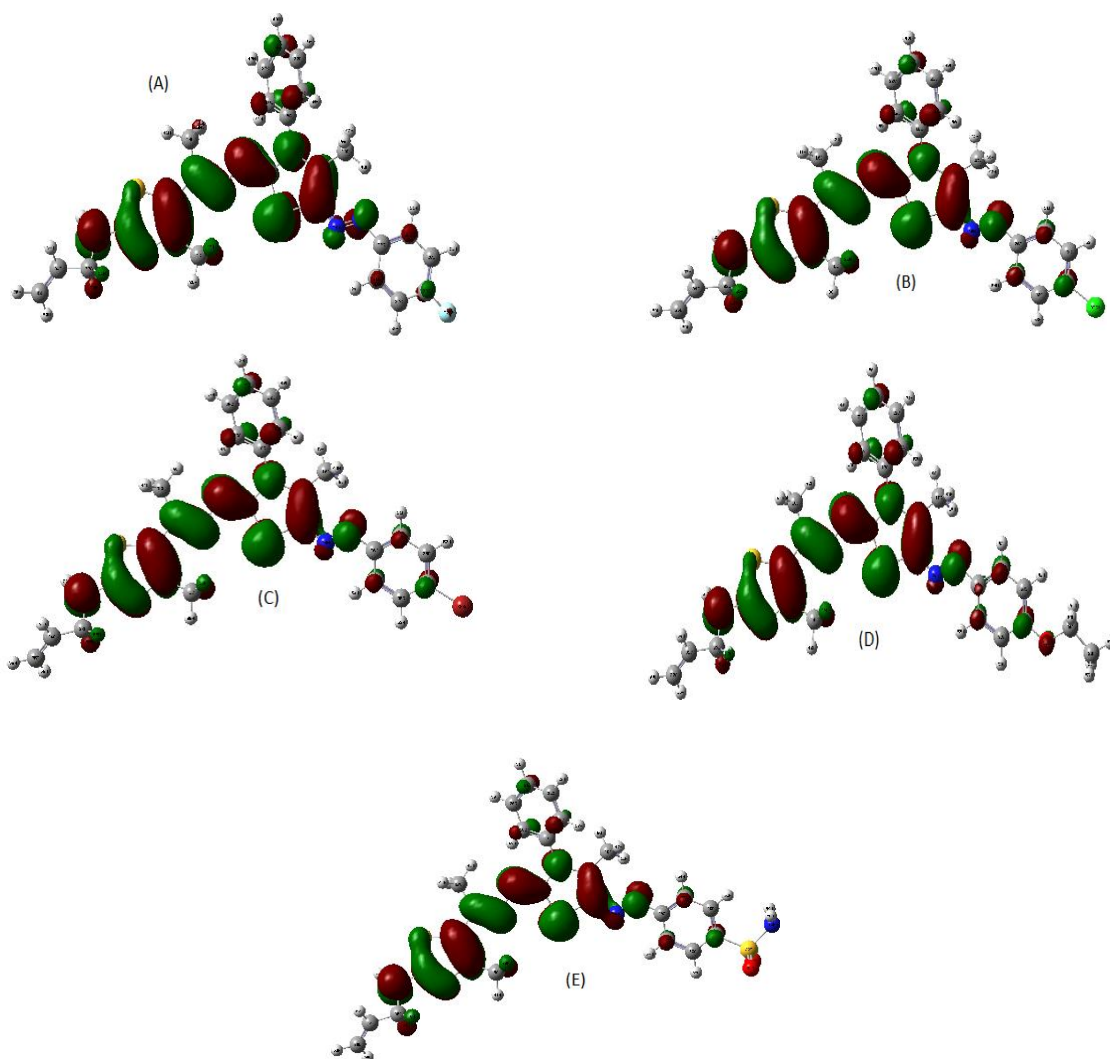


Fig. 4. Frontier HOMO level of arylazobithiazolyhydrazone derivatives (A-E)

QSAR calculations. Docking study

This study is considered the biggest revolution in computational study dealing with drug designing through simulation process. The docking process was executed for each derivative (A-E; as PDB file) against the calf thymus DNA protein (2hio) to give an insight about the degree of interaction in between. The DNA protein used was selected to simulate what may happen inside any infected cell. As we know that, the first target for any treatment drug, is the cell-DNA, so the interaction with DNA, may give the best view about treatment for many microbial diseases. The extracted parameters (Table 6) led to a clear view about the inhibition efficiency of tested compounds. The comparative vision for the data calculated displays a great differentiation between compounds (A-E) especially for values of inhibition constant calculated. Also, the data point to the priority of compound E among the others in agreement with previous computational studies. Such priority of the compound asserts on highly expected inhibition behavior towards pathogen and

its success in the medical field. Figure 6 illustrates the complexes between proposed inhibitors and DNA protein receptor. The Hp and 2D plots introducing the same number of H-bonding were obtained with all complexes. Moreover, nitrogen no. 25 is the sponsor of intra-hydrogen bonding with the protein except for compound B. This compound represents a chloro-substituent, which has a negative effect on the donation feature of the atom (N²⁵) towards the H-bonding. Also, the best prolongation for the DNA helixes was observed with compound E, in agreement with previously reported data in this study.

CONCLUSION

This study is focusing on the effect of substituents on the features of organic compounds as: thermal, kinetic; stability, reactivity and biological suitability. The influence of *p*-substituents (F, Cl, Br, OC₂H₅ and SO₂NH₂) was stated from the thermal and kinetic study. The substituents which have a high inductive effect, led

to difficult degradation over the whole molecule. The type of reactions in degradation process was reduced by increasing heating rate. Also, the kinetic parameter values are directly attached with heating rates. The computational studies also assert on the great influence for the substituents on many significant features of the compound. The physical parameters calculated over optimized structures showed a great difference in between derivatives in coinciding with various substituents. The best features were obtained for derivative E which

includes a highly inductive substituent (SO_2NH_2). Molecular docking against DNA was also tested and the inhibition energy parameters were estimated over docked complexes. Also, the inhibition activity was recorded with derivative E. So promising biological activity can be predicted with one derivative among all. This result asserted on the significant influence of substituents although the moiety of compounds used is fixed.

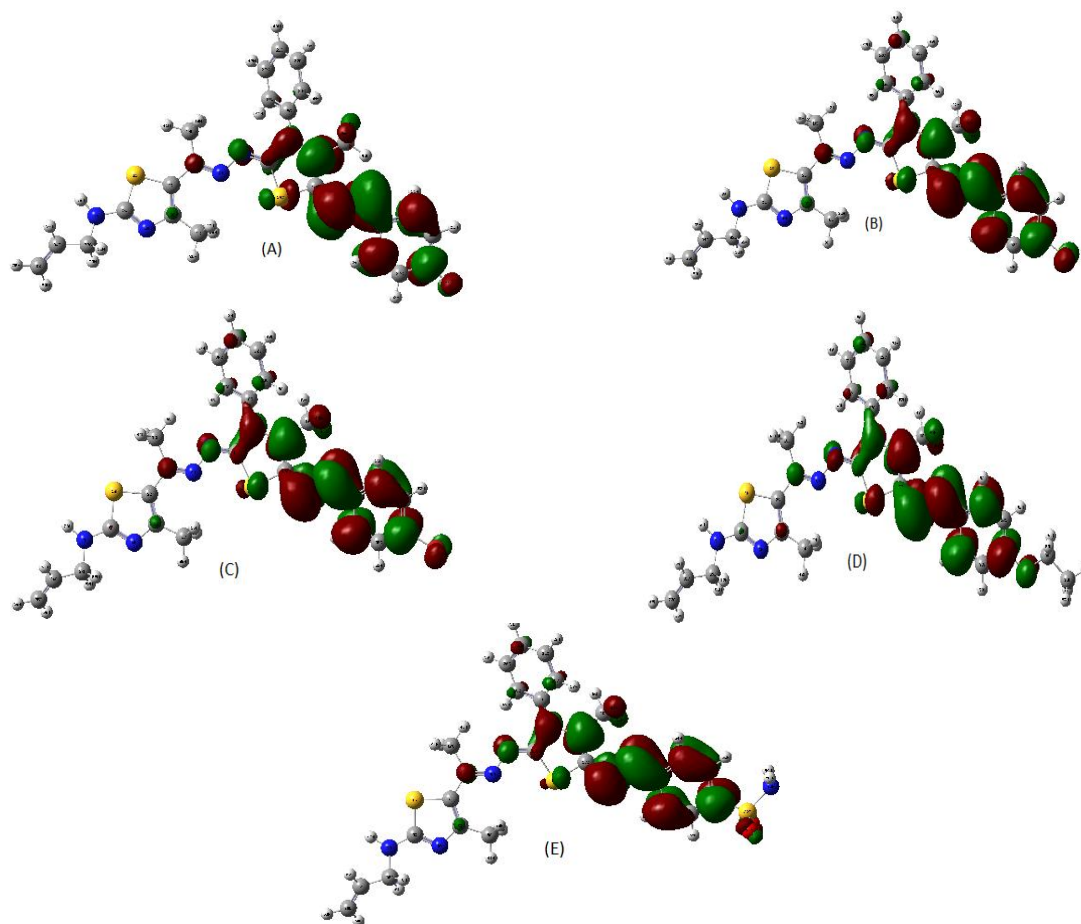


Fig. 5. Frontier LUMO level of arylazobithiazolyhydrazone derivatives (A-E).

Table 6. Docking energy values (k cal/mol) for new arylazobithiazolyhydrazones- DNA receptor (2hio) complexes

Comp.	Est. free energy of binding	Est. inhibition constant (K_i) (μM)	vdW+ bond+ desolve energy	Electrostatic energy	Total intercooled energy	Frequency	Interact surface
A	-6.28	24.72	-8.53	+0.03	-8.50	10%	1128.309
B	-6.82	10.10	-8.98	-0.12	-9.10	10%	1131.124
C	-6.07	35.31	-8.52	+0.06	-8.46	10%	1126.701
D	-6.13	32.17	-8.72	-0.10	-8.82	10%	1147.885
E	-5.86	50.34	-8.50	-0.04	-8.54	20%	1190.344

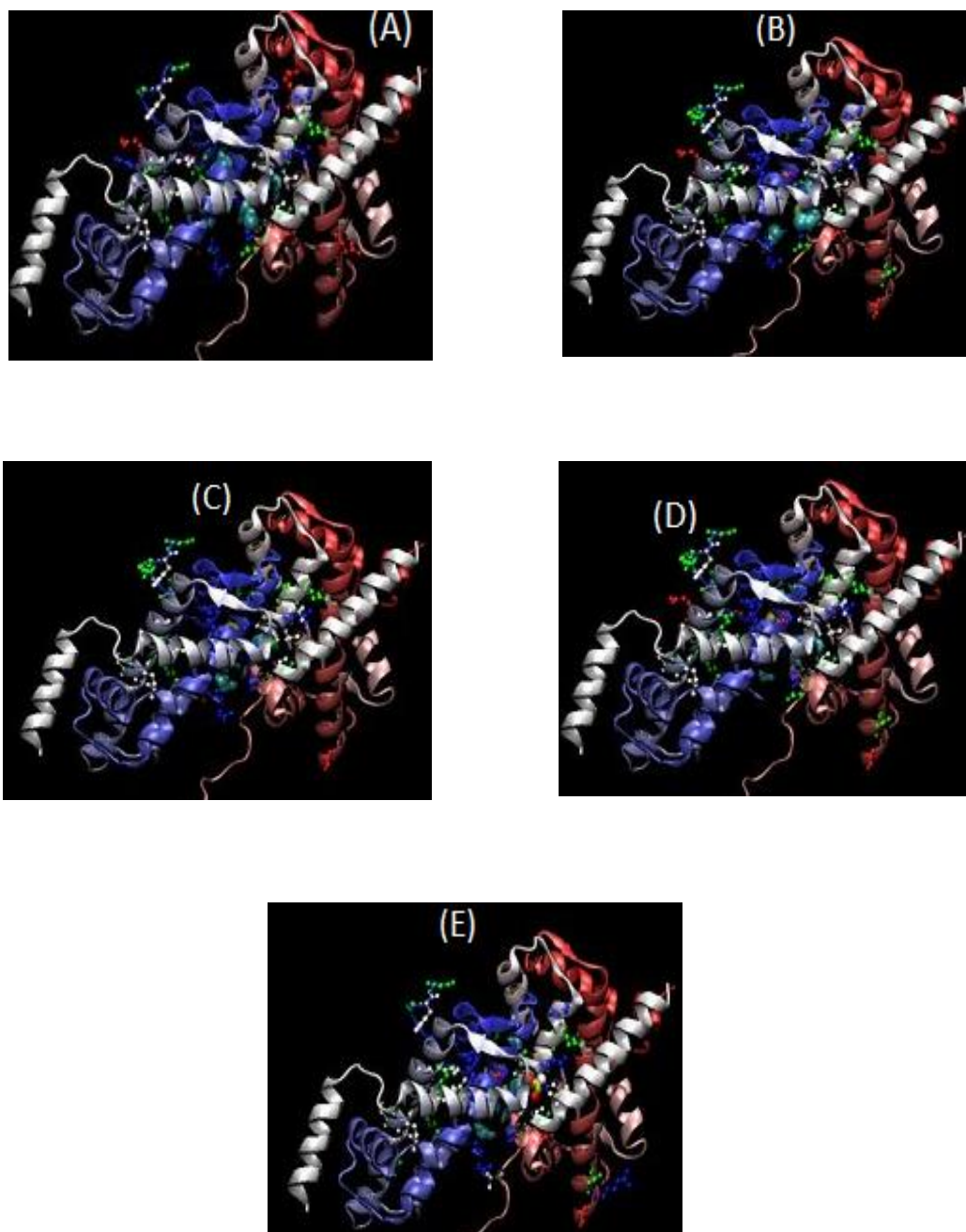


Fig. 6. The docking complexes of arylazobithiazolyhydrazone derivatives (A-E) with DNA protein receptor (2hio)

REFERENCES

1. W. Hussein, G.T. Zitouni, *MOJ Bioorg. Org. Chem.*, **2**, 52 (2018).
2. N. Siddiqui, M.F. Arshad, W. Ahsan, M.S. Alam, *Int. J. Pharm. Sci. Drug. Res.*, **1**, 136 (2009).
3. N. Singh, S.K. Bhati, A. Kumar, *Eur. J. Med. Chem.*, **43**, 2597 (2008).
4. N. Vasu, B.B.K. Goud, Y.B. Kumari, B. Rajitha, *Rasayan J. Chem.*, **6**, 201 (2013).
5. G. Turan-Zitouni, P. Chevallet, F.S. Kilic, K. Erol, *Eur. J. Med. Chem.*, **35**, 635 (2000).
6. E.L. Luzina, A.V. Popov, *Eur. J. Med. Chem.*, **44**, 4944 (2009).
7. R.K. Rawal, R. Tripathi, S.B. Katti, C. Pannecouque, E. De-Clercq, *Eur. J. Med. Chem.*, **43**, 2800 (2008).
8. T. Iino, D. Tsukahara, K. Kamata, K. Sasaki, S. Ohyama, H. Hosaka, T. Hasegawa, M. Chiba, Y. Nagata, J.Eiki, T. Nishimura, *Bioorg. Med. Chem.*, **17**, 2733 (2009).
9. A. Satoh, Y. Nagatomi, Y. Hirata, S. Ito, G. Suzuki, T. Kimura, S. Maehara, H. Hikichi, A. Satow, M. Hata, H. Ohta, H. Kawamoto, *Bioorg. Med. Chem. Lett.*, **19**, 5464 (2009).
10. G. Verma, A. Marella, M. Shaquiquzzaman, M. Akhtar, M.R. Ali, M.M. Alam, *J. Pharm. Bioallied Sci.*, **6**, 69 (2014).

11. S. Rollas, S.G. Kucukguzel, *Molecules*, **12**, 1910 (2007).
12. I. Hussain, A. Ali, *J. Phytochemistry Biochem.*, **1**, 1 (2017).
13. M. Abdelmotaal, A. Nabil, *European Chemical Bulletin*, **7**, 280 (2019).
14. G. Graser-Loescher, A. Schoenhuber, C. Ciglenec, S. Eberl, G. Krupitza, R.M. Mader, S.S. Jadav, V. Jayaprakash, M. Fritzer-Szekeres, T. Szekeres, P. Saiko, *Food Chem. Toxicol.*, **108**, 53(2017).
15. C. Boldron, I. Van der Auwera, C. Deraeve, H. Gornitzka, S. Wera, M. Pitić, F. Van Leuven, B. Meunier, *ChemBioChem.*, **6**, 1976 (2005).
16. S. Ayton, P. Lei, A.I. Bush, *Free Radic. Biol. Med.*, **62**, 76 (2013).
17. L.N. Suvarapu, A.R. Somala, J.R. Koduru, S.O. Baek, V.R. Ammireddy, *Asian J. Chem.*, **24**, 1889 (2012).
18. B.B. Holló, J. Magyar, S. Armaković, G.A. Bogdanović, M.V. Rodić, S. J. Armaković, J. Molnár, G. Spengler, V. M. Leovac, K.M. Szécsényi, *New J. Chem.*, **40**, 5885 (2016).
19. S.S. Kumar, S.Biju, V. Sadasivan, *J. Mol. Struct.*, **1156**, 201 (2018).
20. A.B. Thomas, R.K. Nanda, L.P. Kothapalli, S.C. Hamane, *Arab. J. Chem.*, **9**, 79 (2016).
21. I.H. Hall, S.Y. Chen, K.G. Rajendran, D.X. West, *Appl. Organomet. Chem.*, **10**, 485 (1996).
22. U. Kulandaivelu, V.G. Padmini, K. Suneetha, J.V. Vidyasagar, T.R. Rao, K.N. Jayaveera, A.Basu, V. Jayaprakash, *Arch. Pharm.*, **344**, 84 (2011).
23. N.A. Mohamed, R.R. Mohamed, R.S., Seoudi, *Int. J. Biol. Macromol.*, **63**, 163 (2014).
24. A. Bartyzel, *J. Therm. Anal. Calorim.*, **131**, 1221 (2018).
25. M.N. Patel, N. H. Patel, P.K. Panchal, D.H. Patel, *Synth. React. Inorg. Met. Org. Nano Met. Chem.*, **34**, 873 (2004).
26. V. K. Aghera, P.H. Parsania, *J. Sci. Ind. Res.* **67**, 1083 (2008).
27. B.J. Gangani, J.P. Patel, P.H. Parsania, *Russian J. Phys. Chem. A*, **89**, 2367 (2015).
28. S. Bondock, A.M. Fouda, *Synth. Commun.*, **48**, 561 (2018).
29. I. Althagafi, M.G.Elghalban, F.A.Saad, J.H. Al-Fahemi, N.M. El-Metwally, S. Bondock, L. Almazroai, K.A. Saleh, G.A. Al-Hazmi, *J. Mol. Liq.*, **242**, 662 (2017).
30. G.A. Bain, J.F. Berry, Diamagnetic Corrections and Pascal's Constants, *J. Chem. Educ.*, **85**, 532 (2008).
31. E.S. Freeman, B. Carroll, *J. Phys. Chem.*, **62**, 394 (1958).
32. A.W. Coats, J.P. Redfern, *Nature*, **201**, 68(1964).
33. T. Ozawa, *Bull. Chem. Soc. Japan*, **38**, 1881 (1965).
34. W.W.Wendlandt, *Thermal Methods of Analysis*, New York, Wiley, 1974.
35. J.H. Flynn, *J. Therm. Anal. Calorim.*, **27**, 95 (1983).
36. P. Kofstad, *Nature*, **179**, 1362 (1957).
37. H.W. Horowitz, G.A. Metzger, *Anal. Chem.*, **35**, 1464 (1963).
38. X. Wu., A.K. Ray, *Phys. Rev. B.*, **65**, 85403(2002).
39. M. J. Frisch et al., *Gaussian 09*, Revision D, Gaussian Inc., Wallingford, CT (2010).
40. R.K. Ray, G.R. Kauffman, *Inorg. Chem. Acta*, **173**, 207 (1990).
41. R.C. Chikate, S.B. Padhye, *Polyhedron*, **24**, 1689 (2005).
42. R. Dennington, T. Keith, J. Millam .Gauss View, Version 4.1.2, SemichemInc, Shawnee Mission, KS, 2007.
43. M.M. Al-Iede, J. Karpelowsky, D.A. Fitzgerald, *Pediatr. Pulmonol.*, **51**, 394 (2016).
44. T.A. Halgren, *J. Comput. Chem.*, **17**, 490 (1998).
45. G.M. Morris, D.S. Goodsell, R.S. Halliday, R. Huey, W.E. Hart, R.K. Belew, A.J. Olson, *J. Comput. Chem.*, **19**, 1639 (1998).
46. D.S. Solis, R.J.B. Wets, *Math. Oper. Res.*, **6**, 19 (1981).
47. M.A. Sheraz, S.H. Kazi, S. Ahmed, Z. Anwar, I. Ahmad, *Beilstein J. Org. Chem.*, **10**, 1999 (2014).
48. Z. Razaczynska, A. Danczowska-Burdon, J. Sienkiewicz-Gromiuk, *J. Therm. Anal. Calorim.*, **101**, 671 (2010).
49. M. Juha'sz, Y. Kitahara, S. Takahashi, T. Fujii, *Anal. Lett.*, **45**, 1519 (2012).
50. U. El-Ayaan, N.M. El-Metwally, M.M. Youssef, S. A.A. El Bialy, *Spectrochim. Acta A*, **68**, 1278 (2007).
51. S.K. Tripathi, R. Muttineni, S.K. Singh, *J. Theor. Biol.*, **334**, 87 (2013).
52. C. Fosset, B.A. McGaw, M.D. Reid, *J. Inorg. Biochem.*, **99**, 1018 (2005).
53. N. Terakado, S. Shintani, Y. Nakahara, *Oncol. Rep.*, **7**, 1113 (2000).

Adsorption of bisphenol A and phenoxyacetic acid onto new polymeric adsorbents

G. Akdut¹, F. Bildik², H. Duran¹, A. Tuna³, T. Şişmanoğlu^{1*}, B. F. Şenkal^{2*}

¹Department of Chemistry, Faculty of Engineering, Istanbul University-Cerrahpaşa, Avcılar, Istanbul, Turkey;

²Department of Chemistry, Faculty of Science and Letters, Istanbul Technical University, Maslak, Istanbul, Turkey;

³Institute of Inorganic Chemistry, Johannes Kepler University Linz (JKU), Altenbergerstrasse 69, 4040 Linz, Austria

Received January 4, 2019; Revised May 30, 2019

New quaternary amine-containing resins were prepared and used for adsorption of phenoxyacetic acid (PAC) and bisphenol A (BPA). For this purpose, crosslinked poly (glycidyl methacrylate (GMA)-co-ethylene glycol dimethacrylate (EGDMA)) beads (PGMA) were prepared and modified with N,N-diethylethylenediamine to obtain tertiary amine function carrying (BR) resin. Other quaternary amine function carrying resins were prepared starting from crosslinked poly (vinyl benzyl chloride (VBC)-co-EGDMA) (PVBC) resin. PVBC resin was reacted with imidazole and ethyl piperazine to obtain imidazole- and ethyl piperazine-modified resins, respectively. Then, these resins were reacted with chloroacetamide to prepare quaternary amine resins, PVBCIM (quaternized imidazole modified PVBC), PVBCEP (quaternized ethylpiperazine PVBC). The adsorption isotherm experiments of adsorbed pesticides on the new polymeric resins were performed at 25°C by using Freundlich and Langmuir models. The maximum BPA sorption capacities of the new polymeric adsorbents were obtained as BR>PVBCEP>PVBCIM, respectively. For PAC, the adsorption maximum capacities of the new polymeric adsorbents changed to PVBCEP>PVBCIM>BR. Characterization of adsorbents was performed by SEM and FTIR method before and after adsorption experiments. The adsorption kinetics of pesticides was studied depending on temperature (25°C-40°C) and also kinetic models were applied such as pseudo-first order, corrected-second order and intraparticle diffusion model.

Keywords: Bisphenol A; Phenoxyacetic acid; Pesticide; Adsorption; Polymeric resin.

INTRODUCTION

Environmental pollution increases day by day in a proportion of the population and the industrial development increases. This contamination is mainly caused by the mixing of organic and inorganic chemicals into the groundwater. The increased uses of pesticides in agriculture to control insects increasingly pollute water resources. Since the pesticide structures are rarely biodegradable, this effect is highly pollutant to the environment and some carcinogenic properties for living organisms are observed as well [1]. The use of phenolic materials in pesticides made them harmful to organisms even at low concentrations. They are considered as primary pollutants and classified as hazardous to people's health. Even though the amount of contamination with phenolic materials in drinking water is 0.005 ppm, it causes some significant problems of taste, odor and loss of suitability for use [2].

Bisphenol A (BPA) plays an important role because of its widespread usage in materials as a component of industrial polymers and fungicides [3]. The effect of toxicity of BPA is really serious for freshwater and salty algae, invertebrates and fish. Bisphenol A has been listed by China and the EPA as the main pollutant for the aquatic environment due to its stability, bioaccumulation and toxicity [4]. Wang *et al.* (2015) used modified

montmorillonite to control interfacial hydrophobicity with an improved matrix. The inner layer hydrophilic properties of the clay molecules, the inner layer chelating properties of the alkyltrimethylammonium ions and their adsorption balance with BPA were investigated in details and the BPA concentration level was observed as the inner layer chelate chain length predicted to increase [5]. Mao *et al.* (2014) synthesized a surface-active polymer on modified kaolin and selectively studied adsorption of BPA, 4,4-biphenyldiphenol and 2,6-dichlorophene. It was thought that the chemical process could be also involved in this study as a rate-limiting step for BPA adsorption. This synthesized polymer had proven to have high affinity and selectivity for BPA compared to other components [6]. Zainab *et al.* (2015) used coconut fiber, coconut shell and durian fruit husk from organic agricultural wastes for BPA removal. All three adsorbents showed similar low adsorption. The optimum adsorption time was found to be 24 h [7]. Soni and Padmaja (2014) used active carbon from the palm kernel as adsorbent and investigated the effect of variable pH, concentration, time and temperature parameters. It was found that the adsorption process was spontaneous and exothermic and there was a weak physical interaction between adsorbents. The disadvantage was the quite costly and difficult work and impossibility to recycle [8]. Other similar

* To whom all correspondence should be sent:

E-mail: tusase@istanbul.edu.tr bsenkal@itu.edu.tr

studies in the literature until today were done with polymeric adsorbent [9], nanotube [10], graphene [11], lignin [12], mesoporous silicon dioxide [13], activated sludge [14], modified zeolite [15], chitin [16].

Phenoxy acid belongs to a class of herbicides which exhibits auxin-like activities in excessive use for the control of broad-leaved weeds growing in products such as rice, winter wheat, soya bean, long grass. Phenoxy acetic acid (PAC) is highly toxic and it can be irritant to the skin and eyes. Prolonged exposure may cause serious damage to internal organs and biological systems. It can be transported in the agricultural ecosystem causing pollution in surface and ground waters, because of its water solubility. Young *et al.* (2006) studied the removal of CPA (chlorophenoxyacetic acid), MCPA (4-chloro-2-methylphenoxyacetic acid) with activated carbon [17]. Aksu *et al.* (2004) investigated the removal of 2,4-dichlorophenoxyacetic acid used by activated granular carbon depending on pH, temperature and initial concentration [18]. Moustapha *et al.* (2000) also worked on removal of 2,4-dichloro-phenoxyacetic acid with two different activated carbons in terms of contact time, adsorbent dose, effect of ionic strength, pH variables [19]. Cserhati *et al.* (1998) studied 2,4-dichlorophenoxyacetic acid, 2,4,5-trichlorophenoxyacetic acid, 4-chloro-2-methylphenoxyacetic acid, 2,4-dichlorophenol, 2,4,5-trichlorophenol and p-chlorocresol pesticides [20].

In this study, quaternized amine- and tertiary amine-modified resins were used for removal of pesticides such as bisphenol A (BPA) and phenoxyacetic acid (PAC). Adsorption kinetics of pesticides on the resins was studied at constant concentration from 25°C to 40°C. The sorption experiments of the pesticide were studied with different concentrations at 25°C. The adsorption isotherms were fitted to Langmuir and Freundlich models. SEM and FTIR characterization methods were used to evaluate both sorbent resins and pesticide.

EXPERIMENTAL

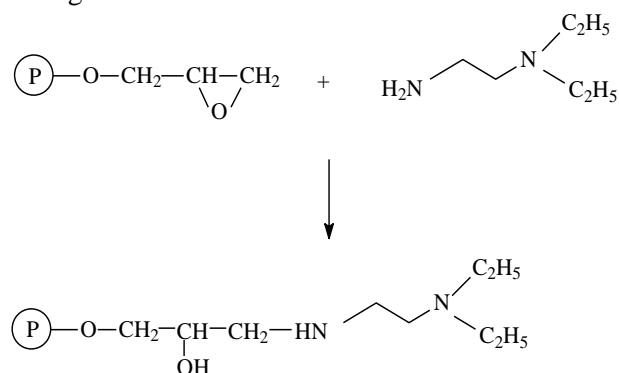
Materials

BPA and PAC were purchased from Sigma-Aldrich and Merck companies. The stock solutions were prepared in aqueous media as 114.12 ppm for BPA and 760 ppm for PAC. The maximum wavelengths of BPA and PAC were determined in aqueous solution, respectively 227 and 276 nm. Glycidyl methacrylate (GMA), ethylene glycol dimethacrylate (EGDMA), ethyl piperazine, imidazole, vinyl benzyl chloride and 2-

chloroacetamide were purchased from Sigma-Aldrich.

Synthesis of the resins

Preparation of BR resin (N,N-diethylethylenediamine modified GMA-EGDMA). Tertiary amine modified methacrylate based resin was synthesized by modification of crosslinked PGMA resin. This resin was prepared starting from copolymerization of GMA (glycidyl methacrylate) (90% mol) and EGDMA (ethylene glycol dimethacrylate) (10% mol) as monomers in the presence of AIBN (azobisisobutyronitrile) as initiator, polyvinylpyrrolidone as stabilizer and toluene as porogen by using suspension polymerization method [21]. In the second step, 5 g of PGMA resin were added in portions to the excess of N,N-diethylethylenediamine in 50 mL of N-methyl-1-pyrrolidone (NMP). The mixture was continuously shaken on a shaker for 24 h at room temperature and heated at 80°C for 2 h. Then, the reaction mixture was cooled and poured into 250 mL of distilled water. Tertiary amine modified resin was filtered and washed with excess of water and 150 ml of methanol, respectively. The obtained resin (BR) was dried under vacuum at room temperature for 24 h (Scheme 1). The yield was 7.59 g.



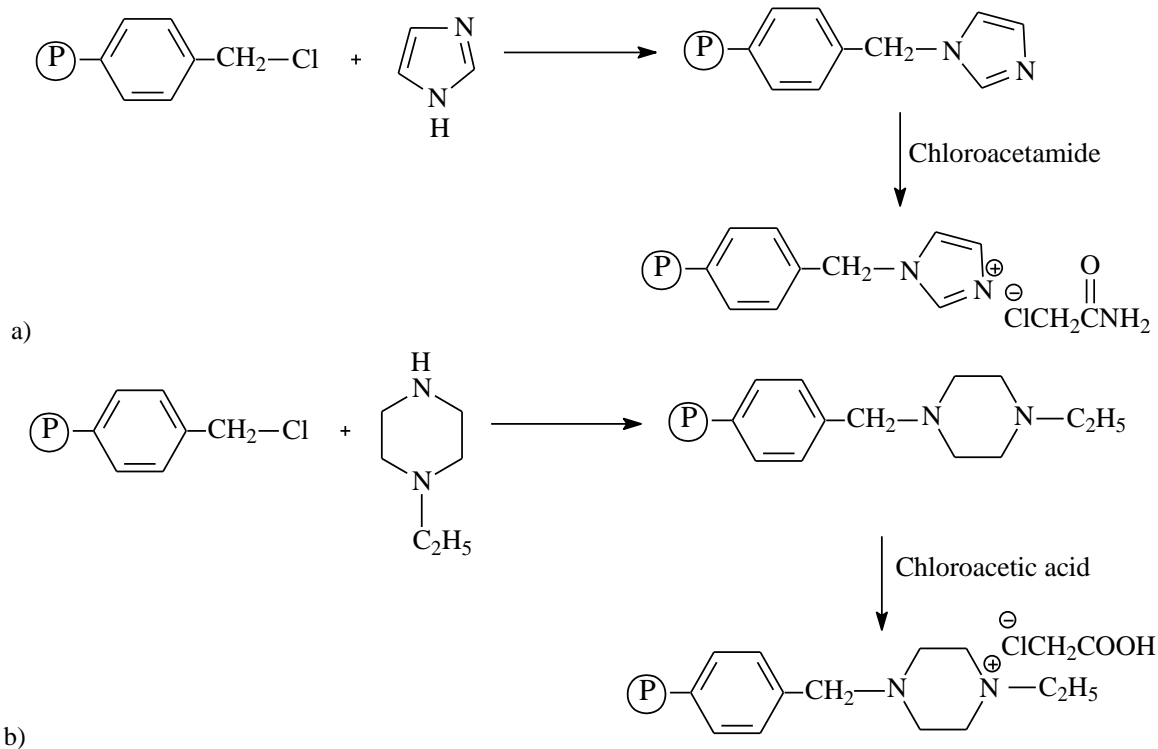
Scheme 1. Structure of BR resin molecule

Preparation of PVBCIM and PVBCEP resins. These resins were prepared starting from modification of crosslinked poly (vinyl benzyl chloride) (PVBC) described in the literature [22]. 5.0 g of PVBC resin was added to 2.50 g of imidazole in 50 ml of NMP and 15 ml of ethyl piperazine solution in 30 ml of NMP at 0°C to obtain imidazole- and ethyl piperazine-modified PVBC, respectively. The reaction mixtures were continuously shaken with a shaker at room temperature for 24 h. Then, the reaction contents were poured into 1 L of water, filtered and washed with excess of water and methanol, respectively. The resins were dried under vacuum at room

temperature for 24 h and the yields were found as 5.8 g for PVBCIM and 8.4 g for PVBCEP.

Quaternization of PVBCIM and PVBCEP. PVBCIM was quaternized with chloroacetamide. For this purpose, 5.0 g of PVBCIM was reacted with 3.5 g of chloroacetamide in 25 ml of DMF solution. The reaction mixture was stirred at room

temperature for 24 h. The reaction mixture was heated at 70°C for 8 h. Then, the reaction mixture was filtered and washed sequentially with DMF, water and ethanol. The quaternized (PVBCIM) resin was filtered and dried under vacuum at room temperature for 24 h to give 7.20 g of the final product (Scheme 2a).



Scheme 2. a) Preparation of quaternized PVBCIM resin; b) Preparation of quaternized PVBCEP resin

Quaternization of PVBCEP was performed by chloroacetic acid. According to the procedure, 18.9 g of chloroacetic acid (0.20 mol) was dissolved in 20 ml of water and this solution was dropped by a dropping funnel into 13.8 g of K_2CO_3 (0.1 mol) in 25 ml of distilled water at 0 °C. Then, 5 g of PVBCEP was added to the solution. The reaction mixture was continuously shaken on the shaker for 48 h at room temperature and was stirred at 70°C for 3 h. At the end of the reaction, quaternized resin (PVBCEP) was filtered and washed with excess of water. PVBCEP was dried under vacuum at room temperature for 24 h. The yield was found as 7.0 g (Scheme 2b).

Adsorption experiments

Preparation of working solutions from the BPA and PAC stock solutions: working BPA solutions were prepared in five different concentrations between 8.67 ppm and 22.5 ppm for the isotherm studies. In the kinetic studies, optimum BPA concentration was chosen as 17.11 ppm. The concentrations of PAC varied from 38 ppm to 380 ppm for the isotherm studies. The best

concentration of PAC for the kinetic studies was chosen to be 121.7 ppm. In adsorption experiments, 0.01 g of resin sample was reacted with 10 mL of pesticide solution for 90 min at 25°C and aliquots were taken every 15 min for spectrophotometric analysis.

Adsorption studies

Adsorption capacity of the sorbents ($mg\ g^{-1}$) was calculated using the following equation (1):

$$q_d = \frac{c_o - c_d}{W} \times V \quad (1)$$

where c_o and c_d are the initial and equilibrium concentration of pesticide, respectively ($mg\ L^{-1}$), W is the weight of sorbent (g), V is the volume of pesticide solution (L). V/W ratio was held as $1\ L\ g^{-1}$ during adsorption isotherm experiments [23].

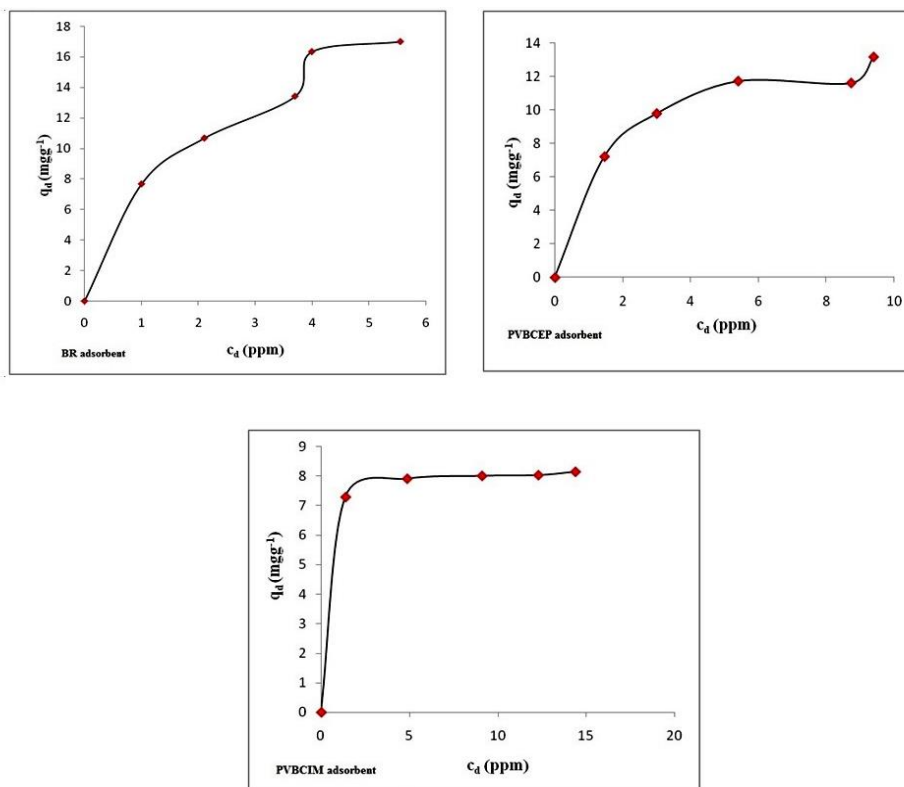


Figure 1. Giles isotherms of BPA (L type)

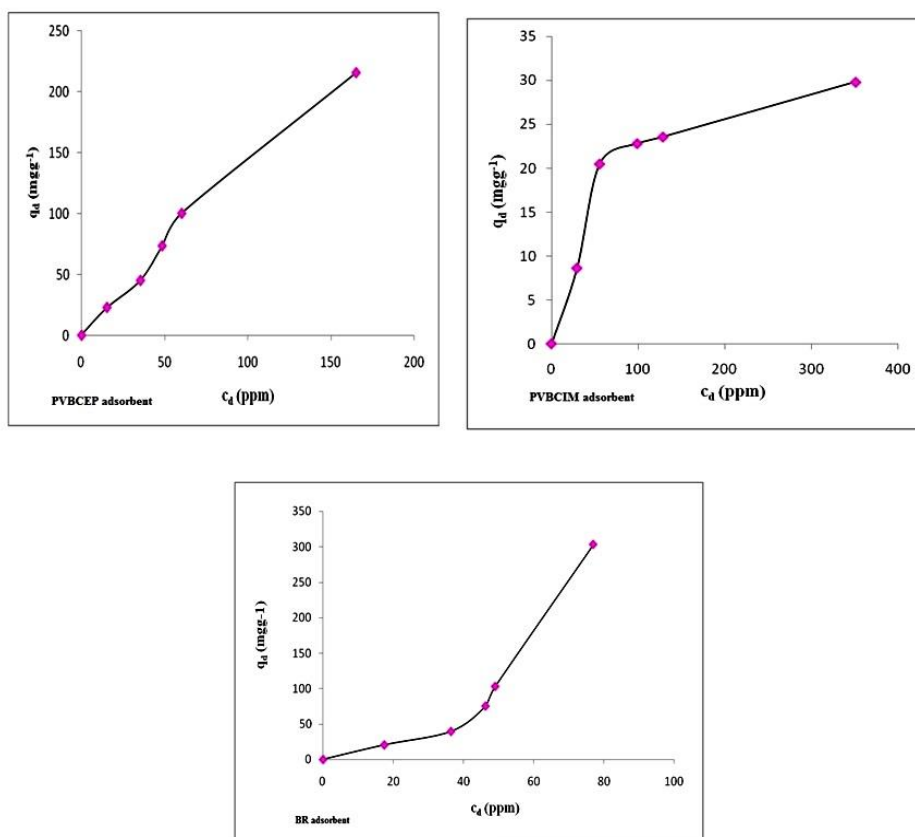


Figure 2. Giles isotherms of PAC (S type)

Table 1. Adsorption isotherm parameters of resins for BPA

Isotherms	PVBCEP	BR	PVBCIM
Freundlich			
K_F	6.77	7.61	7.25
n	0.29	0.48	0.05
R^2	93	97	95
Langmuir			
$b \text{ L mg}^{-1}$	0.676	0.53	593
$q_{\max} \text{ mg g}^{-1}$	14.55	21.7	8.13
R^2	98	99	97

Table 2. Adsorption isotherm parameters of resins for PAC

Isotherms	PVBCEP	BR	PVBCIM
Freundlich			
K_F	1.55	0.097	1.97
n	0.95	1.78	0.5
R^2	98	92	88
Langmuir			
$b \text{ L mg}^{-1}$	0.00195	-0.0083	0.00759
$q_{\max} \text{ mg g}^{-1}$	769	-118	48.31
R^2	98	95	98

Adsorption isotherms

The results of the adsorption studies of BPA and PAC were expressed by Freundlich and Langmuir isotherm models. Adsorption isotherm type graphics of BPA were drawn as q_e vs c_e as seen in Figure 1. The Giles isotherm lines of BR, PVBCEP and PVBC IM appear to be the same as L3, L4 and L2 types, respectively. For PAC, Giles isotherm types of PVBCEP, PVBC and BR were found L4, L3 and S3, respectively in Figure 2 [24]. These L types suggest that first monolayer line and then multilayer line occurs during adsorption process. This S type indicates that the adsorption of pesticide was reluctant onto the adsorbates.

Langmuir isotherm: The Langmuir equation is represented as follows:

$$\frac{1}{q_d} = \frac{1}{q_{\max} b C_d} + \frac{1}{q_{\max}} \quad (2)$$

where C_d gives a straight line, q_{\max} , is the maximum adsorption at monolayer coverage (mol g^{-1}) and b the adsorption equilibrium constant (L

mol^{-1}). $1/q_d$ vs $1/c_d$ with slope b and intercept $1/q_{\max}$ is obtained (Tables 1, 2).

Freundlich isotherm: The Freundlich isotherm model can be applied by the following:

$$q_d = K_F c_d^n \quad (3)$$

The linear equation of the Freundlich isotherm is fitted in the logarithmic form as given below:

$$\log q_d = \log K_F + n \log c_d \quad (4)$$

where: q_d is the amount adsorbed (mol g^{-1}), C_d the equilibrium concentration in aqueous phase (mol L^{-1}) K_F and n are Freundlich constants related to adsorption capacity and adsorption intensity.

Kinetic studies

The kinetics of BPA and PAC were studied at four different temperatures. The concentrations of BPA and PAC used in the kinetic experiments were 17.11 and 121.7 ppm, respectively. In order to investigate the kinetics of pesticides adsorption, pseudo-first-order and pseudo-second-order models were examined (Tables 3-8).

Table 3. Kinetic parameters of the aqueous solution of BPA on PVBCEP resin.

t ⁰ C	q _d exp.	q _{d1} calc.	k ₁ / dk ⁻¹	R ²	q _{d2} calc.	k ₂ / g mg ⁻¹ dk ⁻¹	R ²	k _i / mg g ⁻¹ dk ^{-1/2}	R ²
25	0.0105	0.0087	0.0197	83	0.009	3.2	99.2	0.0003	98.7
								0.0014	97
								0.0007	95
35	0.0088	0.0072	0.0175	81	0.008	8.56	99.8	0.0004	99
								0.0019	100
40	0.0038	0.0036	0.0233	92	0.004	9.34	99.9	0.0004	96
								0.0007	100

Table 4. Kinetic parameters of the aqueous solution of BPA on BR resin.

t ⁰ C	q _d exp.	q _{d1} calc.	k ₁ / dk ⁻¹	R ²	q _{d2} calc.	k ₂ / g mg ⁻¹ dk ⁻¹	R ²	k _i / mg g ⁻¹ dk ^{-1/2}	R ²
25	0.014	0.0019	0.0357	95	0.0137	4.81	99.9	0.0001	98.7
								0.0002	97
30	0.0116	0.0032	0.0255	88	0.012	13	99.8	0.0003	94
35	0.0084	0.0042	0.0245	85	0.0081	15.4	99.7	0.0001	97
								0.0007	99.8
40	0.0098	0.0054	0.068	90	0.01	28.4	99.9	0.0003	98

Table 5. Kinetic parameters of the aqueous solution of BPA on PVBCIM resin.

t ⁰ C	q _d exp.	q _{d1} calc.	k ₁ / dk ⁻¹	R ²	q _{d2} calc.	k ₂ / g mg ⁻¹ dk ⁻¹	R ²	k _i / mg g ⁻¹ dk ^{-1/2}	R ²
25	0.007	0.0083	0.0315	94	0.0081	31.87	98.9	0.0008	98
30	0.0045	0.002	0.0167	80	0.0041	41.85	97.9	0.0001	99.5
								0.0006	100
35	0.0037	0.0016	0.0342	96	0.0037	54.16	98.5	0.0002	99.7
40	0.0021	0.0072	0.0231	91	0.002	113	98.7	0.00007	98

A linear form of pseudo-first-order equation of Lagergren is generally expressed as:

$$\ln (q_d - q_t) = \ln q_d - kt \quad (5)$$

where: k₁ is first order adsorption rate constant (min⁻¹), q_t is amount of adsorbed material at time t (mg g⁻¹), q_d is amount of adsorbed material in equilibrium (mg g⁻¹).

The kinetic data were treated with the following Ho's pseudo-second-order rate equation [25]. The linear form of the equation describing the adsorption kinetics by the pseudo-second-order model is as follows:

$$\frac{t}{q_t} = \frac{1}{h} + \frac{t}{q_d} \quad h = k_2 q_d^2 \quad (6)$$

h (mg g⁻¹ min⁻¹) gives the initial sorption rate. If a graph of t/q_t vs t is drawn, q_d and k₂ are calculated

from the slope and cut-off points [26], where q_d is the amount of pesticide adsorbed at equilibrium (mg g⁻¹); q_t is the amount of pesticide adsorbed at time t (mg g⁻¹); and k₂ is the equilibrium rate constant of pseudo-second-order sorption (g mg⁻¹ min⁻¹). The q_d and k₂ values could be calculated from the slopes (1/q_d) and intercepts (1/k₂q_d²) of the linear plots of t/q_t vs t. The intraparticle diffusion constant is given by Weber and Morris as follows [27]:

$$q_t = k_i t^{1/2} + C \quad (7)$$

where: q_t: amount of adsorbate at any time (mg/g), k_i: intraparticle diffusion rate constant (mg g⁻¹min^{-1/2}), t: time (min). Therefore, k_i value is determined with this equation by plotting a graph of q_t vs t^{1/2}.

Table 6. Kinetic parameters of the aqueous solution of PAC on PVBCEP resin.

t ^o C	q _d exp.	q _{d1} calc.	k ₁ / dk ⁻¹	R ²	q _{d2} calc.	k ₂ / g mg ⁻¹ dk ⁻¹	R ²	k _i / mg g ⁻¹ dk ^{-1/2}	R ²
25	0.0326	0.024	0.024	93	0.033	5.1	99	0.0026	98.9
								0.0033	97
30	0.038	0.027	0.0187	80	0.034	4.04	98.9	0.0004	98.7
								0.0046	97
35	0.0233	0.016	0.0415	98.9	0.0255	2.32	99.9	0.0028	98.7
								0.0009	99.7
40	0.0253	0.024	0.0224	92	0.024	2.18	99.3	0.0015	97

Table 7. Kinetic parameters of the aqueous solution of PAC on BR resin.

t ^o C	q _d exp.	q _{d1} calc.	k ₁ / dk ⁻¹	R ²	q _{d2} calc.	k ₂ / g mg ⁻¹ dk ⁻¹	R ²	k _i / mg g ⁻¹ dk ^{-1/2}	R ²
25	0.06	0.055	0.0493	95	0.067	3	99.7	0.0046	98
30	0.043	0.0135	0.0255	92	0.042	6.51	98.5	0.0013	98
35	0.0355	0.0089	0.0301	96	0.035	11.5	98.9	0.0011	96
40	0.045	0.0028	0.0366	95	0.044	20	99	0.0003	.7

Table 8. Kinetic parameters of the aqueous solution of PAC on PVBCIM resin.

t ^o C	q _d exp.	q _{d1} calc.	k ₁ / dk ⁻¹	R ²	q _{d2} calc.	k ₂ / g mg ⁻¹ dk ⁻¹	R ²	k _i / mg g ⁻¹ dk ^{-1/2}	R ²
25	0.0174	0.011	0.0315	93	0.018	5.56	99.9	0.0011	96.3
30	0.026	0.0078	0.0288	85	0.0264	7.76	99.7	0.0001	98.7
								0.0013	99.8
35	0.0055	0.0048	0.0233	88	0.0056	8.2	98.4	0.0004	95
40	0.0156	0.0053	0.0327	97	0.0158	17.5	99.2	0.0009	98.7
								0.0004	98.3

RESULTS AND DISCUSSION

In this study, three polymeric sorbents were prepared to remove BPA and PAC pesticides from water. BR (N,N-diethylethylenediamine modified GMA-EGDMA) was prepared starting from crosslinked PGMA. The latter was prepared by suspension polymerization of GMA monomer using EGDMA as crosslinking agent, AIBN as initiator and PVP as stabilizer at 65 °C for 5 h. PGMA resin was reacted with excess of N,N-diethylethylenediamine to obtain tertiary amine-modified resin (BR) PVBC resin was added to NMP in imidazole and ethyl piperazine solution in NMP at 0°C to obtain imidazole- and ethyl piperazine-modified PVBC, respectively. The resins were dried under vacuum at room temperature for 24 h giving PVBCIM and PVBCEP. Then, quaternization of PVBCIM with chloroacetamide and quaternization of PVBCEP with chloroacetic acid was performed.

Characterization

Surface structure of samples before and after chemical modification process, as well as after adsorption with dye compounds was analyzed by scanning electron microscopy (SEM) on FEI Quanta FEG 450.

SEM of BR polymer resin: The SEM photographs were made for the adsorbents that best adsorbed pesticides. As shown in Figure 3a, the surface of the BR adsorbent has partially flat floor. But, budding-like structures were observed in certain of its regions. As shown in Figure 3b, after the adsorption of BPA on BR adsorbent, the flat base changed into cracker layers. The budding was seen to increase and spread in the medium.

SEM of PVBCEP polymer resin: As shown in Figure 4a, the characterization images of the pure PVBCEP define that the adsorbent has a large porous smooth-bottomed structure such as the appearance of gravy cheese. After adsorption of PAC on PVBCEP the structure of the ground and large pores are deteriorated and PAC has retained

the dense and angular clusters on the surface (Figure 4b).

Identification of functional groups existing on the surface of samples (before and after sorption process) was stated by using Fourier transform

infrared spectroscopy (Thermo Scientific Nicolet ID5 ATR FTIR). FTIR interpretations of the new polymeric resins that provide the best adsorption for BPA and PAC are given below.

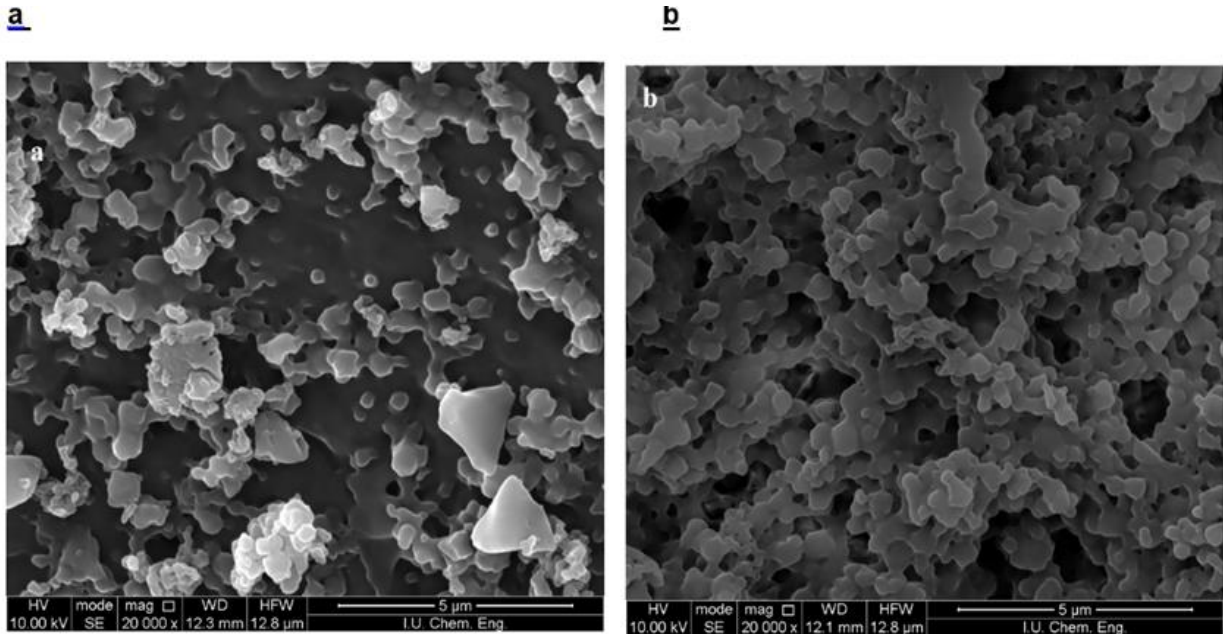


Figure 3. a) SEM image of the pure BR b) SEM image of BR-BPA

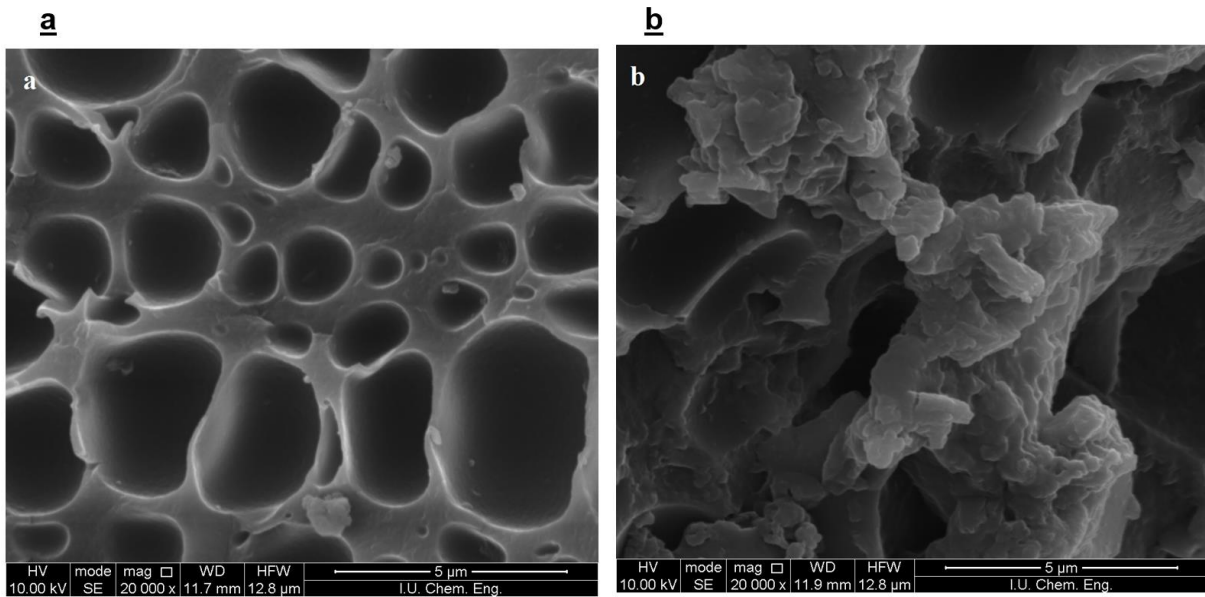


Figure 4. a) SEM image of the pure PVBCEP b) SEM image of PVBCEP-PAC

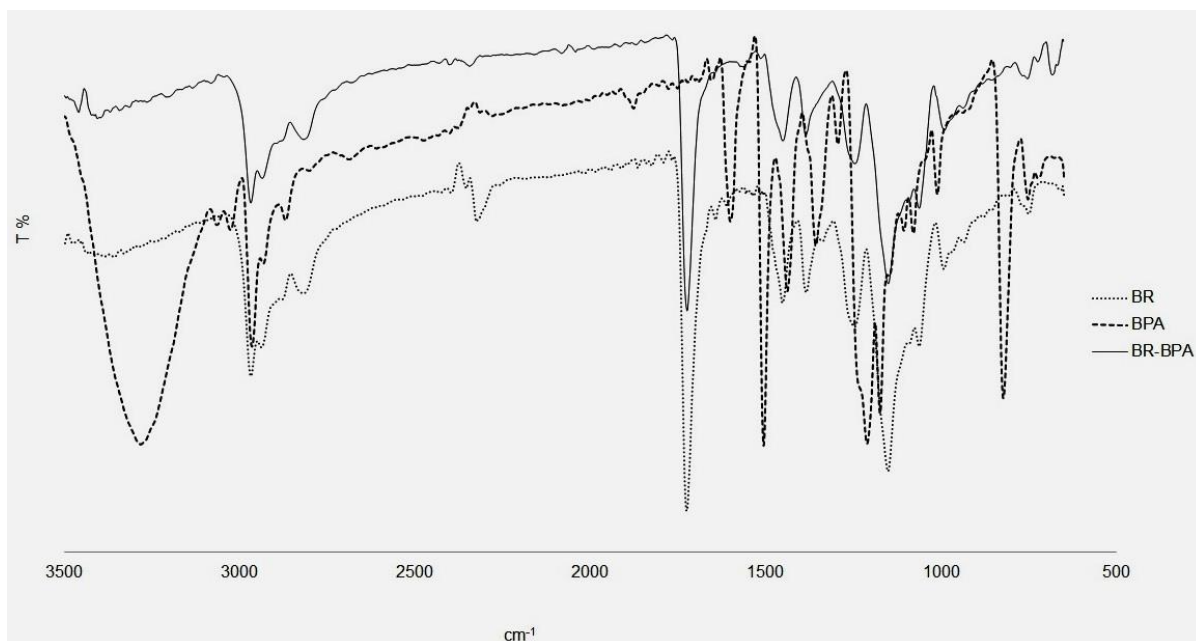


Figure 5. FTIR spectra of adsorption of BPA on BR

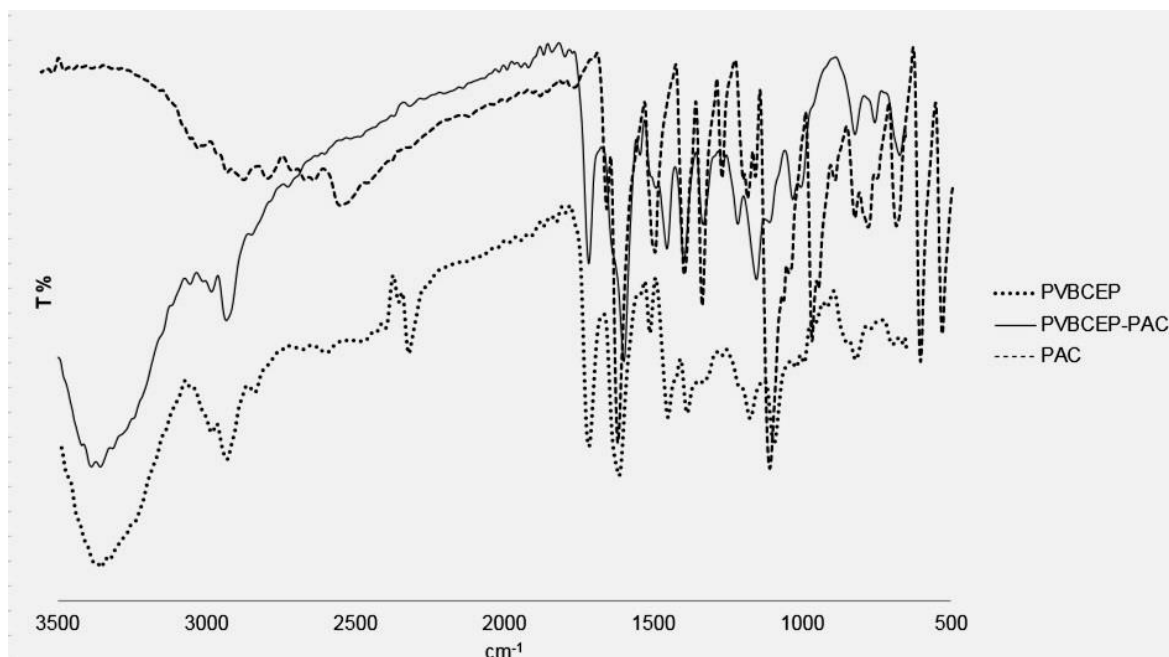


Figure 6. FTIR spectra of adsorption of PAC on PVBCEP

As shown in Figure 5, the IR spectrum of the pure state of the BR polymeric resin shows a strong -OH band peak at 3380 cm^{-1} , and a strong C=O tension band peak at 1663 cm^{-1} in the structure of polyvinylpyrrolidone. The characteristic C-N tension band of the group appears at $1190\text{--}1130\text{ cm}^{-1}$, and the C-H tension band of the methylene group appears at $1485\text{--}1445\text{ cm}^{-1}$. As shown in Figure 5, the BPA material shows the -OH stretching band at 3300 cm^{-1} , the C-H stretch of the aromatic structure at 2967 cm^{-1} . The C-C stretching band appears at 1500 cm^{-1} , the deformation band of isopropyl and methyl groups appears at 1361 cm^{-1} and the

characteristic C-O stretching band on phenol structure appears at 1214 cm^{-1} . Figure 5 also shows that in the pair of BR-BPA after the adsorption the -OH and C-C stretching bands of BPA are not observed in the dual FTIR spectrum. The -OH peak of the BR disappeared in the dual FTIR spectra. We have thought that BPA is adsorbed forming a bond between the -OH group and the adsorbing BR. As shown in Figure 6, in the IR spectrum of the pure state of the PVBCEP polymeric resin, ethylene glycol dimethacrylate (EGDMA) shows the asymmetric stretching band of the methylene group band at 2938 cm^{-1} and the symmetric methylene

group band at 2815 cm^{-1} . Furthermore, the C-N asymmetric stretching bands on the piperazine ring structure exhibit moderate intensity peaks at 1323 cm^{-1} and 1218 cm^{-1} , and the C-N symmetric stretching band appears at 1160 cm^{-1} . For the resin modified with carboxylic acid, O-H band and C=O vibrations bands are observed at 3365 cm^{-1} and 1722 cm^{-1} . As Figure 6 shows, in the pure state of the PAC substance, the OH stretching of COOH vibration is detected at 1750 cm^{-1} , for the structure of PAC at 2550 cm^{-1} . The OH bending band of the carboxylic acids appears at 1435 cm^{-1} and the C-O stretching band - between 1226-1090 cm^{-1} . Also in Figure 6, in the pair of PVBCEP-PAC after the adsorption, the -OH dimer and characteristic -COOH peaks of the PAC do not appear in the dual FTIR spectra. The PVBCEP adsorbent disappeared in the dual FTIR spectra of symmetric methylene and symmetric C-N band peaks. However, O-H and C=O peaks still appear in the adsorbent structure. Here, we have thought that the acid -OH bonds are adsorbed by symmetric C-H and C-N bonds of the piperazine ring.

Adsorption isotherms

Adsorption intensity of BPA onto each of the polymeric resins $n < 1$ was found, as seen in Table 1. The adsorption capacities (K_F) are listed as BR > PVBCIM > PVBCEP. BR was observed to best adsorb the BPA, as seen in Table 1. The average correlation coefficient of adsorption of BPA on BR is 97% for Freundlich isotherm. Table 1 shows that the maximum amount of substance adsorbed in the single layer (q_{max}) is BR > PVBCEP > PVBCIM for the Langmuir isotherm. The average correlation coefficient of adsorption of BPA on BR is 99% for Langmuir isotherm. According to these operating conditions, the highest value of q_{max} for adsorbed BPA on 0.01 g of BR was found to be 21.7 mg g^{-1} . For PAC, the adsorption capacities (K_F) are ranged as PVBCEP > PVBCIM > BR. For both Freundlich and Langmuir the average correlation coefficient of adsorption of PAC on PVBCEP was 98%. The

maximum adsorption at monolayer coverage (q_{max}) was calculated for the adsorption of PAC on PVBCEP as 769 mg g^{-1} , as shown in Table 2. But the value of q_{max} is negative for the adsorption of PAC on BR. This can be explained as follows: negative values for the Langmuir isotherm constants suggest that this model is not suitable to explain the adsorption process because the value of q_{max} is indicative of the surface binding energy and monolayer coverage. As a result, this implies that some heterogeneity in the surface or pores of the polymeric resins will play a weak role in the adsorption of dyes. The isotherm types were S-shaped for $n > 1$, and L-shaped for $n < 1$.

Kinetic and thermodynamic parameters

In this study, the adsorption of BPA and PAC on the polymer resins corresponded to pseudo-second order rate. For pseudo-second order rate, the values of the rate constant increased by increasing the temperature, as seen in Tables 3-8. Intraparticle rate constants were mostly found as k_{i1} and k_{i2} . The first step suggests that diffusion of soluble molecules is directed towards the boundary layer. The second step indicates that gradual adsorption showed diffusion rate of intraparticle at limited places. Thermodynamic parameters were calculated by Arrhenius and Eyring equation [28]. While the values of the free enthalpy change (ΔH°) are positive, the values of the free entropy change (ΔS°) are negative. The negative values of the free entropy change suggest that adsorbate solution in adsorbent is transferred from disorderly to orderly. As a result, adsorption occurred. For BPA, the values of activation energy found are between 52 and 86 kJ/mol (Table 9). For PAC, the values of activation energy are between 48 and 97 kJ/mol (Table 10). These values indicate that physical adsorption occurs. The positive value of free energy exchange indicates that the reaction does not take place spontaneously and this reaction can take place depending on the temperature.

Table 9. Thermodynamic parameter values of BPA adsorbed on polymeric resin.

Adsorbents	$E_a / \text{kJ mol}^{-1}$ (25°C-40°C)	$\Delta H^\circ / \text{kJ mol}^{-1}$ (25°C-40°C)	$\Delta S^\circ / \text{J mol}^{-1}\text{K}^{-1}$ (25°C-40°C)	$\Delta G^\circ / \text{kJ mol}^{-1}$ (25°C)
PVBCEP	52.3	49.8	-66.4	49.8
BR	85.5	49	-65.1	48.5
PVBCIM	62.7	60.2	-15	60.2

Table 10. Thermodynamic parameter values of PAC adsorbed on polymeric resin.

Adsorbents	E_a / kJ mol ⁻¹ (25°C-40°C)	ΔH° / kJ mol ⁻¹ (25°C-40°C)	ΔS° / J mol ⁻¹ K ⁻¹ (25°C-40°C)	ΔG° / kJ mol ⁻¹ (25°C)
PVBCEP	48.1	45.6	-86.3	45.6
BR	97	95	82.5	94.7
PVBCIM	54	51.5	-58.4	52

CONCLUSIONS

Adsorption kinetics of pesticides complied with the pseudo second-order rate equation. Thermodynamic parameters were calculated with these rate constants. In this study, the heat of adsorption is found between 20 and 100 kJ/mol and these values indicate physical adsorption. The adsorption process is usually fast because of the values of $E_a < 100$ kJ/mol. This is due to the presence of weak van der Waals bonds in the medium. When ΔS° is negative, it is considered that ions have an association mechanism, that activated complex formation occurs between the adsorbed material and the adsorbent, and there is a significant change during the adsorption process in the inner structure of the adsorbent.

In this study, it is assumed that the adsorption of pesticides on the new polymeric resin performs well. While the maximum value of adsorption (q_{max}) is found as BR>PVBCEP>PVBCIM for BPA, these values (q_{max}) are found as PVBCEP resin for PAC. The maximum value of adsorption (q_{max}) of BPA on BR and the maximum value of adsorption (q_{max}) of PAC on PVBCEP were calculated as 21.7 and 769 mg.g⁻¹, respectively. As a result, it is considered that the new polymeric resins obtained will be effective in cleaning the pollution caused by pesticides and will contribute to cleaning of wastewater.

Acknowledgement: This study was funded by Istanbul University with the project number 43210.

REFERENCES

- G. Z. Memon, M. I. Bhangar, M. Akhtar, F. N. Talpur, J. R. Memon, *Chem. Eng.*, **138**, 616 (2008).
- Z. Aksu, *Process Biochem.*, **40**, 997 (2005).
- O. Takahashi, S. Oishi, *Environ. Health Perspect.*, **108**, 10 (2000).
- Y.Q. Huang, C.K.C. Wong, J.S. Zheng, H. Bouwmanb, R. Barra, B. Wahlströmd, L. Neretin, M.H. Wong, *Environ. Int.*, **42**, 91 (2012).
- Z. M. Wang, H. Ooga, T. Hirotsu, W. L. Wang, Y. Q. Wu, H.Y. Hu, *Applied Clay Sci.*, **104**, 81 (2015).
- Y. Mao, H. Kong, Y. Guo, S. Chen, Z. Wang, *Desalination and Water Treat.*, **9**, 1 (2014).
- M. L. Zainab, T. Hadibarata, M.H. Puteh, Z. Yusop, *Water, Air, Soil Pollut.*, **226**, 34 (2015).
- H. Soni, P. Padmaja, *Journal of Porous Mater.*, **21(3)**, 275 (2014).
- İ. İ.Yılmaz, S.Yüksel, N. Kabay, M. Yüksel, *J. Chem. Technol. Biotechnol.*, **89**, 835 (2013).
- M. Dehghani, H. A. Mahui, N. Rastkari, R. Saeedi, S. Nazmara, E. Iravani, *Desalination Water Treat.*, **54**, 84 (2013).
- J. Xu, L. Wang, Y. Zhu, *Langmuir*, **28**, 8418 (2012).
- W. Han, L. Luo, S. Zhang, *Int. J. Environ. Sci. Technol.*, **9**, 543 (2012).
- X. Fan, B. Tu, H. Ma, X. Wang, *Bull. Korean Chem. Soc.*, **32**, 2560 (2011).
- H.-Yu Qian, W. Jie, S. Bin, L. Nan, *Bio and Biomedical Eng. (ICBBE)*, (2010), DOI:10.1109/ICBBE.2010.5515079.
- Y. Dong, D. Wu, X. Chen, Y. Lin, *J. Colloid and Interface Sci.*, **34**, 585 (2010).
- T. Şişmanoğlu, *Colloids Surf., A: Physicochemical and Engineering Aspects*, **297**, 38 (2007).
- T.-Y. Kim, S.-Y. Cho, S.-J. Kim, S.Y. Oh, S.-H. Suh, *Revue Roum. Chim.*, **51**, 109 (2006).
- Z. Aksu, E. Kabasakal, *Sep. Purif. Technol.*, **35**, 223 (2004).
- M. Balmauden, A. Assabbane, Y. A. Ichou, *J. Environ. Monitor.*, **2**, 257 (2000).
- T. Cserhati, E. Forgacs, *J. Chromatogr. B*, **717**, 157 (1998).
- B.F. Senkal, E. Yavuz, *J. Appl. Polym. Sci.*, **101**, 348 (2006).
- F. Bildik, E. Yavuz, T. Sismanoglu, B.F. Senkal, *Macromol. Symposia*, **352** (1), 66 (2015), Special Issue: SI DOI: 10.1002/masy.201400155.
- T. Şişmanoğlu, G.S. Pozan, *Desalination Water Treat.*, **57 (28)**, 13318 (2016).
- C.H. Giles, T.H. Macewan, S.N. Nakhwa, D. Smith, *J. Chem. Soc.*, **30**, 3973 (1960).
- Y.S. Ho, G. Mckay, *Process Biochem.*, **34(5)**, 451 (1999).
- S. Azizian, *J. Colloid and Interface Sci.*, **276**, 47 (2004).
- T. Şişmanoğlu, A. Z. Aroguz, *Desalination and Water Treat.*, **54**, 736 (2015).
- Z. Bekçi, Y. Seki, L. Cavas, *J. Hazard. Mater.*, **161**, 1454 (2009).

Semiconducting graphene

S. K. Kolev^{1*}, V. A. Atanasov², H. A. Aleksandrov³, V. N. Popov², T. I. Milenov¹

¹*Institute of Electronics, Bulgarian Academy of Sciences, 72 Tzarigradsko Chaussee Blvd., 1784 Sofia, Bulgaria*

²*Faculty of Physics, Sofia University, 5 J. Bourchier Blvd., Sofia 1164, Bulgaria*

³*Faculty of Chemistry and Pharmacy, Sofia University, 1 J. Bourchier Blvd., Sofia 1164, Bulgaria*

Received, January 18, 2019; Accepted April 17, 2019

In this paper we propose a simple way for structural modification of graphene yielding a non-zero band gap which is mandatory for prospective electronics applications. This can be achieved by creating a buffer layer graphene (BuLG) upon deposition on different crystalline silicon surfaces. Previous calculations have shown that the formation of such buffer layer on 4H-SiC results in lattice deformation of BuLG, due to the 8% mismatch between the (0001)Si crystal surface of SiC and the graphene lattices. Here, for elimination of the lattice deformation, we propose a replacement of the (0001)Si surface of SiC by hydrogen atoms. Using density functional simulations we show that the band gap of the corrugated graphene sheet is $\Delta E = 1.94$ eV (hydrogenated system) or $\Delta E = 1.21$ eV SiC/graphene system. Height of corrugation is equal to $h = 35.0 \pm 5.0$ pm. Two effects are responsible for the band gap opening: corrugation of the sheet, caused by the covalently bonded carbon atoms, and removal of electrons from the bonding π orbitals of graphene.

Keywords: silicon carbide, graphene, band gap, FET

INTRODUCTION

The electronic applications of graphene are hindered because of the vanishing band gap of its electronic band structure [1, 2]. Graphene's semi-metallic character prevents the construction of a field effect transistor (FET) with distinct ON and OFF states. Therefore, regardless of the ballistic transport and the amazing carrier mobility of $200\,000\text{ cm}^2\text{ V}^{-1}\text{ s}^{-1}$ [3], graphene is no match for silicon as a result of its lack of a proper band gap. Additional problems such as the absence of an established technology for its industrial scale production with acceptable quality [4], and the difficulties to be transferred to an insulating layer, make graphene application in electronics even more questionable. Chemical vapor deposition (CVD) technology is also a bad choice for creating graphene – insulator layers [5]. Graphitization of SiC at high temperatures [6, 7] is the other possible wafer-scale technology. The silicon carbide support to the graphene layers is either semiconducting with a band gap of 2.36 eV for 3C(β), or insulating with a band gap of 3.23 eV for 4H and 3.05 eV for 6H(α). This crystal, unfortunately, is too thick for field effect induction needed to switch ON/OFF a graphene FET channel.

Recently, a breakthrough in graphene electronics research has been reported [8]. A buffer layer synthesized on SiC(0001) surface has the properties of a semiconductor, with energy gap larger than 0.5 eV. The energy gap opens as the higher growth temperature improves the order of

covalent bonds between the graphene layer and SiC. The graphene top layer, commensurately bonded to the silicon carbide (0001) surface, is an example of a system, where the alignment of periodic covalent bonds to A or B sites breaks the chiral symmetry [9]. Finite size effect [10], on the other hand, cannot quantitatively explain the energy gap opening. Our interest in the topic is focused on performing *ab initio* simulations, which show that a prescribed bandgap could be opened and modified by a controllable corrugation of BuLG (buffer layer graphene) at the interface of the system of graphene/SiC.

Computational methods

Ab initio geometry optimizations were performed using the CP2K/Quickstep package [11, 12]. The DFT was applied within the generalized gradient approximation (GGA), using Perdew-Burke-Ernzerhof (PBE) functional [13]. Basis set DZVP-MOLOPT-SR-GTH [14], which is optimized for calculating molecular properties in gas and condensed phase, was applied to all atoms in the studied systems. For reducing the computational cost, the Gaussian and Plane-Wave (GPW) method [15, 16], as well as pseudopotentials of Goedecker-Teter-Hutter (GTH) [17, 18] were used. Dispersion interaction was taken into account *via* the DFT + D approach with D3 set [19].

It is usually difficult to achieve convergence of the SCF procedure in systems with small band gap or isoenergetic states, such as metals and semimetals. In order to improve convergence, the

* To whom all correspondence should be sent:

E-mail: skkolev@ie.bas.bg

electronic temperature was introduced, using the Fermi-Dirac distribution method [20]:

$$f(E) = \frac{1}{e^{(E-E_f)/k_B T} + 1}$$

where: $f(E)$ is the probability for an electron to have energy E , E_f is the Fermi energy at temperature $T = 0$ K, k_B is the Boltzmann constant. All calculations were performed at $T = 300$ K. This method allowed for achieving convergence in all cases.

Main hypothesis

The interactions of graphene with the SiC interface have been studied employing theoretical and experimental methods [21-24]. Those investigations describe the top layer on the silicon carbide as a graphene buffer with unique properties. A theoretical DFT study performed by Varchon *et al.* [21] explores the electronic structure of 4H-SiC (3×3 R30 surface cell in Wood's notation) with a graphene buffer layer, demonstrating the opening of a band gap. The connection between graphene (BuLG) corrugation and energy gap opening is explored for the first time in our previous publication, using *ab initio* methods [25].

Here, we continued the research on the nature of the band gap opening by constructing a model, where hydrogen atoms are responsible for sheet corrugation and electron withdraw effect. Another model, featuring a more realistic SiC substrate, was also studied. With every silicon atom from the SiC (0001) substrate, covalently bonded to graphene, an electron from the delocalized π system is removed. This is because the hybridization of the bonded C atom changes from sp^2 to sp^3 and a p electron is withdrawn from the graphene. As both hydrogen and silicon atoms can form covalent bonds with the C atoms from the graphene sheet, similar degree of corrugation and band gap values are expected for both models.

The suggested models are realistic enough to be supported by analytical results (within the continuum model), namely, the energy spectrum for the carriers of periodically corrugated graphene sheet is given by the Mathieu equation which yields an energy gap with the correct order of magnitude for the experimentally relevant values of the height and period of corrugation [25].

Structural model and electronic properties of graphene on (0001)Si plane of 6H- SiC

Our structural model includes a graphene sheet and its silicon carbide substrate. The substrate consists of the Si atoms, covalently bonded to graphene and their neighboring carbon atoms. The initial mutual orientation of graphene and SiC, shown in Figs. 1a and 2a, is taken from experimental data [22, 26]. It was concluded that the lattices of graphene and SiC are 30° rotated with respect to one another [26]. This rotation is taken into account. Silicon carbide geometry is built taking into account the SiC unit cell [27]. The final model is based on a 2×2 graphene cell, situated on top of a 3×3 R30 SiC surface cell, Fig. 1a (the unit cells are marked by blue and purple lines). Silicon atoms that are not in direct contact with carbon atoms from graphene (small green spheres in Fig. 1a) are removed, as they are not expected to form covalent bonds and alter the electronic structure of the graphene layer.

In the first numerical experiment, we replaced the SiC layer with hydrogen atoms covalently bonded to the respective sp^3 -hybridized carbon atoms of BuLG, Fig. 1b. After geometry optimization, this leads to a corrugation in the system with $h_1 = 35.0 \pm 5.0$ pm and a period of 250 – 260 pm, Fig. 1c. As a result, a band gap opens in the system BuLG/ hydrogen atoms with $\Delta E = 1.94$ eV, Fig. 1d. It should be noted that calculations with the same DFT method/basis give a zero band gap for pristine graphene [28].

Having shown that periodic corrugation, caused by covalently bonded hydrogen atoms, opens a bandgap, we built a more realistic model of the system SiC/BuLG, than those used in Ref. [25]. This model takes into account all carbon neighbors of the silicon atoms, Fig. 2a. In the previous model, Ref. [25], some bonds of the silicon atoms were hydrogen terminated. The system consists of 72 graphene carbon atoms, bonded to a SiC layer.

The system has a total spin of zero and is in a singlet ground state. Geometry optimization was performed altering the positions of all atoms, with the exception of silicon. Silicon atoms are fixed, as expected in the rigid silicon carbide crystal. Periodic cell dimensions are as follows: $a = 1529$ pm, $b = 1529$ pm and $c = 1716$ pm, with $\alpha = 90^\circ$, $\beta = 90^\circ$ and $\gamma = 60^\circ$ angles, α - between a and c, β - between b and c, and γ - between a and b.

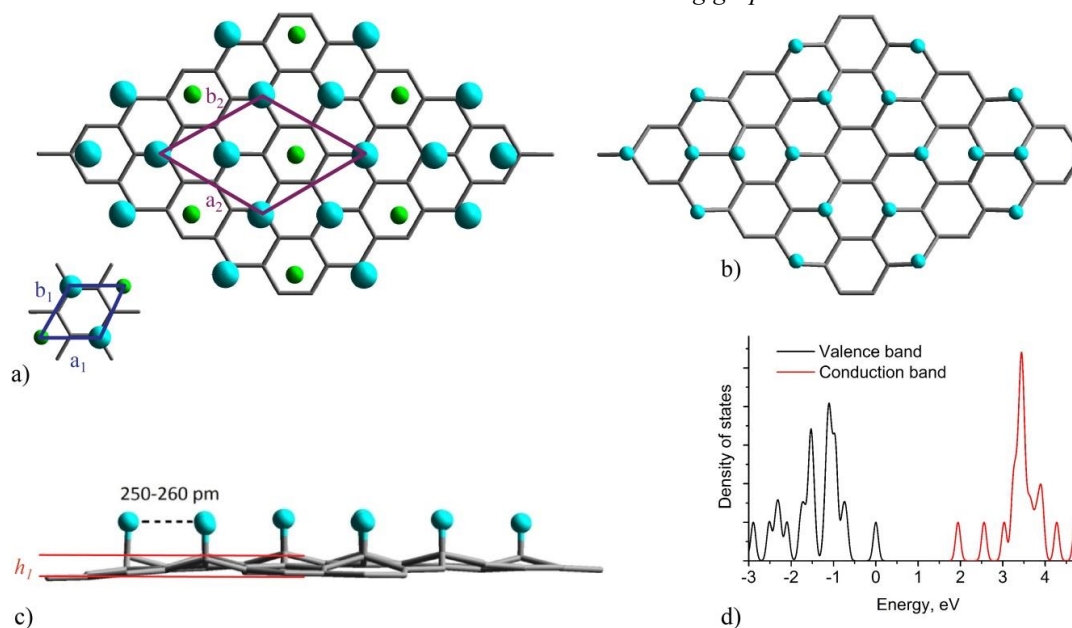


Figure 1. a) The orientation of graphene (dark grey sticks) and nearest atoms from the substrate: the cyan and green spheres represent the Si atoms of the 3×3 R30 surface cell of SiC. The inset shows the basis vectors $a_1 = b_1$ marked by blue lines. The cyan spheres represent Si atoms, closest to the C atoms of graphene. The cyan spheres form a new 2×2 surface cell with $a_2 = b_2$ basis vectors (purple lines) in graphene. b) The cyan spheres represent Si atoms, which are replaced by H atoms. c) The optimized structure with H atoms, where h_1 is the height of the corrugation of BuLG ($h_1 = 35.0 \pm 5.0$ pm). d) Density of states, simulated as molecular orbitals. The valence band (black line) and the conduction band (red) are separated by a gap $\Delta E = 1.94$ eV.

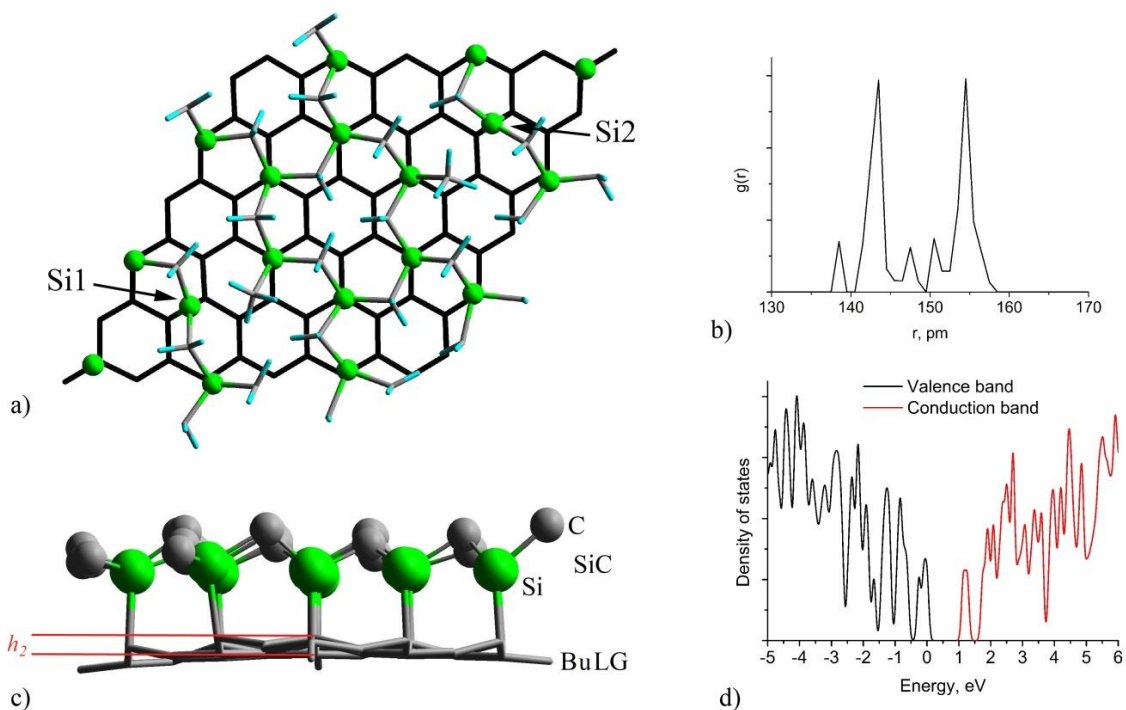


Figure 2. a) The structure of SiC/BuLG model – one unit cell (color coding: C – gray, Si – green, H – light blue). b) The carbon-carbon radial distribution function of graphene. Distances of 143 pm correspond to chemical bonds between sp^2 -hybridized C atoms, while 154 pm is the mean bond length between sp^3 -hybridized C atoms. c) SiC/BuLG structure, viewed along the direction perpendicular of the bisector of the angle between a and b axis, $h_2 = 35.0 \pm 5$ pm. d) Density of states. The valence band (black line) and the conduction band (red line) are separated by an energy gap $\Delta E = 1.21$ eV.

In the optimized structure, the carbon atoms of the graphene layer, bonded to silicon atoms, are sp^3 -hybridized. Most of the Si atoms participate in a covalent bond with one C atom from graphene. Exceptions are Si1 and Si2, shown on Fig. 2a, that form covalent bonds with two carbon atoms. This effect is caused by the proximity of two graphene C atoms to Si1 and Si2, instead of one.

RDF (radial distribution function) of carbon atoms from the graphene layer is presented in Fig 2b. The bonds between sp^2 -hybridized carbon atoms are represented as the first maximum, with mean C-C distances of 143 pm. This value is equivalent to the mean C-C bond lengths of pristine graphene, observed at 142 pm [28]. The second maximum, located at 154 pm, corresponds to single C-C bonds between sp^2 -hybridized and sp^3 -hybridized carbon atoms. The average distance between the pairs of covalently bonded silicon atoms and sp^3 -hybridized carbon atoms is 196 pm. Interaction with the SiC layer induces corrugation in the graphene (BuLG). The corrugation period is in the interval 250 – 260 pm, close to the 267 pm distance between the aligned Si atoms in the 6H-SiC (0001) surface. The corrugation of BuLG is caused by the repeating sp^3 -hybridized carbon atoms covalently bonded to Si. It should be noted that covalently bonded hydrogen atoms (Fig 1c) or silicon atoms (Fig 2c) induce the same degree of corrugation to the BuLG. Its height ($h_1=h_2$) is in the range of 35.0 ± 5.0 pm. Energy gap of the SiC/BuLG system is $\Delta E = 1.21$ eV, Fig 2d. This value is lower by 0.73 eV than the band gap of the previously described hydrogenated system.

CONCLUSIONS

Graphene should possess a band gap for the 2D material to be used in electronic applications, especially for field effect transistors (FETs) construction. A semiconducting material is necessary for the channel of the FETs, as they should possess ON/OFF states as logic elements. Using density functional simulations, we established that the band gap of the corrugated graphene sheet is equal to $\Delta E = 1.94$ eV (hydrogenated system) or $\Delta E = 1.21$ eV (SiC/BuLG system). Results are in agreement with the experimental value $\Delta E > 0.5$ eV for a similar system [8]. The height of corrugation $h = 35.0 \pm 5.0$ pm is equal in both cases. Two synergic effects are responsible for the band gap opening: corrugation of the sheet, caused by the covalently bonded atoms, and removal of electrons from the bonding π orbitals of graphene. In our cases, corrugation is caused by aligned covalently bonded H or Si atoms, with a period of 250 – 260 pm. Also, with every H

or Si atom, an electron from the delocalized π system is removed. This is because the hybridization of the bonded C atom changes from sp^2 to sp^3 and a p electron is withdrawn from the graphene. Both studied models, featuring hydrogen and silicon, show that the nature of the covalent bonded atom is not crucial for obtaining the band gap opening, but rather the synergy between the two effects.

Acknowledgement: The authors gratefully acknowledge the financial support by the National Science Fund of Bulgaria under grant DN18/9-11.12.2017.

REFERENCES

1. K. Novoselov, A. Geim, S. Morozov, D. Jiang, Y. Zhang, S. Dubonos, I. Grigorieva, A. Firsov, *Science*, **306**, 666 (2004).
2. A. Castro Neto, F. Guinea, N. Peres, K. Novoselov, A. Geim, *Rev. Mod. Phys.*, **81**, 109 (2009).
3. A. Geim, K. Novoselov, *Nature Materials*, **6**, 183 (2007).
4. J. Lee, E. Lee, W. Joo, Y. Jang, B. Kim, J. Lim, S. Choi, S. Ahn, J. Ahn, M. Park, C. Yang, B. Choi, S. Hwang, D. Whang, *Science*, **344**, 286 (2014).
5. S. Tang, H. Wang, H. Wang, Q. Sun, X. Zhang, C. Cong, H. Xie, X. Liu, X. Zhou, F. Huang, X. Chen, T. Yu, F. Ding, X. Xie, M. Jiang, *Nature Commun.*, **6**, 6499 (2015).
6. W. de Heer, C. Berger, X. Wu, P. First, E. Conrad, X. Li, T. Li, M. Sprinkle, J. Hass, M. Sadowski, M. Potemski, G. Martinez, *Solid State Commun.*, **143**, 92 (2007).
7. P. Sutter, *Nature Materials* **8**, 171 (2009).
8. M. Nevius, M. Conrad, F. Wang, A. Celis, M. Nair, A. Taleb-Ibrahimi, A. Tejada, E. Conrad, *Phys. Rev. Lett.*, **115**, 136802 (2015).
9. E. McCann, V. Fal'ko, *Phys. Rev. Lett.*, **96**, 086805 (2006).
10. M. Fujita, K. Wakabayashi, K. Nakada, K. Kusakabe, *J. Phys. Soc. Jpn.*, **65**, 1920 (1996).
11. The CP2K developers group, <http://www.cp2k.org/> 2012.
12. J. Van de Vondele, M. Krack, F. Mohamed, M. Parrinello, T. Chassaing, J. Hutter, *Comput. Phys. Commun.*, **167**, 103 (2005).
13. J. Perdew, K. Burke, M. Ernzerhof, *Phys. Rev. Lett.*, **77**, 3865 (2006).
14. J. Van de Vondele, J. Hutter, *J. Chem. Phys.*, **127**, 114105 (2007).
15. G. Lippert, J. Hutter, M. Parrinello, *Molec. Phys.*, **92**, 477 (1997).
16. G. Lippert, J. Hutter, M. Parrinello, *Theor. Chem. Acc.*, **103**, 124 (1999).
17. S. Goedecker, M. Teter, J. Hutter, *Phys. Rev. B*, **54**, 1703 (1996).
18. C. Hartwigsen, S. Goedecker, J. Hutter, *Phys. Rev. B*, **58**, 3641 (1998).

19. S. Grimme, J. Antony, S. Ehrlich, S. Krieg, *J. Chem. Phys.*, **132**, 154104 (2010).
20. J. Lee, *Computational Materials Science: An Introduction*, CRC Press, 2016.
21. F. Varchon, R. Feng, J. Hass, X. Li, B. Nguyen, C. Naud, P. Mallet, J. Veuillen, C. Berger, E. Conrad, L. Magaud, *Phys. Rev. Lett.*, **99**, 126805 (2007).
22. F. Varchon, P. Mallet, J. Veuillen, L. Magaud, *Phys. Rev. B*, **77**, 235412 (2008).
23. C. Riedl, C. Coletti, U. Starke, *J. Phys. D*, **43**, 374009 (2010).
24. S. Goler, C. Coletti, V. Piazza, P. Pingue, F. Colangelo, V. Pellegrini, K. Emtsev, S. Forti, U. Starke, F. Beltram, S. Heun, *Carbon*, **51**, 249 (2013).
25. S. Kolev, V. Atanasov, H. Aleksandrov, T. Milenov, *EPJ B*, **91**, 272 (2018).
26. J. Kang, Y. Ronen, Y. Cohen, D. Convertino, A. Rossi, C. Coletti, S. Heun, L. Sorba, P. Kacman, H. Shtrikman, *Semicond. Sci. Technol.*, **31**, 115005 (2016).
27. T. Yoon, T. Lim, T. Min, S. Hung, N. Jakse, S. Lai, *J. Chem. Phys.*, **139**, 204702 (2013).
28. S. Kolev, I. Balchev, K. Cvetkova, S. Tinchev, T. Milenov, *Journal of Physics: Conference Series*, **780**, 012014 (2017).

Regression model and analysis of MHD mixed convective stagnation point nanofluid flow: SLM and SRM approach

B. Kumar^{1*}, G. S. Seth¹, R. Nandkeolyar²

¹Department of Applied Mathematics, Indian Institute of Technology (ISM), Dhanbad-826004, Jharkhand, India

²Department of Mathematics, National Institute of Technology, Jamshedpur - 831014, Jharkhand, India

Received January 21, 2019; Revised April 4, 2019

The present paper is concerned with mixed convection, viscous and Joule dissipations, thermophoretic and Brownian diffusion effects on the steady stagnation point nanofluid flow with passive control of nanoparticles. Similarity transformation is exerted to convert governing boundary layer partial differential equations into ordinary differential equations without loss of generality. In order to optimize error and assess accuracy of solutions two different spectral schemes are efficiently employed to solve governing equations. The graphs for velocity, temperature and concentration of the present nanofluid flow model, obtained by using SLM (successive linearization method) and SRM (spectral relaxation method) are discussed in detail for various flow controlling parameters. Apart from it, regression analysis is performed for skin friction for making this model more effective in industries and engineering. Findings reflect that a boundary layer is formed even in case of the same stretching and free stream velocities in the presence of mixed convection parameter. Magnetic parameter is assisting parameter for the fluid flow when free stream velocity is dominant over stretching sheet velocity while in the opposite case it acts as opposing parameter for the velocity profile.

Keywords: Regression model, viscous and Joule dissipations, Brownian and thermophoretic diffusions, SLM (successive linearization method), SRM (spectral relaxation method)

INTRODUCTION

19th Century onwards, every country is running to thrive in all fields including technology and industries, for improving themselves and being the best. This race led to massive industrialization and many other activities. Therefore, we are getting beneficial outcomes, as well as direct consequences due to massive release of greenhouse gases. To mitigate the global warming, is a challenge for the world. This objective of reducing heat consumption can be achieved by increasing heat transfer. Therefore, nanofluids are introduced in the recent past, which are colloidal suspensions of nanosized particles in the base fluid. Masuda *et al.* [1] were the first to notice how heat transfer rate and thermal conductivity of liquid increases when ultra-fine particles are dispersed into it. They selected water as a base fluid and powders of Al₂O₃, TiO₂ and SiO₂ as ultrafine particles. Choi [2] coined the term nanofluid in his pioneering research. Some of the other relevant investigations are due to articles [3-5].

The models for fluid flow over a stretching/shrinking sheet are very important because of their large potential to deal with many industrial and engineering areas. They also have manifold applications in manufacturing of long and uniform metal parts, melt spinning technique for cooling liquid, metalworking process, etc.

The pioneering attempt to observe a boundary layer flow over a continuous moving surface was done by Sakiadis [6]. Theoretically, a flow adjacent to a linearly stretching plate is studied by Crane [7]. Makinde and Aziz [8] efficiently employed the convective heated boundary condition to study nanofluid flow past a stretching sheet and found that as thermophoretic and Brownian diffusions become stronger; Sherwood number increases while Nusselt number decreases. Bhatti *et al.* [9] have taken a porous shrinking sheet to analyse the nonlinear thermal radiation effect on MHD nanofluid flow. Recently some other relevant research investigations are done by several authors [10-12], etc.

Natural convection is a process in which fluid motion is dependent on the density difference in the fluid, encountered as a result of temperature gradients. The forced convection is a process in which fluid motion is developed by an external source like fan, pump, etc. When these two mechanisms occur simultaneously, then it is termed as mixed convection and is used in many thermal engineering processes. Various engineering and industrial processes such as transpiration cooling, aerodynamic extrusion, continuous filament extrusion, etc., can be qualitatively analysed by such types of models. Ghaly [13] has taken synchronized action of thermal radiation, buoyancy

* To whom all correspondence should be sent:
E-mail: chauhanbhuvan6@gmail.com

force and magnetic field on the flow-field and suggested that local shear stress is decreasing function of radiation. MHD mixed convection flow with buoyancy effect is studied by Makinde *et al.* [14] taking viscous and Joule dissipations into account and reported that in case of a shrinking sheet dual solutions exist. They also found that skin friction decreases while local Nusselt number increases with enhancement in buoyancy force. Rashidi *et al.* [15] developed a very interesting model for forced convection flow of a nanofluid. Some more studies on this topic are due to articles [16-18].

Due to the wide use in engineering and industries, the flow near the stagnation point is investigated by many authors. The application of the flow behaviour near a fixed point is found in many problems such as manufacturing of plastic substance, metallurgy, lubricants theory, polymer extrusion, etc. Mustafa *et al.* [19] reported the boundary layer solutions of a stagnation point flow adjacent to a stretching sheet by homotopy analysis method. Rahman *et al.* [20] have taken inclined stretching cylinder and analysed the thermophysical aspect of stagnation point flow. Some other studies are due to articles [21, 22]

In the present investigation, our purpose is to present a boundary layer solution and observe the effect of various terms, *viz.* viscous and Joule dissipations, mixed convection, Brownian and thermophoretic diffusions on a stagnation point flow with passive control of nanoparticles by two different spectral schemes, *i.e.* SLM and SRM. As per authors concern, this model is not yet studied by a spectral scheme. There are several applications of such types of fluid flow models such as industrial cooling [23], nuclear reactor cooling [24], enhance the critical heat flux in pool boiling [25], reducing pollution and heating buildings [26], thermal energy storage [27], drug delivery [28], direct absorption solar collectors [29], friction reduction [30], etc.

MATHEMATICAL MODELLING OF THE PROBLEM

The present system deals with the steady two-dimensional, viscous, incompressible and electrically conducting stagnation point flow of a nanofluid over a stretching sheet with mixed convection, heat generation, viscous and Joule dissipations, Brownian and thermophoretic diffusions. The key assumptions which are made while deriving the governing equations are: the nanoparticles and base fluid are assumed in thermal equilibrium and chemical reaction between them is neglected; the nanofluid is viscous, incompressible

and electrically conducting; the magnetic Reynolds number is small enough to discard the induced magnetic field; there is no external electric field so the induced electric field due to polarization of charges is negligible; and the Boussinesq approximation is taken into account, *i. e.* density variation obtained by concentration or temperature difference is neglected except in case of buoyancy force. The geometry of the concerned problem is presented in figure 1(a).

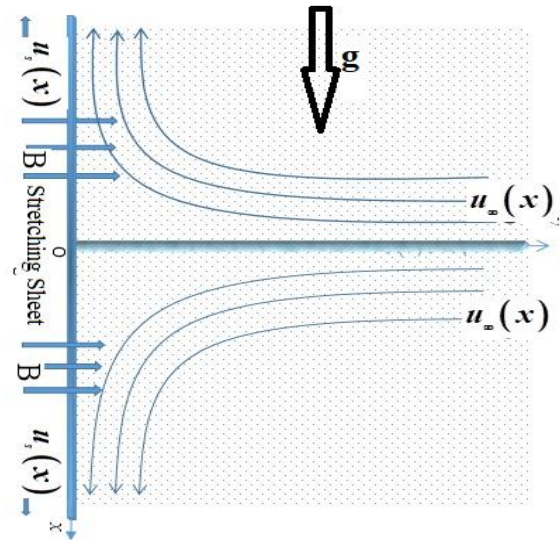


Fig 1(a). Schematic diagram and coordinate system of the flow problem.

The nanofluid is impinging normally over the stretching sheet and the stretching velocity is in the form of power law as $u_s = ax^n$. Free stream velocity of fluid is also taken in power law form as $u_\infty = bx^n$ where a , b and n are constants, *i.e.* fluid flow and stretching sheet are in upward direction along the x -axis. The symbols $T = T_s$ and $T = T_\infty$ are for constant temperature of fluid at the surface and in the free stream, respectively. The symbol C_∞ is for fluid concentration in the free stream while nanoparticle volume fraction C is controlled passively at the surface, as suggested by Kuznetsov and Nield [31]. For controlling boundary layer, transverse magnetic field having intensity B is exerted perpendicular to the sheet, *i. e.* along the y axis.

Using these key assumptions, the governing boundary layer equations, *i.e.* continuity, momentum, energy and concentration equations, are expressed, respectively, as follows:

$$\frac{\partial u}{\partial x} + \frac{\partial v}{\partial y} = 0, \tag{1}$$

$$u \frac{\partial u}{\partial x} + v \frac{\partial u}{\partial y} = \nu \left(\frac{\partial^2 u}{\partial y^2} \right) + u_\infty \left(\frac{\partial u_\infty}{\partial x} \right) +$$

$$\frac{\sigma}{\rho_{nf}} B^2 (u_\infty - u) + \frac{g}{\rho_{nf}} (1 - C_\infty) \rho_{nf\infty} \beta (T - T_\infty) - \frac{g}{\rho_{nf}} (C - C_\infty) (\rho_{np} - \rho_{nf\infty})$$

$$(\rho c_p)_{nf} \left(u \frac{\partial T}{\partial x} + v \frac{\partial T}{\partial y} \right) = k \left(\frac{\partial^2 T}{\partial y^2} \right) + \sigma B^2 (u_\infty - u)^2 + \mu \left(\frac{\partial u}{\partial y} \right)^2 + Q(T - T_\infty)$$

$$+ (\rho c_p)_{np} \left[D_B \left(\frac{\partial C}{\partial y} \frac{\partial T}{\partial y} \right) + \frac{D_T}{T_\infty} \left(\frac{\partial T}{\partial y} \right)^2 \right], \tag{3}$$

$$u \frac{\partial C}{\partial x} + v \frac{\partial C}{\partial y} = \frac{D_T}{T_\infty} \left(\frac{\partial^2 T}{\partial y^2} \right) + D_B \left(\frac{\partial^2 C}{\partial y^2} \right). \tag{4}$$

Related boundary conditions are:

$$\left. \begin{aligned} u = u_s, v = 0, \frac{\partial C}{\partial y} = - \left(\frac{D_T}{D_B T_\infty} \right) \frac{\partial T}{\partial y}, \\ T = T_s, \text{ at } y = 0, \\ u \rightarrow u_\infty, C \rightarrow C_\infty, T \rightarrow T_\infty, \text{ as } y \rightarrow \infty, \end{aligned} \right\} \tag{5}$$

where meanings of symbols are given in the nomenclature section.

The similarity of flow states for two geometrically similar bodies for which the flow around the test body and the flow around prototype can be considered the same or similar if the Reynolds numbers in the two cases are equal [32, 33]. It will be true for other similarity parameters like Prandtl number, Schmidt number, etc. Due to this reason, we have considered it as a similar problem and similar solutions will be obtained. For similar solution of governing boundary layer equations (2), (3) and (4) along with boundary constraint (5), we have taken the following similarity transformations

$$\left. \begin{aligned} \eta = y \sqrt{\frac{(n+1)u_s}{2\nu x}}, \psi = \sqrt{\frac{2u_s \nu x}{n+1}} f(\eta), \\ \phi(\eta) = \frac{C - C_\infty}{C_\infty}, \theta(\eta) = \frac{T - T_\infty}{T_s - T_\infty}, \end{aligned} \right\} \tag{6}$$

where η is similarity variable and ψ is stream function while ϕ and θ are non-dimensional concentration and temperature, respectively.

Using these similarity variables, our problem was reduced to the following form:

$$f''' + ff'' - \frac{2n}{n+1} f'^2 - \frac{2M}{n+1} (f' - s) + \frac{2\lambda}{n+1} (\theta - Nr\phi) + \frac{2n}{n+1} s^2 = 0, \tag{7}$$

$$\frac{1}{Pr} \theta'' + f\theta' + Nt(\theta')^2 + Nb\theta'\phi' + Ec f''^2 + \alpha\theta + \frac{2MEc}{n+1} (f' - s)^2 = 0, \tag{8}$$

$$\phi'' + Scf\phi' + \frac{Nt}{Nb} \theta'' = 0. \tag{9}$$

The boundary conditions (5) were reduced to the following form:

$$\left. \begin{aligned} f(\eta) = 0, f'(\eta) = 1, \\ Nb\phi'(\eta) + Nt\theta'(\eta) = 0, \theta(\eta) = 1, \text{ at } \eta = 0, \\ f'(\eta) \rightarrow s, \phi(\eta) \rightarrow 0, \theta(\eta) \rightarrow 0, \text{ as } \eta \rightarrow \infty, \end{aligned} \right\} \tag{10}$$

where:

$$\begin{aligned} M &= \frac{\sigma B^2}{\rho_{nf} a}, \lambda = (1 - C_\infty) \rho_{f\infty} \frac{Gr_x}{Re_x^2}, \\ Gr_x &= \frac{g\beta(T_s - T_\infty)x^3}{\nu^2}, Re_x = \frac{u_s x}{\nu}, \\ Nr &= \frac{(\rho_p - \rho_{f\infty})C_\infty}{\rho_{f\infty}\beta(1 - C_\infty)(T_s - T_\infty)}, \\ Nt &= \frac{(\rho c_p)_{np} D_T (T_w - T_\infty)}{(\rho c_p)_{nf} T_\infty \nu}, Ec = \frac{u_s^2}{(c_p)_{nf} (T_s - T_\infty)}, \\ Nb &= \frac{(\rho c_p)_{np} D_B (C_\infty)}{(\rho c_p)_{nf} \nu}, \alpha = \frac{2Q_0}{(n+1)a(\rho c)_f}, \\ Sc &= PrLn = \frac{\nu}{D_B}, Pr = \frac{\nu}{\alpha}, Ln = \frac{\alpha}{D_B}, s = \frac{b}{a}. \end{aligned}$$

For engineering purpose, it is important to find a dimensionless expression for skin friction Cf_x and local Nusselt number Nu_x which are defined respectively as:

$$Cf_x = \frac{\tau_s}{\rho u_s^2} \text{ and } Nu_x = \frac{xq_s}{k(T_s - T_\infty)}. \tag{11}$$

Here τ_s is the shear stress at the surface and q_s heat flux at the surface which are defined by:

$$\tau_s = \mu \left(\frac{\partial u}{\partial y} \right)_{y=0} \text{ and } q_s = -k \left(\frac{\partial T}{\partial y} \right)_{y=0}. \tag{12}$$

Using similarity variable, we got the following dimensionless form of skin friction and local Nusselt number:

$$\left. \begin{aligned} Cf_x Re_x^{1/2} &= \sqrt{\frac{(n+1)}{2}} f''(0), \\ Nu_x Re_x^{-1/2} &= -\sqrt{\frac{(n+1)}{2}} \theta'(0). \end{aligned} \right\} \tag{13}$$

Here, $\theta'(0)$ is wall temperature gradient and $f''(0)$ is wall velocity gradient.

SOLUTION METHODOLOGY

For finding solution of equations (7) to (9) along with boundary constraints (10) we have used two different spectral approaches, i. e. successive linearization method [34] and spectral relaxation method [35], to avoid inaccuracy of results.

Spectral methods take on a global approach to deal with the problem, i.e. the value of a derivative at a certain point in space depends on the solution at all the other points in space, and not just the neighbouring grid points. For this reason, spectral methods have excellent error properties with the so-called "exponential convergence" being the fastest possible, when the solution is smooth. Spectral methods are distinguished not only by the fundamental type of the method (Galerkin collocation, Galerkin with numerical integration), but also by the particular choice of the trial functions. Due to this fact, spectral methods usually have a very high order of approximation. In fact, spectral methods were among the first to be used in practical flow simulations. Because of their simplicity, rapid convergence and high accuracy, we conclude that the SLM and SRM have great potential of being used in place of the traditional methods such as finite difference method, shooting technique along with Runge Kutta method, finite element method, etc., in solving nonlinear boundary value problems.

SUCCESSIVE LINEARIZATION METHOD (SLM)

For applying this technique, the functions $f(\eta)$, $\theta(\eta)$, and $\phi(\eta)$ can be assumed as:

$$\left. \begin{aligned} f(\eta) &= f_j(\eta) + \sum_{w=0}^{j-1} F_w(\eta), \\ \theta(\eta) &= \theta_j(\eta) + \sum_{w=0}^{j-1} \Theta_w(\eta), \\ \phi(\eta) &= \phi_j(\eta) + \sum_{w=0}^{j-1} \Phi_w(\eta), \end{aligned} \right\} \quad (14)$$

where functions $f(\eta)$, $\theta(\eta)$, and $\phi(\eta)$ are unknown and $F_w(\eta)$, $\Theta_w(\eta)$, and $\Phi_w(\eta)$, are successive approximations. The next algorithm to use SLM is to choose initial guess, i.e:

$$\left. \begin{aligned} F_0(\eta) &= 1 - s + s\eta - (1 - s)e^{-\eta}, \\ \Theta_0(\eta) &= e^{-\eta}, \quad \Phi_0(\eta) = -\frac{Nt}{Nb}e^{-\eta}. \end{aligned} \right\} \quad (15)$$

Here F_0 , Θ_w and Φ_0 are the initial guesses that satisfy boundary conditions for f , θ and ϕ . The

solutions of $f(\eta)$, $\theta(\eta)$, and $\phi(\eta)$, after M iterations can be expressed as:

$$\left. \begin{aligned} f(\eta) &\approx \sum_{w=0}^M F_w(\eta), \theta(\eta) \approx \sum_{w=0}^M \Theta_w(\eta), \\ \phi(\eta) &\approx \sum_{w=0}^M \Phi_w(\eta). \end{aligned} \right\} \quad (16)$$

The Chebyshev spectral collocation scheme is utilized to obtain a solution of these linearised equations. This scheme uses those polynomials which are defined on $[-1, 1]$ closed interval. So, for using this method we have to convert the domain $[0, \infty)$ to $[-1, 1]$ with the help of the domain truncation methodology. In this method, the solution of the problem is obtained in the interval $[0, L^*]$ in place of $[0, \infty)$ by utilising the following transformation:

$$\frac{\eta}{L^*} = \frac{\zeta + 1}{2}, \quad -1 \leq \zeta \leq 1. \quad (17)$$

Here L^* is the scaling parameter. This parameter is very significant due to its use in implementing boundary conditions at infinity. Let P be the number of collocation points and Gauss-Lobatto collocation points method is used to discretize the domain $[-1, 1]$ which is defined as follows:

$$\zeta = \cos \frac{\pi i}{P}, \quad i=0,1,2,\dots,P. \quad (18)$$

At these P collocation points the functions F_j , Θ_j and Φ_j for $j \geq 1$ are approximated with the help of k th Chebyshev polynomial (T_k^*) as:

$$\left. \begin{aligned} F_j(\zeta) &\approx \sum_{k=0}^P F_j(\zeta_k) T_k^*(\zeta_k), \\ \Theta_j(\zeta) &\approx \sum_{k=0}^P \Theta_j(\zeta_k) T_k^*(\zeta_k), \\ \Phi_j(\zeta) &\approx \sum_{k=0}^P \Phi_j(\zeta_k) T_k^*(\zeta_k), \end{aligned} \right\} \quad (19)$$

k th Chebyshev polynomial is defined as:

$$T_k^*(\zeta) = \cos[k \cos^{-1}(\zeta)]. \quad (20)$$

At the collocation points, the r^{th} derivatives of functions F_j , Θ_j and Φ_j are constructed as:

$$\left. \begin{aligned} \frac{d^r F_j}{d\eta^r} &= \sum_{k=0}^P S_{ki}^r F_j(\zeta_k), \\ \frac{d^r \Theta_j}{d\eta^r} &= \sum_{k=0}^P S_{ki}^r \Theta_j(\zeta_k), \\ \frac{d^r \Phi_j}{d\eta^r} &= \sum_{k=0}^P S_{ki}^r \Phi_j(\zeta_k). \end{aligned} \right\} \quad (21)$$

Here $S = 2D/L^*$ where D is a matrix called Chebyshev differentiation matrix and the entries of this matrix are as follows:

$$\left. \begin{aligned} D_{00} &= \frac{2P^2+1}{6}, D_{ik} = \frac{c_i(-1)^{i+k}}{c_k \zeta_i - \zeta_k}, \\ & \quad i \neq k; k=0,..,P, \\ D_{PP} &= -\frac{2P^2+1}{6}, D_{kk} = -\frac{\zeta_k}{2(1-\zeta_k^2)}, \\ & \quad k=1,..,P-1. \end{aligned} \right\} \quad (22)$$

In this procedure, we get the following matrix equation:

$$A_{j-1} X_j = R_{j-1}, \quad (23)$$

where A_{j-1} is a $(3P+3) \times (3P+3)$. square matrix. X_j and R_{j-1} are $(3P+3) \times 1$ column vectors defined by:

$$A_{j-1} = \begin{bmatrix} A_{11} & A_{12} & A_{13} \\ A_{21} & A_{22} & A_{23} \\ A_{31} & A_{32} & A_{33} \end{bmatrix}, \quad (24)$$

$$x_j = \begin{bmatrix} F_j \\ \Theta_j \\ \Phi_j \end{bmatrix}, \quad R_{j-1} = \begin{bmatrix} r_{1,j-1} \\ r_{2,j-1} \\ r_{3,j-1} \end{bmatrix}$$

where:

$$F_j = [f_j(\zeta_0), f_j(\zeta_1), \dots, f_j(\zeta_{P-1}), f_j(\zeta_P)]^T,$$

$$\Theta_j = [\theta_j(\zeta_0), \theta_j(\zeta_1), \dots, \theta_j(\zeta_{P-1}), \theta_j(\zeta_P)]^T,$$

$$\Phi_j = [\phi_j(\zeta_0), \phi_j(\zeta_1), \dots, \phi_j(\zeta_{P-1}), \phi_j(\zeta_P)]^T,$$

$$r_{1,j-1} = [r_{1,j-1}(\zeta_0), r_{1,j-1}(\zeta_1), \dots, r_{1,j-1}(\zeta_P)]^T,$$

$$r_{2,j-1} = [r_{2,j-1}(\zeta_0), r_{2,j-1}(\zeta_1), \dots, r_{2,j-1}(\zeta_P)]^T,$$

$$r_{3,j-1} = [r_{3,j-1}(\zeta_0), r_{3,j-1}(\zeta_1), \dots, r_{3,j-1}(\zeta_P)]^T,$$

$$A_{1,1} = a_{1,j-1} D^3 + a_{2,j-1} D^2 + a_{3,j-1} D + a_{4,j-1} I,$$

$$A_{1,2} = a_{5,j-1} I, A_{1,3} = a_{6,j-1} I,$$

$$A_{2,1} = b_{1,j-1} D^2 + b_{2,j-1} D + b_{3,j-1} I,$$

$$A_{2,2} = b_{4,j-1} I + b_{5,j-1} D + b_{6,j-1} D^2,$$

$$A_{2,3} = b_{7,j-1} I, A_{3,1} = c_{1,j-1} D^2 + c_{2,j-1} D + c_{3,j-1} I,$$

$$A_{3,1} = c_{1,j-1} D^2 + c_{2,j-1} D + c_{3,j-1} I,$$

$$A_{3,2} = c_{4,j-1} D^2 + c_{5,j-1} D + c_{6,j-1} I, A_{3,3} = c_{7,j-1} D.$$

In these equations, T shows transpose and $a_{k,j-1}$, $b_{k,j-1}$, $c_{k,j-1}$, $d_{k,j-1}$ are diagonal matrices. I and O are identity matrix and zero matrix, respectively, of order $(P+1) \times (P+1)$. Ultimately, the solution is given by:

$$X_j = A_{j-1}^{-1} R_{j-1}. \quad (25)$$

The brief explanation of SRM to solve the system of equations (7) to (9) with boundary conditions (10) is provided in this section. Gauss Seidel approach is utilized in this method to linearize and decouple a system of differential equations. We have denoted the current iteration label by $(r+1)$ and the previous iteration which is assumed to be known is denoted by r . For applying SRM algorithm, we have assumed the following:

$$f'_{r+1} = p_r, f_{r+1}(0) = 0 \quad (26)$$

The linearised and decoupled form of equations (7) to (9) with boundary conditions (10) is given by:

$$p_{r+1}'' + f_{r+1} p_{r+1}' - \frac{2M}{n+1} p_{r+1} = \frac{2n}{n+1} p_r^2 - \quad (27)$$

$$\frac{2Ms}{n+1} - \frac{2\lambda}{n+1} (\theta_{r+1} - Nr\phi_{r+1}) - \frac{2n}{n+1} s^2$$

$$\frac{1}{Pr} \theta_{r+1}'' + f_{r+1} \theta_{r+1}' + \alpha \theta_{r+1} = -Nt(\theta_r')^2 - \quad (28)$$

$$Nb\theta_r' \phi_r' - Ec(p_{r+1}')^2 - \frac{2MEc}{n+1} (p_{r+1} - s)^2$$

$$\phi_{r+1}'' + Scf_{r+1} \phi_{r+1}' = -\frac{Nt}{Nb} \theta_{r+1}'' \quad (29)$$

with the boundary conditions:

$$\left. \begin{aligned} p_{r+1}(\eta) = 1, Nb\phi_{r+1}'(\eta) + Nt\theta_{r+1}'(\eta) = 0, \\ \theta_{r+1}(\eta) = 1, \text{ at } \eta = 0, \\ p_{r+1}(\eta) \rightarrow s, \phi_{r+1}(\eta) \rightarrow 0, \\ \theta_{r+1}(\eta) \rightarrow 0, \text{ as } \eta \rightarrow \infty. \end{aligned} \right\} \quad (30)$$

To solve these decoupled equations, Chebyshev spectral collocation technique was used in which domain is transformed from the interval $[0, L^*]$ to $[-1, 1]$, with suitable transformation where L^* is scaling parameter. Equations (26) to (29) can be transformed as follows:

$$A_1 f_{r+1} = B_1, A_2 p_{r+1} = B_2,$$

$$A_3 \theta_{r+1} = B_3, A_4 \phi_{r+1} = B_4,$$

where

$$A_1 = D^1, B_1 = p_r,$$

$$A_2 = D^2 + \text{diag}(f_{r+1})D - \text{diag}\left(\frac{2M}{n+1}\right)I,$$

$$B_2 = \frac{2n}{n+1} p_r^2 - \frac{2Ms}{n+1} - \frac{2\lambda}{n+1} (\theta_{r+1} - Nr\phi_{r+1}) - \frac{2ns^2}{n+1},$$

$$A_3 = \text{diag}(1/\text{Pr})D^2 + \text{diag}(f_{r+1})D + \text{diag}(\alpha)I,$$

$$B_3 = -\text{Nt}(\theta'_r)^2 - \text{Nb}\theta'_r\phi'_r - \text{Ec}(p'_{r+1})^2$$

$$-\frac{2\text{MEc}}{n+1}(p_{r+1}-s)^2,$$

$$A_4 = D^2 + \text{diag}(\text{Sc}f_{r+1})D, B_4 = -\frac{\text{Nt}}{\text{Nb}}\theta'_{r+1}.$$

Here $\text{Diag}()$ and I are diagonal and identity matrices, respectively, of order $(P+1)\times(P+1)$, where P is the number of grid points. The initial guess that is chosen to solve equations (26) to (29) that satisfies boundary condition (30) is given by:

$$f_0 = 1-s + s\eta - (1-s)e^{-\eta}, p_0 = s + (1-s)e^{-\eta},$$

$$\theta_0(\eta) = e^{-\eta}, \phi_0(\eta) = -\frac{\text{Nt}}{\text{Nb}}e^{-\eta}.$$

SOLUTION ERROR (SRM)

The solution error method is used to check the convergence of the solutions. In this method, the norm of the difference of the solution at various iterations is calculated and if this value tends to very small then the method converges. The errors [36] in the solution of $f(\eta)$, $\theta(\eta)$, and $\phi(\eta)$ are given as:

$$\text{errorF} = P f_{r+1}^{n+1} - f_r^{n+1} P_\infty,$$

$$\text{errorT} = P \theta_{r+1}^{n+1} - \theta_r^{n+1} P_\infty,$$

$$\text{errorG} = P \phi_{r+1}^{n+1} - \phi_r^{n+1} P_\infty.$$

The errors in the solutions are portrayed in Figs. 1(b)-1(d). After fifty iterations we got the minimum error.

VALIDATION OF APPROXIMATE SOLUTION

To validate our results, we have compared skin friction and local Nusselt number for different input parameters *via* two different approaches, SLM and SRM which are presented in Tables 1 and 2.

There is an excellent agreement between the results obtained by these schemes. In addition to it, a comparison of local Nusselt number between our results and those of Ishfaq *et al.* [37] was performed by nullifying extra parameters (see table 3). Excellent agreement between them leads to improvement of the present solutions.

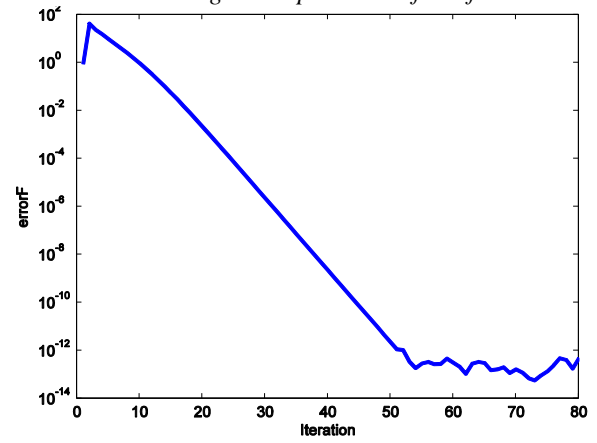


Fig 1(b). Solution error for $f(\eta)$

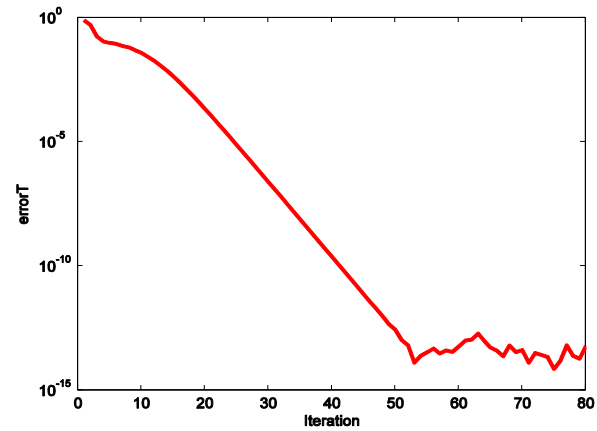


Fig 1(c). Solution error for $\phi(\eta)$

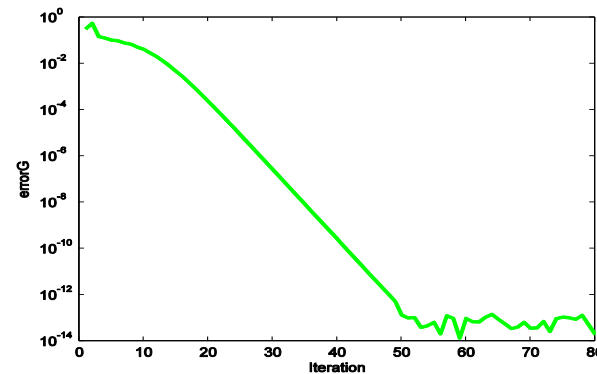


Fig 1(d). Solution error for $\theta(\eta)$.

Table 1. Values of skin friction and local Nusselt number for different flow parameters by SLM

M	λ	Sc	Nt	Nb	s	$Cf_x Re_x^{1/2}$ (SLM)	$Nu_x Re_x^{-1/2}$ (SLM)	CPU Time (Sec)
1						1.15150341	-1.37468956	3.247
3						0.88942638	-1.27033132	5.965
5						0.65057101	-1.18196765	8.742
	0					-1.12725825	-1.09985601	3.321
	5					-0.02590419	-1.2873988	6.231
	10					1.01728621	-1.32014235	8.796
		1				1.02180356	-1.40933744	2.987
		2				1.01355207	-1.36085112	5.654
		4				1.02375922	-1.2854098	8.215
			0.1			0.9111903	-1.41121177	3.984
			0.2			1.01728621	-1.32014235	6.742
			0.3			1.12567155	-1.22570304	9.281
				0.1		1.12872826	-1.29920906	2.946
				0.2		1.01728621	-1.32014235	5.852
				0.3		0.97949569	-1.32637838	8.742
					0.5	1.01728621	-1.32014235	4.511
					1	2.13083584	-1.50721597	6.423
					1.5	3.71647164	-1.2249959	9.836

Table 2. Values of skin friction and local Nusselt number for different flow parameters by SRM

M	λ	Sc	Nt	Nb	s	$Cf_x Re_x^{1/2}$ (SRM)	$Nu_x Re_x^{-1/2}$ (SRM)	CPU Time (Sec)
1						1.151512	-1.37463	4.852
3						0.889423	-1.27035	7.499
5						0.650573	-1.18198	10.842
	0					-1.127248	-1.09981	3.427
	5					-0.025904	-1.2873	6.732
	10					1.017285	-1.32017	9.537
		1				1.021802	-1.40931	5.632
		2				1.013553	-1.36082	8.432
		4				1.0237129	-1.2854	11.211
			0.1			0.91119	-1.41121	3.673
			0.2			1.017285	-1.32017	5.763
			0.3			1.125673	-1.22570	7.834
				0.1		1.128729	-1.29924	3.984
				0.2		1.017285	-1.32017	5.975
				0.3		0.979474	-1.32632	9.392
					0.5	1.017285	-1.32017	4.521
					1	2.130834	-1.50724	8.291
					1.5	3.716474	-1.2249	11.211

Table 3. Comparison of local Nusselt number $Nu_x Re_x^{-1/2}$ with Ishfaq *et al.* [37] when Nb = 0.1 and Sc = 10

Nt	Pr = 14.2		Pr = 21	
	Present result (SLM)	Ishfaq <i>et al.</i> [37]	Present result (SLM)	Ishfaq <i>et al.</i> [37]
0.1	2.48347	2.4835	3.02857	3.0286
0.2	2.18151	2.1815	2.61673	2.6167
0.3	1.89587	1.8959	2.22533	2.2253
0.4	1.63714	1.6371	1.87618	1.8762
0.5	1.41258	1.4126	1.58418	1.5842

RESULTS AND DISCUSSION

The numerical computation of the present model is performed in this article by using two different schemes, i.e. SRM and SLM, for selected flow controlling parameters such as M, Nb, Ec, etc. For the current study default values of input parameters for numerical simulation are taken as M

= 2, n = 1, λ = 10, Nr = 0.2, s = 0.5, Pr = 6.2, Nb = 0.2, Nt = 0.2, Ec = 0.1, Sc = 3, and α = 0.2 until otherwise stated. In table 1 it is clearly depicted that parameters λ , Nt, s have a tendency to enhance skin friction at the surface while parameters M and Nb have the reverse effect on it. The parameters M, Sc and Nt show a decreasing nature for local

Nusselt number but λ and Nb have tendency to enhance the rate of heat transfer in magnitude.

The distribution of velocity with various flow controlling parameters is displayed in figures 1(e) to 1(h).

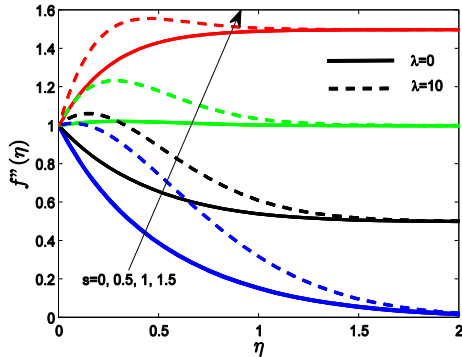


Fig1(e). Velocity profiles for different values of s

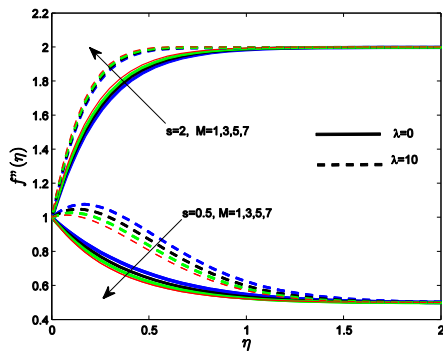


Fig 1(f). Velocity profiles for different values of M

The velocity distribution for disparate values of the stagnation parameter along with the mixed convection parameter is portrayed in Fig. 1(e). It is suggested here that when a free stream is moving faster than the stretching velocity, i. e. $s > 1$, the increment in s increases velocity distribution and the same effect is observed in $s < 1$ case. It is the main observing point here that in absence of a mixed convection parameter there is no boundary layer when stretching and free stream velocity are the same but in presence of mixed convection a boundary layer is observed to form and more precisely, the momentum boundary layer thickness tends to decrease as increment in s .

This phenomenon is the sole contribution of buoyancy forces acting on the flow-field. The nature of velocity for different values of M and two different values of s and λ is revealed in Fig. 1(f).

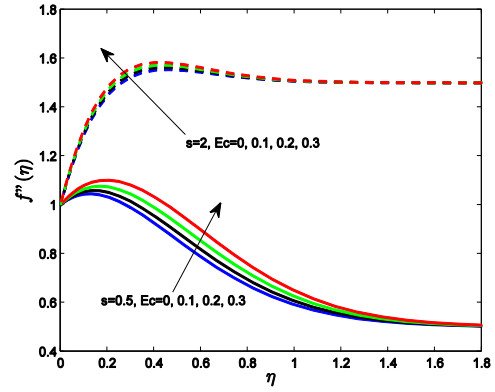


Fig 1(g). Velocity profiles for different values of Ec

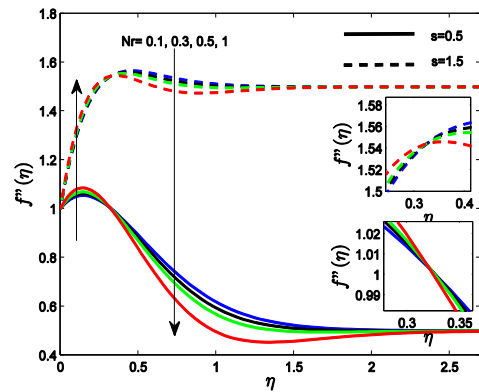


Fig 1(h). Velocity profiles for different values of Nr

It is widely accepted that M has a tendency to slow down the velocity because Lorentz force behaves as a resistive force that retards the motion. But in the present situation there is a dual nature of velocity for two different values of s . When $s > 1$, M acts as assisting parameter for flow while for $s < 1$, M has a tendency to decrease the velocity. This event is due to the fact that when $s > 1$ free stream velocity is dominant over stretching velocity. Tendency of M for $s > 1$ is also reported in [38, 39]. Fig. 1(g) displays the velocity distribution for various values of Eckert number. It is concluded from the figure that increment in parameter Ec boosts the velocity and increases boundary layer thickness due to an increment in kinetic energy. The velocity behaviour for parameter Nr is depicted in Fig. 1(h) which indicates a dual behaviour of buoyancy ratio parameter on fluid velocity, i. e. near the sheet velocity distribution increases and as going away from sheet, it acts as opposing parameter for the flow.

Figures 2(a) to 2(d) display the temperature distribution for various pertaining parameters.

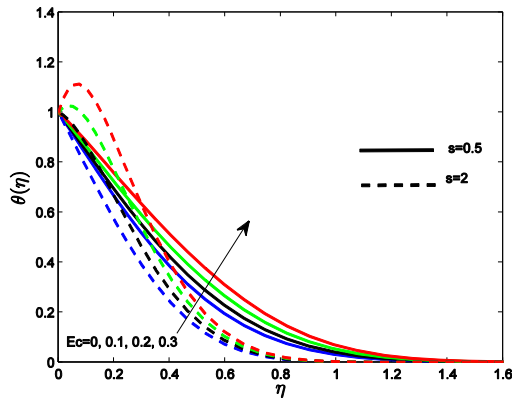


Fig 2(a). Temperature profiles for different values of Ec.

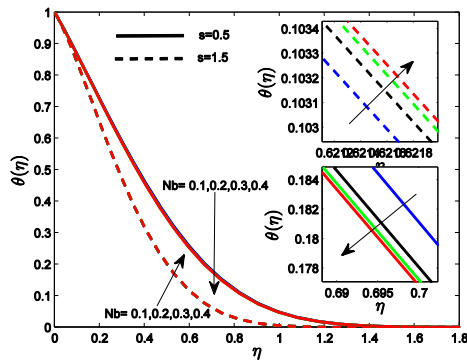


Fig 2(b). Temperature profiles for different values of Nb.

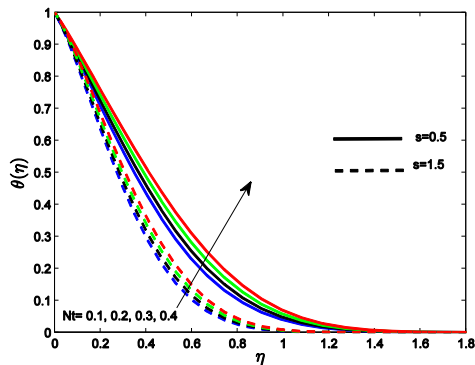


Fig 2(c). Temperature profiles for different values of Nt.

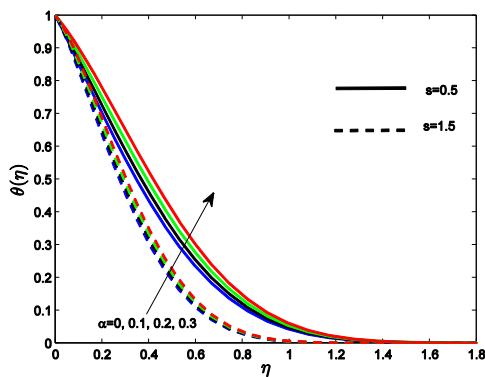


Fig 2(d). Temperature profiles for different values of alpha.

It is interesting to note from Figs. 2(a)-2(d) that the thermal boundary layer is thinner in case of $s > 1$ than that of $s < 1$. Fig. 2(a) illustrates the temperature profiles for various values of Ec. It can be seen here that when $s < 1$ or $s > 1$, increasing behaviour of temperature profile is found with an increase in Eckert number. When $s > 1$ a hump is found in the region near the sheet on increasing Ec, also fluid temperature approaches free stream value quicker for $s > 1$. This influence of Ec on the temperature profile is encountered due to the increasing nature of viscous and Joule dissipations. The tendency of viscous and Joule heating is to generate heat, which is due to friction between two adjacent electrically conducting fluid layers thereby increasing fluid temperature. Temperature distribution for different values of Brownian motion parameter is displayed in Fig. 2(b) which depicts the opposite nature of temperature towards Brownian motion parameter for $s < 1$, but for $s > 1$ Nb acts as assisting parameter for the temperature profile. Same behaviour of Nb for $s < 1$ is also found by Halim *et al.* [40]. The behaviour of temperature distribution towards parameter Nt can be seen in Fig. 2(c). The fact which is visualized here is that parameter Nt acts as assisting parameter for temperature distribution and significant increment is found in thermal boundary layer width. Increment in Nt means increase in thermophoretic phenomenon which is the particle analogous phenomenon. Therefore, nanoparticles transport thermal energy with increment in Nt due to collision of particles from hot surface into boundary layer, so increment in temperature is found. Fig. 2(d) displays the heat generation effect on the temperature profile which indicates that increment in temperature is found on increasing heat generation parameter. It is quite obvious that the heat source emits heat in the flow region, therefore, fluid temperature rises.

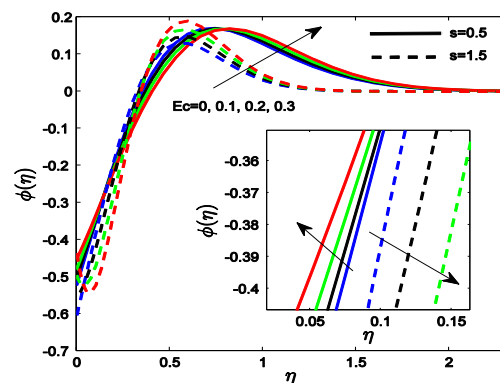


Fig 2(e). Concentration profiles for different values of Ec.

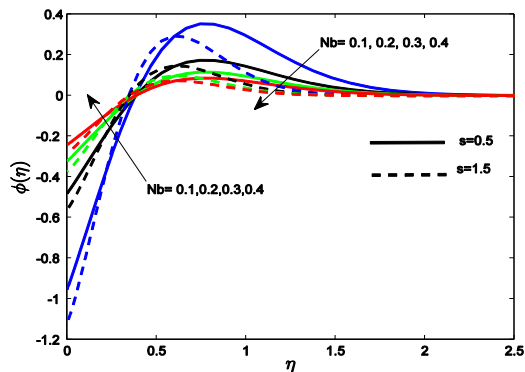


Fig 2(f). Concentration profiles for different values of Nb.

The concentration distribution for various values of input parameters is shown in Figs. 2(e) to 2(g). These profiles start with a negative value and after obtaining a positive peak they start approaching towards free stream. The numerical values of concentration are negative in the region close to the

stretching sheet. This may be due to passive control of species concentration and it is dominant in the region close to sheet than that in the region away from the sheet within the concentration boundary layer.

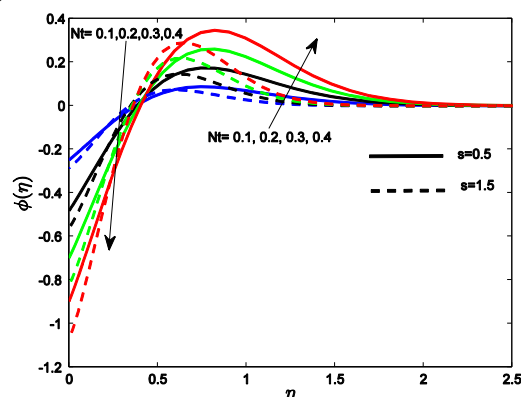


Fig 2(g). Concentration profiles for different values of Nt

Table 4. Error bound and quadratic regression coefficients for the estimated $Cf_x Re_x^{1/2}$

s	n	Cf	e ₁	e ₂	e ₃	e ₄	e ₅	m _f
0.5	1	-0.89501	-0.24844	0.44092	0.02051	-0.00262	-0.01327	2.55E-05
	2	-0.91406	-0.11542	0.22577	0.00418	-0.00107	-0.00375	5.21E-06
1.5	1	1.75346	0.14461	0.37040	-0.00036	0.00013	-0.0146	5.87E-04
	2	1.74464	0.073601	0.19009	-0.00098	-0.00031	-0.00387	2.60E-04

Fig. 2(e) presents the effect of parameter Ec on concentration distribution and it is visualised here that, when $s < 1$ initial concentration decreases in magnitude and when $s > 1$ initial increment in concentration is found but in both cases concentration profiles obtain a positive peak and finally tend to increase as approaching the free stream. This event is the contribution of increment in kinetic energy and reduction of nanoparticle migration as increment in Ec. Fig. 2(f) portrays the influence of Nb which indicates that enhancement in Nb tends to dilute concentration throughout the boundary layer because increment in Nb leads to increase the diffusion of nanoparticles inside the boundary layer. However, opposite impact of Nt can be seen from Fig. 2(g) because increment in Nt increases thermophoretic phenomena, which leads to weaken the transport of nanoparticles near the sheet. These two figures also suggest that when $s < 1$, this phenomenon is stronger than that when $s > 1$.

A QUADRATIC MULTIPLE REGRESSION MODEL

In this section estimation of skin friction is performed with the help of quadratic regression model. For performing it on skin friction we have

generated values of M and λ randomly from the set of 100 values that are taken from the interval [0.5 2] and [0 10], respectively, while values of other parameters are taken fixed. The approximated quadratic regression model for $Cf_x \sqrt{Re_x}$ is given as follows:

$$Cf_{est} = Cf + e_1 M + e_2 \lambda + e_3 M^2 + e_4 \lambda^2 + e_5 M \lambda, \quad (31)$$

Following formula is used to find the maximum relative error:

$$\epsilon_1 = |Cf_{est} - Cf| / |Cf|. \quad (32)$$

Table 4 presents the regression coefficients of this estimation along with the maximum relative error. It is visible from table 4 that whether free stream velocity is dominant over the stretching sheet or conversely, the regression coefficient of λ is greater than the regression coefficient of M which reflects that small variation in λ leads to larger perturbation in skin friction in comparison to M. It is also interesting to note that when n increases, the regression coefficients of both M and λ decrease in magnitude.

CONCLUSION

Throughout the present mathematical model of stagnation point nanofluid flow over stretching sheet, our main focus is to find flow controlling parameters effect on fluid velocity, concentration,

temperature along with skin friction and heat flux. The parameters s and Ec have tendency to enhance fluid velocity. Apart from it when $s < 1$ the magnetic parameter shows the obvious result, i.e. decrement in velocity distribution but when $s > 1$ the magnetic parameter acts as assisting parameter for fluid velocity. The parameter Nr enhances the velocity near the sheet but while approaching free stream it tends to decrease. Temperature distribution is enhanced due to increment in parameters Ec , Nt and α . The parameter Nb acts as assisting parameter for temperature for $s > 1$ while for $s < 1$, it acts as opposing parameter. Parameter Nb leads to dilute concentration throughout the boundary layer while thermophoretic parameter increases it.

REFERENCES

- H. Masuda, A. Ebata, K. Teramae, *Netsu Bussei*, **7**, 227 (1993).
- S. U. S. Choi, *ASME-Publications-Fed.*, **231**, 99 (1995).
- M. M. Rashidi, M. M. Bhatti, M. A. Abbas, M. E. Ali, *Entropy*, **18**, 117 (2016).
- M. A. Abbas, Y. Bai, M. M. Rashidi, M. M. Bhatti, *Entropy*, **18**, 90 (2016).
- T. Abbas, M. Ayub, M. M. Bhatti, M. M. Rashidi, M. E. Ali, *Entropy*, **18**, 223 (2016).
- B. C. Sakiadis, *AIChE J.*, **7**, 26 (1961).
- L. J. Crane, *Z. Angew. Math. Phys.*, **21**, 645 (1970).
- O. D. Makinde, A. Aziz, *Int. J. Therm. Sci.*, **50**, 1326 (2011).
- M. M. Bhatti, T. Abbas, M. M. Rashidi, *J. Magn.*, **21**, 468 (2016).
- M. Khan, A. Shahid, M. Malik, T. Salahuddin, *J. Mol. Liq.*, **251**, 7 (2018).
- B. J. Gireesha, B. Mahanthesh, G. Thammanna, P. Sampathkumar, *J. Mol. Liq.*, **256**, 139 (2018).
- S. Gupta, D. Kumar, J. Singh, *Int. J. Heat Mass Transf.*, **118**, 378 (2018).
- A. Y. Ghaly, *Chaos, Solitons Fract.*, **13**, 1843 (2002).
- O. D. Makinde, W. A. Khan, Z. H. Khan, *Int. J. Heat Mass Transf.*, **62**, 526 (2013).
- M. M. Rashidi, M. Nasiri, M. S. Shadloo, Z. Yang, *Heat Transfer Eng.*, **38**, 853 (2017).
- M. Waqas, M. Farooq, M. I. Khan, A. Alsaedi, T. Hayat, T. Yasmeen, *Int. J. Heat Mass Transf.*, **102**, 766 (2016).
- G. S. Seth, R. Tripathi, R. Sharma, A. J. Chamkha, *J. Mech.*, **33**, 87 (2017).
- V. M. Job, S. R. Gunakala, *Int. J. Heat Mass Transf.*, **120**, 970 (2018).
- M. Mustafa, T. Hayat, I. Pop, S. Asghar, S. Obaidat, *Int. J. Heat Mass Transf.*, **54**, 5588 (2011).
- K. U. Rehman, A. A. Khan, M. Y. Malik, O. D. Makinde, *J. Braz. Soc. Mech. Sci. Eng.*, **39**, 3669 (2017).
- M. M. Rashidi, N. Freidoonimehr, *Int. J. Comput. Meth. Eng. Sci. Mech.*, **5**, 345 (2014).
- G. S. Seth, B. Kumar, R. Nandkeolyar, *J. Nanofluids*, **8**, 620 (2019).
- I. C. Nelson, D. Banerjee, R. Ponnappan, *J. Thermophys. Heat Tr.*, **23**, 752 (2009).
- J. Buongiorno, L. W. Hu, S. J. Kim, R. Hannink, B.A.O. Truong, E. Forrest, *Nucl. Technol.*, **162**, 80 (2008).
- S. M. You, J. H. Kim, K.H. Kim, *Appl. Phys. Lett.*, **83**, 3374 (2003).
- D. P. Kulkarni, D. K. Das, R. S. Vajjha, *Appl. Energ.*, **86**, 2566 (2009).
- A. Sharma, V. V. Tyagi, C. R. Chen, D. Buddhi, *Renew. Sust. Energ. Rev.*, **13**, 318 (2009).
- X. Sun, Z. Liu, K. Welsher, J. T. Robinson, A. Goodwin, S. Zaric, H. Dai, *Nano Res.*, **1**, 203 (2008).
- T. P. Otanicar, P. E. Phelan, R. S. Prasher, G. Rosengarten, R. A. Taylor, *J. Renew. Sustain. Energ.*, **2**, 033102 (2010).
- J. Zhou, Z. Wu, Z. Zhang, W. Liu, Q. Xue, *Tribol. Lett.*, **8**, 213 (2000).
- A. V. Kuznetsov, D. A. Nield, *Int. J. Therm. Sci.*, **77**, 126 (2014).
- G. K. Batchelor, *An Introduction to Fluid Dynamics*, Cambridge University Press, Cambridge, 1988.
- S. W. Yuan, *Foundations of fluid mechanics*, Prentice Hall, 1967.
- S. S. Motsa, P. Sibanda, *Comput. & Math. with Appl.*, **63**, 1197 (2012).
- S. S. Motsa, Z. Makukula, *Open Phys.*, **11**, 363 (2013).
- R. Nandkeolyar, M. Narayana, S. S. Motsa, P. Sibanda, *J. Therm. Sci. Eng. Appl.*, **10**, 061005 (2018).
- N. Ishfaq, Z. H. Khan, W. A. Khan, R. J. Culham, *J. Hydrodyn. Ser. B*, **28**, 596 (2016).
- G. S. Seth, R. N. Jana, M. K. Maiti, *Revue Roumaine des Sci. Tech. Ser. de Mécanique Appliquée*, **26**, 383 (1981).
- S. Sarkar, G. S. Seth, *J. Aerosp. Eng.*, **30**, Article ID 16081 (2016).
- N. A. Halim, R. U. Haq, N. F. M. Noor, *Meccanica*, **52**, 1527 (2017).

NOMENCLATURE

a, b	arbitrary constants	S	stagnation parameter
B	magnetic field, T	T	fluid temperature, K
C	nanoparticle volume fraction, kg / m^3	T_s	fluid temperature at stretching sheet, K
Cf_x	skin friction coefficient	T_∞	ambient fluid temperature, K
C_∞	ambient species concentration, kg / m^3	u	fluid velocity component in the x direction, ms^{-1}
c_p	specific heat at a constant pressure, $\text{J kg}^{-1} \text{K}^{-1}$	u_s	stretching velocity, ms^{-1}
D_B	coefficient of Brownian diffusion	u_∞	free stream fluid velocity, ms^{-1}
D_T	coefficient of thermophoretic diffusion	v	fluid velocity component in the y direction, ms^{-1}
Ec	Eckert number	x, y	coordinate directions, m
f	stream function	α	heat generation parameter
g	gravitational acceleration, ms^{-2}	β	nanofluid volumetric expansion coefficient, K^{-1}
k	thermal conductivity, $\text{Wm}^{-1}\text{K}^{-1}$	$\theta(\eta)$	dimensionless temperature
Sc	Schmidt number	μ	dynamic viscosity, $\text{kg m}^{-1} \text{s}^{-1}$
M	magnetic parameter	ν	kinematic viscosity, m^2s^{-1}
Nb	Brownian motion parameter	ρ_{nf}	nanofluid density, kg m^3
Nr	buoyancy ratio parameter	$\rho_{nf\infty}$	nanofluid reference density, kg m^3
Nt	thermophoretic parameter	ρ_{np}	density of nanoparticles, kg m^3
Nu_x	local Nusselt number	$(\rho c_p)_{nf}$	nanofluid heat capacity
n	constant	$(\rho c_p)_{np}$	nanoparticles heat capacity
Pr	Prandtl number	σ	electric conductivity, S m^{-1}
Q	heat generation coefficient	λ	mixed convection parameter
q_s	heat flux at the surface, Wm^{-2}	τ_s	surface shear stress N m^{-2}
Re_x	local Reynolds number	$\phi(\eta)$	dimensionless concentration

Computer modelling and optimization of the structure-activity relationship by using surface fitting methods

F. I. Sapundzhi

South-West University "Neofit Rilski", 2700 Blagoevgrad, Bulgaria

Received March 18, 2019, Accepted June 1, 2019

Mu-opioid receptor (MOR) is an attractive target for computer modelling because it plays an important role as a pain-relieving drug. The main objective of the present work was to find a function for modelling of the structure-activity relationship (SAR) of a series of mu-opioid ligands and the results from *in silico* docking with a model of MOR (PDBid:4dkl). The relationship of the biological activity of the ligands with the optimization functions from docking experiments and with the total energies (MolDock optimization function) was modelled using a response surface methodology. Our analysis indicates that the third-order polynomial could be successfully used for modelling SAR between the biological effect of the mu-opioid ligands and results from docking. Docking studies could help to better understand the relationship between *in vitro* biological effects and docking studies and to answer whether the models of the biological macromolecules (in our case MOR) correspond to the real 3D structures.

Keywords: Computer modelling, Response surface methodology, QSAR, Docking, Ligand-receptor interaction, Mu-opioid receptor.

INTRODUCTION

Endogenous opioid systems play a critical role in modulating a large number of sensory, motivational, emotional, and cognitive functions. Endogenous opioid peptides (EOP) are small molecules that are naturally produced in the central nervous system and in various glands throughout the body. They function both as hormones and as neuromodulators. Through these mechanisms, EOP produce physiological effects as preventing diarrhea to inducing, euphoria, analgesia, etc.

Computer modelling and structure-activity relationship approaches have played an important role in the search and prediction of new biologically active ligands based on the properties of the drugs with known biological activities. The discovery of novel potent and selective ligands to MOR is related to a large amount of investigations with enkephalin and dalargin analogues [1-4]. The enkephalins are EOP and they are typically assigned to mu-, kappa-, and delta- opioid receptors. In recent years *in silico* drug design has extensive impact in the field of drug discovery and natural sciences [5,6]. Design of selective and effective ligands for MOR is related for most researchers with different enkephalin and dalargin analogues. These analogues were synthesized and biologically tested in previous studies by Pencheva *et. al* [7,8]. Computer modelling and docking experiments with investigated ligands were presented in [9,10,11].

The main purpose of this study is to investigate the relationship between the values of the biological activity of the investigated ligands and the results of the *in silico* docking and also to calculate the minimum energy conformation for each obtained ligand-receptor complex after the docking procedure. We try to find a function with two variables such as $z = f(x, y)$ from some class of polynomials, that fits given n distinct data points $\{(x_i, y_i, z_i)\}_{i=1}^n$ in R^3 using response surface methodology. Researches in this direction are presented in the publications [9-15].

MATERIALS AND METHODS

Objects

- *Receptor-MOR:* A model of mu-opioid receptor (MOR) with crystal structure published in RCSB Protein Data Base (www.rcsb.org) (PDBid:4dkl) was used.

- *Ligands:* A series of mu-opioid ligands investigated for their potency to MOR with *in vitro* bioassay in a previous study [7,8] were selected for docking studies with the model of MOR. The ligands are presented in Table 1.

- *Software*

Docking procedure: The structures of the mu-opioid ligands were prepared for docking in software Avogadro (open source, <http://avogadro.openmolecules.net/>).

* To whom all correspondence should be sent:
E-mail: sapundzhi@swu.bg

The total energies for the obtained ligand-receptor complexes after docking procedure in GOLD 5.2 [16,17] were calculated by the software Molegro Molecular Viewer (MMV Version 2.5) using MolDock optimization function [18].

Table 1. Ligands used in this study. The potency is the concentration which produces 50% of the maximal response of the tissue – IC_{50} [7,8].

Ligands	IC_{50}
[Cys(O ₂ NH ₂) ² -Met ⁵]-enk	1378
Dalargin	12.3
Dalarginamide	5.8
Dalarginethylamide	6
DAMGO	5.8
[L-Ala ²]-dalargin	234
[Leu ⁵]-enkephalin	65.3
[Met ⁵]-dalargin	11.9
[Met ⁵]-enkephalin	28.6
N-Me-[L-Phe ⁴]-dalarginamide	0.57

• *Surface fitted methodology:* The surface fitting of the experimental data with Curve Fitting Toolbox of MATLAB [19] can be presented as follows:

$$(1) \min_{(a_{00}, \dots, a_{0n})} F(a_{00}, \dots, a_{0n}) = \sum_{s=1}^m \left(z_s - \sum_{0 \leq i+j \leq n} a_{ij} x_s^i y_s^j \right)^2$$

$$(2) z = \sum_{0 \leq i+j \leq n} a_{ij} x^i y^j$$

where:

- s - number of points;
- m - number of ligand-receptor complexes;
- z - dependent variable;
- x, y - independent variables;
- z_1, z_2, \dots, z_n - represent the values of *in vitro* parameters;
- x_1, x_2, \dots, x_n - represent the results from the docking procedure (scoring functions);
- y_1, y_2, \dots, y_n - represent the total energies for the ligand-receptor complexes;
- a_{ij} - parameters of the model;
- n - degree of the polynomial ($0 \leq i + j \leq n$), which gives the number of coefficients to be fit and the highest power of the predictor variable.

To investigate the fitting behaviour of the degree of some polynomial functions, a set of fittings was carried out, starting from the first-degree to the third-degree polynomial. The Surface Fitting Toolbox of MATLAB was applied for analysing

the behaviour of one variable which depended on more independent variables and the individual model could be interpreted as a surface fitting function of the experimental data by the least squares method [20] (<http://www.mathworks.com/products/matlab>). The following parameters were used to evaluate the goodness of fit:

- *SSE (Sum of squares due to error):*

$$(3) SSE = \sum_{i=1}^n \omega_i (y_i - \hat{y}_i)^2$$

where: y_i is the measured value of the data, \hat{y}_i is the predicted value, n - the number of performed experiments, ω_i is the relative weight of each data point, usually $\omega_i = 1$. The value of *SSE* close to 0 shows that the model has a smaller random error component and the fit will be more useful for prediction [19,20].

- *R-Square (R^2)* – the square of the correlation between the response values and the predicted response values. R^2 is the square of the multiple correlation coefficient and the coefficient of multiple determination.

$$(4) R^2 = \frac{SSR}{SST} = 1 - \frac{SSE}{SST};$$

$$SSR = \sum_{i=1}^n \omega_i (\hat{y}_i - \bar{y}_i)^2$$

$$SST = \sum_{i=1}^n \omega_i (y_i - \bar{y}_i)^2$$

The values of R^2 closer to 1 indicate that a greater proportion of variance is accounted for by the model [20].

$$(5) Adjusted R^2 = 1 - \frac{SSE}{SST}$$

Adj R² is the best indicator of the fit quality when two models are compared. This parameter can take any value less than or equal to 1, with a value closer to 1 indicating a better fit.

- *RMSE (Root Mean Squared Error)*

$$(6) RMSE = s = \sqrt{MSE}$$

RMSE represents the standard error of the regression and is an estimate of the standard deviation of the random component in the data. *MSE* is the mean square error or the residual mean

F. I. Sapundzhi: Modelling and optimization of the structure-activity relationship by surface fitting methods
square. The values of *RMSE* closer to 0 indicate a fit that is more useful for prediction [21].

RESULTS AND DISCUSSION

For the purpose of the *in silico* docking the crystal structure of MOR was obtained from RCSB (PDB id:4dkl). From the literature the binding sites of MOR are known [22]. These are the residues within a radius of about 10 Å of the asparagine (Asp) acid residue located in the transmembrane helix 3 - Asp147. Computer modelling and molecular docking experiments with MOR and the investigated ligands (Table 1) were carried out with the software GOLD 5.2 and all optimization functions: ASP, ChemPLP, GoldScore, ChemScore functions [16,17]. These functions were used to rank the mu-opioid ligand conformations by evaluating the binding density of each of the probable complexes.

In order to investigate the appropriate relationship between biological activity of the mu-opioid ligands and docking results (the values of the optimization functions) the Surface Curve Fitting Toolbox in software MATLAB was applied. The total energies of the formed ligand-receptor complexes after *in silico* docking were calculated by MolDock scoring function in software MMV 2.5 [21-25].

Parametric curves used in computer graphics are often based on polynomials. For surfaces, *X*, *Y*, and *Z* must be matrices with the same number of elements – in our case ten data points. Sizes are compatible if *X* is a vector of length *n*, *Y* is a vector of length *m* and *Z* is a 2D matrix of size [*m*, *n*]. The Curve Fitting application expects inputs where $length(X) = n$, $length(Y) = m$ and $size(Z) =$

[*m*, *n*]. By applying the polynomial least squares surface fitting technique, a first- to a third-order polynomial was fitted to the experimental data in *R*³. Experimental data were modelled by polynomials with varying degrees of *x* and *y*. The polynomial models have the following equations:

$$\text{Poly11: } f(x, y) = a_{00} + a_{10}x + a_{01}y$$

$$\text{Poly12: } f(x, y) = a_{00} + a_{10}x + a_{01}y + a_{11}xy + a_{02}y^2$$

$$\text{Poly21: } f(x, y) = a_{00} + a_{10}x + a_{01}y + a_{11}xy + a_{20}x^2$$

$$\text{Poly22: } f(x, y) = a_{00} + a_{10}x + a_{01}y + a_{20}x^2 + a_{11}xy + a_{02}y^2$$

$$\text{Poly13: } f(x, y) = a_{00} + a_{10}x + a_{01}y + a_{11}xy + a_{02}y^2 + a_{12}xy^2 + a_{03}y^3$$

$$\text{Poly31: } f(x, y) = a_{00} + a_{10}x + a_{01}y + a_{20}x^2 + a_{11}xy + a_{30}x^3 + a_{21}x^2y$$

$$\text{Poly32: } f(x, y) = a_{00} + a_{10}x + a_{01}y + a_{20}x^2 + a_{11}xy + a_{02}y^2 + a_{30}x^3 + a_{21}x^2y + a_{12}xy^2$$

$$\text{Poly23: } f(x, y) = a_{00} + a_{10}x + a_{01}y + a_{20}x^2 + a_{11}xy + a_{02}y^2 + a_{21}x^2y + a_{12}xy^2 + a_{03}y^3$$

The experimental data can be represented as follows:

- 1) the values of *z* represent the values of *IC*₅₀;
- 2) the values of *x* represent the docking results from GOLD - the values of ASP, ChemPLP, ChemScore and GoldScore functions;
- 3) the values of *y* represent the total energies calculated from MMV for ligand-receptor complex forming after the docking - the values of MolDock function [20].

Table 2. The experimental data for the ASP function and MolDock function.

Ligands	IC ₅₀	ASP Score	MolDock
[Cys(O ₂ NH ₂) ² -Met ⁵]-enk	1378	42.64	272.726
Dalargin	12.3	45.69	496.613
Dalarginamide	5.8	48.04	743.587
Dalarginethylamide	6	49.94	438.743
DAMGO	5.8	45.97	77.749
[L-Ala ²]-dalargin	234	46.93	73.823
[Leu ⁵]-enkephalin	65.3	41.59	430.507
[Met ⁵]-dalargin	11.9	48.95	769.467
[Met ⁵]-enkephalin	28.6	46.98	439.083
N-Me-[L-Phe ⁴]-dalarginamide	0.57	42.61	632.829

Table 3. The experimental data for ChemPLP function and MolDock function.

Ligands	IC ₅₀	ChemPLP	MolDock
[Cys(O ₂ NH ₂) ² -Met ⁵]-enk	1378	85.24	-113.502
Dalargin	12.3	100.41	-162.681
Dalarginamide	5.8	97.06	-148.977
Dalarginethylamide	6	92.08	-157.038
DAMGO	5.8	80.67	-29.582
[L-Ala ²]-dalargin	234	84.69	-10.891
[Leu ⁵]-enkephalin	65.3	85.89	-133.004
[Met ⁵]-dalargin	11.9	98.6	-145.639
[Met ⁵]-enkephalin	28.6	87.64	-144.788
N-Me-[L-Phe ⁴]-dalarginamide	0.57	79.34	-76.62

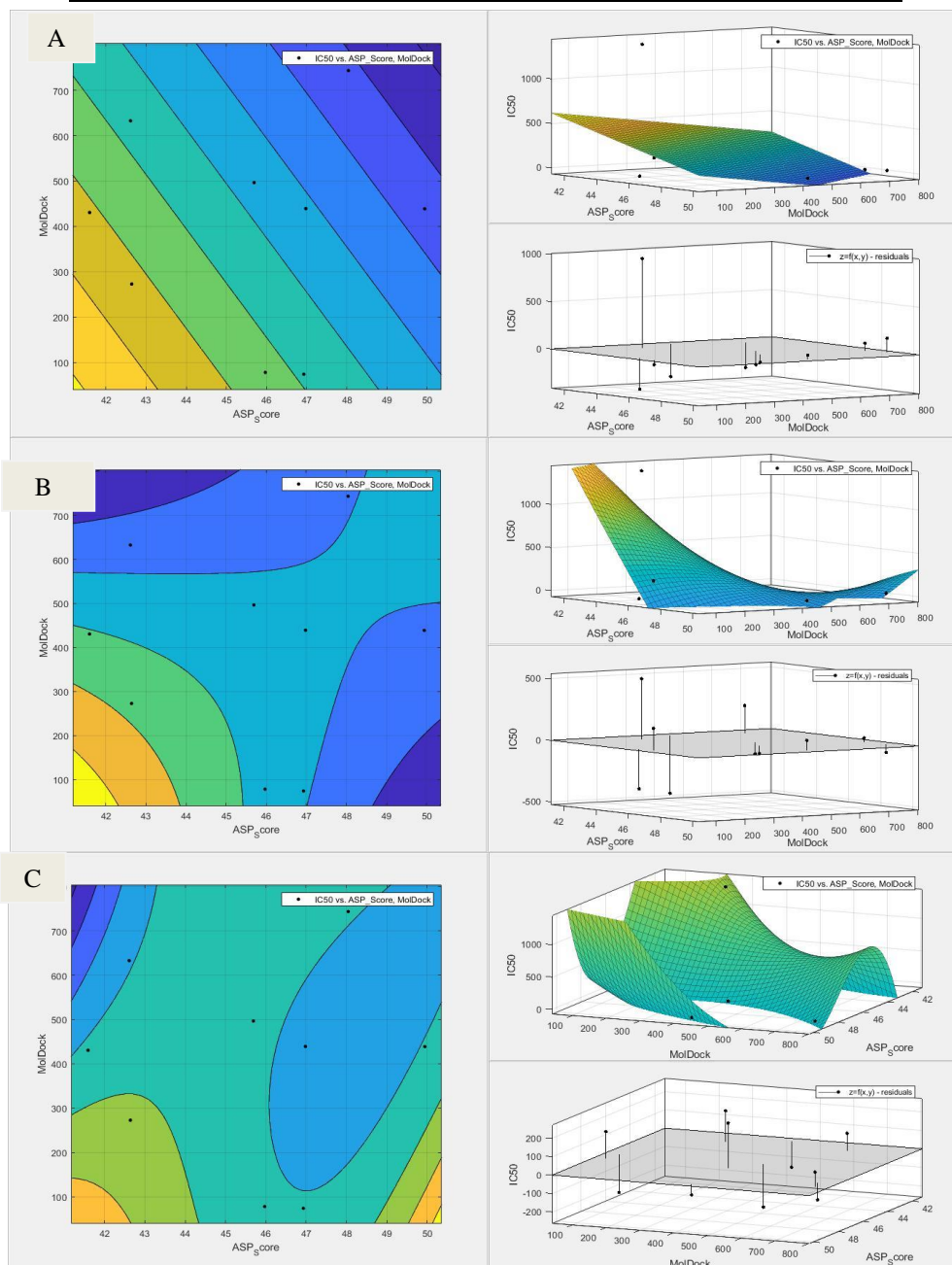


Figure 1. 3D plot of the experimental data with first to third degree of polynomials, which represent the biological activity of the ligands as a function of the values of ASP scoring function from GOLD and the values of the total energies– MolDock function. The plots represent the *Residuals Plot* and *2D contour plot* of the 3D surface for the obtained polynomial models.

Table 4. The experimental data for ChemScore function and MolDock function.

Ligands	IC ₅₀	ChemScore	MolDock
[Cys(O ₂ NH ₂) ² -Met ⁵]-enk	1378	19.6	-107.904
Dalargin	12.3	20.67	-135.245
Dalarginamide	5.8	28.75	-148.221
Dalarginethylamide	6	29.02	-163.106
DAMGO	5.8	14.31	-93.278
[L-Ala ²]-dalargin	234	21.28	-130.171
[Leu ⁵]-enkephalin	65.3	25.95	-148.483
[Met ⁵]-dalargin	11.9	23.27	-173.298
[Met ⁵]-enkephalin	28.6	25.11	-120.651
N-Me-[L-Phe ⁴]-dalarginamide	0.57	20.08	-107.216

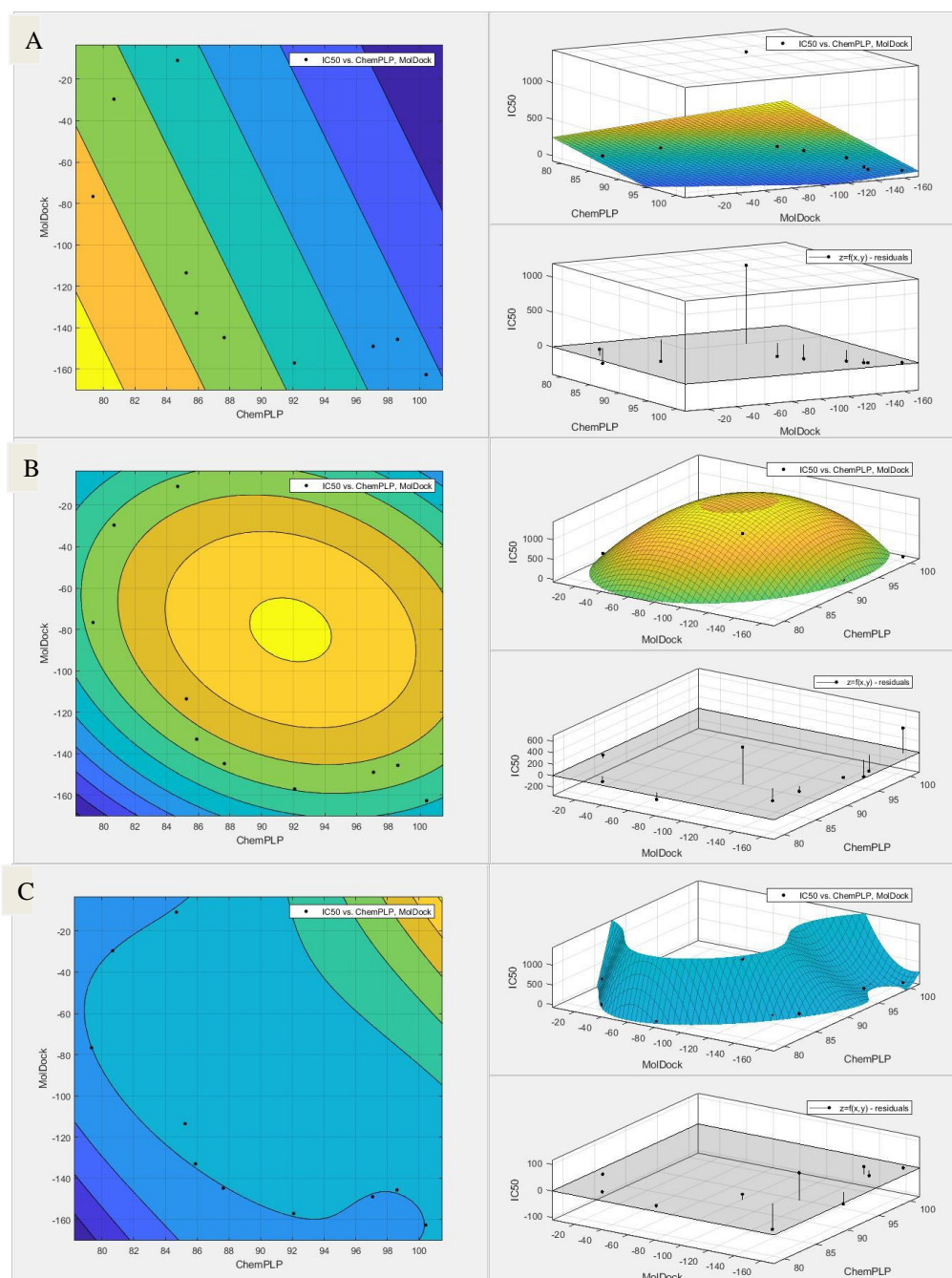


Figure 2. 3D plot of the experimental data with first to third degree of polynomials, which represent the IC_{50} of the ligands as a function of the values of ChemPLP function from GOLD and the values of the total energies – MolDock function. The plots represent the Residuals Plot and 2D contour plot of the 3D surface for the obtained polynomial models.

Table 5. The experimental data for GoldScore function and MolDock function.

Ligands	IC ₅₀	GoldScore	MolDock
[Cys(O ₂ NH ₂) ² -Met ⁵]-enk	1378	94,39	-227,91
Dalargin	12,3	81,75	-75,84
Dalarginamide	5.8	95.4	-238.1
Dalarginethylamide	6	100.37	6.29
DAMGO	5.8	75.37	-169.4
[L-Ala ²]-dalargin	234	53.13	-96.83
[Leu ⁵]-enkephalin	65.3	95.27	-106.4
[Met ⁵]-dalargin	11.9	95.43	-146.42
[Met ⁵]-enkephalin	28.6	89.48	-105.67
N-Me-[L-Phe ⁴]-dalarginamide	0.57	77.04	-89.527

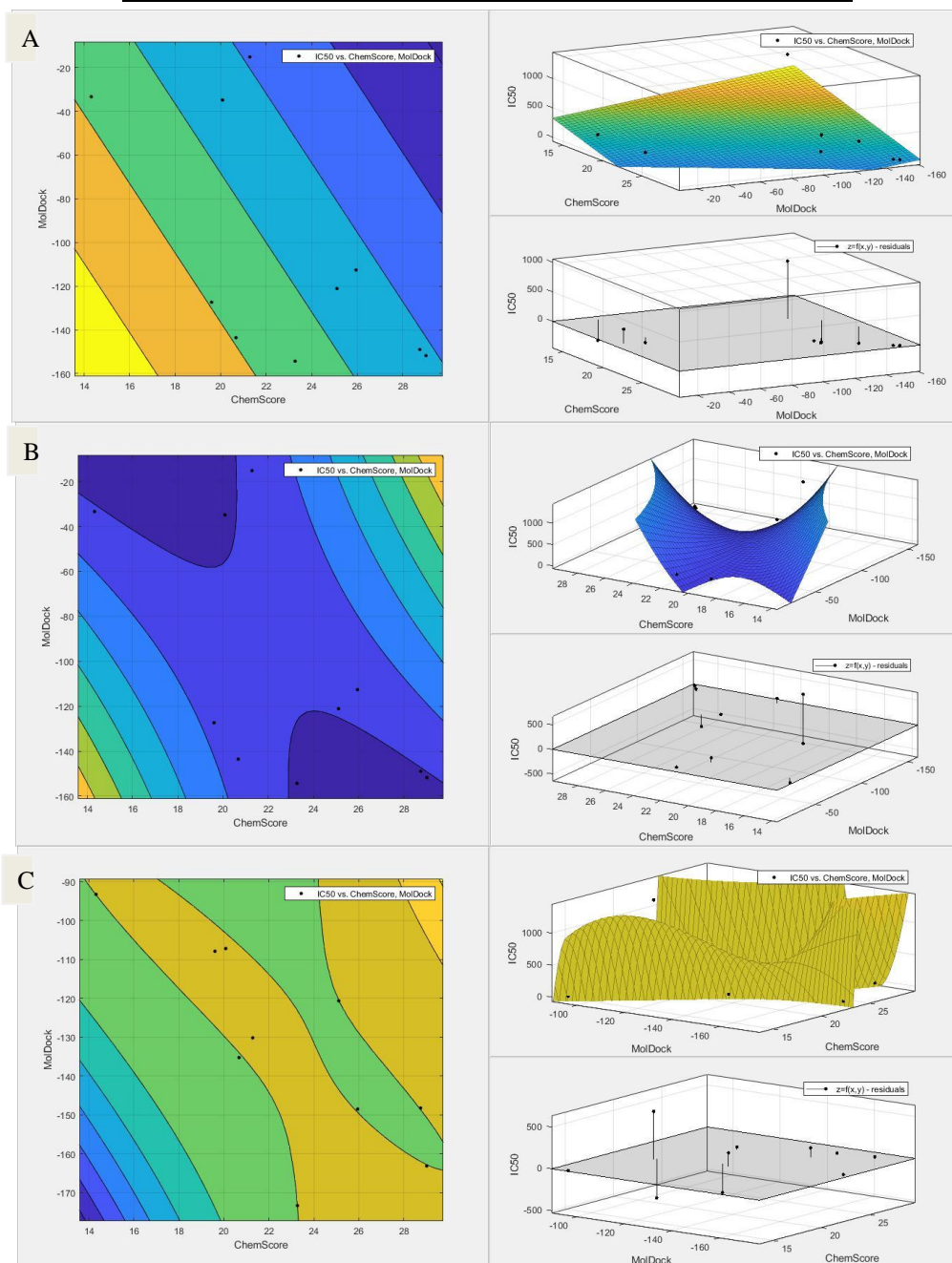


Figure 3. 3D plot of the experimental data with first to third degree of polynomials, which represent the IC₅₀ of the ligands as a function of the values of ChemScore function from GOLD and the values of the total energies – MolDock function. The plots represent the *Residuals Plot* and *2D contour plot* of the 3D surface for the obtained polynomial models.

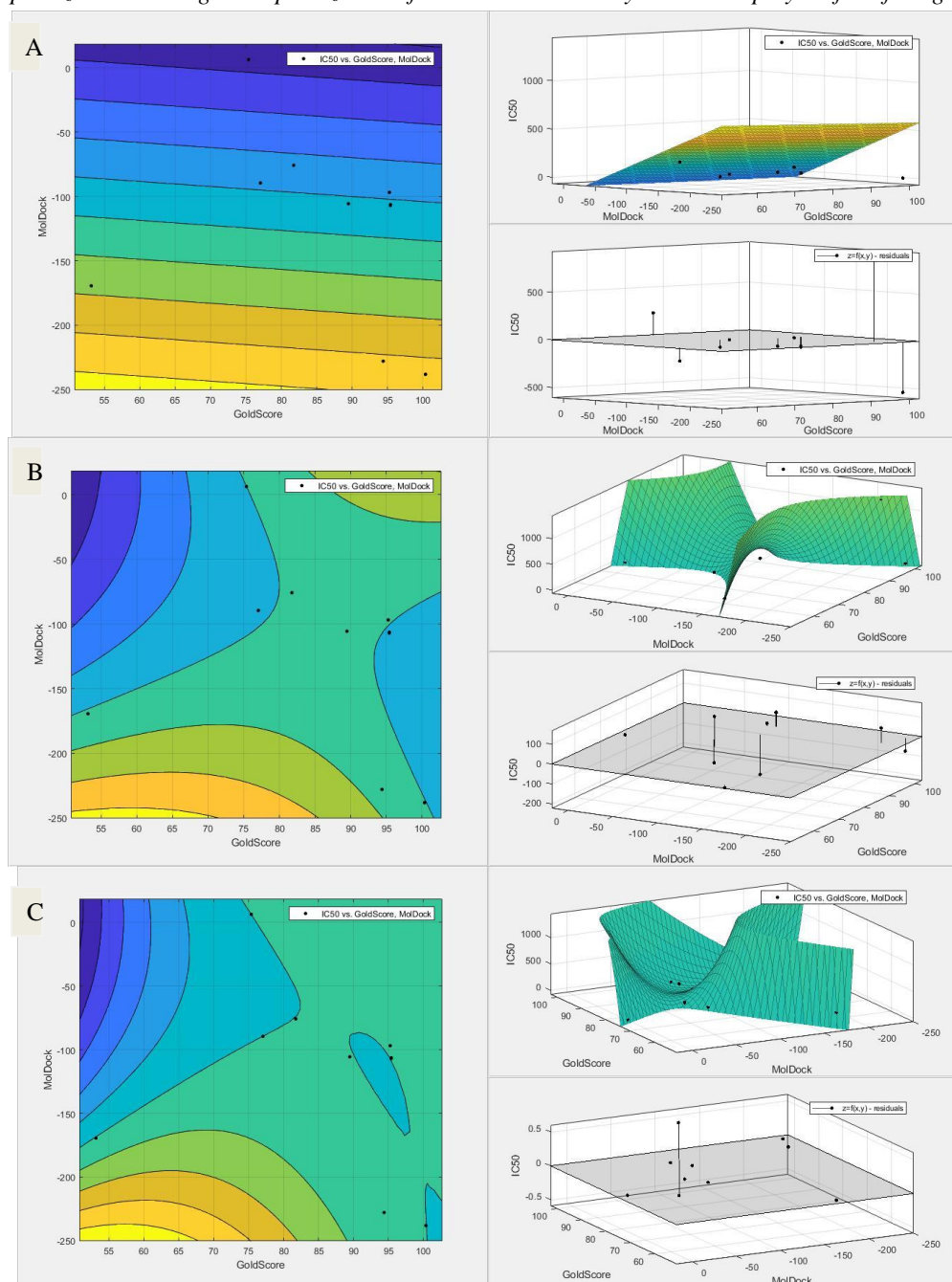


Figure 4. 3D plot of the experimental data with first to third degree of polynomials, which represent the IC_{50} of the ligands as a function of the values of GoldScore function from GOLD and the values of the total energies – MolDock function. The plots represent the *Residuals Plot* and *2D contour plot* of the 3D surface for the obtained polynomial models.

All polynomial models from first to third degree were evaluated on how well they fitted the data and how precisely they could predict. The models were estimated with the statistical criteria of goodness of fit – SSE , R^2 , *adjusted R^2* , $RMSE$. The obtained results for the statistic parameters are presented in Table 6. The best results of the parameters used for surface fitting in MATLAB can be represented as follows: the values of z represent the values of IC_{50} , the values of x represent the values of GoldScore function from GOLD and the values of y represent the values of the total energies for ligand-receptor

complexes – MolDock optimization function from MMV. As can be seen from the results in Table 6 the goodness of fit statistics shows that the obtained model for fitting of the experimental data for GoldScore with the third degree for x and the second degree for y is a good one – Poly32. This model is with the highest value of $R^2 = 1$ for MOR and the value closer to 1 indicating that a greater proportion of variance is explained by the model. The values of $SSE=0.580$ for the polynomial model Poly32 are less than 1. This value shows that the model has a smaller random error component and

the fit will be more useful for prediction. The values of $Adj R^2$ for the model Poly32 are less than 1. This statistic parameter is a good indicator of the fit quality when two models are compared and with a value closer to 1 indicating a better fit. The values of the $RMSE=0.761$ for model Poly32 are less than

1 and indicate a fit that is more useful for prediction. This shows that the obtained polynomial model for the surface fitting data is a good model, it explains a high proportion of the variability in experimental data, and is able to predict new observations with high certainty [8-15].

Table 6. The goodness of fit for the polynomial models obtained by the least squares method in MATLAB for all optimization functions from docking experiments.

Degree (x, y)	ASP function			
	<i>SSE</i>	R^2	<i>Adj R</i> ²	<i>RMSE</i>
11	1.268	0.233	0.01382	425.7
12	6.908	0.582	0.428	371.7
21	7.34	0.556	0.201	383.1
13	2.226	0.865	0.596	272.4
31	3.673	0.777	0.333	349.9
22	6.895	0.583	0.061	415.2
32	2.613	0.842	-0.4224	511.2
23	1.031	0.937	0.439	321
Degree (x, y)	ChemPLP function			
	<i>SSE</i>	R^2	<i>Adj R</i> ²	<i>RMSE</i>
11	1.551	0.061	-0.206	470.8
12	1.035	0.373	-0.126	455
21	1.242	0.248	-0.352	498.4
13	8.768	0.4697	-0.590	540.6
31	1.082	0.345	-0.963	600.6
22	9.068	0.451	-0.233	476.1
32	2.534	0.984	0.8621	159.2
23	7568	0.9954	0.9588	86.99
Degree (x, y)	ChemScore function			
	<i>SSE</i>	R^2	<i>Adj R</i> ²	<i>RMSE</i>
11	1.466	0.113	-0.140	457.7
12	1.402	0.152	-0.525	529.5
21	1.145	0.307	-0.246	478.6
13	1.112	0.327	-1.017	608.8
31	9.738	0.411	-0.766	569.7
22	1.142	0.309	-0.553	534.3
32	7.267	0.56	-2.96	853
23	7.817	0.5273	-3.255	884.1
Degree (x,y)	GoldScore function			
	<i>SSE</i>	R^2	<i>Adj R</i> ²	<i>RMSE</i>
11	1.145	0.307	0.109	404.4
12	9.93	0.399	-0.081	445.6
21	9.014	0.454	0.018	424.6
13	3.349	0.979	0.939	105.7
31	7.404	0.9552	0.865	157.1
22	1.006	0.939	0.863	158.6
32	0.580	1	1	0.761
23	3.293	1	1	1.815

Table 7. The mean values (confidence bounds) of the coefficients of the polynomial models for all scoring functions.

F. I. Sapundzhi: Modelling and optimization of the structure-activity relationship by surface fitting methods

Coefficients of the models	Mean (with 95% confidence bounds)			
	<i>Poly11</i>	<i>ASP</i>	<i>ChemPLP</i>	<i>ChemScore</i>
a_{00}	174.8 (-143.5, 493.1)	174.8 (-177.2, 526.8)	915.5 (-1065, 2896)	174.8 (-127.6, 477.2)
a_{10}	-154.7 (-496.5, 187.1)	-145.6 (-688.6, 397.4)	-0.2719 (-122, 121.5)	-18.51 (-347, 310)
a_{01}	-111 (-452.8, 230.8)	-68.19 (-611.2, 474.8)	5.533 (-15.84, 26.9)	-241.5 (-570, 86.98)
Poly12				
a_{00}	187.1 (-261, 635.2)	821.8 (-312.4, 1956)	196 (-500.6, 892.6)	19.22 (-575.9, 614.3)
a_{10}	-204 (-560.1, 152.1)	386.4 (-658.4, 1431)	31.81 (-865.2, 928.8)	94.85 (-588.7, 778.4)
a_{01}	-247 (-623.2, 129.3)	809.3 (-805.8, 2424)	210.7 (-721.3, 1143)	-182.9 (-628.1, 262.2)
a_{11}	426.7 (-111.7, 965)	452.5 (-505.8, 1411)	133.6 (-614.1, 881.3)	248.3 (-957, 1454)
a_{02}	-95.01 (-473, 283)	-388.5 (-1310, 532.6)	77.86 (-789, 944.7)	232.8 (-541.1, 1007)
Poly21				
a_{00}	60.8 (-438.2, 559.8)	462.9 (-337.5, 1263)	284.2 (-235.4, 803.7)	407.6 (-288.7, 1104)
a_{10}	-213.9 (-590.5, 162.7)	142.7 (-773.4, 1059)	127.5 (-595.6, 850.7)	-342.5 (-1152, 467.1)
a_{01}	-227.8 (-609.3, 153.6)	357.8 (-890.1, 1606)	243.7 (-422.5, 910)	-438.7 (-1033, 155.5)
a_{20}	52.29 (-375.6, 480.2)	162.3 (-928.7, 1253)	-555.3 (-1867, 755.9)	-252.4 (-853.1, 348.2)
a_{11}	390.2 (-150.5, 930.9)	660.6 (-1227, 2548)	-572 (-2195, 1051)	25.74 (-519.7, 571.2)
Poly22				
a_{00}	167.6 (-657.9, 993.1)	1167 (-640, 2974)	304.6 (-517.9, 1127)	371.2 (89.77, 652.6)
a_{10}	-200.1 (-647.3, 247)	531.2 (-764.8, 1827)	108.6 (-894.3, 1111)	-321.9 (-648.6, 4.736)
a_{01}	-249.7 (-711.8, 212.5)	1015 (-961.7, 2991)	219.9 (-796.3, 1236)	-568.3 (-816.3, -320.3)
a_{20}	16.84 (-520.2, 553.9)	-521.7 (-2446, 1403)	-577 (-2257, 1102)	-708.8 (-1039, -378.5)
a_{11}	423.3 (-234.8, 1081)	-272.7 (-3159, 2614)	-621.3 (-2965, 1722)	1382 (679.7, 2085)
a_{02}	-89.48 (-578.5, 399.5)	-780 (-2560, 1000)	-38.4 (-1042, 965.2)	824.3 (418.8, 1230)
Poly13				
a_{00}	158.8 (-276.6, 594.3)	1409 (-2429, 5247)	234.4 (-983.9, 1453)	-289.3 (-767.5, 188.8)
a_{10}	-40 (-445.3, 365.3)	1219 (-4430, 6867)	-116 (-1891, 1659)	587.6 (316.5, 858.8)
a_{01}	-1972 (-4721, 777.5)	3271 (-1.026e+04, 1.68)	970.2 (-4172, 6112)	607.7 (-549.8, 1765)
a_{11}	-348.1 (-1843, 1147)	1841 (-6129, 9810)	-630.8 (-5514, 4252)	-543 (-1274, 188.4)
a_{02}	399.2 (-314.9, 1113)	1121 (-6928, 9169)	-588 (-5994, 4818)	268.2 (-304.8, 841.2)
a_{12}	-272.4 (-1110, 565.4)	95.85 (-1828, 2020)	-45.43 (-2676, 2585)	-2563 (-3446, -1679)
a_{03}	1164 (-593.2, 2921)	-1258 (-8341, 5824)	-689 (-5876, 4498)	-1414 (-2097, -730.9)
Poly31				
a_{00}	223.2 (-428.8, 875.2)	367 (-911.6, 1646)	189 (-690.7, 1069)	366.9 (22.73, 711)
a_{10}	-703.9 (-2078, 669.9)	-341.2 (-3027, 2344)	-203.8 (-2306, 1898)	223.6 (-572, 1019)
a_{01}	-66.77 (-742.2, 608.7)	240 (-1721, 2202)	143.7 (-952, 1239)	-865.7 (-1448, -284)
a_{20}	2.19 (-491, 495.3)	66.34 (-1944, 2077)	-512.8 (-3160, 2134)	-425.5 (-1508, 657.1)
a_{11}	406.2 (-268.3, 1081)	465.3 (-3158, 4088)	-615.1 (-3491, 2261)	-374.6 (-873.3, 124.2)
a_{30}	302 (-434.4, 1038)	206.1 (-1970, 2382)	466.5 (-2046, 2979)	-495.9 (-1043, 51.49)
a_{21}	-239.9 (-1138, 658.1)	-99.04 (-3350, 3152)	435.7 (-2778, 3649)	957.6 (174.2, 1741)
Poly32				
a_{00}	107.9 (-5450, 5665)	1855 (-1383, 5093)	421.8 (-8336, 9180)	516.8 (483.2, 550.5)
a_{10}	-969.4 (-1.617e+04, 1.424)	-369.5 (-3464, 2725)	-1171 (-2.608e+04, 2.374)	-1551 (-1680, -1423)
a_{01}	212.8 (-6959, 7385)	2074 (-2484, 6632)	-331.4 (-1.373e+04, 1.307)	-1535 (-1628, -1441)
a_{20}	55.06 (-3116, 3226)	-1546 (-6211, 3119)	-2092 (-4.102e+04, 3.684)	208.9 (159.1, 258.7)
a_{11}	174.1 (-6338, 6686)	-1384 (-1.011e+04, 7343)	-3278 (-6.486e+04, 5.83)	3076 (2864, 3288)
a_{02}	198.3 (-5595, 5991)	-875.1 (-6346, 4596)	-921.5 (-2.2e+04, 2.016)	1280 (1215, 1345)
a_{30}	434.4 (-6797, 7666)	1312 (-6512, 9136)	3538 (-6.532e+04, 7.239)	1262 (1117, 1406)
a_{21}	-651.7 (-1.043e+04, 9123)	2162 (-1.636e+04, 2.068)	7456 (-1.476e+05, 1.625)	-823.7 (-1002, -645.9)
a_{12}	182 (-1.024, 1.061e+04)	2340 (-1.064e+04, 1.532)	4276 (-9.045e+04, 9.9)	-983.2 (-1124, -842.7)
Poly23				
a_{00}	248.3 (-3526, 4022)	2716 (-636.1, 6068)	587.8 (-1.111e+04, 1.228)	61.97 (5.138, 118.8)
a_{10}	-47.46 (-1995, 1900)	1669 (-3961, 7300)	475.7 (-1.723e+04, 1.818)	-110.2 (-202.6, -17.83)
a_{01}	-1997 (-1.867e+04, 1.468)	6528 (-8424, 2.148e+04)	1749 (-3.361e+04, 3.711)	-267.8 (-403.8, -131.8)
a_{20}	-94.89 (-2443, 2253)	-1277 (-4198, 1644)	-975.7 (-2.485e+04, 2.29)	-148.3 (-194, -102.7)
a_{11}	-618.2 (-8522, 7286)	1504 (-1.073e+04, 1.374)	-2601 (-5.809e+04, 5.288)	720.5 (551.5, 889.5)
a_{02}	549 (-3418, 4516)	1743 (-8543, 1.203e+04)	-1818 (-4.463e+04, 4.099)	620.3 (560.2, 680.4)
a_{21}	-349.5 (-6542, 5844)	-1636 (-4580, 1309)	-466.7 (-1.841e+04, 1.748)	482 (391.5, 572.5)
a_{12}	-211.3 (-4228, 3805)	-1099 (-5758, 3560)	-1475 (-3.462e+04, 3.167)	-676 (-929.5, -422.5)
a_{03}	1344 (-8493, 1.118e+04)	-2921 (-1.178e+04, 5941)	-1703 (-3.951e+04, 3.61)	-471.5 (-599.9, -343.1)

By using a polynomial least squares surface fitting technique, a third order for x and second order for y were fitted to the data (Poly32). The coefficients of the surface fitting for MOR by

polynomials from first to third degree for all scoring functions in 3D are presented in Table 7.

The best results for fitting of experimental data according to the results in Tables 2-5 were obtained or surface fitting by a polynomial model Poly32 in 3D for determining the relationship between biological activities and docking results of the investigated compounds. By using a polynomial least squares surface fitting technique, a polynomial model of third order for x and of second order for y was fitted to the data and it is represented as follows:

$$f(x, y) = a_{00} + a_{10}x + a_{01}y + a_{20}x^2 + a_{11}xy + a_{02}y^2 + a_{30}x^3 + a_{21}x^2y + a_{12}xy^2$$

where: x is normalized by mean 85.76 and standard deviation 14.31 and y is normalized by mean -121 and standard deviation 72.99.

After analysing the results from Table 6 we can conclude that the best values were obtained for the potency of the mu-opioid ligands as a function of the values of GoldScore function and the values of the total energies (MolDock function) for the formed ligand-receptor complexes for a polynomial model of third order for x and of second order for y (Poly32). The established values of the statistical parameters are important because they give the best description of the fitting of the experimental data for MOR with polynomials of two variables. Surface curve fitting gives detailed account of interrelation of dependent variable with respect to independent variables. In the present work, one dependent and two independent variables were considered to evolve the best fit model. The Curve fitting finds the values of the coefficients (parameters) which make a function match the data as closely as possible. The best values of the coefficients are known when the value of R^2 becomes 1. The fitting models and methods used here depend on the input data set.

CONCLUSIONS

In this work, two dependent variables and one independent variable data points were taken into consideration for fitting the 3D graph. The obtained model for the experimental data showed good fitting properties and significant predictive ability. Therefore, this model of a third-degree polynomial is suitable to determine the relationship structure-biological activity. The GoldScore and MolDock optimization functions could be used for describing the biological activity of newly designed compounds. This would be helpful in shortening the drug design process.

Acknowledgment: This paper is partially supported by SWU "Neofit Rilski", Bulgaria, Project RPY – B4/19; Project of the National Science Fund of Bulgaria, BNSF H27/36; National Scientific Program "Information and Communication Technologies for a Single Digital Market in Science, Education and Security (ICTinSES)", financed by the Ministry of Education and Science.

REFERENCES

1. P. Law, Y. Wong, H. Loh, *Ann. Rev. Pharmacol.Toxicol.*, **40**, 389 (2000).
2. J. Lord, A. Waterfield, J. Hughes, H. Kosterlitz, *Nature*, **267**, 495 (1977).
3. J. Froehlich, *Alcohol Health Res. World*, **21**(2), 132 (1997).
4. R. Maldonado, R. Severini, W. Hans, B. Kiefer, P. Melchiorri, L. Negri, *British Journal of Pharmacology*, **132**, 1485 (2001).
5. R. Bodnar, *J. Peptides*, **60**, 65 (2013).
6. U. Rester, *Curr. Opin. Drug Discov. Devel.*, **11**, 559 (2008).
7. N. Pencheva, P. Milanov, L. Vezekov, T. Pajpanova, E. Naydenova, *Eur. J. Pharmacol.*, **498**, 249 (2004).
8. N. Pencheva, A. Bocheva, E. Dimitrov, C. Ivancheva, *Eur. J. Pharmacol.*, **304**, 99 (1996).
9. F. Sapundzhi, T. Dzimbova, N. Pencheva, P. Milanov, *Bulg. Chem. Commun.*, **2**, 613 (2015).
10. F. Sapundzhi, Mathematical and computer modelling of ligand-target interactions. PhD desertion. South-West University "Neofit Rilski", Blagoevgrad, Bulgaria (2015).
11. . I. Sapundzhi, Mathematical and computer modelling of drug-receptor interactions, , University Publishing house "Neofit Rilski", Blagoevgrad, ISBN 978-954-00-0190-6, 2019 (in Bulgarian).
12. F. I. Sapundzhi, Modeling of the interrelation structure – biological activity, University Publishing house "Neofit Rilski", Blagoevgrad, ISBN 978-954-00-0191-3, 2019 (in Bulgarian).
13. F. Sapundzhi, T. Dzimbova, N. Pencheva, P. Milanov, *Bulg. Chem. Commun.*, **49**, Special Issue E, 23 (2016).
14. F. Sapundzhi, T. Dzimbova, N. Pencheva, P. Milanov, *Bulg. Chem. Commun.*, **49**(4), 768 (2017).
15. F. Sapundzhi, T. Dzimbova, P. Milanov, N. Pencheva, *Journal of Computational Methods in Molecular Design*, **5**, 98 (2015).
16. GOLD, version 5.2 UserGuide, *CCDC Software Ltd.: Cambridge, UK*, 2010.
17. G. Jones, P. Willett, R. Glen, A. Leach, R. Taylor, *J. Mol. Biol.*, **267**, 727 (1997).
18. M. Verdonk, J. Cole, M. Hartshorn, C. Murray, R. Taylor. *Proteins*, **52**, 609 (2003).
19. <http://www.mathworks.com/products/matlab>
20. J. Shim, A. Coop, A. MacKerell, *J. Phys. Chem. B.*, **117** (26), 7907 (2013).
21. F. Sapundzhi, T. Dzimbova, N. Pencheva, P. Milanov, *Der Pharma Chemica*, **8**, 118 (2016).

22. F. Sapundzhi, T. Dzimbova, N. Pencheva, P. Milanov, *Bulg. Chem. Commun.*, **50**, Special Issue B, 44 (2018).
23. F. Sapundzhi, M. Popstoilov, *Bulg. Chem. Commun.*, **50**, Special Issue B, 115 (2018).
24. F. Sapundzhi, T. Dzimbova, N. Pencheva, P. Milanov. *Bulg. Chem. Commun.*, **50**, Special Issue B, 15 (2018).
25. F. Sapundzhi, *International Journal of Online and Biomedical Engineering*, **15 (12)**, 88-96, (2019).
26. F. Sapundzhi, *International Journal of Online and Biomedical Engineering*, **15 (11)**, 139-145, (2019).
27. F. Sapundzhi, T. Dzimbova, *International Journal of Online and Biomedical Engineering*, **15 (15)**, (2019), in press.
28. J. Clark, Y. Itzhak, V. Hruby, H. Yamamura, G. Pasternak, *Eur. J. Pharmacol.*, **128**, 303 (1986).
29. R. Reinscheid, H. Nothacker, A. Bourson, A. Ardati, R. Henningsen, J. Bunzow, D. Grandy, H. Langen, F. Monsma, O. Civelli, *Science*, **270**, 792 (1995).
30. R. Mavrevski, M. Traykov M., I. Trenchev, M. Trencheva, *WSEAS Transactions on Systems and Control*, **13**, 242 (2018).
31. K. Befort, L. Tabbara, S. Bausch, C. Chavkin, C. Evans, B. Kieffer, *Mol. Pharmacol.*, **49**, 216 (1996).
32. R. Thomsen, M. Christensen, *J. Med. Chem.*, **49**, 3315 (2006).
33. P. Lancaster, *Ser. C: Math. Phys. Sci.*, **49**, 91 (1979).
34. D. Sun, A. Whitty, J. Papadatos, M. Newman, J. Donnelly, S. Bowes, S. Josiah, *J. Biomol. Screen.*, **10**, 508 (2005).

Trifunctionalized allenes. Part II. A practical regioselective synthesis of 4-phosphorylated β -hydroxyallenecarboxylates

I. E. Ismailov, I. K. Ivanov, V. Ch. Christov*

Department of Chemistry, Faculty of Natural Sciences, Konstantin Preslavsky University of Shumen, 115 Universitetska St., 9712 Shumen, Bulgaria

Received March 25, 2019; Accepted May 19, 2019

Dedicated to Prof. Dr. Toru Minami from Kyushu Institute of Technology, Tobata, Kitakyushu, Japan, on the occasion of his 80th anniversary

The paper discusses a practical regioselective synthesis of 4-phosphorylated 6-hydroxyhepta-2,3-dienoates by an atom-economical [2,3]-sigmatropic rearrangement of the mediated ethyl 2-(dimethoxyphosphanyl)oxy- or 2-(diphenylphosphino)oxy-6-(tetrahydro-2*H*-pyran-2-yloxy)-hept-3-ynoates which can be easily prepared *via* reaction of the protected ethyl 2-hydroxy-6-(tetrahydro-2*H*-pyran-2-yloxy)-hept-3-ynoate with dimethyl chlorophosphite or chlorodiphenyl phosphine, respectively, in the presence of a base.

Keywords: synthesis, protection of hydroxy group, [2,3]-sigmatropic rearrangement, 4-phosphorylated 6-hydroxyhepta-2,3-dienoates.

INTRODUCTION

Allenes are considered to be unique compounds in organic chemistry due to their adjacent orthogonal π -bonds. During the last three decades synthesis and applications of allene derivatives have been increased in preparative organic chemistry. The availability of two π electron clouds that are separated by a single sp hybridized carbon atom is the main structural characteristic of allenes, and it is this unique structural and electronic arrangement that presupposes the extraordinary reactivity profile displayed by allenic compounds [1-5].

Functionalized allenes have provoked a growing interest because of their versatility as key building blocks for organic synthesis. Functionalized allenes could be used in a number of transformations due to their high reactive capacity. The synthetic capacity of functionalized allenes has been explored thoroughly in recent years, and this has led to the development of new methods in constructing a variety of functionalized heterocyclic and carbocyclic systems [6-11].

There are many methods which construct hydroxyallenes, including prototropic rearrangement of propargylic alcohols [12,13], metal-catalyzed nucleophilic addition of propargylic derivatives to aldehydes [14-18], Cu(I)-catalyzed reaction of propargylic chlorides with Grignard reagents [19,20], metal-catalyzed reaction of propargylic oxiranes with organometallic compounds [21-25] and ketones [26,27].

The most general methods for the synthesis of allenecarboxylates involve the Wittig [28-30], Wittig-Horner [31] or the Horner-Wadsworth-Emons [32] olefination of ketenes, iron-catalyzed olefination of ketenes with diazoacetate [33], etc. [34]. Also, there are methods for the synthesis of phosphorus-containing allenes (phosphonates [35-38], phosphinates [39,40], and phosphine oxides [41-46]) including reactions of α -alkynols with chloride-containing derivatives of phosphorus acids followed by [2,3]-sigmatropic rearrangement. Several diethylphosphono-substituted α -allenic alcohols were prepared by Brel [47,48] directly from alcohols by Horner-Mark rearrangement of unstable propargylic phosphites.

We have set in our research program on the chemistry of the trifunctionalized allenes to develop an efficient and regioselective method in order to introduce the phosphonate or phosphine oxide in the fourth-position, as well as the β -hydroxy group in the sixth position to the ester group of the allenecarboxylates. These groups provoke attention due to the useful functionalities in organic synthesis. More precisely, the focus is on the applications of these groups as temporary transformers of chemical reactivity of the allenic system in the synthesis of heterocyclic compounds.

Following our previous papers on the synthesis [49-52] and cyclization reactions [52-58] of bifunctionalized allenes, we have found a pragmatic synthesis of trifunctionalized allenes, namely the 4-phosphorylated β -hydroxyallenecarboxylates (4-phosphorylated 6-hydroxyhepta-2,3-dienoates).

* To whom all correspondence should be sent:
E-mail: vchristo@shu.bg

EXPERIMENTAL

General information

All newly synthesized compounds were purified by column chromatography and characterized on the basis of NMR, IR, and microanalytical data. NMR spectra were recorded on DRX Bruker Avance-250 (^1H at 250.1 MHz, ^{13}C at 62.9 MHz, ^{31}P at 101.2 MHz) and Bruker Avance II+600 (^1H at 600.1 MHz, ^{13}C at 150.9 MHz, ^{31}P at 242.9 MHz) spectrometers for solutions in CDCl_3 . All ^1H and ^{13}C NMR experiments were performed referring to the signal of internal TMS and ^{31}P NMR experiments were performed referring to the signal of external 85% H_3PO_4 . J values are given in Hertz. IR spectra were recorded with an FT-IR Afinity-1 Shimadzu spectrophotometer. Elemental analyses were carried out by the Microanalytical Service Laboratory using Vario EL3 CHNS(O). Column chromatography was performed on Kieselgel F25460 (70–230 mesh ASTM, 0.063–0.200 mm, Merck). Et_2O and THF were distilled from Na wire/benzophenone, CH_2Cl_2 was distilled over CaH_2 , and other organic solvents used in this study were dried over appropriate drying agents by standard methods and distilled prior to use. All other chemicals used in this study were commercially available and were used without additional purification unless otherwise noted. Reactions were carried out in oven-dried glassware under an argon atmosphere and exclusion of moisture. All compounds were checked for purity on TLC plates Kieselgel F₂₅₄ 60 (Merck). Procedure for the synthesis of the 2-(1-methyl-but-3-ynoxy)-tetrahydro-2H-pyran **2** (87% yield) by protection of the hydroxy-group in treatment of the pent-4-yn-2-ol **1** with DHP (3,4-dihydro-2H-pyran) in the presence of PPTS (pyridinium *p*-toluenesulfonate) as a catalyst is described in the literature [59–62].

Procedure for synthesis of ethyl 2-hydroxy-2-methyl-6-(tetrahydro-2H-pyran-2-yloxy)-hept-3-ynoate **5**

Ethylmagnesium bromide [prepared from magnesium (1.2 g, 50.0 mmol) and ethyl bromide (5.5 g, 50.0 mmol) in dry THF (50 mL)] was added dropwise under stirring to 2-(1-methyl-but-3-ynoxy)-tetrahydro-2H-pyran **2** (50.0 mmol) and then the mixture was refluxed for 2 h. The solution of the prepared alkynyl magnesium bromides was added dropwise under stirring to ethyl 2-oxopropanoate **4** (100.0 mmol). The mixture was refluxed for 2 h and after cooling was hydrolyzed with a saturated aqueous solution of ammonium chloride. The organic layer was separated, washed with water, and dried over anhydrous sodium sulfate. Solvent and the excess of the ester were

removed by distillation. Purification of the residue was achieved by column chromatography (silica gel, Kieselgel Merck 60 F254) with ethyl acetate-hexane. The pure product **5** had the following properties:

Ethyl 2-hydroxy-2-methyl-6-(tetrahydro-2H-pyran-2-yloxy)-hept-3-ynoate (5). Colourless oil, yield: 78%. Eluent for TLC: ethyl acetate:hexane = 1:9, R_f 0.48; IR (neat, cm^{-1}): 1123 (C–O–C), 1443, 1490 (Ph), 1723 (C=O), 2251 (C≡C), 3412 (OH). $^1\text{H-NMR}$ (250.1 MHz): δ_{H} 1.12–1.23, 3.64–3.74, 4.81–4.90 (overlapping multiplets, 9H, OTHP), 1.21 (t, $J=6.4$ Hz, 3H, MeCH_2O), 1.27 (d, $J=6.9$ Hz, 3H, MeCHO), 1.54 (s, 3H, MeC-OH), 2.64–2.73 (m, 2H, CH_2), 3.79–3.86 (m, 1H, OCHMe), 4.27–4.36 (m, 2H, OCH_2Me), 4.52 (s, 1H, OH). $^{13}\text{C-NMR}$ (62.9 MHz) δ_{C} 14.0 (CH_3), 19.1 (CH_2), 22.5 (CH_3), 25.7 (CH_3), 25.9 (CH_2), 26.2 (CH_3), 31.7 (CH_2), 62.5 (CH_2), 63.2 (CH_2), 72.1 (C), 76.2 (CH), 77.1 (C), 78.3 (C), 96.1 (CH), 165.8 (C). Anal. Calcd for $\text{C}_{15}\text{H}_{24}\text{O}_5$ requires: C 63.36, H 8.51. Found: C 63.42, H 8.55.

Procedure for synthesis of ethyl 4-(dimethylphosphoryl)-2-methyl-6-(tetrahydro-2H-pyran-2-yloxy)-hepta-2,3-dienoate **7**

To a solution of phosphorus trichloride (2.75 g, 20 mmol) and triethylamine (2.23 g, 22 mmol) in dry diethyl ether (60 mL) a solution of ethyl 2-hydroxy-2-methyl-6-(tetrahydro-2H-pyran-2-yloxy)-hept-3-ynoate **5** (20 mmol) in the same solvent (20 mL) was added dropwise at -70°C with stirring. After 30 min of stirring at the same conditions a solution of pyridine (3.16 g, 44 mmol) and of methanol (1.28 g, 40 mmol) in dry diethyl ether (50 mL) were added. The reaction mixture was stirred for an hour at the same temperature and for 4 h at room temperature. The mixture was then washed with water, 2N HCl, extracted with ether, washed with saturated NaCl, and dried over anhydrous sodium sulfate. After evaporation of the solvent, the residue was chromatographed on a column (silica gel, Kieselgel Merck 60 F₂₅₄) with a mixture of ethyl acetate and hexane as an eluent to give the pure product **7** as oil, which had the following properties:

Ethyl 4-(dimethylphosphoryl)-2-methyl-6-(tetrahydro-2H-pyran-2-yloxy)-hepta-2,3-dienoate (7). Orange oil, yield: 70%. Eluent for TLC: ethyl acetate:hexane = 1:4, R_f 0.43; IR (neat, cm^{-1}): 1125 (C–O–C), 1260 (P=O), 1439, 1491 (Ph), 1727 (C=O), 1952 (C=C=C). $^1\text{H-NMR}$ (600.1 MHz): δ_{H} 1.12–1.25, 3.64–3.77, 4.54–4.61 (overlapping multiplets, 9H, OTHP), 1.27 (t, $J=6.6$ Hz, 3H, MeCH_2O), 1.26–1.29 (m, 3H, Me-CHO), 1.89–1.94 (m, 3H, Me-C=), 2.47–2.64 (m, 2H, CH_2), 3.80 (d,

$J=12.7$ Hz, 6H, 2MeO), 4.06-4.14 (m, 2H, MeCH₂O), 4.36-4.43 (m, 1H, MeCHO). ¹³C-NMR (150.9 MHz) δ_c 14.1 (CH₃), 16.4 ($J=4.7$ Hz, CH₃), 19.0 (CH₂), 22.8 (CH₃), 24.6 (CH₂), 30.7 (CH₂), 37.5 ($J=5.6$ Hz, CH₂), 52.2 ($J=14.7$ Hz, CH₃), 59.8 (CH₂), 62.5 (CH₂), 69.2 ($J=8.1$ Hz, CH), 93.8 ($J=182.7$ Hz, C), 95.9 (CH), 97.1 ($J=7.8$ Hz, C), 166.9 ($J=5.0$ Hz, C), 218.0 ($J=0.8$ Hz, C). ³¹P-NMR (242.9 MHz): δ_p 24.9. Anal. Calcd for C₁₇H₂₉O₇P requires: C 54.25, H 7.77. Found: C 54.28, H 7.73.

Procedure for the synthesis of ethyl 4-(diphenylphosphinoyl)-2-methyl-6-(tetrahydro-2H-pyran-2-yloxy)-hepta-2,3-dienoate 9

To a solution of ethyl 2-hydroxy-2-methyl-6-(tetrahydro-2H-pyran-2-yloxy)-hept-3-ynoate **5** (20 mmol) and triethylamine (2.23 g, 22 mmol) in dry diethyl ether (60 mL) at -70°C, a solution of freshly distilled diphenylchloro phosphine (4.41 g, 20 mmol) in the same solvent (20 mL) was added dropwise with stirring. The reaction mixture was stirred for an hour at the same temperature and for 6 h at room temperature and then washed with water, 2N HCl, extracted with diethyl ether, and the extract was washed with saturated NaCl, and dried over anhydrous sodium sulfate. The solvent was removed using a rotatory evaporator, and the residue was purified by column chromatography on silica gel (Kieselgel Merck 60 F₂₅₄) with ethyl acetate-hexane to give the pure product **9** as oil, which had the following properties:

Ethyl 4-(diphenylphosphinoyl)-2-methyl-6-(tetrahydro-2H-pyran-2-yloxy)-hepta-2,3-dienoate (9). Colourless oil, yield: 76%. Eluent for TLC: ethyl acetate:hexane = 1:1, R_f 0.51; IR (neat, cm⁻¹): 1121 (C-O-C), 1178 (P=O), 1439, 1485 (Ph), 1715 (C=O), 1939 (C=C=C). ¹H-NMR (600.1 MHz): δ_H 1.11-1.24, 3.63-3.80, 4.56-4.63 (overlapping multiplets, 9H, OTHP), 1.24 (t, $J=6.8$ Hz, 3H, MeCH₂O), 1.28 (m, 3H, Me-CHO), 1.90-1.94 (m, 3H, Me-C=), 2.46-2.66 (m, 2H, CH₂), 4.11-4.22 (m, 2H, MeCH₂O), 4.27-4.37 (m, 1H, Me-CH), 7.46-7.94 (m, 10H, 2Ph). ¹³C-NMR (150.9 MHz) δ_c 14.3 (CH₃), 16.3 ($J=4.6$ Hz, CH₃), 19.0 (CH₂), 23.0 (CH₃), 25.4 (CH₂), 30.8 (CH₂), 39.8 ($J=6.0$ Hz, CH₂), 60.0 (CH₂), 62.8 (CH₂), 72.8 ($J=7.7$ Hz, CH), 93.6 ($J=183.2$ Hz, C), 94.8 (CH), 101.5 ($J=7.9$ Hz, C), 128.9-135.1 (2Ph), 166.5 ($J=5.0$ Hz, C), 211.5 ($J=0.6$ Hz, C). ³¹P-NMR (242.9 MHz): δ_p 31.3. Anal. Calcd for C₂₇H₃₃O₅P requires: C 69.22, H 7.10. Found: C 69.28, H 7.15.

Procedure for the synthesis of ethyl 4-(dimethylphosphoryl)-6-hydroxy-2-methyl-hepta-2,3-dienoate 10 and ethyl 4-(diphenylphosphinoyl)-6-hydroxy-2-methyl-hepta-2,3-dienoate 11

A solution of ethyl 4-(dimethylphosphoryl)-2-methyl-6-(tetrahydro-2H-pyran-2-yloxy)-hepta-2,3-dienoate **7** or ethyl 4-(diphenylphosphinoyl)-2-methyl-6-(tetrahydro-2H-pyran-2-yloxy)-hepta-2,3-dienoate **9** (5 mmol) and PPTS (0.5 mmol) in ethanol (10 mL) was stirred at room temperature for 5 h. The mixture was then washed with water, extracted with methylene chloride and dried over anhydrous sodium sulfate. After evaporation of the solvent, the residue was chromatographed on a column (silica gel, Kieselgel Merck 60 F₂₅₄) with a mixture of ethyl acetate and hexane as an eluent to give the pure products **10** or **11** as oils, which had the following properties:

Ethyl 4-(dimethylphosphoryl)-6-hydroxy-2-methyl-hepta-2,3-dienoate (10). Yellow oil, yield: 85%. Eluent for TLC: ethyl acetate:hexane = 1:4, R_f 0.62; IR (neat, cm⁻¹): 1260 (P=O), 1437, 1490 (Ph), 1724 (C=O), 1949 (C=C=C), 3392 (OH). ¹H-NMR (600.1 MHz): δ_H 1.16 (d, $J=6.1$ Hz, 3H, MeCHO), 1.25 (t, $J=6.2$ Hz, 3H, MeCH₂O), 1.87-1.92 (m, 3H, Me-C=), 2.50-2.70 (m, 2H, CH₂), 2.92 (s, 1H, OH), 3.79 (d, $J=12.9$ Hz, 6H, 2MeO), 4.07-4.15 (m, 2H, MeCH₂O), 4.31-4.37 (m, 1H, Me-CH). ¹³C-NMR (150.9 MHz) δ_c 14.3 (CH₃), 16.7 ($J=4.6$ Hz, CH₃), 23.2 ($J=4.7$ Hz, CH₃), 38.0 ($J=5.6$ Hz, CH₂), 52.1 ($J=14.9$ Hz, CH₃), 60.6 (CH₂), 61.5 ($J=7.9$ Hz, CH), 92.9 ($J=182.5$ Hz, C), 98.1 ($J=7.9$ Hz, C), 167.1 ($J=4.8$ Hz, C), 217.7 ($J=0.7$ Hz, C). ³¹P-NMR (242.9 MHz): δ_p 24.3. Anal. Calcd for C₁₂H₂₁O₆P requires: C 49.31, H 7.24. Found: C 49.26, H 7.20.

Ethyl 4-(diphenylphosphinoyl)-6-hydroxy-2-methyl-hepta-2,3-dienoate (11). Colourless oil, yield: 89%. Eluent for TLC: ethyl acetate:hexane = 1:2, R_f 0.62; IR (neat, cm⁻¹): 1179 (P=O), 1439, 1485 (Ph), 1719 (C=O), 1941 (C=C=C), 3389 (OH). ¹H-NMR (600.1 MHz): δ_H 1.20 (d, $J=6.1$ Hz, 3H, Me-CHO), 1.25 (t, $J=6.7$ Hz, 3H, MeCH₂O), 1.88-1.93 (m, 3H, Me-C=), 2.44-2.63 (m, 2H, CH₂), 2.84 (s, 1H, OH), 4.10-4.16 (m, 2H, MeCH₂O), 4.18-4.24 (m, 1H, Me-CHO), 7.43-7.88 (m, 10H, 2Ph). ¹³C-NMR (150.9 MHz) δ_c 14.4 (CH₃), 16.0 ($J=4.7$ Hz, CH₃), 22.8 ($J=4.6$ Hz, CH₃), 40.0 ($J=5.7$ Hz, CH₂), 59.9 (CH₂), 71.5 ($J=7.6$ Hz, CH), 95.4 ($J=183.4$ Hz, C), 128.5-134.6 (2Ph), 165.8 ($J=4.9$ Hz, C), 167.2 ($J=4.8$ Hz, C), 210.5 ($J=0.7$ Hz, C). ³¹P-NMR (242.9 MHz): δ_p 31.5. Anal. Calcd for C₂₂H₂₅O₄P requires: C 68.74, H 6.56. Found: C 68.78, H 6.63.

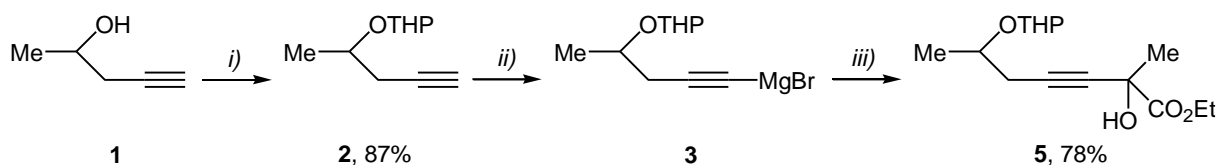
RESULTS AND DISCUSSION

In order to assess the approach towards the target 1,1,3-trifunctionalized allenes, a range of 4-phosphorylated 6-hydroxy-allenecarboxylates **7**, **9**, **10**, and **11** were prepared by the following four-step

procedure including: i) protection of hydroxy group in pent-4-yn-2-ol; ii) subsequent reaction with Grignard reagent and ethyl 2-oxopropanoate to give ethyl 2,6-dihydroxy-hept-3-ynoate with protected hydroxy group at sixth position; iii) interaction with chloride of phosphorus acid in the presence of a base; and finally iv) [2,3]-sigmatropic rearrangement of the mediated protected ethyl 2-(dimethoxyphosphanyl)oxy- or 2-(diphenylphosphino)oxy-6-hydroxy-hept-3-ynoates.

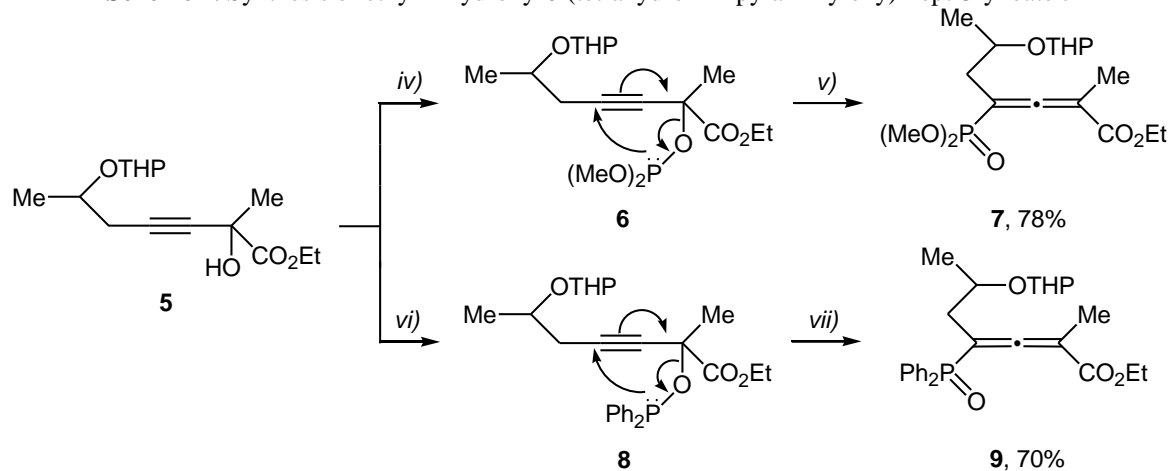
As a starting point for our investigation, we first examined the protection of hydroxy group in pent-4-yn-2-ol **1** with DHP in the presence of PPTS [59-62] (Scheme 1). Thus, the 2-(but-3-ynyloxy)-tetrahydro-2*H*-pyran formed **2** was isolated by column chromatography with very good yield (87%). Reaction of the protected alkynols **2** with

ethyl magnesium bromide and subsequent dropwise addition of *in situ* generated alkynyl magnesium bromide **3** to ethyl 2-oxopropanoate **4** and reflux for 2 h gives the ethyl 2-hydroxy-6-(tetrahydro-2*H*-pyran-2-yloxy)-hept-3-ynoates **5**, which are stable and were isolated by column chromatography in 78% yields as is shown in Scheme 1. With the required ethyl 2,6-dihydroxy-hept-3-ynoate **5** with protected hydroxy group at sixth position in hand, we were then able to investigate the proposed reactions with the corresponding chloro-containing phosphorus reagents such as dimethyl chlorophosphite and chlorodiphenyl phosphine in the presence of a base and subsequent [2,3]-sigmatropic rearrangement of the mediated phosphites **6** or phosphonites **8**.



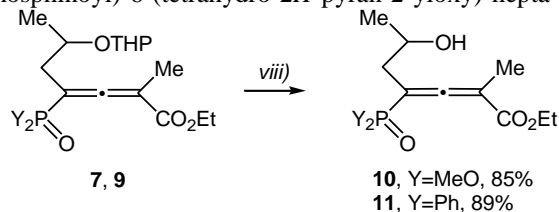
Reagents and conditions: i) DHP (1.5 eq), PPTS (0.1 eq), CH_2Cl_2 , rt, 2h, distillation; ii) EtMgBr (1 eq), THF, reflux, 2h; iii) dropwise addition of **3** to $\text{MeC(O)CO}_2\text{Et}$ (**4**) (2 eq), reflux, 2h, column chromatography.

Scheme 1. Synthesis of ethyl 2-hydroxy-6-(tetrahydro-2*H*-pyran-2-yloxy)-hept-3-ynoate **5**



Reagents and conditions: iv) PCl_3 (1 eq), Et_3N (1.1 eq), Et_2O , -70°C , 30 min stirring, pyridine (2.2 eq), MeOH (2 eq), Et_2O , -70°C ; v) [2,3- σ]-rearrangement, -70°C , 1h, rt, 4h, column chromatography; iv) $\text{Ph}_2\text{P(O)Cl}$ (1 eq), Et_3N (1.1 eq), Et_2O , -70°C ; v) [2,3- σ]-rearrangement, -70°C , 1h, rt, 6h, column chromatography.

Scheme 2. Synthesis of ethyl 4-(dimethylphosphoryl)-6-(tetrahydro-2*H*-pyran-2-yloxy)-hepta-2,3-dienoate **7** and ethyl 4-(diphenylphosphinoyl)-6-(tetrahydro-2*H*-pyran-2-yloxy)-hepta-2,3-dienoate **9**



Reagents and conditions: viii) PPTS (0.1 eq), EtOH , rt, 6h, stirring, column chromatography.

Scheme 3. Synthesis of ethyl 4-(dimethylphosphoryl)-6-hydroxyhepta-2,3-dienoate **10** and ethyl 4-(diphenylphosphinoyl)-6-hydroxyhepta-2,3-dienoate **11**

In the first instance, the ethyl 4-(dimethylphosphoryl)-6-(tetrahydro-2*H*-pyran-2-ylxy)-hepta-2,3-dienoate **7** can be readily prepared via an atom-economical 2,3-sigmatropic rearrangement of the ethyl 2-(dimethoxyphosphanyl)oxy-6-(tetrahydro-2*H*-pyran-2-ylxy)-hept-3-ynoate **6**, intermediate formed by reaction of the ethyl 2-hydroxy-6-(tetrahydro-2*H*-pyran-2-ylxy)-hept-3-ynoate **5** with dimethyl chlorophosphite, prepared *in situ* from phosphorus trichloride and 2 *equiv* of methanol in the presence of triethylamine, and 2 *equiv* of pyridine, according to Scheme 2.

Next, the reaction of ethyl 2-hydroxy-6-(tetrahydro-2*H*-pyran-2-ylxy)-hept-3-ynoate **5** with chlorodiphenyl phosphine in the presence of triethylamine at -70°C gave the expected ethyl 4-(diphenylphosphinoyl)-2-methyl-6-(tetrahydro-2*H*-pyran-2-ylxy)-hepta-2,3-dienoate **9** in very good yield (70%) as a result of [2,3]-sigmatropic rearrangement of the ethyl 2-(diphenylphosphino)oxy-6-(tetrahydro-2*H*-pyran-2-ylxy)-hept-3-ynoate **8** for 6 h at room temperature, according to the reaction sequence outlined in Scheme 2.

A new family of 4-phosphorylated 6-hydroxyhepta-2,3-dienoates with protected hydroxy group **7** and **9** were synthesized via an atom-economical and regioselective [2,3]-sigmatropic rearrangement of the intermediate formed hydroxy- and carboxy-substituted propargyl phosphites **6** or phosphinites **8** in the reaction of protected hydroxy- and carboxy-substituted alkynols **5** with dimethylchloro phosphite or chlorodiphenyl phosphine in the presence of triethylamine. Compounds **7** and **9** were stable enough to be handled at ambient temperature. The hydroxy group was deprotected by stirring the ethanol solution of the protected ethyl 4-(dimethylphosphoryl)- or 4-(diphenylphosphinoyl)-6-(tetrahydro-2*H*-pyran-2-ylxy)-hepta-2,3-dienoate **7** or **9** in the presence of 0.1 *equiv* PPTS at room temperature for 6 h to give the ethyl 4-(dimethylphosphoryl)-6-hydroxy-hepta-2,3-dienoate **10** and the ethyl 4-(diphenylphosphinoyl)-6-hydroxy-hepta-2,3-dienoate **11**, according to Scheme 3.

After a conventional work-up, all allenic products **7**, **9**, **10**, and **11** were isolated by column chromatography as stable yellow, orange or colourless oils and identified by ¹H, ¹³C, and ³¹P NMR and IR spectra, as well as by elemental analysis.

A series of new 4-phosphorylated 6-hydroxyhepta-2,3-dienoates with protected **7** and **9** and unprotected hydroxy group **10** and **11** were

synthesized by a convenient, expedient, atom-economical and regioselective method.

CONCLUSIONS

In conclusion, we could state that a convenient and practical regioselective synthesis of a new family of 1,1,3-trifunctionalized allenes has been explored. 4-Phosphorylated 6-hydroxyhepta-2,3-dienoates were derived from [2,3]-sigmatropic rearrangement of the intermediate hydroxy- and carboxy-substituted propargyl phosphites or phosphinites formed in the reaction of protected hydroxy- and carboxy-substituted alkynols with dimethylchloro phosphite or chlorodiphenyl phosphine in the presence of a base.

Currently, we are working on further progress of this potentially important synthetic methodology. At the same time, we are making research on the synthetic application of the prepared 4-phosphorylated 6-hydroxyhepta-2,3-dienoates with protected or unprotected hydroxy group for synthesis of different heterocyclic compounds in our laboratory as a part of our general synthetic strategy for studying the nature of the electrophilic cyclization and cycloisomerization reactions of trifunctionalized allenes. The results will be reported in due course. What could be emphasized on is that the results of the preliminary study of the biological activity of the compounds are encouraging. It is the antibacterial and antifungal activities of selected compounds, as well as the potential precursors of effective anticancer drugs that are currently analysed by our University researchers.

Acknowledgements: Support from the Research Fund of the Konstantin Preslavsky University of Shumen (Projects Nos. RD-08-158 / 2018 and RD-08-94 / 2019) is acknowledged. Dr. Ismailov thanks the Bulgarian Ministry of Education and Science under the National Program for Research "Young Scientists and Postdoctoral Students" for support of this work.

REFERENCES

1. S. Patai (ed.), The Chemistry of Ketenes, Allenes and Related Compounds, John Wiley & Sons, New York, 1980.
2. S. R. Landor (ed.), The Chemistry of the Allenes, Vol. 1–3, Academic Press, London, 1982.
3. H. F. Schuster, G. M. Coppola, Allenes in Organic Synthesis, John Wiley & Sons, New York, 1988.
4. C. J. Elsevier, in: (Houben-Weyl) Methods of Organic Chemistry, R. W. Helmchen; J. Mulzer, E. Schaumann (eds.), Vol. E21a, Thieme, Stuttgart, 1995, p. 537.

5. N. Krause, A. S. K. Hashmi, (eds.), *Modern Allene Chemistry*, Vol. 1 and 2, Wiley-VCH, Weinheim, 2004.
6. R. W. Bates, V. Satcharoen, *Chem. Soc. Rev.*, **31**, 12 (2002).
7. N. Krause, A. S. K. Hashmi (eds.), *Modern Allene Chemistry*, Wiley-VCH, Weinheim, 2004, Vol. 1 & 2.
8. S. Ma, *Aldrichimica Acta*, **40**, 91 (2007).
9. K. M. Brummond, J. E. DeForrest, *Synthesis*, 795 (2007).
10. T. M. V. D. Pinho e Melo, *Curr. Org. Chem.*, **13**, 1406 (2009);
11. T. G. Back, K. N. Clary, D. Gao, *Chem. Rev.*, **110**, 4498 (2010).
12. S. Phadtare, J. Zemlicka, *J. Am. Chem. Soc.*, **111**, 5925 (1989).
13. S. Ma, H. Hou, S. Zhao, G. Wang, *Synthesis*, 1643 (2002).
14. P. Crabbé, H. Fillion, D. André, J.-L. Luche, *J. Chem. Soc. Chem. Commun.*, 859 (1979).
15. Y. Deng, X. Jin, S. Ma, *J. Org. Chem.*, **72**, 5901 (2007).
16. A. Alexakis, I. Marek, P. Mangeney, J. F. Normant, *Tetrahedron*, **47**, 1677 (1991).
17. J. A. Marshall, K. G. Pinney, *J. Org. Chem.*, **58**, 7180 (1993).
18. C. Deutsch, B. H. Lipshutz, N. Krause, *Angew. Chem. Int. Ed.*, **46**, 1650 (2007)
19. J. Ye, S. Li, B. Chen, W. Fan, J. Kuang, J. Liu, Y. Liu, B. Miao, B. Wan, Y. Wang, X. Xie, Q. Yu, W. Yuan, S. Ma, *Org. Lett.*, **14**, 1346 (2012).
20. G. P. Boldrini, L. Lodi, E. Tagliavini, C. Tarasco, C. Trombini, A. Umanl-Ronchi, *J. Org. Chem.*, **52**, 5447 (1987).
21. R. W. Hoffman, U. Weldmann, *Chem. Ber.*, **118**, 3966 (1985).
22. E. J. Corey, R. Imwinkelried, S. Pikul, Y. B. Xiang, *J. Am. Chem. Soc.*, **111**, 5493 (1989).
23. E. J. Corey, C.-M. Yu, D.-H. Lee, *J. Am. Chem. Soc.*, **112**, 878 (1990).
24. E. J. Corey, G. B. Jones, *Tetrahedron Lett.*, **32**, 5713 (1991).
25. J. Li, W. Kong, C. Fu, S. Ma, *J. Org. Chem.*, **74**, 5104 (2009).
26. J. Li, C. Zhou, C. Fu, S. Ma, *Tetrahedron*, **65**, 3695 (2009).
27. A. Alexakis, I. Marek, P. Mangeney, J. F. Normant, *Tetrahedron Lett.*, **30**, 2387 (1989).
28. H. J. Bestmann, H. Hartung, *Angew. Chem. Int. Ed. Engl.*, **2**, 214 (1963).
29. G. Aksnes, P. Froeyen, *Acta Chim. Scand.*, **22**, 2347 (1968).
30. R. W. Lang, H. -J. Hansen, *Helv. Chim. Acta*, **63**, 438 (1980).
31. H. Fillion, A. Hseine, M. -H. Pera, V. Dufaud, B. Refouvelet, *Synthesis*, 708 (1987).
32. K. Tanaka, K. Otsubo, K. Fujii, *Synlett*, 933 (1995).
33. C. -Y. Li, X. -B. Wang, X. -L. Sun, Y. Tang, J. -C. Zheng, Z. -H. Xu, Y. -G. Zhou, L. -X. Dai, *J. Am. Chem. Soc.*, **129**, 1494 (2007).
34. M. Miesch, *Synthesis*, 746 (2003) and references cited therein.
35. R. Zimmer, *Synthesis*, 165 (1993).
36. J. A. Marshall, Y. Tang, *J. Org. Chem.*, **58**, 3233 (1993).
37. V. Mark, The Uncatalyzed Rearrangements of Tervalent Phosphorus Esters, in: *Selective Organic Transformations*, B. S. Thyagarajan (ed.), John Wiley & Sons, New York, 1970, p. 319.
38. P. D. Landor, in: *The Chemistry of the Allenes*, Vol. 1, S. R. Landor (ed.), Academic Press, New York, 1982, p. 174.
39. R. W. Saalfrank, C.-J. Lurz, in: *Methoden der Organischen Chemie (Houben Weyl)*, H. Kropf, E. Scheumann (eds.), Thieme, Stuttgart, 1993, p. 2959.
40. A. S. K. Hashmi, *Synthesis of Allenes*, in: *Modern Allene Chemistry*, Vol. 1, N. Krause, A. S. K. Hashmi (eds.), Wiley-VCH, Weinheim, 2004, p. 3.
41. R. S. Macomber, *J. Am. Chem. Soc.*, **99**, 3072 (1977).
42. S. E. Denmark, J. E. Marlin, *J. Org. Chem.*, **56**, 1003 (1991).
43. B. Cai, G. M. Blackburn, *Synth. Commun.*, **27**, 3943 (1997).
44. R. W. Saalfrank, M. Haubner, C. Deutscher, U. Bauer, *Eur. J. Org. Chem.*, 2367 (1999).
45. A. P. Boiselle, N. A. Meinhardt, *J. Org. Chem.*, **27**, 1828 (1962).
46. V. Mark, *Tetrahedron Lett.*, **3**, 281 (1962).
47. K. C. Nicolaou, P. Maligres, J. Shin, E. de Leon, D. Rideout, *J. Am. Chem. Soc.*, **112**, 7825 (1990).
48. M. L. Curfin, W. H. Okamura, *J. Org. Chem.*, **55**, 5278 (1990).
49. I. E. Ismailov, I. K. Ivanov, V. Ch. Christov, *Molecules*, **19**, 6309 (2014).
50. I. E. Ismailov, I. K. Ivanov, V. Ch. Christov, *Bulg. Chem. Commun.*, **46**, Special Issue A, 39 (2014).
51. I. E. Ismailov, I. K. Ivanov, V. Ch. Christov, *Bulg. Chem. Commun.*, **49**, Special Issue B, **49**, 25 (2017).
52. I. K. Ivanov, I. D. Parushev, V. Ch. Christov, *Heteroatom. Chem.*, **24**, 322 (2013).
53. I. E. Ismailov, I. K. Ivanov, V. Ch. Christov, *Molecules*, **19**, 11056 (2014).
54. V. Ch. Christov, I. E. Ismailov, I. K. Ivanov, *Molecules*, **20**, 7263 (2015).
55. I. K. Ivanov, I. D. Parushev, V. Ch. Christov, *Heteroatom. Chem.*, **25**, 60 (2014).
56. H. H. Hasanov, I. K. Ivanov, V. Ch. Christov, *Heteroatom. Chem.* **28**, e21357 (2017).
57. H. H. Hasanov, I. K. Ivanov, V. Ch. Christov, *Phosphorus, Sulfur, Silicon* **193**, 611 (2018).
58. H. H. Hasanov, I. K. Ivanov, V. Ch. Christov, *Phosphorus, Sulfur, Silicon* **193**, 797 (2018).
59. D. N. Robertson, *J. Org. Chem.*, **25**, 931 (1960).
60. M. Miyashita, A. Yoshikoshi, P. A. Griecolb, *J. Org. Chem.*, **42**, 3772 (1977).
61. M. C. Joshi, P. Joshi, D. S. Rawat, *ARKIVOC*, **xvi**, 65 (2006).
62. B. Partha, I. Pimkov, *US Patent 8378123 B2* (2011).

Synthesis of novel polyaniline composites with *Eriobotrya japonica* leaves for removal of Methyl Red dye from wastewater

F. Kanwal, R. Rehman*, H.A. Warraich

Institute of Chemistry, University of the Punjab, Lahore-54590, Pakistan

Received April 2, 2019; Revised June 17, 2019

Polyaniline (PANI) and its biocomposite with *Eriobotrya japonica* (PANI/EJ) leaves were synthesized using chemical oxidative polymerization, characterized by FTIR and UV/Vis spectrophotometry, and used for adsorption studies of Methyl red (MR) dye. Optimum conditions for PANI: 30 min contact time, 20°C temperature, adsorbent dose 0.8 g in 25 mL solution of MR dye and pH 1; and for PANI/EJ: 35 min contact time, 20°C temperature, adsorbent dose 1.0 g in 25 mL solution of MR dye and pH 2. Langmuir isotherm depicts that monolayer chemisorption of MR dye occurred on PANI and its composite binding sites. The maximum adsorption capacity of PANI is 2.407 mg/g while for PANI/EJ it is 3.842 mg/g. ΔG° negative value indicates the feasibility and spontaneity of the adsorption. Freundlich isotherm explains the physio-sorption and heterogeneity of the adsorption. The K_F values of PANI and PANI/EJ are 0.366 and 0.641, respectively. Results revealed that PANI/EJ is a better eco-friendly biocomposite for removal of Methyl red dye from water as compared to PANI.

Keywords: Polyaniline composite, *Eriobotrya japonica* leaves, Methyl red dye, adsorption.

INTRODUCTION

Environmental degradation in Pakistan is mainly caused by the rapid industrialisation including dyes and inorganic waste material in wastewater. Dyes have been used for colouring in various industries, paper, textile, soap, cosmetic, etc. The release of coloured waste water is hazardous for the environment and it poses a threat of bioaccumulation which in turn may damage human food chain [1]. Azo dyes are the main contributor to the water pollution as they are persistent, and they are the most commonly used colorants in the industries [2]. They have a nitrogen-to-nitrogen double bond backbone: R—N=N—R' [3]. Azo dyes directly influence human health by triggering allergic reactions or cancer [4].

Methyl Red is an anionic azo dye which is commonly used in paper and textile industry [5]. It acts as an eye, throat and skin irritant [6]. It is, thus, necessary to remove dye from industrial waste water and to decolourise it. Several processes can be used to remove MR dye from industrial wastewater. Xylene can be used as an extractant to remove it, but it is an expensive [7]. Other processes include photocatalytic degradation, coagulation and electro Fenton's and hypochlorite treatment but they are not cost effective [6, 8-10].

In the past two decades, conducting polymers have been increasingly used for their adsorption capability and polyaniline (PANI) is the most efficient among them. Biomass from different plants

has also been used for adsorption but it is not as efficient [11]. In this research work, PANI and its biocomposite with leaves of *Eriobotrya japonica* (PANI/EJ) were synthesized and used for batch mode adsorption of MR dye.

EXPERIMENTAL

Instruments used were: digital balance, FT-IR spectrophotometer, UV/Visible spectrophotometer (721 Visible Spectrophotometer). Chemicals used were: aniline, FeCl₃, HCl, DMF, acetone and ethanol. Aniline was used after distillation. 10 g of freshly purified aniline was taken in a three-necked flask which was placed in an ice bath on a stirrer and temperature was maintained at 0 °C. Whole of the process was performed in an inert environment using nitrogen. Solution of hydrated ferric chloride (0.75M) was prepared and added to aniline in the flask with vigorous shaking. Mixture was continuously stirred at 0°C for 24 h. The end of the reaction was indicated by the formation of a dark green precipitate in the solution.

The purification of the prepared precipitates was carried out by filtration through a pyrex sintered glass crucible and vacuum pump apparatus. The precipitates were then washed with distilled water followed by acetone and methanol until the filtrate became completely neutral. The residue was then dried in an oven at 60°C for 48 h. This process was performed twice till the required amount was obtained [11-13].

* To whom all correspondence should be sent:

E-mail: grinorganic@yahoo.com

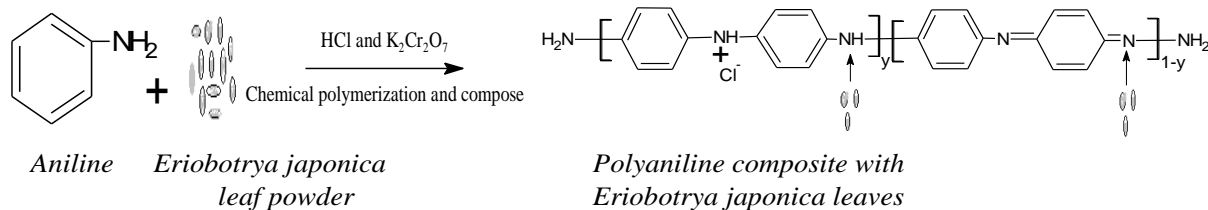


Fig.1. Schematic presentation of the synthesis of polyaniline composite.

Synthesis of PANI composite with *Eriobotrya japonica* leaves

Polymerization was carried out in a similar way as reported earlier using 2 g of powdered leaves in the reaction mixture. Fig. 1 shows the chemical reaction schematically. The product was characterized by UV/Vis and FT-IR spectrophotometry [14-16].

Preparation of stock solution and standards for adsorption studies of MR dye

For the stock solution of 1000 ppm, 2.69 g of Methyl red was dissolved in 1000 ml of water and it was diluted for preparing further standards.

Adsorption studies

The adsorption studies of MR dye were carried out in batch mode for both PANI and its composite. The removal of MR dye was calculated by eq. 1:

$$\text{Adsorption \% age} = [(C_{in} - C_{fin}) / C_{in}] \times 100 \quad (1)$$

where C_{in} is the initial concentration of MR dye while C_{fin} is the final concentration after adsorption has taken place.

RESULTS AND DISCUSSION

UV/Vis spectroscopic analysis

UV/Vis spectra of PANI and PANI/EJ were taken after dissolving them in dimethyl formamide. The λ_{max} of PANI and its composite are given in Table 1 and graphically shown in Fig. 2. Absorption at $\lambda_{max}1$ 280 nm is due to a $\pi - \pi^*$ transition of aniline in the benzenoid ring [17]. Absorption at 525 nm is attributed to transition of benzenoid ring into quinonoid ring.

Table 1. λ_{max} of PANI and PANI/EJ

Sample	λ_{max1} (nm)	Absorbance 1	λ_{max2} (nm)	Absorbance 2
PANI	280	1.632	525	0.572
PANI/EJ	290	1.67	550	0.558

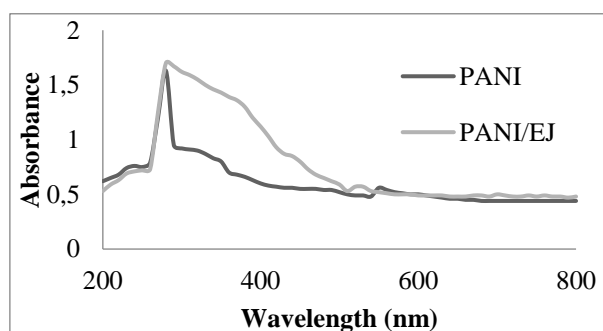


Fig. 2. Comparative UV-Vis spectra of PANI and PANI/EJ

FT-IR characterization

FT-IR was used to characterize PANI and its composite (PANI/EJ) and relevant peaks are compared in Fig. 3 [18]. By comparing the FT-IR spectra of PANI and its composite (PANI/EJ) it was observed that the band (due to amino group (N-H) stretching frequency [19]) for PANI at 3295 cm^{-1} is

shifted to 3205 cm^{-1} in case of PANI/EJ. The absorption band at 1577 cm^{-1} is due to benzenoid to quinoid rings nitrogen bond. In case of PANI/EJ it is shifted to 1698 cm^{-1} . Peaks due to secondary amine stretching [20] are shifted from 1226 cm^{-1} (PANI) to 1288 cm^{-1} (PANI/EJ). Bands in the range of 1571-1116 cm^{-1} are due to the conductive nature of PANI.

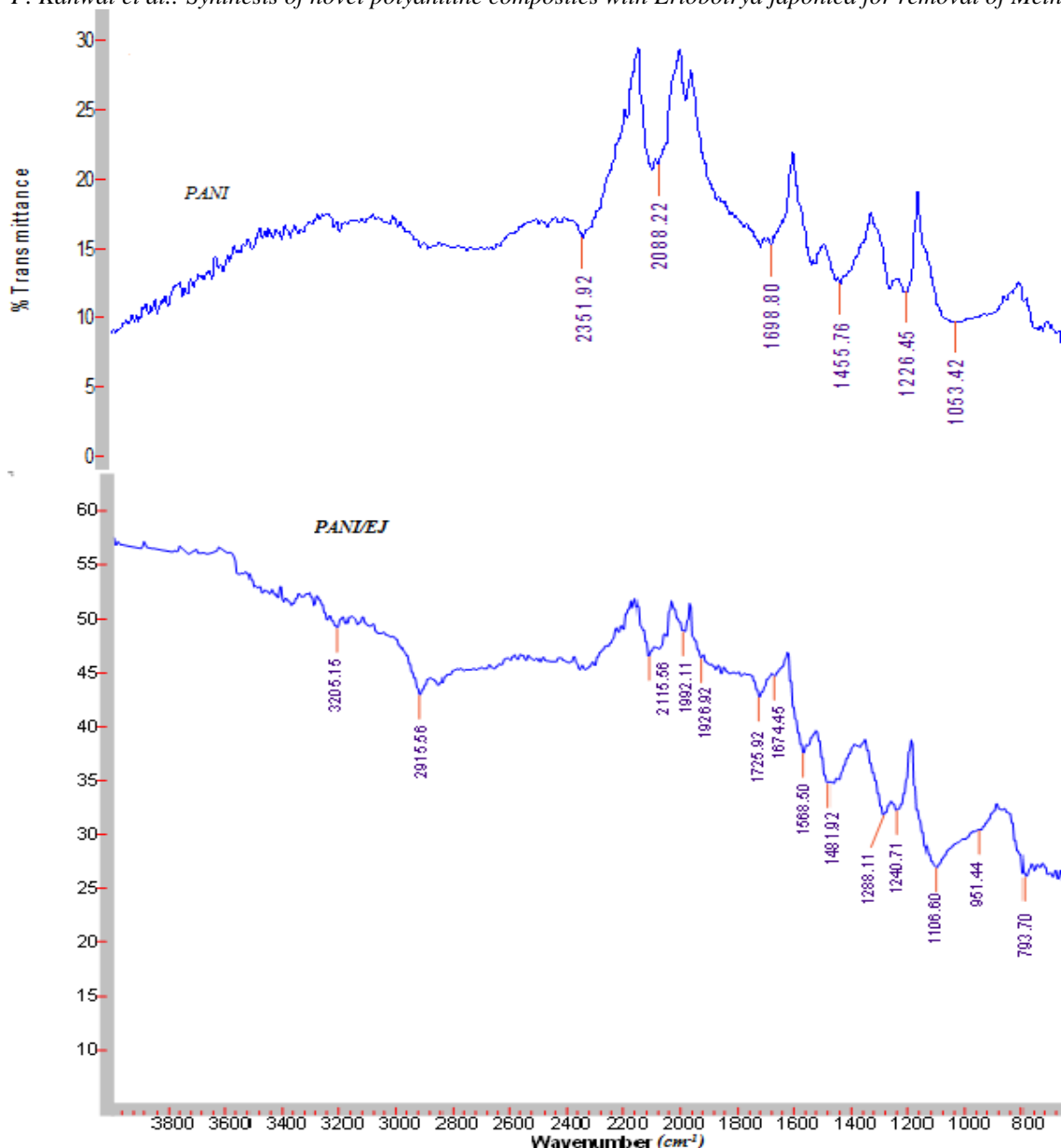


Fig. 3. Comparative FT-IR spectra of PANI and PANI/EJ.

BATCH ADSORPTION EXPERIMENTS

Contact time

Adsorbent dose

The effect of various adsorbent doses is shown in Fig. 4. The maximum removal of Methyl Red was observed with 0.8 g of PANI (84.44% removal) and 1.0 g of PANI/EJ (94.60% removal). The results revealed that preventing the PANI/EJ particles from aggregation and exposing MR dye towards available active sites for adsorption showed greater efficiency in its removal. In case of PANI adsorption firstly increases and then decreases because of adsorbent particles coagulation, due to which the number of sites available for adsorption decreases [18].

Adsorption phenomenon is time dependent. The effect of different time intervals is shown in Fig. 5 for removal of MR dye by PANI and PANI/EJ composite. The maximum removal value was 89.52 % for PANI for 30 min, and 95.24% for PANI/EJ composite for 35 min. The increased time interval for maximum removal of MR dye using PANI/EJ composite showed that it has less adsorption sites which are available for adsorption of metal ions. There is more contact time for PANI/EJ which allows more adsorbate-adsorbent interaction, thus increased adsorption. After the maximum removal of MR dye, the adsorption decreased with increase in contact time because all available sites were

F. Kanwal et al.: Synthesis of novel polyaniline composites with *Eriobotrya japonica* for removal of Methyl Red dye ... occupied. PANI/EJ was more appropriate for removal of Methyl red dye than PANI.

Solution pH

The results of the pH study are shown in Fig. 6. Solution pH corresponds to the functionality of adsorbent and dye in the solution. As Methyl red is an acidic dye, hydrogen bonding, π - π interaction and electrostatic forces between the dye and the functional group on PANI surface occur in the acidic medium. The maximum removal value was 95.56 % for PANI composite at pH 1 and 99.68 % for PANI/EJ composite at pH 2. PANI/EJ was more appropriate for removal of MR dye than PANI [14].

Table 2. Langmuir Isotherm parameters

Adsorbent	PANI	PANI/EJ
Slope	4.5545	1.2961
Intercept	0.4154	0.2603
R ²	0.8382	0.9707
q _m (mg/g)	2.407	3.842
b (L/mg)	0.091	0.201
R _L	0.1208	0.0585
ΔG° (KJ/mol)	-5.933	-3.975

Table 4. Other reported PANI composites used for contaminants removal on a lab scale.

Dyes	Composite	Removal capacity (mg/g)	Reference
Tartrazine	Chitosan/PANI	584.0	[21]
Crystal violet	PANI / <i>Tectona grandis</i> saw dust	263.2	[22]
Methyl orange	ZnO/PANI	240.84	[23]
Congo red	PANI/lignocellulose	1672.5	[24]
Congo red	Polyaniline/carboxymethyl cellulose/TiO ₂	119.9	[25]
Green SF dye	Heulandite/PANI	44.6	[26]

The negative sign of ΔG° showed that the adsorption process is feasible and spontaneous. Results revealed that PANI/EJ shows better adsorption than PANI, where 'n' and 'K_F' are Freundlich isotherm constants. 'K_F' value was 0.366 and 0.641 for PANI and PANI/EJ, respectively. For

Table 3. Freundlich Isotherm parameters

Adsorbent	PANI	PANI/EJ
Slope	1.0337	0.7462
Intercept	0.4366	0.1931
R ²	0.6124	0.9739
K _f	0.366	0.641
n	0.967	1.34
1/n	1.0337	0.7462

Adsorption Isotherm

The Langmuir and Freundlich isotherm parameters for PANI and PANI/EJ are shown in Tables 2 and 3, respectively.

Langmuir isotherm indicated that monolayer chemisorptive removal of MR dye has occurred on the homogeneously distributed composites' binding sites [11-13]. It is predominant over the Freundlich model. This means that chemisorption is predominant over physio-sorption, as indicated by the greater R² value of Langmuir than Freundlich. Maximum adsorption capacity (q_m) values for PANI and PANI/EJ are 2.407 and 3.482 mg/g, respectively. Table 4 shows examples of other PANI composites previously used for dyes removal on lab scale.

MR dye the value of 'n' was 0.697 for PANI and 1.340 for PANI/EJ. Separation factor R_L value is between 0 and 1, indicating the favourability of this process [15]. At higher values of 'n' the affinity and heterogeneity of adsorbent sites will be greater.

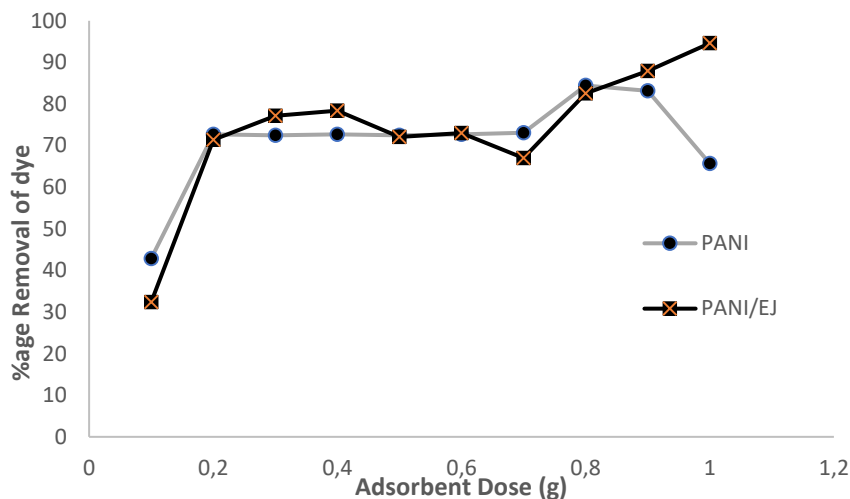


Fig.4. Comparative graph showing the effect of adsorbent dose on % absorbance of MR dye on PANI and PANI/EJ

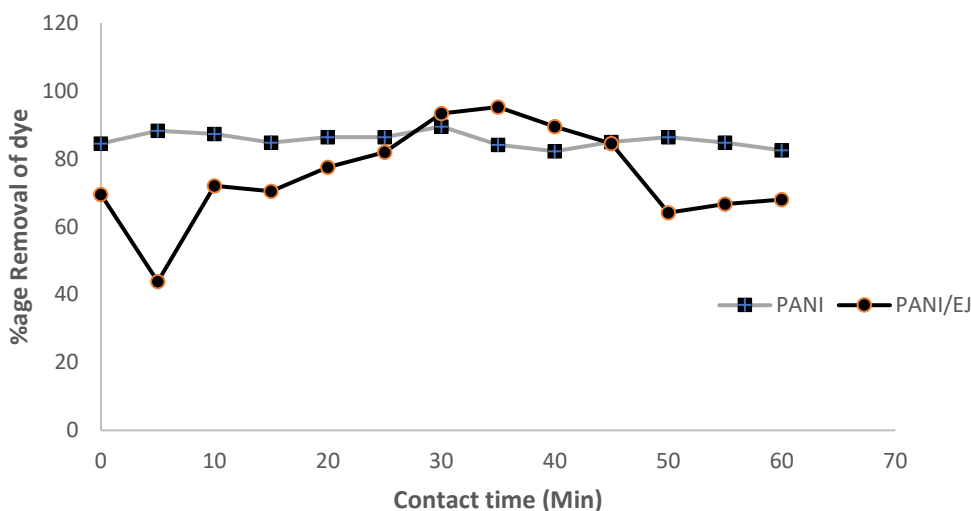


Fig. 5. Comparative graph showing the effect of contact time on the % absorption of MR dye by PANI and PANI/EJ

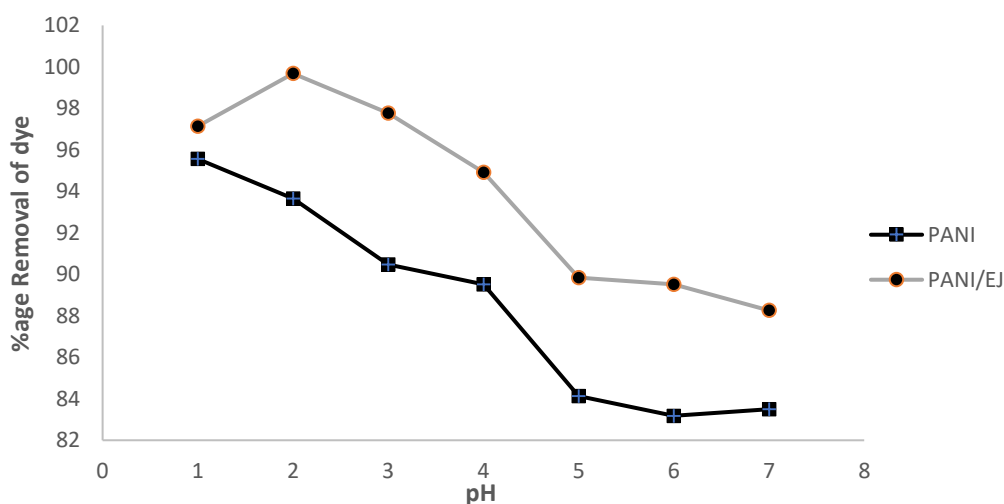


Fig.6. Comparative graph showing the effect of pH on the % adsorption of MR dye on PANI and PANI/EJ

CONCLUSION

Polyaniline composites PANI and PANI/EJ were synthesized, characterized and used as adsorbents

for MR dye removal from water. It was observed that PANI composite formation enhanced the adsorption capacity due to morphology modification and

F. Kanwal et al.: Synthesis of novel polyaniline composites with *Eriobotrya japonica* for removal of Methyl Red dye ... prevention of polyaniline particles aggregation. The batch experiments showed that Langmuir adsorption isothermal model is better fitted during adsorption of MR dye, which suggested that chemisorption occurred during removal. The negative value of ΔG° confirmed the spontaneity and feasibility of the adsorption process. The observed trend of adsorption is:



Results revealed that polyaniline composite with *Eriobotrya japonica* leaves (PANI/EJ) is a good adsorbent for removal of Methyl Red dye.

REFERENCES

1. J.X. Lin, S.L. Zhan, M.H. Fang, *J. Environ. Manag.*, **87**,193 (2008).
2. R.G. Saratale, G.D. Saratale, J.S. Chang, S.P. Govindwar, *J. Taiwan Inst. Chem. Eng.*, **42**, 138 (2011).
3. IUPAC, Compendium of Chemical Terminology, 2nd edn. (the "Gold Book") (1997). Online corrected version: "azo compounds" (2009).
4. K. Nadafi, M. Vosoughi, A. Asadi, M. O. Borna, M. Shirmardi, *J. Water Chem. Tech.*, **36**, 125 (2014).
5. H. Lachheb, E. Puzenat, A. Houas, *Catalysis B Environ.*, **39**, 75 (2002).
6. Y. Badr, M.G. Abdul El-Wahed, M.A. Mahmoud, *J. Hazard. Mater.*, **154**, 245 (2008).
7. G. Muthuraman, T.T. Teng, *Prog. Nat. Sci.*, **19**, 1215 (2009).
8. H.T. Boon, T.T. Teng, A.K. Mohamed Omar, *Water Res.*, **34**, 597 (2000).
9. G. Mascolo, R. Comparelli, M.L. Curri, *J. Hazard. Mater.*, **142**,130 (2007).
10. A. A. Babaei, E. C. Lima, A. Takdastan, N. Alavi, G. Goudarzi, M. Vosoughi, G. Hassani, M. Shirmardi, *Water Sci. Tech.*, **74**, 1202 (2016).
11. F. Kanwal, R. Rehman, I.Q. Bakhsh, *J. Cleaner Production*, **196**, 350 (2018).
12. F. Kanwal, R. Rehman, S. Rasul, K. Liaqat, *Bulgarian Chem. Commun.*, **48**, 379 (2016).
13. A. B. Albadarin, M. N. Collins, M. Naushad, S. Shirazian, G. Walker, C. Mangwandi, *Chem. Eng. J.*, **307**, 264 (2017).
14. M. Naushad, S. Vasudevan, G. Sharma, A. Kumar, Z. ALOthman, *Deswater*, **57**, 18551 (2016).
15. F. Kanwal, R. Rehman, J. Anwar, S. Rasul, *Asian J. Chem.*, **26**, 4963(2014).
16. M. Naushad, Z. Abdullah ALOthman, M. Rabiul Awual, S. M. Alfadul, T. Ahamad, *Deswater*, **57**, 13527 (2016).
17. T. Tarawou, M. Horsfall Jr, J. L.Vicente, *Chem. & Biodiversity*, **4**(9), 2236 (2007).
18. K.Y. Xu, X. Zheng, C.L. Li, W.L. She, *Phys. Rev.*, **71**, 066604 (2005).
19. J.B. Pendry, A.J. Holden, W.J. Stewart, I. Youngs, *Phys. Rev. Lett.*, **76**, 4773 (1996).
20. L. Ai, J. Jiang, R. Zhang, *SynMat*, **160**, 762 (2010).
21. S. Sahnoun, M. Boutahala, *Int. J. BioMacromol.*, **114**, 1345 (2018).
22. F. Mashkoo, A. Nasar, *Groundwater Sustainable Develop.*, **8**, 390 (2019).
23. A. Deb, M. Kanmani, A. Debnath, K. L. Bhowmik, B. Saha, *Ultrasonics Sonochem.*, **54**, 290 (2019).
24. S. Debnath, N. Ballav, A. Maity, K. Pillay, *Int. J. BioMacromol.*, **75**, 199 (2015).
25. M. Tanzifi, M. Tavakkoli Yarak, M. Karami, S. Karimi, A. Dehghani Kiadehi, K. Karimipour, S. Wang, *J. Colloid Inter. Sci.*, **519**, 154 (2018).
26. M. R. Abukhadra, M. Rabia, M. Shaban, F. Verpoort, *Adv. Powder Tech.*, **29**, 2501 (2018).

UV-spectrophotometric approach in comparative studies of Gliclazide modified-release tablets

N. I. Marchokova^{1*}, V. B. Petkova¹, M. V. Dimitrov²

¹Department of Social Pharmacy, Faculty of Pharmacy, Medical University of Sofia, Sofia, Bulgaria

²Department of Pharmaceutical Technology and Biopharmacy, Faculty of Pharmacy, Medical University of Sofia, Sofia, Bulgaria

Received April 19, 2019; Accepted May 15, 2019

The aim of the present work was to study the applicability of the UV-spectrophotometric method for routine determination of the content and release kinetics of Gliclazide from different pharmaceutical modified-release drug products. *In vitro* release behavior in a phosphate buffer with pH 7.4 was investigated for all tested products and the obtained data were evaluated using various kinetic models - zero and first order, Higuchi and Korsmeyer-Peppas models. The most appropriate model was defined by means of a correlation coefficient.

The results from the drug release study conducted in a phosphate buffer with pH 7.4 evidenced a comparable behavior between the original and the generic drug products. The fact was confirmed by the calculated difference factor - f_1 . Value below 15 was achieved for all generic products. The release of Gliclazide from the original and from two of the generic products followed first-order kinetics while for the other generic products the release was described by zero-order kinetics. A Non-Fickian, super case II transport mechanism was specific for all tested products.

Keywords: Gliclazide, modified-release tablets, drug release, kinetic models

INTRODUCTION

Gliclazide is an oral hypoglycaemic agent which possesses good tolerability, rarely causing hypoglycaemia [1]. Gliclazide controls not only the glycemic level, but also inhibits key mechanisms in diabetic angiopathy [2].

The slow release of the active substance (Gliclazide) from Diamicon MR modified-release tablets is due to the utilized polymer, namely: hydroxypropyl methylcellulose (hypromellose). Hypromellose is cellulose, in part being O-methylated and O-(2-hydroxypropylated). It is applied in tablet formulations as a binder, a polymer in the film-coating suspension and as a matrix which provides the extended-release of a drug [3].

Mechanisms such as dissolution, diffusion and erosion characterize the drug release from hydrophilic matrices [4]. When the matrix comes into contact with the dissolution medium two fronts are formed around it – penetration front (a front between the non-relaxed polymer and the gel) and dissolution front (a front between the gel and the dissolution medium). Observed at the first front are processes of hydration and swelling, while dissolution of the hydrated matrix takes place at the second front [5]. Factors which affect the release of the drug are the molecular size and drug water solubility, as well as the amount of drug in a tablet [6]. Concentration of the utilized polymer is another

significant factor which affects the drug release [7]. Water-soluble drugs are released through the hydrophilic matrices by diffusion, while with drugs of low water-solubility diffusion and erosion take place [8].

The kinetics of drug release could be evaluated by using different kinetic models.

The zero order describes systems where drug release rate is independent of its concentration, while the first order describes concentration-dependent drug release [9]. The Higuchi model describes drug release from a matrix system. The amount of released drug is in proportion to the square root of time [10]. The power law describes drug release from polymeric systems. It is applied in cases when the release mechanism is unknown or when the drug release is carried out by more than one phenomenon. According to the value of the exponent of release n , the mechanism of transport could be Fickian or Non-Fickian [11]. When n is 0.5 drug release is carried out by diffusion, $n=1$ indicates release by swelling, $0.5 < n < 1.0$ is an indicator of both diffusion and swelling. These values are only valid for the release of active substance from a matrix of planar geometry. Values are different for matrices of cylindrical or spherical geometry [12,13].

The aim of the present work was to study the applicability of the UV-spectrophotometric method for routine determination of the content and release kinetics of Gliclazide from different pharmaceutical modified-release drug products.

* To whom all correspondence should be sent:
E-mail: nmarchokova@gmail.com

MATERIALS AND METHODS

Materials

Gliclazide, potassium phosphate (Merck, Germany), sodium hydroxide (Merck, Germany) and purified water were used in the preparation of a phosphate buffer with pH 7.4. The original product Diaprel MR 60 mg modified-release tablets, batch № 601062, (Les Laboratoires Servier) and the three generic products (Normodiab MR 60 mg modified-release tablets, batch № 248216, (Actavis Group PTC ehf.), Gliclazide Zentiva 60 mg modified-release tablets, batch № 5151700, (Zentiva), Madras MR 60 mg modified-release tablets, batch № 5151952, (Stada Arzneimittel AG)), each of them containing 60 mg of Gliclazide, were purchased from pharmacies in Sofia, Bulgaria. All products were within their shelf life at the time of the conducted study. The products were denoted with the first letter of their trade name, respectively D, N, G and M.

Methods

Preparation of standard calibration curve in a phosphate buffer with pH 7.4. Accurately weighed 6.7; 5.5; 4.4; 3.3 and 1.7 mg of Gliclazide were separately put in volumetric flasks of 100 ml. Added in each flask were 3 ml methanol in order to dissolve the active substance. The volume was adjusted up to the mark with a phosphate buffer with pH 7.4. Pipetted out was 1 ml of each solution which was transferred to a series of 5 ml-volumetric flasks and the volume was topped up with the phosphate buffer of pH 7.4. Concentrations of 0.0134, 0.011, 0.0088, 0.0066, and 0.0034 mg/ml were obtained.

In vitro drug release studies. A test was carried out by using the RC-8D Dissolution tester apparatus, Minhua Pharmaceutical Machinery Co., Limited, China. Use was made of an apparatus 2 (paddle method). The dissolution medium used was a phosphate buffer with pH 7.4. The test was conducted at a rotation speed of 75 ± 2 rpm, in a 900 ml volume and set temperature of 37 ± 0.5 °C. Tablets of each product were investigated in the dissolution apparatus. 10 ml samples were withdrawn every hour and the quantity withdrawn was replaced by 10 ml of dissolution medium. Each sample was filtered through a membrane filter and the amount of released drug was determined using a spectrophotometric method. A Rayleigh-UV-9200, Beijing Beifen-Ruili Analytical Instrument Co., Ltd., China, spectrophotometer was used. The amount of released drug was determined at 226 ± 2 nm wavelength. The percentage of released Gliclazide was calculated by employing a standard calibration curve obtained in advance.

Determining the drug release kinetics. Use was made of the following kinetic models:

$$\text{Zero-order kinetics: } C_t = k_0 t \quad (1)$$

First-order kinetics:

$$C_t = C_0 \cdot e^{-k_1 t} \quad (2)$$

$$\text{Higuchi model [10]: } C_t = k_2 \sqrt{t} \quad (3)$$

Korsmeyer-Peppas model [11]:

$$C_t/C_\infty = k t^n \quad (4)$$

where, C_0 is the initial amount of drug in the dosage form, C_t is the amount of drug released at time t , C_t/C_∞ is the fraction of drug released at time t , k_0 , k_1 , k_2 are release constants, k is a constant which incorporates the structural and geometrical characteristics of the dosage form, n is the release exponent.

Determining the difference factor (f_1). The difference factor (f_1) was defined as follows:

$$f_1 = \left\{ \left[\sum_{t=1}^n |R_t - T_t| \right] / \left[\sum_{t=1}^n R_t \right] \right\} \times 100$$

where n is the number of time points, R_t is the average percentage of original drug dissolved at time t , T_t is the average percentage of generic drug dissolved at time t . The dissolution profiles are similar when the values for f_1 are between 0 and 15 [14].

RESULTS AND DISCUSSION

Validation of the UV-spectrophotometric method

The UV-spectrophotometric method used for assay of Gliclazide was validated in terms of selectivity and linearity.

Selectivity

Selectivity of the method used was proved by analyzing a standard solution, a sample solution and placebo (placebo contained the used excipients without the active substance). The standard and the sample solutions had similar absorbance maxima at 226 nm wavelength. The placebo solution showed zero absorbance at the same wavelength which proved the selectivity of the method in use.

Linearity

The absorbance of each concentration at $\lambda = 226$ nm was measured and the obtained results are summarized in table 1.

Table 1. Linearity of Gliclazide at 226 nm wavelength

Concentration, mg/ml	Absorbance, AU
0.0134	0.443
0.011	0.376
0.0088	0.302
0.0066	0.246
0.0034	0.146

Determination of drug release kinetics

Linear regression analysis was performed. A linearity curve was plotted for absorbance against concentration in a phosphate buffer with pH 7.4 (Fig.1).

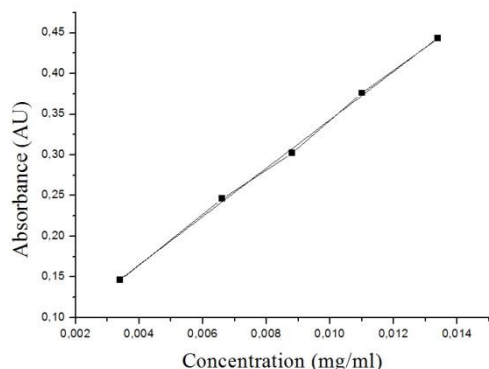


Fig. 1. Linear relationship of Gliclazide concentration against the absorbance in a phosphate buffer of pH 7.4.

The regression equation which described the linear relationship was as follows: $y = 0.0461 + 29.688x$. The correlation coefficient (R^2) was found to be 0.99946 for concentrations ranging from 0.0034 to 0.0134 mg/ml. The slope is 29.688 and the intercept is 0.0461.

In vitro drug release studies

In vitro drug release of Gliclazide from the original drug product (Diaprel MR 60 mg modified-release tablets) and three generic products (Normodiab MR 60 mg, Gliclazide Zentiva 60 mg and Madras MR 60 mg modified-release tablets) was investigated in a phosphate buffer with pH 7.4. The obtained results are presented graphically (Fig. 2) as % of drug released against time.

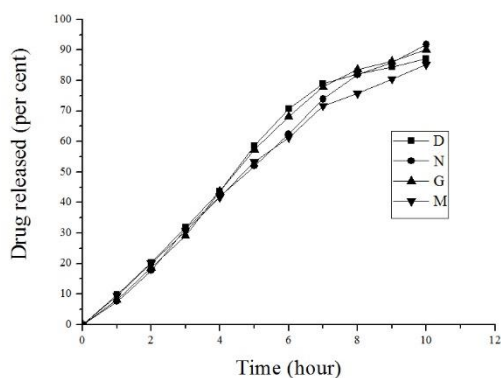


Fig. 2. Phosphate buffer with pH 7.4.

The percentage of drug released after 2 h was between 17 and 21 %, after 4 h between 41-44% and after 9 h - more than 80%.

Data from the *in vitro* release were fitted into different kinetic models (zero and first order, Higuchi and Korsmeyer-Peppas models) in order to determine the mechanism of drug release. A criterion for determining the most appropriate model was the value of the correlation coefficient (R). The obtained results are presented in table 2.

Table 2. Kinetic parameters of drug release - correlation coefficient and release exponent

Drug product	Phosphate buffer pH 7.4				
	Zero order (R)	First order (R)	Higuchi (R)	Korsmeyer-Peppas	
				R	n
D	0.979	0.990	0.967	0.991	0.987
N	0.994	0.976	0.965	0.995	1.093
G	0.986	0.988	0.964	0.992	1.080
M	0.990	0.993	0.973	0.995	0.969

Figs. 3-6 are graphic presentations of the various kinetic models – zero- and first-order, Higuchi and Korsmeyer-Peppas models.

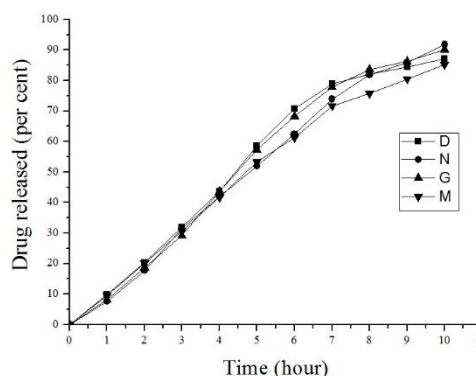


Fig. 3. Zero order.

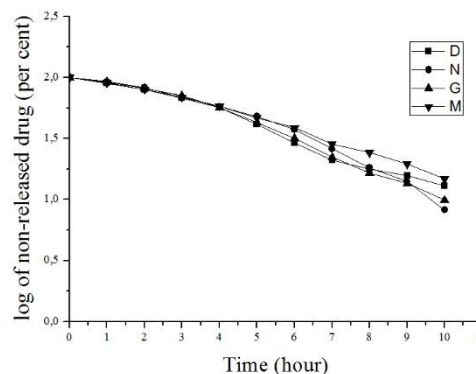


Fig. 4. First order.

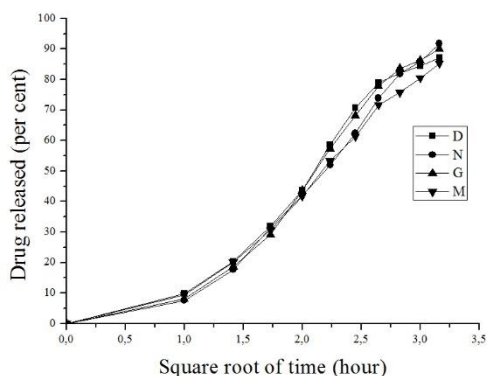


Fig. 5. Higuchi model.

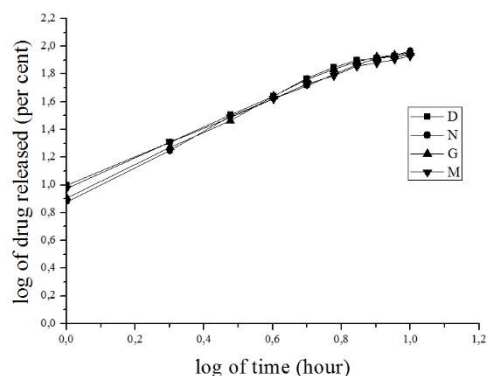


Fig. 6. Korsmeyer-Peppas model.

Three of the products (D, G and M) demonstrated the best linearity in the phosphate buffer of pH 7.4 when the data were fitted to first order. The correlation coefficient was 0.990, 0.988 and 0.993, respectively. The values of the correlation coefficient for generic products G and M were at the limits of zero and first order. The difference in the values was ± 0.002 for G and ± 0.003 for M. Generic product N released the active substance according to zero order ($R=0.994$).

According to Korsmeyer-Peppas model, the value of the release exponent is used to characterize the type of release mechanism. Values above 0.89, valid for polymeric matrices with geometry of a cylinder, define super case II transport mechanism [11]. For all tested drug products the values obtained for the release exponent were above 0.89, namely, from 0.969 to 1.093. Therefore, the Non-Fickian release mechanism was determined and more precisely the release from the tablets followed super case II transport.

Determining the difference factor (f_1)

The dissolution profiles of the original and the three generic products were compared by calculating the difference factor. The obtained results are presented in table 3.

The values obtained for the difference factor were less than 15. Therefore the requirement for f_1 was achieved for all generic products and is a proof that the dissolution profiles of the tested generic products are similar to the dissolution profile of the original drug product.

Table 3. Difference factor

Generic products	D, batch № 601062 pH 7.4
N, batch № 248216	6.04
G, batch № 5151700	3.03
M, batch № 5151952	6.65

CONCLUSIONS

The dissolution behavior of generic products was comparable to that of the original product in the phosphate buffer with pH 7.4, which was confirmed by the values obtained for the difference factor. The release of Gliclazide from the original and two of the generic products followed first order, while for the other generic product the release was better described by zero-order kinetics. Non – Fickian, super case II transport mechanism was specific for all tested products.

REFERENCES

1. K.J. Palmer, R.N. Brogden, *Drugs*, **46**, 92 (1993).
2. G. Scherthaner, *Metab., Clin. Exp.*, **52**, 29 (2003).
3. T.L. Rogers, in: Handbook of Pharmaceutical Excipients, R.C. Rowe, P.J. Sheskey, M.E. Quinn (eds.), 6th edn., Pharmaceutical Press, London, 2009, p. 326.
4. M.H. Shoaib, J. Tazeen, H.A. Merchant, R.I. Yousuf, *Pak. J. Pharm. Sci.*, **19**, 119 (2006).
5. K.C.Sung, P.R. Nixon, J.W. Skoug, T. Robert Ju, P. Gao, E.M. Topp, M.V. Patel, *Int. J. Pharm.*, **142**, 53 (1996).
6. K. Tahara, K. Yamamoto, T. Nishihata, *J. Controlled Release*, **35**, 59 (1995).
7. M.U. Ghorri, B.R. Conway, *Am. J. Pharmacol. Sci.*, **3**, 103 (2015).
8. M. Rane, J. Parmar, A. Rajabi-Siahboomi, *Pharma Times*, **42**, 41 (2010).
9. S.A. Chime, G.C. Onunkwo, I.I. Onyishi, *Res. J. Pharm., Biol. Chem. Sci.*, **4**, 97 (2013).
10. T. Higuchi, *J. Pharm. Sci.*, **52**, 1145 (1963).
11. M. L. Bruschi, in: Strategies to modify the Drug Release from Pharmaceutical Systems, Woodhead Publishing Limited, UK, 2015, p. 63.
12. J. Siepmann, N.A. Peppas, *Adv. Drug Delivery Rev.*, **48**, 139 (2001).
13. P. Costa, J.M.S. Lobo, *Eur. J. Pharm. Sci.*, **13**, 123 (2001).
14. Food and Drug Administration, Center for Drug Evaluation and Research, U.S. Department of Health and Human Services, Guidance for Industry. Dissolution Testing of Immediate Release Solid Oral Dosage Forms, 1997.

Sulfamic acid-functionalized silica-coated magnetite nanoparticles as a recyclable catalyst for the facial synthesis of benzimidazole derivatives

D. Azarifar¹, M. Farbodmehr¹, O. Badalkhani¹, M. Jaymand²

¹Department of Chemistry, Bu-Ali Sina University, Zip Code 65178, Hamedan, Iran

²Immunology Research Center, Tabriz University of Medical Sciences, Tabriz, Iran

Received September 3, 2018; Revised August 28, 2018

Sulfamic acid-functionalized silica-coated magnetic nanoparticles (SO₃H-Fe₃O₄@SiO₂ MNPs) were synthesized and applied as an effective catalyst for the synthesis of benzimidazole derivatives through the reaction between aldehydes and *o*-phenylenediamine or 4-methylbenzene-1,2-diamine under ultrasound-promoted conditions. The reactions were optimized in the terms of solvent, time, temperature, and amount of catalyst. The reactions proceed smoothly under mild conditions to yield the respective products in excellent yields and in short reaction times (45 minutes). The identified catalyst can be easily separated by an external magnetic field and reused for five fresh runs without significant loss of catalytic activity.

Keywords: Heterocycles, Benzimidazoles, Sulfonated magnetic nanoparticles, Nanocatalyst, Green chemistry, Ultrasound-promoted

INTRODUCTION

It is an unquestionable fact that environmental issues are some of the important concerns during past few decades. The major portion of environmental pollution is related to growth of industrialization (*e.g.*, chemical technologies). Therefore, many approaches have been developed for the preparation and use of efficient and recoverable heterogeneous catalysts in the case of chemical products. These catalysts have emerged as useful for making organic transformations academically and industrially eco-friendly and economically viable [1]. In this context, nanoparticles have received a great deal of attention as heterogeneous catalysts, in part due to their interesting structural properties and high catalytic activities [2-5]. In recent years, a growing number of approaches have been developed for preparation of supported heterogeneous nanocatalysts by immobilizing different homogeneous precursors on a solid support. These immobilized nanocatalysts offer many advantages over their non-supported counterparts in being low- or non-toxic, air- and moisture-compatible, easily separable and recyclable [6-8]. Despite the above mentioned advantages, these nanocatalysts often suffer from the tedious task of recycling *via* expensive ultra-centrifugation, which limits their utility as catalysts.

However, the issues of separation and reusability of these nanocatalysts have been solved using magnetic nanoparticles (MNPs) as excellent supports amenable to simple magnetic separation [9-12].

Magnetic nanoparticles (MNPs) have been extensively used in biomedical and pharmaceutical areas [13, 14], and have found potential applications for cell [15] and protein separation [16], drug delivery systems [17], magnetic resonance imaging (MRI) [18], and hyperthermia cancer treatment [19]. Moreover, MNPs are good supports for immobilization of homogeneous catalysts [20], and can be effectively functionalized through appropriate surface modifications [21-37]. Therefore, MNPs-supported catalytic systems can be considered as powerful candidates due to their high surface area, magnetic properties, facile separation, and low cost [38, 39]. Based on these attractive properties, many MNPs-supported catalysts have been successfully utilized for catalyzing a broad series of chemical reactions such as oxidation [40], polymerization [41], and even enzymatic reactions [42]. In recent years, a variety of magnetic nano-oxides functionalized using different acidic groups such as phosphotungstic acid (H₃PW₁₂O₄₀), Preyssler-type heteropolyacids, sulfamic, and sulfonic acids have been prepared and successfully applied for selectively catalyzing various chemical reactions [43,44].

These NPs have superior properties including high magnetic strength, easy construction, eco-friendliness, and diverse potential applications in different fields [45-47].

* To whom all correspondence should be sent:
E-mail: o.badalkhani@yahoo.com;
m.jaymand@yahoo.com; m.jaymand@gmail.com;
jaymandm@tbzmed.ac.ir

Nitrogen-containing heterocyclic compounds are well-documented and many of them widely occur naturally. Many of these compounds constitute the largest portion of chemical entities which provide useful scaffolds for many natural products, fine chemicals and biologically active pharmaceuticals that have vital importance to life [48-51]. Among these heterocyclic compounds, benzimidazole derivatives are of particular interest due to their applications in medicinal chemistry and modern drug industry, based on their significant biological and pharmaceutical properties such as anticancer, anti-HIV, anti-tumor, antibacterial, antiviral, antifungal and antihistamine activities [52-61].

There are several previously reported methods for the synthesis of benzimidazole derivatives using various catalytic reagents such as sulfamic acid [62], silica sulfuric acid [63], *p*-TSA [64], Lewis acid [65], FeCl₃·6H₂O [66], nano-TiCl₄·SiO₂ [67], poly(*N,N*-dibromo-*N*-ethyl-benzene-1,3-disulfonamide) (PBBS) and *N,N,N,N*-tetrabromobenzene-1,3-disulfonamide (TBBDA) [68], sulfonic acid-functionalized imidazolium salts/FeCl₃ [69], nano indium oxide [70], nano-solid acid catalysts [71], *P*-TsOH [72] and Shirasagi KL [73]. Most of the mentioned synthesis methods suffer from some disadvantages, such as large amount of catalysts, tedious work up procedures, difficult isolation of the catalyst, and also the applied catalysts cannot be recovered and reused.

In continuation of our interest for developing more benign, eco-friendly, and efficient heterogeneous nanocatalysts and their application for the synthesis of various heterocyclic compounds including benzimidazoles [74, 75], herein, we are encouraged to examine for the first time the catalytic capability of our previously synthesized sulfamic acid-functionalized silica-coated magnetic nanoparticles (SO₃H-Fe₃O₄@SiO₂ MNPs) [76], as an efficient and magnetically recoverable heterogeneous catalyst for the synthesis of benzimidazole derivatives. The reactions were optimized in the terms of solvent, time, temperature, and amount of catalyst.

EXPERIMENTAL

Materials and methods

Chemicals used in this work were purchased from Fluka (Switzerland) or Merck (Darmstadt, Germany) chemical companies and were used without purification. Fourier Transform Infrared (FTIR) spectra were recorded in KBr pellets on a Shimadzu 435-U-04 FTIR spectrometer (Kyoto, Japan). Proton nuclear magnetic resonance (¹H NMR) spectra were obtained on a 400 MHz Bruker

instrument (Bruker, Ettlingen, Germany) in DMSO-*d*₆ or CDCl₃ as solvents and tetramethylsilane (TMS) as internal standard. Ultrasonication was performed in a Sonica- 2200 ETH series ultrasound cleaner with a frequency of 45 kHz. Melting points were measured on a SMPI apparatus (UK).

Synthesis of the catalyst (SO₃H-Fe₃O₄@SiO₂)

The catalyst has been previously synthesized and fully characterized by our research group as reported [76]. In brief, the Fe₃O₄ NPs were synthesized according to the method reported by Rafiee *et al.* [77], and then a silica layer was coated on the surface of the Fe₃O₄ NPs in order to protect the MNPs from possible oxidation or aggregation [78, 79]. The synthesized Fe₃O₄@SiO₂ NPs were functionalized using 3-chloropropyltrimethoxysilane (Fe₃O₄@SiO₂-Cl) [80]. Then, the Fe₃O₄@SiO₂-Cl NPs were reacted with ethylene diamine through a substitution nucleophilic reaction to afford diamine-functionalized MNPs (Fe₃O₄@SiO₂@NH-NH₂). Ultimately, the Fe₃O₄@SiO₂@NH-NH₂ MNPs were reacted with chlorosulfonic acid, which resulted in the sulfonation of both amino groups to produce SOH-Fe₃O₄@SiO₂ MNPs. The successful synthesis of the catalyst was established by performing different analytical techniques in our previous work [76].

General procedure for the SO₃H-Fe₃O₄@SiO₂-catalyzed synthesis of benzimidazole derivatives (3a-i)

A mixture of *o*-phenylenediamine or 4-methylbenzene-1,2-diamine (**1**; 1 mmol), aldehyde (**2**; 1 or 2 mmol), and 0.02 g of the catalyst (SO₃H-Fe₃O₄@SiO₂) in ethanol (5 mL) was sonicated at 50 °C. After completion of the reaction (during 45 min monitored by TLC) the reaction mixture was diluted with hot ethanol (5 mL) and stirred until the solid materials dissolved completely. The catalyst was recovered magnetically using an external magnetic bar. Afterward, distilled water (20 mL) was added to the reaction mixture and the solid products were collected by filtration and dried in air. Finally, the crude products were washed in diethyl ether for purification. All synthesized products are known compounds (**3a-i**) which were characterized by their melting points, as well as spectral (FTIR and ¹H NMR) analyses and compared with their corresponding data reported in the literature.

Some selected data

1-benzyl-6-methyl-2-phenyl-1H-benzoimidazole (**3a**): mp: 160-163 °C; FTIR (KBr, ν_{max} /cm⁻¹):

3051, 2926, 2855, 1612, 1594, 1502, 1448, 1413, 1371, 1223; ¹H NMR (400 MHz, DMSO-*d*₆): 2.40 (s, 3H, CH₃), 5.55 (s, 2H, CH₂), 6.98-7.71 (m, 13H, H-Ar), 9.33 ppm.

1-(2-chlorophenylmethyl)-2-(2-chlorophenyl)-1H-benzoimidazole (3b): mp: 157-159 °C; FTIR (KBr, ν_{\max} /cm⁻¹): 3059, 2950, 1612, 1572, 1522, 1441, 1396, 1355, 1280; ¹H NMR (90 MHz, DMSO-*d*₆): 5.33 (s, 2H, CH₂), 6.54-7.83 (m, 12H, H-Ar), 9.33 ppm.

1-(4-hydroxyphenylmethyl)-2-(4-hydroxyphenyl)-1H-benzoimidazol (3c): mp: 252-254 °C; FTIR (KBr, ν_{\max} /cm⁻¹): 3448, 3026, 2925, 2854, 1612, 1597, 1515, 1444, 1395, 1266; ¹H NMR (90 MHz, DMSO-*d*₆): 5.33 (s, 2H, CH₂), 6.79-7.16 (m, 12H, H-Ar), 9.33, 9.89 (s, 2H, OH) ppm.

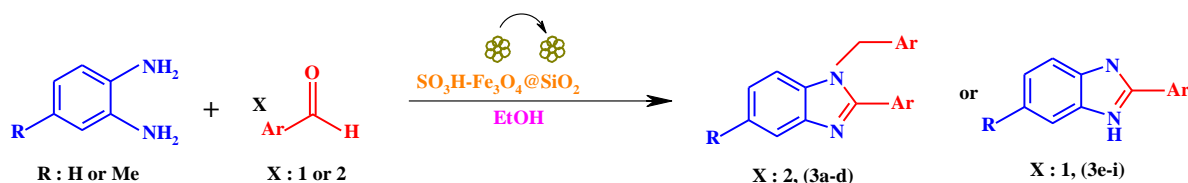
2-(4-fluorophenyl)-6-methyl-1H-benzoimidazole (3f): mp: 183-186 °C; FTIR (KBr, ν_{\max} /cm⁻¹): 3452, 3068, 2924, 2854, 1630, 1609, 1506, 1472, 1447, 1431, 1383, 1227; ¹H NMR (400 MHz, DMSO-*d*₆): 2.50 (s, 3H, Me), 7.03-8.20 (m, 7H, H-Ar), 12.75 (s, 1H, NH) ppm.

2-(4-hydroxyphenyl)-6-methyl-1H-benzoimidazole (3g): mp: 252-257 °C; FTIR (KBr, ν_{\max} /cm⁻¹): 3398, 3064, 2923, 2854, 1631, 1610, 1595, 1513, 1447, 1395, 1255; ¹H NMR (400 MHz, DMSO-*d*₆): 1.08 (s, 3H, Me), 6.91-7.41 (m, 7H, H-Ar), 7.99 (s, 1H, NH), 9.98 (s, 1H, OH) ppm.

RESULTS AND DISCUSSION

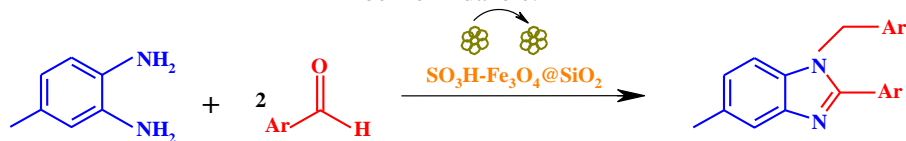
In this research, following our previously reported procedure [76], for the first time we have chosen and employed the SO₃H-Fe₃O₄@SiO₂ MNPs as an efficient and recyclable catalyst in the facial and green synthesis of benzimidazole derivatives (Scheme 1). The applied catalyst in the present investigation involves the organo sulfamic acid moiety which has been supported covalently on the surface of silica-coated MNPs.

Optimization of the reactions



Scheme 1. Synthesis of 2-arylmethyl-1-*H*-1,3-benzimidazoles (**3a-d**), and 2-aryl-benzimidazoles (**3e-i**) catalyzed by SO₃H-Fe₃O₄@SiO₂ MNPs.

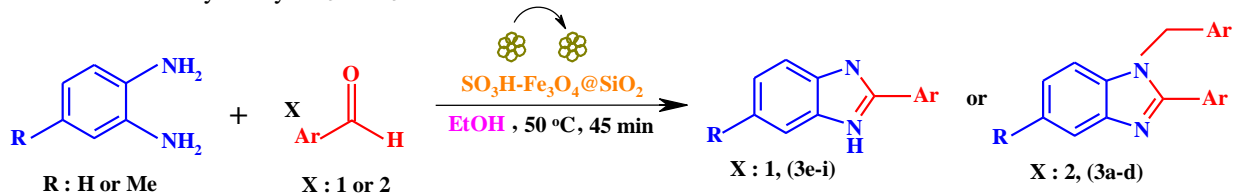
The catalytic capability of the SO₃H-Fe₃O₄@SiO₂ MNPs was investigated in the synthesis of benzimidazole derivatives by the reaction of aldehydes and *o*-phenylenediamine or 4-methylbenzene-1,2-diamine under ultra-sonicate conditions. In order to optimize the reaction conditions, the reaction of benzaldehyde (**1**) and 4-methylbenzene-1,2-diamine (**2**) was chosen as model reaction and the effects of different reaction parameters were studied. The results obtained are summarized in Table 1. The effects of temperature, different solvents, and various amounts of the catalyst were screened under different reaction conditions (reflux, ultrasonic, solvent-free, and room temperature). The most appropriate reaction condition was obtained using ethanol as the solvent, 0.02 g of the catalyst per mmol of aldehyde at 50 °C for 45 min under ultra-sonicate conditions (entry 15). Upon increasing of the catalyst amount no improvement in the reaction yield and rate was observed (entry 16). The reaction was also examined in absence of the catalyst under the same conditions which resulted in low rate and trace yield (entry 17). This achievement interested us to extend the scope of the explained methodology to a diverse series of substituted aromatic aldehydes (**1a-i**) in the reaction with *o*-phenylenediamine or 4-methylbenzene-1,2-diamine (**2**) under the optimized conditions (Scheme 1). In general, all reactions proceeded smoothly to furnish the respective products in relatively short reaction times with excellent and comparable yields irrespective of the nature of the substituent groups bonded to the aromatic ring. All the products (**3a-i**) obtained were known compounds which were characterized on the basis of their physical and spectral (FTIR and ¹HNMR) analysis and compared with the corresponding data reported in the literature (Table 2).

Table 1. Screening the reaction parameters for the model synthesis of 1-benzyl-6-methyl-2-phenyl-1*H*-benzimidazole.^a

Entry	Catalyst (g)	Solvent	Temperature (°C)	Reaction conditions	Time (h)	Yield (%) ^b
1	0.01	H ₂ O	r.t.	Thermal	4.5	trace
2	0.01	EtOH	r.t.	Thermal	4.5	38
3	0.01	H ₂ O /EtOH 1:1	r.t.	Thermal	4.5	23
4	0.01	CH ₃ CN	r.t.	Thermal	4.5	31
5	0.01	EtOH	45	Thermal	4	45
6	0.01	EtOH	60	Thermal	4	52
7	0.01	EtOH	80	Thermal	3.5	59
8	0.01	EtOH	80	Reflux	3	75
9	0.01	EtOH	40	Ultra-sonicate	2	62
10	0.01	EtOH	50	Ultra-sonicate	1	90
11	0.01	EtOH	60	Ultra-sonicate	1.5	70
12	0.01	no solvent	60	Thermal	3	68
13	0.01	no solvent	80	Thermal	2	73
14	0.01	no solvent	100	Thermal	2.5	59
15	0.02	EtOH	50	Ultra-sonicate	0.75	91
16	0.03	EtOH	50	Ultra-sonicate	1.5	72
17	no catalyst	EtOH	50	Ultra-sonicate	4	10

^aConditions: benzaldehyde (2 mmol), 4-methylbenzene-1,2-diamine (1 mmol), solvent (5 mL).

^b Isolated pure yield.

Table 2. Synthesis of 2-aryl-1-arylmethyl-1*H*-1,3-benzimidazoles (**3a-d**) and 2-aryl-benzimidazoles (**3e-i**) catalyzed by SO₃H-Fe₃O₄@SiO₂ MNPs under ultra-sonicate conditions at 50 °C.^a

Entry	Ar	Product	Yield (%) ^b	Mp (°C)	
				Found	Reported
1	C ₆ H ₅	3a	91	160-163	159-161[63]
2	2-ClC ₆ H ₄	3b	83	157-159	158-159[74]
3	4-OHC ₆ H ₄	3c	78	252-254	254-256[74]
4	3-NO ₂ C ₆ H ₄	3d	88	165-168	167-168[74]
5	3-NO ₂ C ₆ H ₄	3e	93	196-198	186-188 [83]
6	4-FC ₆ H ₄	3f	83	183-186	182-183[81]
7	4-OHC ₆ H ₄	3g	80	252-257	244-246[82]
8	4-ClC ₆ H ₄	3h	87	281-282	281-283[83]
9	4-MeC ₆ H ₄	3i	79	273-276	268-270[83]

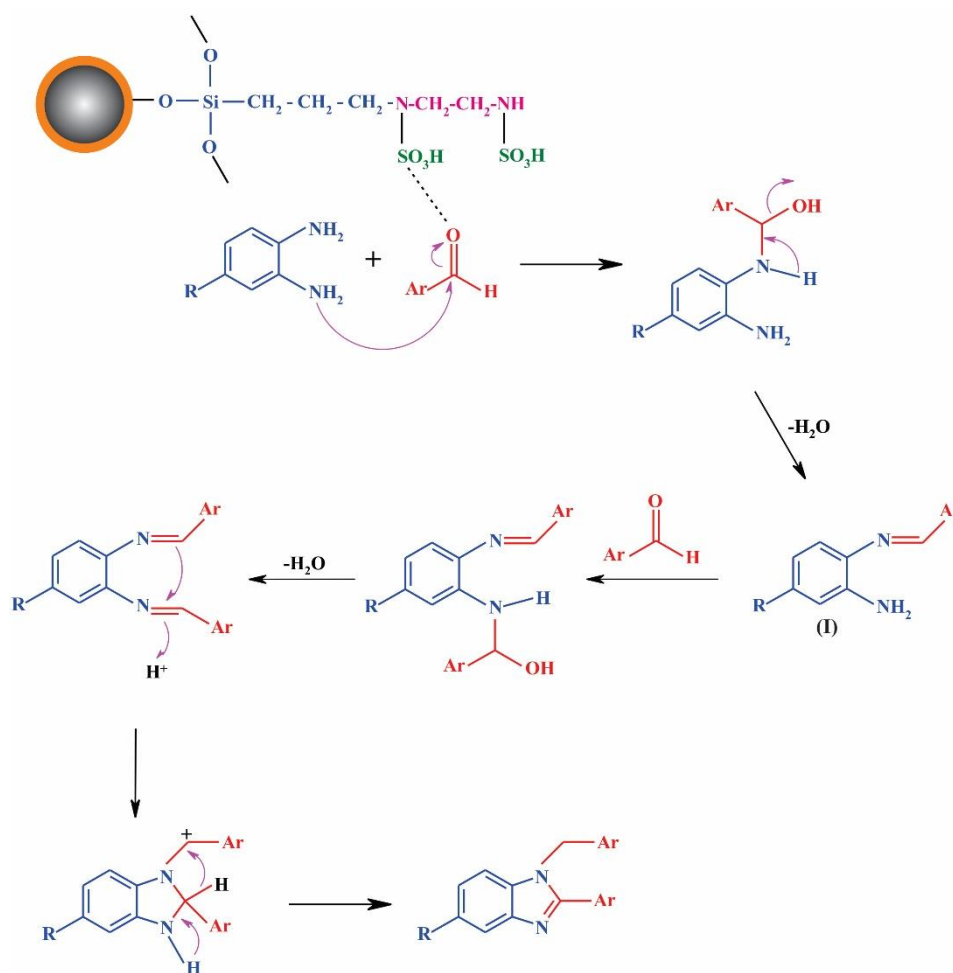
^a Conditions: aldehyde (**1**; x mmol), *o*-phenylenediamine or 4-methylbenzene-1,2-diamine (**2**; 1 mmol), catalyst (0.02 g), ethanol (5 mL), ultra-sonicate conditions, 50 °C, 45 min.

^b Isolated pure yield.

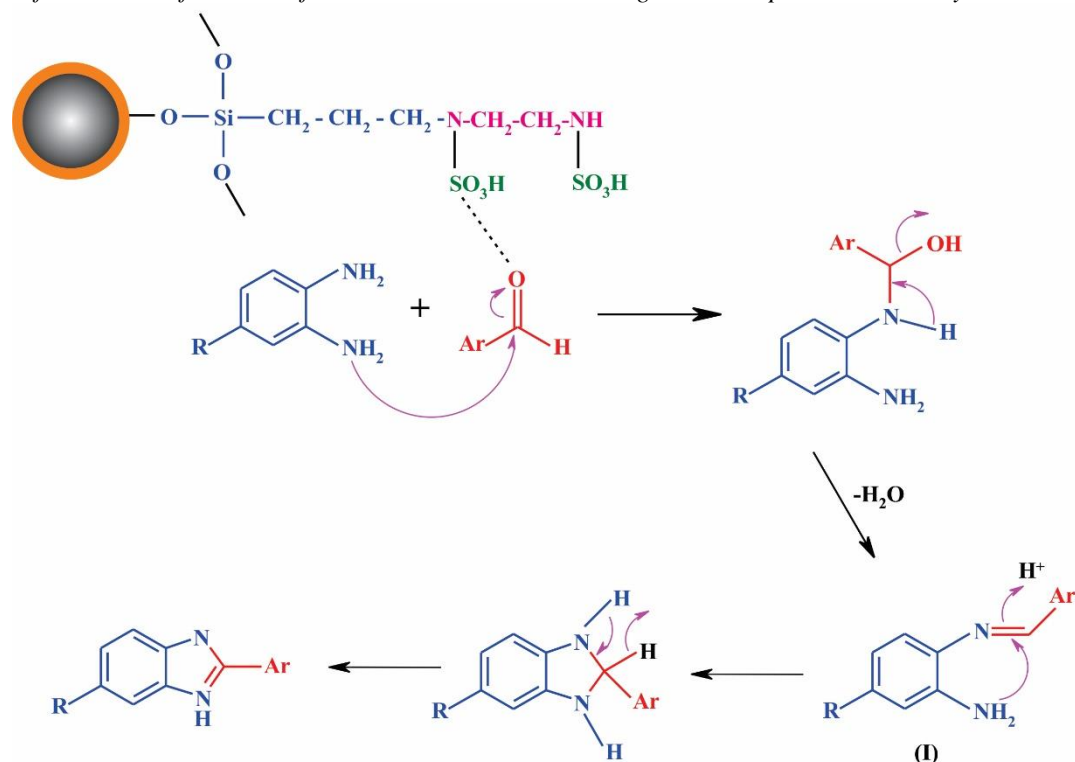
The proposed mechanism for describing the formation of 2-aryl-1-arylmethyl-1*H*-1,3-benzimidazoles (**3a-d**) is depicted in Scheme 2. First, nucleophilic addition of the amine group of *o*-phenylenediamine or 4-methylbenzene-1,2-diamine (**2**) was carried out on the catalyst-activated aldehyde (**1**) to form the Knoevenagel type intermediate **I**. The amine group of this intermediate reacts with the second molecule of catalyst-activated aldehyde followed by intramolecular nucleophilic cyclization, as well as dehydration to afford the expected products (**3a-d**). The suggested mechanism for the synthesis of 2-aryl-benzimidazoles (**3e-i**) is similar, as shown in Scheme 3. First, the nucleophilic addition of the amine group of *o*-phenylenediamine or 4-methylbenzene-1,2-

diamine (**2**) on the catalyst-activated aldehyde (**1**) leads to formation of Knoevenagel type intermediate **I**. In the following step, the intermediate **I** undergoes intramolecular nucleophilic cyclization followed by dehydration to furnish the expected products (**3e-i**).

On the other hand, the suggested mechanism for the synthesis of 2-aryl-benzimidazoles (**3e-i**) is similar, as shown in Scheme 3. First, the nucleophilic addition of the amine group of *o*-phenylenediamine or 4-methylbenzene-1,2-diamine (**2**) on the catalyst-activated aldehyde (**1**) leads to formation of Knoevenagel type intermediate **I**. In the following step, the intermediate **I** undergoes intramolecular nucleophilic cyclization followed by dehydration to furnish the expected products (**3e-i**).



Scheme 2. Proposed mechanism for the SO₃H-Fe₃O₄@SiO₂ MNPs-catalyzed synthesis of 2-aryl-1-arylmethyl-1*H*-1,3-benzimidazoles.



Scheme 3. Proposed mechanism for the $\text{SO}_3\text{H-Fe}_3\text{O}_4@\text{SiO}_2$ MNPs-catalyzed synthesis of 2-arylbenzimidazoles.

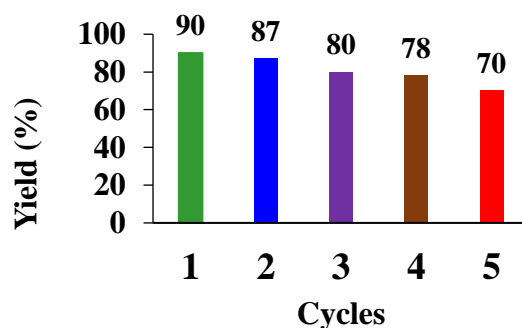


Figure 1. Catalytic reusability of $\text{SO}_3\text{H-Fe}_3\text{O}_4@\text{SiO}_2$ MNPs in the synthesis of 1-benzyl-5-methyl-2-phenyl-1H-benzimidazole.

Reusability of the catalyst

The reusability of the catalyst $\text{SO}_3\text{H-Fe}_3\text{O}_4@\text{SiO}_2$ was examined for the model reaction of benzaldehyde and 4-methylbenzene-1,2-diamine. The recycling process involves the isolation of the catalyst after the end of reaction using an external magnet bar. The recovered catalyst was washed with ethanol followed by drying in an oven overnight. As shown in Figure 1, the recovered catalyst can be used for five consecutive fresh runs without any significant loss of the catalytic activity.

CONCLUSIONS

We have developed a facial and green procedure for the synthesis of benzimidazole derivatives through the reaction of aromatic aldehydes with *o*-phenylenediamine or 4-methylbenzene-1,2-diamine under ultrasonic conditions in the presence of $\text{SO}_3\text{H-Fe}_3\text{O}_4@\text{SiO}_2$ MNPs as an effective and magnetically recyclable nanocatalyst. The reactions were optimized in terms of solvent, time, temperature, and amount of catalyst. The reactions proceed smoothly under mild conditions to yield the respective products in excellent yields and in short reaction times. It was demonstrated that the

D. Azarifar et al.: Sulfamic acid-functionalized silica-coated magnetite nanoparticles as a recyclable catalyst... developed SO₃H-Fe₃O₄@SiO₂ MNPs can be reused for five fresh runs without significant loss of catalytic activity.

Supporting Information: Supplementary data associated with this manuscript can be found in the online version at DOI: 10.34049/bcc.51.4.4829.

Acknowledgment: The authors are grateful for technical supports from the Research Council of the Bu-Ali Sina University to carry out this project.

Conflict of interests: The authors declare no conflict of interests.

REFERENCES

1. A. Corma, H. Garcia, *Catal. Today*, **38**, 257 (1997).
2. A. Schatz, O. Reiser, W.J. Stark, *Chem. Eur. J.*, **16**, 8950 (2010).
3. N. Yan, C.X. Xiao, Y. Kou, *Coord. Chem. Rev.*, **254**, 1179 (2010).
4. A. Gholizadeh, A. Malekzadeh, M. Ghiasi, *Bulg. Chem. Commun.*, **48**, 430 (2016).
5. V. Polshettiwar, R.S. Varma, *Green Chem.*, **12**, 743 (2010).
6. R. Yolanda de Miguel, *J. Chem. Soc., Perkin Trans.*, **1**, 4213 (2000).
7. R.A. Sheldon, H. van Bekkum, *Fine chemicals through Heterogeneous Catalysis*, Wiley-VCH, Weinheim, 2001.
8. J.H. Clark, D.J. Macquarrie, *Green Chemistry and Technology*, Blackwell, Abingdon, 2002.
9. C.W. Lim, I.S. Lee, *Nano Today*, **5**, 412 (2010).
10. S. Shylesh, V. Schunemann, W.R. Thiel, *Angew. Chem., Int. Ed.*, **49**, 3428 (2010).
11. Y.H. Zhu, L.P. Stubbs, F. Ho, R.Z. Liu, C.P. Ship, J.A. Maguire, N.S. Hosmane, *Chem. Cat. Chem.*, **2**, 365 (2010).
12. V. Polshettiwar, R. Luque, A. Fihri, H.B. Zhu, M. Bouhrara, J.M. Bassett, *Chem. Rev.*, **111**, 3036 (2011).
13. N. Poorgholy, B. Massoumi, M. Jaymand, *Int. J. Biol. Macromol.*, **97**, 654 (2017).
14. Z.J. Wei, C.Y. Wang, H. Liu, S.W. Zou, Z. Tong, *Colloids Surf. B: Biointerfaces*, **91**, 97 (2012).
15. J. Ying, R.M. Lee, P.S. Williams, J.C. Jeffrey, S.F. Sherif, B. Brian, Z. Maciej, *Biotechnol. Bioeng.*, **96**, 1139 (2007).
16. H. Gu, K. Xu, C. Xu, B. Xu, *Chem. Commun.*, **941** (2006).
17. A. Jafarizad, A. Taghizadehgh-Alehjougi, M. Eskandani, M. Hatamzadeh, M. Abbasian, R. Mohammad-Rezaei, M. Mohammadzadeh, B. Toğar, M. Jaymand, *Bio-Med. Mater. Eng.*, **29**, 177 (2018).
18. S. Hina, M.I. Rajoka, P.B. Savage, S. Roohi, T.H. Bokhari, *Bulg. Chem. Commun.*, **47**, 747 (2015).
19. I. Akira, T. Kouji, K. Kazuyoshi, S. Masashige, H. Hiroyuki, M. Kazuhiko, S. Toshiaki, K. Takeshi, *Cancer Sci.*, **94**, 308 (2003).
20. M. Kooti, M. Afshari, *Mater. Res. Bull.*, **47**, 3473 (2012).
21. A. Megia-Fernandez, M. Ortega-Munoz, J. Lopez-Jaramillo, F. Hernandez-Mateo, F. Santoyo-Gonzalez, *Adv. Synth. Catal.*, **352**, 3306 (2010).
22. S. Shylesh, I. Wang, W.R. Thiel, *Adv. Synth. Catal.*, **352**, 425 (2010).
23. B.G. Wang, B.C. Ma, Q.O. Wang, W. Wang, *Adv. Synth. Catal.*, **352**, 2923 (2010).
24. G.H. Liu, H.Y. Gu, Y.Q. Sun, J. Long, Y.L. Xu, H.X. Li, *Adv. Synth. Catal.*, **353**, 1317 (2011).
25. M. Stein, J. Wieland, P. Steurer, F. Tolle, R. Mulhaupt, *B. Breit, Adv. Synth. Catal.*, **353**, 523 (2011).
26. R. Arundhathi, D. Damodara, P.R. Likhar, M.L. Kantam, P. Saravanan, T. Magdaleno, S.H. Kwon, *Adv. Synth. Catal.*, **353**, 1591 (2011).
27. H. Firouzabadi, N. Iranpoor, M. Gholinejad, J. Hoseini, *Adv. Synth. Catal.*, 2011, 353, 125.
28. A.J. Amali, R.K. Rana, *Green Chem.*, **11**, 1781 (2009).
29. K. Mori, N. Yoshioka, Y. Kondo, T. Takeuchi, H. Yamashita, *Green Chem.*, **11**, 1337 (2009).
30. R.L. Oliveira, P.K. Kiyohara, L.M. Rossi, *Green Chem.*, **12**, 144 (2010).
31. T.Q. Zeng, G.H. Song, A. Moores, C.J. Li, *Synlett.*, **12**, 2002 (2009).
32. M.M. Ye, Q. Zhang, Y.X. Ge, J.P. Hu, Z.D. Lu, L. He, Z.L. Chen, Y.D. Yin, *Chem. Eur. J.*, **16**, 6243 (2010).
33. T.Q. Zeng, L. Yang, R. Hudson, G.H. Song, A.R. Moores, C.J. Li, *Org. Lett.*, **13**, 442 (2011).
34. B. Sreedhar, A.S. Kumar, D. Yada, *Synlett.*, **8**, 1081 (2011).
35. R. Cano, D.J. Ramon, M. Yus, *J. Org. Chem.*, **76**, 5547 (2011).
36. R. Cano, D.J. Ramon, M. Yus, *Tetrahedron*, **67**, 5432 (2011).
37. R. Cano, D.J. Ramon, M. Yus, *Synlett.*, **14**, 2017 (2011).
38. V. Polshettiwar, R. Luque, A. Fihri, H. Zhu, M. Bouhrara, *Chem. Rev.*, **111**, 3036 (2011).
39. V. Roberto Calderone, N. Raveendran Shiju, D. Curulla-Ferre, *Angew. Chem., Int. Ed.*, **52**, 4397 (2013).
40. B. Dutta, S. Jana, A. Bhattacharjee, P. Gutlich, S.I. Iijima, S. Koner, *Inorg. Chim. Acta*, **363**, 696 (2010).
41. W. Long, C.S. Gill, S. Choi, C.W. Jones, *Dalton Trans.*, **39**, 1470 (2010).
42. J. Lee, Y. Lee, J.K. Youn, B. Na, T. Yu, H. Kim, S.M. Lee, Y.M. Koo, J.H. Kwak, H.G. Park, H.N. Chang, M. Hwang, J.G. Park, J. Kim, T. Hyeon, *Small.*, **4**, 143 (2008).
43. B. Karimi, M. Khalkhali, *J. Mol. Catal. A: Chem.*, **232**, 113 (2005).
44. I.K. Mbaraka, D.R. Radu, V.S. Lin, B.H. Shanks, *J. Catal.*, **219**, 329 (2003).
45. N. Poorgholy, B. Massoumi, M. Jaymand, *Int. J. Biol. Macromol.*, **97**, 654 (2017).
46. A. Farnoudian-Habibi, S. Kangari, B. Massoumi, M. Jaymand, *RSC Adv.*, **5**, 102895 (2015).

47. D. Astruc, F. Lu, J.R. Aranzaes, *Angew. Chem., Int. Ed.*, **44**, 7852 (2005).
48. E.J. Noga, G.T. Barthalmus, M.K. Mitchell, *Cell Biol. Int. Rep.*, **10**, 239 (1986).
49. F.M. Awadallah, F. Muller, A.H. Lehmann, A.H. Abadi, *Bioorg. Med. Chem.*, **15**, 5811 (2007).
50. B. Maleki, D. Azarifar, H. Veisi, S.F. Hojati, H. Salehabadi, R. Nejat Yami, *Chin. Chem. Lett.*, **21**, 1346 (2010).
51. N. Hazeri, G. Marandi, M.T. Maghsoodlou, S. Khorassani, *Lett. Org. Chem.*, **8**, 12 (2011).
52. A. A. Spasov, I. N. Yozhitsa, I. I. Bugaeva, V. A. Anisimova, *Pharm. Chem. J.*, **33**, 232 (1999).
53. M. Ouattara, D. Sissouma, M.W. Kone, H.E. Menan, S.A. Toure, L. Ouattara, *Trop. J. Pharm. Res.*, **10**, 767 (2011).
54. M. Goebel, G. Wolber, P. Markt, B. Staels, T. Unger, U. Kintscher, R. Gust, *Bioorg. Med. Chem.*, **18**, 5885 (2010).
55. T. Roth, L.M. Morningstar, L.P. Boyer, M.S. Hughes, R.W. Buckheitjr, Michejda JC, *J. Med. Chem.*, **40**, 4199 (1997).
56. S. Demirayak, U.A. Mohsen, A.C. Karaburun, *Eur. J. Med. Chem.*, **37**, 255 (2002).
57. L.D. Viala, O. Giaa, S.M. Magnoa, A.D. Settimob, A.M. Marinib, G. Primofioreb, F.D. Settimob, S. Salerno, *II Farmaco*, **56**, 159 (2001).
58. W. A. Denny, G. W. Rewcastle, B. C. Bagley, *J. Med. Chem.*, **33**, 814 (1990).
59. J. Mann, A. Baron Y Opoku-Boahen, E Johanson, G.Parkmson, L. R Kelland, S Neidle, *J. Med. Chem.*, **44**, 138 (2001).
60. Y. He, B. Wu, J., Yang, D. Robinson, L. Risen, R. Ranken, L. Blyn, S. Sheng, E.E.Swayze, *Bioorg Med Chem Lett*, **13**, 3253 (2003).
61. T.M. Migawa, L.J. Girardet, A.J. Walker, W.G. Koszalka, D.S. Chamberjain, C. Drach, *J. Med. Chem.*, **41**, 1242 (1998).
62. M. Chakrabarty, S. Karmakar, A. Mukherji, S. Arima, Y. Harigaya, *Heterocycles*, **68**, 967 (2006).
63. P. Salehi, M. Dabiri, M. A. Zolfigol, S. Otokesh, M. Baghbanzadeh, *Tetrahedron Letters*, **47**, 2557 (2006).
64. T. Yoshiyuki, Y. Kazuaki, D. Hokkaido, *Koagakubu Kenkyu Hokoku, Chem Abstr.*, **93**, 45 (1980).
65. W. H. Sun, S. H Shao, Y. Chen, H. M. Hu, R. A. Sheldon, H. G. Wang, X. B. Leng, X.L. Jin, *Organometallics*, **21**, 4350 (2002).
66. M. P. Singh, S. Sasmal, W. Lu, M.N. Chatterjee, *Synthesis*, **10**, 1380 (2000).
67. B.F. Mirjalili, A. Bamoniri, L. Zamani, *Scientia Iranica C.*, **19**, 565 (2012).
68. R. Ghorbani-Vaghei, H. Veisi, *Mol. Div.*, **14**, 249 (2010).
69. A. Khazaei, M. A. Zolfigol, A. R. Moosavi-Zare, A. Zare, E. Ghaemi, V. Khakyzadeh, *Scientia Iranica*, **18**, 1365 (2011).
70. S. Santra, A. Majee, A. Hajra, *Tetrahedron Lett.*, **53**, 1974 (2012).
71. A. Teimouri, A. R. Najafi-Chermahini, H. Salavati, L. Ghorbanian, *J. Mol. Catal.*, **373**, 38 (2013).
72. S. Paul, M. Gupta, R. Gupta, *Synth. Commun.* **32**, 3541 (2002).
73. Y. Kawashita, C. Ueba, M. Hayashi, *Tetrahedron Lett.*, **47**, 4231 (2006).
74. D. Azarifar, M. Pirhayati, B. Maleki, M. Sanginabadi, R. Nejat Yami, *J. Serb. Chem. Soc.*, **75**, 1181 (2010).
75. K. Khosravi, A. Mobinikhaledi, S. Kazemi, D. Azarifar, P. Rahmani, *Iran. J. Catal.*, **4**, 25 (2014).
76. D. Azarifar, O. Badalkhani, Y. Abbasi, *J. Sulf. Chem.*, **37**, 656 (2016).
77. E. Rafiee, S. Eavani, *Green Chem.*, **13**, 2116 (2011).
78. M. Yamaura, R.L. Camilo, L.C. Sampaio, M.A. Macedo, M. Nakamura, H.E. Toma, *J. Magn. Magn. Mater.*, **279**, 210 (2004).
79. M. Bagherzadeh, M.M. Haghdoost, F. Matlobi-Moghaddam, B. Koushki-Forushani, S. Saryazdi, E. Payab, *J. Coord. Chem.*, **66**, 3025 (2013).
80. T. Zeng, L. Yang, R. Hudson, G. Song, A.R. Moores, C.J. Li, *Org. Lett.*, **13**, 442 (2011).
81. R. Wang, X. X. Lub, X. Q. Yu, L. Shi, Y. Sun, *J. Mol. Catal. Chem.*, **266**, 198 (2007).
82. C. Mukhopadhyay, T. Kumar, *Tetrahedron Lett.*, **49**, 6237 (2008).
83. H. Ghafuri, E. Esmaili, M. Talebi, *C. R. Chimie*, **19**, 942 (2016).

Effects of tomato processing on carotenoids antioxidant activity and stability during one-year storage

J. M. Zdravković^{1*}, N. V. Pavlović¹, J. D. Mladenović², N. M. Vragolović Bošković³,
N. M. Zdravković⁴

¹ University of Kragujevac, Faculty of Agriculture, Cara Dušana 34, Čačak, Serbia

² Institute for Vegetable Crops, Karadjordjeva 71, 11420 Smederevska Palanka, Serbia

³ University of Belgrade, Faculty of Technology and Metallurgy, Karnegijeva 4, Belgrade, Serbia

⁴ Institute of Veterinary Medicine of Serbia, Vojvode Toze 14, Belgrade, Serbia

Received April 1, 2019; Accepted May 28, 2019

The degradation of carotenoids (lycopene and β -carotene) and total antioxidant activity was investigated after one-year storage of pasteurized tomato juice. Tomato juice, thermally treated for 7 min at 100°C, was subjected to one-year storage a) in the light at 20°C; b) in the dark at 20°C and c) in the dark at 4°C. β -Carotene had the fastest dynamics of degradation and was dissolved in the largest quantities, regardless of the storage conditions. For all investigated components the fastest decomposition was observed in the first two months, when the sample was stored in the light at 20°C. Lycopene was most stable in the sample stored in the dark at 4°C. Partial regression coefficients for all researched traits proved a significant difference of ratio for storing in the light (20°C) compared to the variants stored in the dark at 20°C and 4°C, lycopene $p=0.0041^{**}$, $p=0.0304^{**}$; β -carotene, $p=0.0009^{**}$ and $p=0.0183^{**}$; antioxidative activity $p<0.0001^{**}$ and $p=0.009^{**}$.

Keywords: tomato juice, 1-year storage, lycopene, β -carotene, antioxidative activity

INTRODUCTION

In the last two decades consumption of tomato in the world has significantly increased, mostly due to its nutritional importance and beneficial effects on cardiovascular diseases [1-3] and some cancers. Demand is focused on products based on tomato (ketchup and tomato juice) which, like fresh tomatoes, have antioxidant, anti-inflammatory, anti-mutagenic and anti-cancerous impact [4,5]. Tomato fruits can obtain optimal combination of antioxidants, so they are therefore important for human diet. When it comes to storing and processing of tomato fruits, research studies have examined most particularly the loss of nutrients, changes that occur during exposure to high temperatures, the length of processing time, the influence of light or oxygen, the length of shelf life [6,7]. Only few researchers studied the problem of storing products and decomposition process of some nutrients and length of storage [8]. However, technological processing and storing conditions influence the nutritive quality of tomato products and their stability to varying degrees [9]. Of all the processing techniques, high temperatures have the greatest impact on the level of natural nutrients in vegetables. Depending on the length of treatment, the level of impact can be high or low [10].

Beta-carotene and lycopene participate with 7 and 87%, respectively, of total carotenoids in mature red, tomato fruits [11].

Lycopene belongs to a family of carotenoids in its natural all-*trans* form. In tomato juice, as a result of oxidation, lycopene molecules divide, which leads to discoloration and bad taste. Effects of heat, oxygen, light and presence of oils on the lycopene stability have been proved in many studies. Opposing data regarding stability of tomato carotenoids during thermal treatment can be found in the literature.

Interestingly, while some studies show that compounds with antioxidative effects such as lycopene or β -carotene during some processing could be increased comparing to fresh fruit [12,13], other results show that the lycopene levels do not significantly vary in tomato puree packages if stored in the dark at 5, 15 and 25°C and in the light at 25°C for 6 months [14]. Also Tamburini *et al.* [15] did not find any changes in the lycopene content of tomato puree during storing for 1 year time, an increase in the lycopene level and stable β -carotene in processed tomato product have been published [7, 16]. After industrial processing β -carotene and lycopene remained stable during 12 months of storage depending on the terms of storage [17].

However, there are some controversies about some circumstances that lead to occurrence of isomerisation, such as optimal humidity and storage temperature [18]. Processed tomato products such

* To whom all correspondence should be sent:

E-mail: jasna.zdravkovic@gmail.com

as pulp, puree and paste exhibit degradation of antioxidants and antioxidative activity after 3 months of storage in each temperature conditions (30, 40 and 50°C) [19]. As the time of the storage increases for all storage treatments, the level of lycopene significantly decreases [20,21]. There is also a problem with the change in colour during storage. Even without oxygen to start the oxidation process, lycopene is slowly decomposed by auto-catalytic mechanism [22]. There are few research data on the level of lycopene after thermal treatment of stored tomato products in final food preparation procedures, i.e the amount of lycopene that consumers actually intake [23]). This appoints to attention for *cis*-lycopen supply in order to optimise tomato processing and storage condition in order to provide high quality food rich in nutrients and additional antioxidant value.

The other flavonoid in this research focus, β -carotene, is 20% lost after 7 months of storage [24], also after as much as 3 months of storage at 30, 40 and 50°C, the level of β -carotene decreased [19]. Similar result was presented in the study [25], where the loss of β -carotene and lycopene has been compared to the loss of ascorbic acid (vitamin C). Carotenoids were lost during storage but significantly less comparing to the thermo-labile ascorbic acid, which was significantly lost during heat treatment (compared to fresh fruits) and this loss is even greater during storage.

Antioxidative capacity is connected to the quantity and composition of bioactive compounds from the natural combination of different phyto-nutrients [26,27]. A certain number of studies proved that processed vegetables have the same nutritive value as fresh. This directly impacts the end users regarding processed food and increases the conscience of the health benefits of the processed vegetables in prevention of chronic diseases. Dewanto *et al.* [28] and Perez-Conesa *et al.* [29] proved that the high level of anti-oxidative capacity of products was preserved despite the heat treatment and loss of a strong antioxidant such as ascorbic acid. Total antioxidative activity was significantly increased after heat treatment for 2, 15 and 30 min at 88°C to 5.29 ± 0.26 , 5.53 ± 0.24 and 6.70 ± 0.25 μmol during the processing. Similar results had Odriozola-Serrano *et al.* [30] who found significant changes of antioxidative capacity among treated and fresh juices right after processing. However, after 56 days of storage at 4°C the antioxidative activity dropped to 35.7%, and authors concluded that antioxidative activity may suffer significant reduction in tomato products towards expiration date [19].

Different behaviour of carotenoids and total antioxidative activity in heat-treated mature tomato fruits juice should result in one-year research of expiration date which would contribute to clarification of degradation of bioactive components during storage time in preserving tomato products as high nutritive level food.

MATERIAL AND METHOD

Juice was prepared from one genotype – selected, high inbred tomato line (SPO).

Epidermis and seeds were separated. Pulp was thermally treated (cooked) at 100°C for 7 minutes and aseptically poured in glass containers which were hermetically sealed by metal lid. Samples were stored for one year in three conditions: at day light at 20°C, in the dark at 20°C and in the dark at 4°C. The lycopene level, β -carotene and total antioxidative activity were checked every two months. Testing was done on a sample of ten bottles from each repetition treatment.

Total antioxidative activity (TAA) was determined spectrophotometrically at 517 nm DPPH (1.1-diphenyl-2-picrylhydrazyl) by applying method [31].

In order to determine the level of lycopene, 20 g of tomato was extracted in 100 cm³ 96% C₂H₅OH. After 24 h of extraction (maceration), the sample was filtered. The dry extract was dissolved in 10 cm³ of acetone-hexane (ratio 4:6) mixture and filtered through Whatman No.4 filter paper. The extract was diluted 10 times and the absorbance at wavelengths 453, 505, 645 and 663 nm was measured [32]. Spectrophotometric measurements of samples were performed on the UV-VIS spectrophotometer MA9523-SPEKOL 211 (Iskra, Horjul, Slovenia). The level of lycopene (mg lycopene/ 100 mL extract) was calculated:

$$\text{Lycopene (mg/100 mL)} = -0.0458 \times A_{663} + 0.204 \times A_{645} + 0.372 \times A_{505} - 0.0806 \times A_{453}$$

Levels of β -carotene were determined according to the method described in [32]. The dried ethanol extract (100 mg) was vigorously shaken with 10 ml of acetone-hexane mixture (4:6) for 1 min and filtered through Whatman No. 4 filter paper. The absorbance of the filtrate was measured at 453, 505, 645 and 663 nm. Content of β -carotene was calculated according to the following equation:

$$\beta\text{-carotene (mg/100 ml)} = 0.216A_{663} - 1.22A_{645} - 0.304A_{505} + 0.452A_{453}$$

Tendency of change of average values [33], specifically linear-shaped tendency was tested:

$$\hat{y} = a + bx$$

where:

$$b = \frac{\sum x_i y_i - n \cdot \bar{x} \cdot \bar{y}}{\sum x_i^2 - n \cdot \bar{x}^2}$$

$$y = a \cdot x + b$$

and logarithmic tendency:

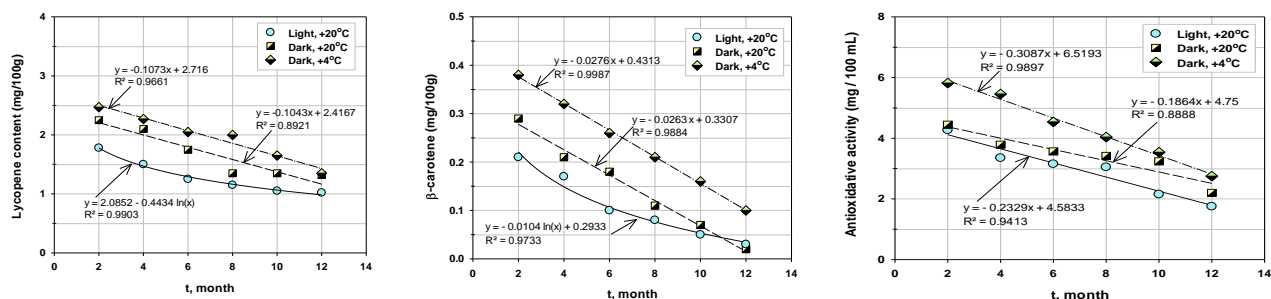
$$y = a \cdot \ln(x) + b,$$

where: a and b are constants, ln is the natural logarithm.

Adjustment to linear shape tendency was tested by the determination coefficient $R^2 > 0.6$.

The differences between the way of storage of samples and respective mutual dependence [34] were determined on the basis of partial regression coefficients.

Degradation index for studied nutrients was expressed as the ratio of their respective initial value and values measured in time.

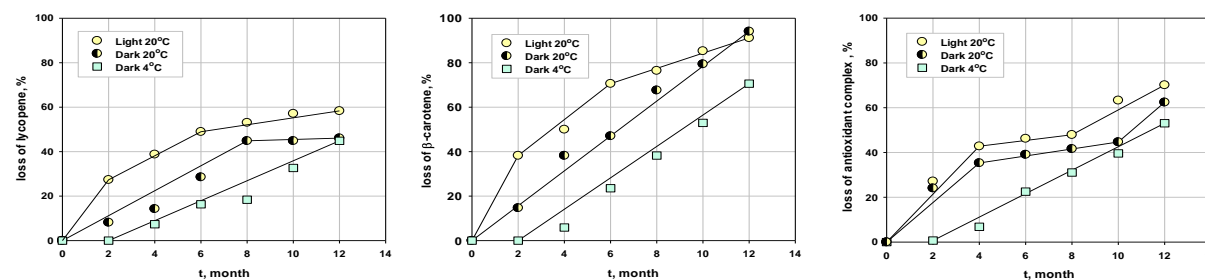


a) lycopene

b) β -carotene

c) antioxidative activity

Figure 1. Average values, tendency to change the content of lycopene (a), β -carotene (b) and total antioxidative activity (c), after one-year storage in the light (20°C), in the dark (20°C) and in the dark (4°C)



a)

b)

c)

Figure 2. Percentage loss of lycopene (a), β -carotene (b) and TA activity (c) depending on time and storage conditions.

RESULTS AND DISCUSSION

In the aspect of lycopene levels, the least satisfactory storage conditions are at 20°C in daylight. Tendency of lycopene loss has logarithmic nature for all three evaluated conditions of tomato juice storage. There is high reliability in predicting lycopene levels as determination coefficients are $R^2 = 0.9903$ for daylight storage conditions, $R^2 = 0.8921$ for dark place storage at 20°C, and $R^2 = 0.9661$ in dark on 4°C (Fig 1a).

Complementary to lycopene, the change in β -carotene levels depends on shelf life, and temperature situation of tomato juice storage. Amount of β -carotene linearly drops after a whole year of testing in dark at both 4°C and 20°C (both with R^2 values close to 1, 0.9987 and 0.9984 respectively), but in daylight the loss is presented in logarithmic style (Fig. 1b). The TA activity linearly

decreases for all 3 tested tomato juice storage conditions, with high R^2 values (Fig 1c).

The dependences of lycopene, β -carotene and TA activity loss are presented on Figures 2a-2c, respectively, as a function of storage time. The figures show also the lines that follow the trend of the displayed values and which slope is equivalent to the degradation rate of the corresponding component. The greatest losses of lycopene (up to 58%) were registered in samples that were stored at 20°C in daylight. The rate of lycopene degradation was the highest in the first two months of storage and decreased from the second to the twelfth month.

In dark storage at 20°C the rate of lycopene degradation was constant till the 8th month and after that the sample had the same quantity of lycopene, which means that the degradation ends (Fig 2a). The best result for lycopene preservation in tomato juice was for storage in the dark at 4°C. It is

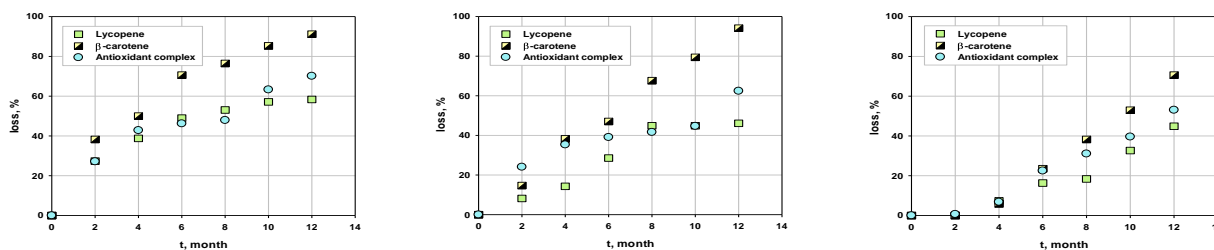
interesting that after 12 months of storage the amount of lycopene in samples stored in the dark at different temperatures was the same (Fig 2a). Hsu *et al.* [35] also found that nutrients degraded most quickly in the first phases of storage. These researchers found that in the first 14 days of storage, carotenoid and lycopene degraded quickly (16% and 12%, respectively) compared to control, while later degradation during 14 to 28 days of storage was not significant. The sample researched in this paper, which was stored in the dark at 20°C had almost the same amount of lycopene since the 8th month of storage which means that there was no degradation of lycopene in the last four months. This is in accordance with Ordonez-Santos *et al.* [20], where researchers aimed to follow the dynamics during storage of tomato pulp up to 180 days (half of the time compared to the storage time in our experiment) where the level of lycopene showed significant changes during the storage period. In some other studies, there were no changes in the level of lycopene in tomato puree during one year of storage [15], while some authors reported increased lycopene level in tomato products comparing to fresh tomato: 36% increase in lycopene and stable β -carotene [7] and 30% increase in lycopene [16].

Significant loss of β -carotene in all storage conditions is shown on Fig 2b. The parameter which significantly impacts the loss of this compound is the temperature. Whether the sample was stored in light or in dark, the temperature of 20°C caused great losses of β -carotene. The rate of degradation changed during storage in light, similar to lycopene, degradation was the most intensive in the first two months, but in time it was less comprehensive. The slowest degradation in daylight at 20 °C, was between the 6th and 12th month of storage. In the first two months there was no drop in β -carotene level in tomato juice while stored in cold and dark conditions. In the next 10 months the rate of degradation was constant and same as the rate of degradation in the dark at 20°C.

Lavelli and Giovanelli [19] found that the level of β -carotene decreased after 3 months of storage at 30, 40 and 50°C and concluded that storage conditions play an important role in preservation of this particular nutrient during storage.

For preserving TA activity (Fig. 2c), the temperature of storage has fundamental significance. The highest loss was observed in

samples stored at 20°C, and less TAA was lost in samples stored at 4°C. During the first four months of storage at 20°C the degradation of TAA was intensive. After the 4th month the rate of degradation of TAA was significantly lower but after the 8th month the rate of degradation of this component was higher. For samples stored in the dark at 4°C, there was no change in TAA during the first two months. After two months of storage, the rate of degradation was constant and all the time the loss of TAA was lower compared to the samples stored at higher temperatures. These conclusions are in accordance with the results obtained by Odriozola-Serrano *et al.* [30], who found a decrease in TAA of 35.7% after 56 days of storage at 4°C, although in our research at the same temperature the level of loss of TAA was lower (Fig. 2c). Three studied parameters lycopene, β -carotene and TA activity, as well as the dependence of their losses as a function of storage period in different conditions are shown in Figs. 3a-3c. In all cases, the greatest loss was observed for β -carotene, and the smallest one for lycopene. Degradation of carotenoids and especially of β -carotene has been explained by Boon *et al.* [36] claiming that carotenoids belong to a group of non-stable bioactive substances, with many mechanisms of degradation in some tomato products. Our results are significantly different from those of Koh *et al.* [17], who displayed a stable level of β -carotene and lycopene in tomato juice: after one year of observation, the level of lycopene was 96% and β -carotene was 100% preserved. According to our results the amount of these bioactive substances was not constant in any storing conditions. Our results are in accordance with those of most researchers who found that the phyto-nutrients were lost during storage [19, 24, 25]. They studied the changes of β -carotene in juice after 7 months of storage at 22°C for 12 varieties and found a difference in the level of β -carotene comparing fresh and processed fruits. The loss of β -carotene was 20% during extraction and other 20% was found after 7 months of storage [19]. Rate of lycopene degradation in juice stored in daylight differs from that on storing in dark at 20°C and in dark at 4°C. After one year, degradation rate of lycopene for storing in light was 2.4; for storing in the dark at 20°C the rate was 1.86 and at 4°C the rate was 1.81 (Table 1).



a) light 20 °C

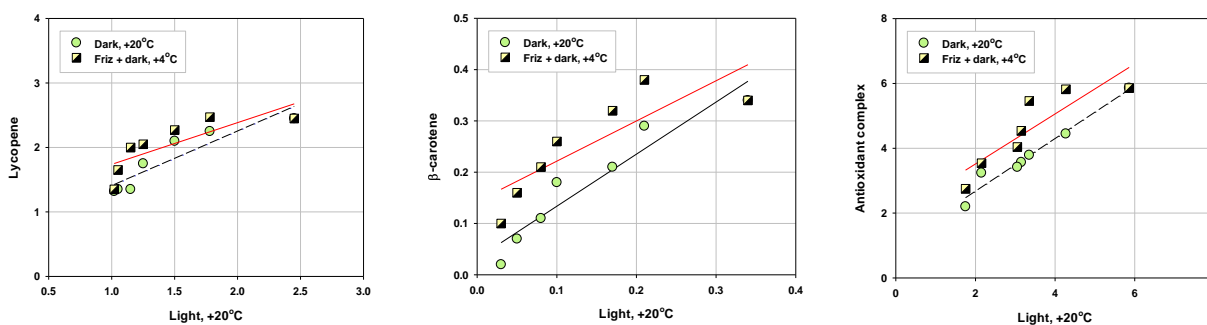
b) dark 20°C

c) dark 4°C

Figure 3. Percentage of lycopene (a), β -carotene (b) and antioxidative activity (c) complex loss depending on time in different storage conditions

Table 1. Index of lycopene and β -carotene and antioxidative activity degradation in different conditions during one year

Months of storage	Lycopene			β -Carotene			TA activity		
	Light, 20°C	Dark, 20°C	Dark 4°C	Light, 20°C	Dark 20°C	Dark 4°C	Light, 20°C	Dark, 20°C	Dark 4°C
2	1.38	1.09	0.99	1.62	1.17	1.00	1.37	1.32	1.00
4	1.63	1.17	1.08	2.00	1.62	1.06	1.75	1.55	1.07
6	1.96	1.40	1.20	3.40	1.89	1.31	1.86	1.64	1.29
8	2.13	1.81	1.23	4.25	3.09	1.62	1.92	1.71	1.45
10	2.33	1.81	1.48	6.80	4.86	2.13	2.73	1.81	1.66
12	2.40	1.86	1.81	8.50	6.80	3.40	3.35	2.66	2.13



a) $\bar{y}=0.069+1.068x^2-0.272x^3$,
 $p=0.0041^{**}$, $p=0.0304^{**}$

b) $\bar{y}=-0.019+1.067x^2-0.144x^3$,
 $p=0.0009^{**}$, $p=0.0183^{**}$

c) $\bar{y}=-0.011+0.826x^2+0.133x^3$
 $p<0.0001^{**}$, $p=0.009^{**}$

Figure 4. Regression analysis of the change in the level of lycopene (a), β -carotene (b) and antioxidative activity (c) for storing in light (+20°C) and in dark (+20°C and +4°C)

Our results were partially in accordance with Sharma and Le Maguer [37] who found 2.7 and 7.5 times higher rates of lycopene degradation in thermally treated tomato puree stored for 60 days in the dark at 25°C comparing to samples stored at 5 and 20°C, respectively, in the same conditions. Our results were in accordance with those of Min *et al.* [38] who found no significant differences in the level of lycopene for 1.5 months of storage in the dark at 4°C. In these storing conditions and in this period no degradation was observed in our research. Our results were opposite to those of Rajchl *et al.* [39] who found a decrease in lycopene of 24% in commercial ketchup after 19 days of storage at 25°C, having in mind that ketchup is a thermally treated tomato juice. The results of this

research could be compared with the similar research of Marković *et al.* [14] where tomato juice was stored in the dark at 5, 15 and 25°C and in light at 25°C for 6 months and where the variation of lycopene was not significant comparing to the level of lycopene at the beginning of the storage for a short period of time. With the increase in time of storage for all treatments the level of lycopene significantly decreased. The obtained results of storing in light at 20°C showed that lycopene quickly degraded comparing to the treatments in dark after 2 months (27.35%), (Fig 1a).

Losses of β -carotene in light were 8.50 times higher comparing to one year of storage in light at 20°C. High loss was registered while storing in the dark at 20°C after 12 months (index of degradation

6.80). When stored in the dark at 4°C, the losses of β -carotene were the lowest (3.4 times after 12 months) (Table 1). This is in accordance with Gupta et al. [21] where storage of samples at 4, 25 and 37°C for 52 weeks resulted in degradation of lycopene and the variation was explained as a function of tomato variety, processing method, temperature and duration of storage.

The regression coefficients pointed to a significant difference between lycopene, β -carotene and TA activity in terms of storage in light and in dark (Fig 3). For all the researched traits, partial regression coefficients proved a significant difference between storage in light (20°C) and in dark at 20°C and 4°C, as well as high dependence of storing in the dark at 4°C. Differences in loss of lycopene, β -carotene and total antioxidative activity were at the level of statistical significance among storing in light (20°C) and storing in dark both at 20°C and at 4°C. Partial regression coefficients proved high dependence and significant difference in the preservation of antioxidative activity for storing in light in favour of storing at the dark (20°C and 4°C) (Fig. 4).

Dynamics of loss was different depending on storing conditions. Repeated thermal treatment of tomato puree exhibited the existence of many mechanisms of degradation: possible auto-oxidation and isomerisation of carotene, as well as increased extraction of carotenoids at high temperatures [40]. Additional information could give the possibility of optimization of processing for obtaining products with high nutritional values after extended period of storage [41]. Tomato products in most cases are thermally treated once more during cooking (depending on the meal prepared). For qualitative products we need more information regarding production process, genotype selection, agro technique of crop growing, determination of optimal time of yield, etc. Understanding of mechanisms of biochemical changes that take place in the tissue during processing is of a great importance. This represents important steps that will lead to innovation in food industry.

CONCLUSION

Generally, from these dependencies the following conclusions can be drawn:

- The fastest and most intense degradation was found for β -carotene regardless of the storing conditions;
- All studied components underwent the fastest decomposition in the first two months, when the sample was kept in light at 20°C;

- Lycopene was most stable in the sample stored in the dark at 4°C;
- For all studied components in the sample stored in the dark at 4°C there was no change in composition in the first two months.

Acknowledgement: This study was supported by the Serbian Ministry of Education, Science and Technological Development: Projects No. TR31059 (Integrating biotechnology approach in breeding vegetable crops for sustainable agricultural systems).

REFERENCES

1. H. D. Sesso, S. Liu, J. M. Gaziano, J. E. Buring, *J. Nutr.*, **133**, 2336, (2003).
2. A. Osińska, M. Osiński, A. Krasnińska, B. Begier-Krasnińska, *Kardiologia i Torakochirurgia Polska*, **14**, 133, (2017).
3. K. Yamagata, Chapter 7 Genetics and Molecular Biology, Carotenoids, 2017. DOI: 10.5772/67464.
4. J. K. Willcox, G. L. Catignani, S. Lazarus, *Crit. Rev. Food Sci.*, **43**, 1 (2013).
5. S. M. D. Grieb, R. P. Theis, D. Burr, D. Benardot, T. Siddiqui, N. R. Asal, *J. Am. Diet. Assoc.*, **109**, 656, (2009).
6. J. Shi, M. Le Maguer, *Crit. Rev. Biotech.*, **20**, 293, (2000).
7. A. A. Abushita, H. G. Daood, P. A. Biacs, *J. Agric. Food Chem.*, **48**, 2075 (2000).
8. S. M. Wasim, J.P. Singh, *J. Chem. Environ.*, **19**, 82, (2015).
9. F. J. García-Alonso, S. Bravo, J. Casas, D. Pérez-Conesa, K. Jacob, M. L. Periago, *J. Agr. Food Chem.*, **57**, 6815, (2009).
10. D. Murador, D. Cunha, V. Rosso, *Food Res. Int.*, **65**, 177, (2014).
11. J. Singh, M. Rai, *Indian J. Hortic.*, **54**, 33, (2006).
12. G. Graziani, R. Pernice, S. Lanzuise, P. Vitagliano, M. Anese, V. Fogliano, *Eur. Food Res. Technol.*, **216**, 116 (2003).
13. C. H. Chang, H. Y. Lin, C. Y. Chang, Y. C. Liu, *J. Food Eng.*, **77**, 478, (2006).
14. K. Marković, M. Hruška, N. Vahčić, *Acta Aliment. Hung.*, **36**, 89, (2007).
15. R. Tamburini, L. Sandei, A. Aldini, F. De, C. Leoni, *Industria Conserve*, **74**, 341, (1999).
16. R. Re, P. M. Bramley, C. Rice-Evans, *Free Radical Res.*, **36**, (2002).
17. E. Koh, S. Charoenprasent, A. E. Mitchell, *J. Sci. Food Agr.*, **92**, 23, (2012).
18. S. Xianquan, J. Shi, Y. Kakuda, J. Yueming, *J. Med. Food*, **8**, 413, (2005).
19. V. Lavelli, G. Giovanelli, *J. Sci. Food Agr.*, **9**, 966 (2003).
20. L. E. Ordonez-Santos, L. Vazquez-Oderiz, E. Arbones-Macineira, M. A. Romero-Rodriguez, *Food Chem.*, **112**, 146 (2009).

21. R. Gupta, V. M. Balasubramaniam, S. J. Schwartz, D. M. Francis, *J. Agr. Food Chem.*, **58**, 8305 (2010).
22. J. S. Smith, Y. H. Hui, *Food Processing, Principles and applications*, Blackwell Publishing Company, USA, 2004, Print ISBN: 9780813819426, Online ISBN: 9780470290118.
23. G. B. Martinez-Hernandez, M. Boluda-Aguilar, A. Taboada-Rodriguez, S. Soto-Jover, F. Marin-Iniesta, A. Lopez-Gomez, *Food Eng. Rev.*, **8**, 52 (2015).
24. J. M. Dietz, W. A. Gould, *J. Food Sci.*, **51**, 847 (2006).
25. A. Vashista, A. Kawatra, S. Sehgal, *Plant Food Hum. Nutr.*, **58**, 1 (2003).
26. M. V. Eberhardt, C. Y. Lee, R. H. Liu, *Nature*, **405** (6789), 903 (2000).
27. C. Sánchez-Moreno, L. Plaza, B. de Ancos, P. M. Cano, *Food Chem.*, **98**, 749 (2006).
28. V. Dewanto, X. Z. Wu, K. K. Adom, R. H. Liu, *J. Agr. Food Chem.*, **50**, 3010, (2002).
29. D. Perez-Conesa, J. Garcia-Alonso, V. Garcia-Valverde, M. D. Iniesta, K. Jacob, L. M. Sanchez-Siles, *Innov. Food Sci. Emerg. Technol.*, **10**, 179 (2009).
30. I. Odriozola-Serrano, R. Soliva-Fortuny, V. Gimeno-Ano, O. Martin-Belloso, *J. Food Eng.*, **89**, 210 (2008).
31. F. Xu, L. Li, X. Huang, H. Cheng, Y. Wang, S. Cheng, *J. Med. Plants Res.*, **4**, 2544 (2010)
32. M. Nagata, I. Yamashita, *J. Food Sci. Tec.*, **39**, 925 (1992).
33. R. Njegić, M. Žižić, M. Lovrić, D. Pavličić (Fundamentals of Ancient Analysis - III Edition). Beograd, Srbija: Savremena administracija, 1991.
34. R.A. Hoshmand, *Statistical Methods for Environmental et Agricultural Sciences*. (2nd edition) CRC Press, Boca Raton, New York, USA. 1998, ISBN: 0-8493-3152-8.
35. K.C. Hsu, F. J. Tan, H. Y. Chi, *LWT – Food Sci. Technol.*, **41**, 367 (2008).
36. C.S. Boon, D. McClements, J. Weiss, E. A. Decker, *Crit. Rev. Food Sci.*, **50**, 515 (2010).
37. S.K. Sharma, M. Le Maguer, *Ital. J. Food Sci.*, **2**, 107, (1996).
38. S. Min, Z. T. Jin, Q. H. Zhang, *J. Agr. Food Chem.*, **51**, 3338, (2003).
39. A. Rajchl, M. Voldrich, H. Čížkova, M. Hronova, R. S. Evcik, J. Dobias, J. Pivonka, *J. Food Eng.*, **99**, 465 (2010).
40. S. Luterotti, D. Bicanic, K. Marković, M. Franko, *Food Control*, **48**, 67 (2015).
41. E. Capanoglu, J. Beekwilder, D. Boyacioglu, R. C. H. De Vos, R. D. Hall, *Crit. Rev. Food Sci.*, **50**, 919 (2010).

Calibration of a system for air-borne gamma spectrometry survey and mapping implementation

I. I. Iliev^{1,2*}

¹ Sofia University „St. Kliment Ohridski“, Faculty of Physics, 5, James Bourchier Blvd., 1164 Sofia, Bulgaria

² Theta-consult Ltd., 5A, James Bourchier Blvd., 1164 Sofia, Bulgaria

Received April 4, 2019; Revised May 25, 2019

Depending on the area of the territory that has to be surveyed and the desired resolution of the gamma- spectrometry map, the operation method has to be chosen. It includes the type of air-craft, detector system, flight plan – speed, height, direction and distance between profiles. In the current article gamma-spectrometry mapping over 4.4 km², using helicopter and in compliance with IAEA’s recommendations, is described. The factors, that affect the measurement were reviewed and taken into account in choosing the calibration method. Its validity is proven by two comparisons. The first one is between the results from high altitude measurements and the expected attenuation of the cosmic radiation in the atmosphere. The second one is between values from the mapping after the calibration and results from sampling ground measurements. The calculation done upon the task completion is explained. Representative part of the results from the particular mapping is given as color images extracted from the genuine gamma maps.

Keywords: Airborne, Radioactive pollution, Gamma-mapping, Spectrometry, NaI(Tl), Calibration method

INTRODUCTION

Airborne-gamma mapping could be implemented in many different ways (IAEA, 1991) [3], (A. Elkhadragy *et al.*, 2017) [5], (Horsfall, 1997) [6], (Grasty and Minty, 1995) [7]. Using the modern technology, it is possible to cover all the segments in scaling (Kaiser *et al.*, 2016) [12], (Gabrlík and Lazna, 2018) [11]. According to the required space resolution and minimum detectable activity (MDA), we choose the proper parameters of the detector system, the aircraft and the flight plan. For accurate results the most important thing stays the adequate calibration.

In the current article the calibration methods used during an implementation of middle scaled air-borne gamma spectrometry mapping is described. It is performed over two fields of 3.2 km² and 1.2 km² flat land territory on the Danube river coast near Oryahovo, Bulgaria, using a helicopter and a 16 liter NaI(Tl) scintillating detector system. The site conditions do not allow trivial calibration. The main task is choosing the best fitting methods, adapting them to the specific conditions and verifying the results after adaptation of the particularly chosen method.

Our team works on such projects for more than 25 years. We have already implemented many terrestrial radiation surveys using from handheld to large sodium detectors. Our latest measurements include pixelated cadmium zinc telluride (CZT) detector for stationary gamma-mapping, *in-situ* HP Ge detector and UAVs carrying different detectors

(Iliev and Dankov, 2018)[9]. We completed an air-borne gamma spectrometry mapping in 2013, using a helicopter. Later, in 2018, we had the opportunity to work again on gamma-spectrometry mapping using the same detectors, but with another helicopter and new software, which required new setting of the system and new calibration. Its basic principles are summarized in this article.

As the results from the survey have to be representative in the face of the regulatory units, we followed all the precepts of the International Atomic Energy Agency (IAEA). Most of them are in the two TECDOCs 1092 and 1363 [1, 2], Technical Report Series – No. 323 [3] and ICRU report No. 53 [4]. The report No. 323 [3] recommends five energy windows to be taken into account for geophysical surveying:

Table 1. Radionuclides suggested by IAEA for monitoring during airborne gamma-spectrometry mapping and their energy regions of interest (ROIs).

Window	Lower [MeV]	Upper [MeV]	Peak [MeV]	Radio-nuclide
Total counts	0.41	2.81		
Potassium	1.37	1.57	1.46	K-40
Uranium	1.66	1.86	1.765	Bi-214
Thorium	2.41	2.81	2.614	Tl-208
Cosmic	3.0	and higher		

EXPERIMENTAL

Equipment

In the current survey we used a complete gamma spectrometry system, which has 4 NaI(Tl)

* To whom all correspondence should be sent:
E-mail: i.iliev@thetaconsult.com

I. I. Iliev: Calibration of a system for air-borne gamma spectrometry survey and mapping implementation

scintillating detectors. Each detector is with a volume of 4 liters and has its own photomultiplier tube (PMT) and 1024 channel analyzer (MCA). The energy resolution is better than 8% for ^{137}Cs and the sensitivity is 144 cps/(nSv/h) for ^{137}Cs and 96 cps/(nSv/h) for ^{60}Co .

Each pair of detectors is in a rugged plastic box (Fig.1).



Fig. 1. Opened detector protection box, keeping a pair of NaI(Tl) detectors used in the survey.

The information is transferred to a PC through an interface box using standard TCP/IP which makes it flexible. We used a rugged laptop Getac V200 with two GPS modules (integrated and external). The software allows us to monitor the whole data stream at real time. It displays the current spectrum from each detector, dose rate alarm if a threshold is passed, the recognized radionuclide, GPS coordinates and all the other monitored parameters as altitude, flight height, detector temperature, PMT high voltage, gain, etc. The data can be exported to many different popular file formats for post-processing with other software tools. All the equipment is installed on a helicopter Schweizer 333 (269D) (Fig. 2) and can operate autonomously, but we had one operator on board for immediate support to prevent any simple failures.

The territory to be investigated was relatively small (3.2 km² and 1.2 km²) and there was no near suitable runway for a fixed-wing airplane, that is why we chose a rotorcraft.

The most important benefit of the helicopter is its lower speed, which, with an optimum at about 60-80 km/h, allows better space resolution of the gamma map. This is a starting point for most of the other parameters of the flight plan.

Another starting point is the requirement for the achieved MDA. It is fundamental for all the other calculations and requirements to the detector system and to the survey methods. The requested MDA was 1 kBq/m² for ^{137}Cs .

Calibrations on the ground

The detector system needs a series of calibrations of different parameters (IAEA-1363,

2003) [2], (Grasty and Minty, 1995) [7]. The high voltage and gain calibrations are part of the energy calibration and are both performed automatically on the basis of the ^{40}K energy peak in the spectrum. It is performed on every start of the system and corrects the drift of the peak through neighbor channels. To reduce its duration there is additional amount of ^{40}K in the detector box, which is removed during the flight to reduce the intrinsic background. As long as the measured radioactivity during flight is relatively low, compared to the system counting speed, correction for the dead time will practically not change the results and it is not done.



Fig. 2. The spectrometry system installed on Schweizer 333 (269D).

The efficiency calibration was performed on the ground using ^{137}Cs and ^{60}Co with known activity and at a certain distance. The response of the system in the particular ROI *versus* source activity gives the system efficiency. As another part of the efficient calibration can be considered the determination of the MDA for the technogenic radionuclides. It is done in the same way, on the ground using ^{137}Cs and ^{60}Co . But this time by finding the distance from which the system unambiguously recognizes the presence of the source. As we know, for a point source far enough from the detectors, the response is inversely proportional to the square of the distance, so we can calculate the attenuation of the gamma-field intensity by the particular distance. For calculating

I. I. Iliev: Calibration of a system for air-borne gamma spectrometry survey and mapping implementation

the MDA, we used the net signal (excluding the background spectrum). Even if the natural background is higher, the ^{137}Cs or ^{60}Co MDA will not be affected because the recognition algorithm works for every single ROI.

Flight plan

We chose the height of the flight to be the maximum height that allows the required MDA to be achieved on the basis of the calculated MDA during the calibrations on the ground. The resultant height for $\text{MDA} = 1 \text{ kBq/m}^2$ (^{137}Cs) was about 70 m. To ensure reserve in the achieved MDA we did not use the maximum height, but reduced it to 60 m. The spot “seen” by the detector was the spot from which 60-70% of the signal was coming. It was a circle on the ground with a radius equal to the flight height. According to this rule, the distance between flight profiles should be 120 m at maximum, and we chose 100 m to ensure 20% overlay in case of deviation from the straight line during the flight. The integration time of the detector system is 1 sec but a moving average was calculated over the last 5 sec. It means that, if we want symmetric pixels on the map, the speed of the aircraft has to be not more than 120 m/s and the best choice would be anything below 24 m/s. We used the lowest possible speed in which the particular helicopter and pilot could ensure stable flight. It was about 17 m/s which gave us integration time of about 7 s – better than the integration time of 5 s.

With the chosen parameters the first measurement flight gave basic information about the distribution of the contamination interpreted using infinite model. If some artificial contamination is found, according to its distribution, we have to plan a second flight. The plan, most often, uses a point model for point source, where the helicopter needs to hang above the source for more precise determination of its activity and line model for objects as rivers, channels or pipes, where the new flight profile should follow the object line.

As seen on Fig. 3, proper distribution modeling can be critical in defining the contamination shape, size and position.

Calibration of the system in the air

The background during flight consists of four components: intrinsic, cosmic, radon and fallout. They affect the system simultaneously, and we have to separate them in order to take into account their exact effect over the spectrum. As there were no representative data for the fallout background and after several measurements on the ground

surface near the monitored terrain, showing insignificant presence of fallout, we did not make any fallout corrections.

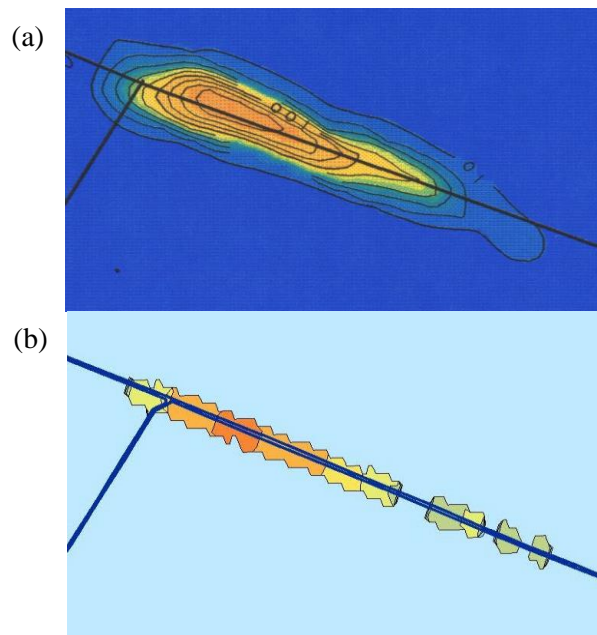


Fig. 3. Comparison between infinite model (a) used in previous surveys and line model (b) over the same water channel.

The presence of radon can be tracked by observing the counts in ^{214}Bi ROI (561 to 657 keV), as ^{214}Bi is a stable radon daughter with gamma emission at 609 keV. Its photo peak is masked by the Compton continuum of the other monitored isotopes (K, U and Th) and its quantitative evaluation requires additional spectral integrations and more complex calculations (IAEA-1363, 2003) [2] or special calibration. The radon concentration in the area was monitored with measurements on the ground and considered as insignificant for our purposes. Over the water, the average of the corrected NORM ROIs should be very close to 0, but not 0. If a high level of U is seen, this may indicate the presence of radon. However, during the flights the ^{214}Bi ROI was also monitored in case of considerable deviations. Two different measurements at the same position and same height should provide similar Bi/U ratio. A higher ratio could indicate a higher radon level during the corresponding measurement period.

The intrinsic and cosmic background corrections start with acquisition of a 15 min spectrum at each altitude – 1800 m, 2300 m and 2800 m. The height of the flight should be more than 1000 m and the weather has to be clear. The 15 min are divided into three 5 min intervals. On fig. 5 each blue dot gives the result for 5 min integration. The cosmic background depends on the altitude and can be

calculated for a certain geographic region (EAURADOS, 2004) [8], but the most accurate way to evaluate it is to be empirically reached with real measurement of the particular system. According to some initial information about the detector system response to high energy cosmic radiation given by the manufacturer like the limit of the energy range and anisotropy, the theoretical model that we considered as best for our purpose could be represented as follows:

$$D = A \cdot \exp(0.00038 \cdot h) + B \quad (1)$$

where:

D = cosmic dose rate;

A = cosmic dose rate at sea level;

h = altitude;

B = aircraft background dose rate.

In Eqn. 1 we have to consider that the cosmic dose rate (D) and the cosmic dose rate at sea level (A) are values measured by the particular detector system, and are not the real cosmic dose rates, because of the detector system specifics.

During the flight planning there was a potential problem that we had to solve. First calibration flight had to be over water to eliminate the gamma-rays coming from the ground. Near the current terrain there was a water basin that we could use – Danube river, but it was not allowed to perform our flights at higher altitudes above it, because it is a restricted border area. So we had to use flights at high altitudes and heights only over the ground (soil and rocks). This made the calibration method more specific and had to be validated. We suggested this to be done in two approaches. The first one was to create a graph of the cosmic radiation background, in the cosmic ROI, against altitude. Similarity between the fit on the graph and Eqn. 1 could prove the validity of the calibration method.

The second approach to the calibration validation is a comparison to direct sampling measurement done on the ground with an *in-situ* HP Ge spectrometer. It is calibrated to show specific activity for the particular geometry and for the same radionuclides (^{40}K , $\text{Th}_{\text{equivalent}}$, $\text{U}_{\text{equivalent}}$). The sampling points coordinates are chosen after the map is created. The criteria are – one sample measurement in the area with the lowest activity and one with the highest activity, in order to cover the full range of the mapped values.

The other background components could also be extracted from the results of the height flights measurements. With higher altitudes the cosmic background increases, the Earth gamma-rays are reduced by the flight height and the aircraft background stays constant. With building a graph of the counts for every region of interest (ROI)

against the altitude, we can evaluate each background component. The cosmic radiation affects all the ROIs, but the ROI that is above 3MeV is affected only by the cosmic rays. Using this effect, and knowing the detector efficiency for every ROI, we can calculate the net counts coming from the cosmic rays. The procedure for separation of the background components we used for this calculation is fully described by Grasty and Minty, 1995 [7] and TECDOC-1363 [2].

A linear regression (fig. 4) of the cosmic window counts on another ROI counts yields the cosmic sensitivity represented by the slope of the regression line and its zero intercept is the aircraft background for that ROI:

$$N_{\text{ROI}} = a_{\text{ROI}} + b_{\text{ROI}} \cdot N_{\text{COS}} \quad (2)$$

where:

N_{ROI} = aircraft + cosmic background count rate in the particular ROI;

N_{COS} = cosmic ROI counts;

a_{ROI} = aircraft background in the particular ROI;

b_{ROI} = cosmic background in the particular ROI normalized to unit counts in the cosmic ROI.

The self-background calibration should be performed every time the helicopter or part of it changes, because this component of the background includes the effect of the fuel, the pilot and even the presence of an operator onboard and includes not only the possible internal activity, but also gamma-rays attenuation or even secondary radiation from the interactions between cosmic high-energy radiation and any part of the aircraft.

RESULTS AND DISCUSSION

Fig. 5 shows the measured total counts in the cosmic ROI against altitude. It has an exponential fit, very similar to the expected one in Eqn. 1. This is enough to conclude that the results from the first approach are acceptable.

Creating the maps

The representations of Normally Occurring Radioactive Materials (NORM) and technogenic radioactive contamination distributions have principal differences. NORM always exist and we can only evaluate their values in units of mass concentration. At the same time for technogenic radionuclides Search and Investigation Algorithm (SIA) is used. The algorithm is based on monitoring the variance in each region of interest (ROI) of the energy spectrum. When the variance is noticeable, or in other words – meets some criteria, then the net value in the ROI is being calculated and given as a result in activity. And finally the activity is

I. I. Iliev: Calibration of a system for air-borne gamma spectrometry survey and mapping implementation

represented as a point or infinitely distributed, depending on the distribution model. Even if we do not know the SIA mathematics we can use it to find the MDA empirically, by finding the minimum activity that shows on the data records. The ratio between the K, U and Th ROI should also be consistent. It's not possible to have a high content of Th and no U or K, because of the Compton counts due to Th in these ROIs.

Activity calculations are based on the function describing the sensitivity of the detector *versus* height. The activity was calculated for every single ROI. The result is given in Bq/m² for the infinite contamination model and in Bq for the point source model for each radionuclide corresponding to the particular ROI.

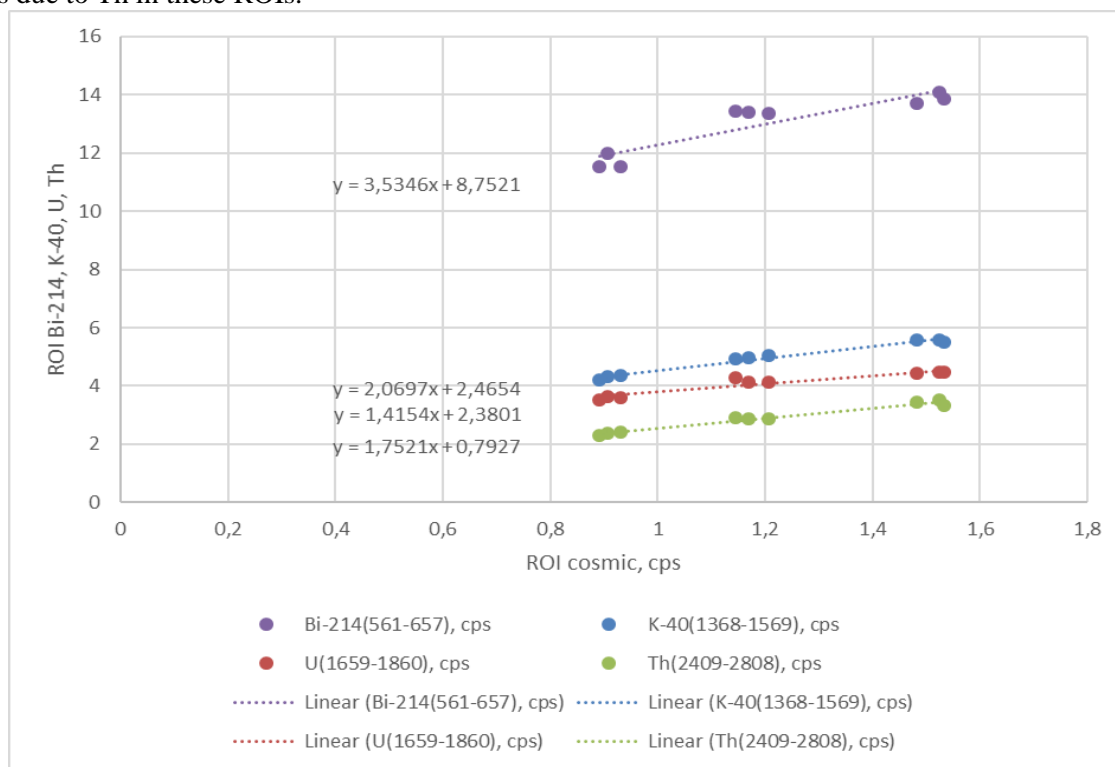


Fig. 4. Results from the height flights: each color represents different ROI; each graph can be fitted to linear regression of the ROI to the cosmic ROI; each point represents a measurement with 5 min integration time. The slope of the regression represents the cosmic sensitivity and the zero intercept is the intrinsic background.

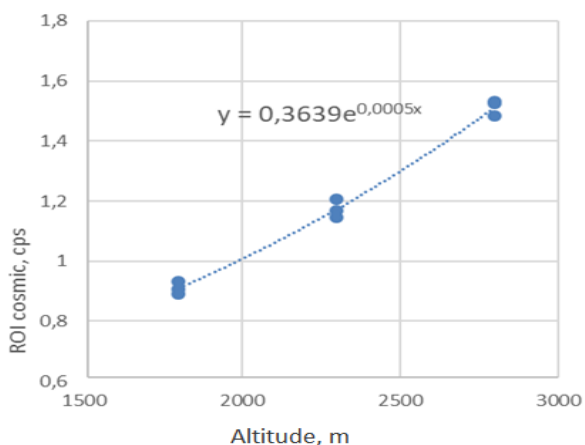


Fig. 5. Exponential fit of the measured cosmic background. Each blue point represents integration for 5 min

Concentration calculations are equivalent to the

activity calculation, but a relaxation coefficient β is taken into account (ICRU Report-53, 1994)[4]. It represents the vertical distribution of the nuclides in the soil (defined by the relaxation mass per unit area). Value of β mainly depends on contamination's age. At the same time, most of the gamma rays are attenuated in the upper 30 cm of the soil, and almost none of the gamma radiation is coming from more than 50 cm under the ground surface (IAEA-1363, 2003) [2]. In this manner, mass or volume concentrations can be evaluated only for the upper layer of the soil.

Ground dose rate calculations were done in three steps. First is the measured dose rate at the point of the detector, from which the intrinsic background, the cosmic background and local radon background should be subtracted. The second step is to correct for the height, using the equivalent height at standard conditions and the height-to-sensitivity

function. Other function parameters are air pressure and air temperature as well. The third step is to add the cosmic background calculated at ground level.

The result consists of a variety of maps representing concentrations of the monitored radioisotopes and calculated dose rates. In Fig. 6, a simple preview of the maps is shown in the form of color images extracted from the genuine maps, just for illustrative purposes. The “x” marks show the sampling coordinates for the measurements on the ground.

The results from the second approach also confirmed the applicability of the calibration method in the particular conditions.

The first thing we have to know about uncertainty is that it is quite high. But we have to consider that this survey method is mainly indicative and for rough evaluations. The method has first been created for geological purposes. It is macroscopic and its idea is to be used over a wide open territory in order to find some regions of interest. If we use the detector system on the ground or in short-distance geometry the uncertainty will be lower and can be defined, but on 60 m above cross-country terrain there are many valuable factors affecting the result. The most important is the accurate measurement of the distance to the object on the ground.

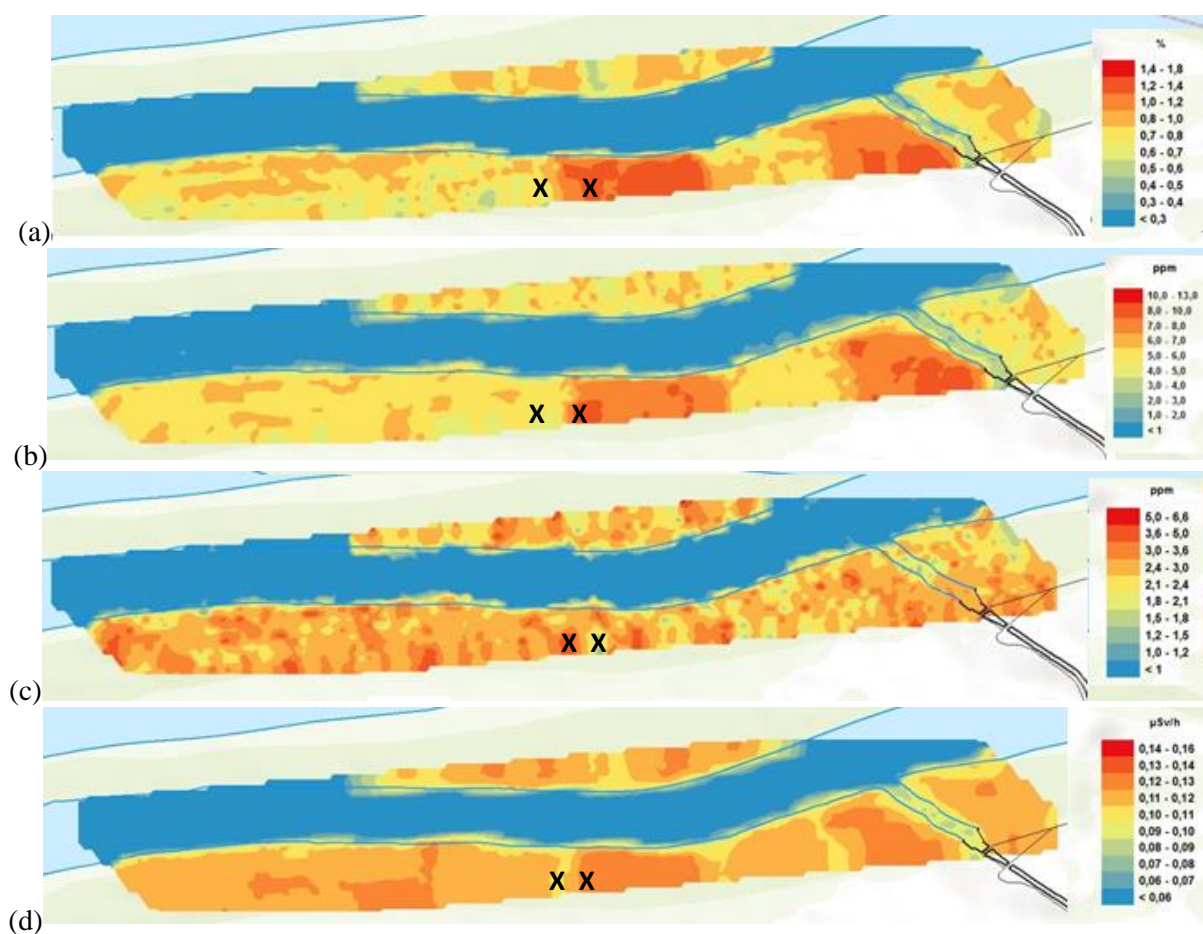


Fig. 6. Images from the resulting gamma maps of NORM: (a) ^{40}K in %; (b) $T_{\text{equivalent}}$ in ppm; (c) $U_{\text{equivalent}}$ in ppm; (d) ground dose rate calculated according to TECDOC-1363 [2] in $\mu\text{Sv/h}$. The “x” marks show the ground measurements positions.

The barometric altimeter gives us altitude, but not exactly the distance and the GPS altitude, even when corrected with the geoidal shape of the Earth, does not provide definable precision. The atmospheric pressure, temperature and humidity also significantly affect the attenuation in air, but usually in open space they can vary and change quickly. With the current system it is not possible

to monitor all these parameters. The amount of the gamma-photons reaching the detector also depends on the substrate under the contamination. Its density and Z_{eff} affect its backscattering. Very significant error could appear when the model we choose does not correspond to the real contamination shape. As we usually start with an infinite model, the system result will be divided to

the “visible” area of the detector and the result for the surface activity will always be underestimated. For point source estimation, in the activity calculation we assume that the source is right under the helicopter, but in practice there could be a difference. For an accurate quantitative evaluation of the activity of the contamination we have to know all the affecting factors which will lead the investigation to another direction. Because of all mentioned above, in our survey we consider the uncertainty evaluation as not reasonably achievable.

CONCLUSION

The airborne gamma-spectrometry mapping is a macroscopic method for quick investigation of large territories and its nature does not assume high accuracy. In any case, improving the calibration can enhance the reliability of the results.

Because of the increasing contribution of cosmic radiation with height, it should be considered during the interpretation of the results. It is not possible to exclude the cosmic radiation on the base of its energy, because it covers all the spectrum and even causes secondary radiation after interaction with the flying vehicle. Building a graph of the counts in the cosmic ROI to altitude we can quantitatively verify our system response to this kind of radiation. And plotting graphs for each relation between cosmic ROI and every other ROI shows linear regressions. Their slope and zero intercept are the sensitivity to cosmic radiation and the intrinsic background, respectively. Comparison of the resultant altitude function of the cosmic radiation contribution and a typical one shows satisfactory incidence, as the comparison between the results for activity and those from a stationary spectrometer for *in-situ* measurements.

REFERENCES

1. IAEA-TECDOC-1092, Generic procedures for monitoring in a nuclear or radiological emergency, International Atomic Energy Agency IAEA, 1999.

2. IAEA-TECDOC-1363, Guidelines for radioelement mapping using gamma ray spectrometry data, IAEA, 2003.
3. IAEA, Airborne Gamma Ray Spectrometer Surveying, Technical Report Series, No. 323, IAEA, Vienna, 1991.
4. ICRU, Report-53, Gamma-Ray Spectrometry in the Environment, International commission on radiation units and measurements, U.S.A, 1994.
5. A.A. Elkhadragy, A.A. Ismail, M.M. Eltarras, A.A. Azzazy *NRIAG Journal of Astronomy and Geophysics*, **6**, 148 (2017), DOI: 10.1016/j.nrjag.2016.12.001.
6. K. R. Horsfall, *AGSO Journal of Australian Geology & Geophysics*, **17(2)**, 23 (1997).
7. R. L. Grasty, B. R. S. Minty, A guide to the technical specifications for airborne gamma-ray surveys, *AGSO, Record* **1995/60**, (1995).
8. EURADOS working group 5: D.T. Bartlett, P. Beck, P. Bilski, J.-F. Bottollier-Depois, L. Lindborg, H. Schraube, F. Spurný, F. Wissmann, E. Felsberger, W. Heinrich, B. Lewis, D. O’Sullivan, G. Reitz, U. Schrewe, L. Tommasino, G. Dietze, I. McAulay, J. Siedenburg, A. Ruge, K. Schnuer, K. Ulbak, J.C. Saez-Vergara, H. Roos, G.A. Taylor, R. Grillmaier, W. Friedberg, K. O’Brien, M. Pelliccioni, B. Wiegel, EC Issue No. **140**, Radiation Protection, (2004) ISBN 92-894-8448-9, EC.
9. I. Iliev, P. Dankov, Distance methods for gamma-mapping with unmanned aerial vehicles (UAV), *Annual of Sofia University “St. Kliment Ohridski” Faculty of Physics*, **111**, p. 142 (2018).
10. Yu.L. Zabulonov, V.M. Burtnyak, I.O. Zolkin, Airborne gamma spectrometric survey in the Chernobyl exclusion zone based on oktokopter UAV type, *Problems of Atomic Science and Technology*, 2015.
11. P. Gabrlík, T. Lazna, *IFAC-PapersOnLine*, **51**, 256 (2018).
12. R. Kaiser, I. Darby, M. Matos, M. Bogovac, R. Murphy, Ph. Ortega, UAV-based mobile gamma spectrometry, IAEA Physics Section, University of Adelaide, 2016, http://www.physics.adelaide.edu.au/cssm/workshops/inpc2016/talks/Kaiser_Thu_R1_16_05.pdf.

Removal of chromium from aqueous solution using chitosan: An experimental study

M. Didarul Islam^{1*}, Sh. Rahaman², J. Hasan Jiban², M. Muhtasim Mahdi²

¹*Applied Chemistry and Chemical Engineering, Faculty of Engineering and Technology, University of Dhaka, Dhaka, Bangladesh*

²*Institute of Leather Engineering and Technology, University of Dhaka, Dhaka, Bangladesh*

Received April 22, 2019, Revised May 22, 2019

In this work, the effectiveness of using chitosan for the treatment of chromium from aqueous solution was studied. Parameters that influence the adsorption process such as adsorbent dose, contact time and pH are studied in batch experiments. It was found that 40 mg dose, contact time of 180 min and pH of 3 are the optimum conditions for the removal of chromium from aqueous solution. The experimental equilibrium adsorption data fitted well to the Langmuir isotherm model, which indicates that adsorption of chromium on the surface of chitosan is monolayer coverage of the adsorbate on the outer surface of the adsorbent under these experimental conditions. The adsorption kinetics followed the pseudo-second-order kinetic model which suggests that the adsorption process is chemisorption and the rate-determining step is probably surface adsorption. This adsorbent was successfully used for the treatment of different operational sectional tannery effluents and it was found that about 83.58 and 90.27% of chromium were removed from chrome tanning and re-tanning, respectively. At the same time other physicochemical properties such as turbidity, conductivity, BOD, COD and TDS were significantly reduced.

Keywords: Chitosan, isotherm, kinetics, adsorption.

INTRODUCTION

Tannery industry represents one of the most important economic sectors in many countries and according to 2003 data leather industry produces 18 billion square feet of leather per year whose estimated value is about \$40 billion [1]. During the conversion of rawhide to leather several mechanical and chemical operations are required involving many chemicals like acid, alkali, oil grease, chloride, metalorganic dyes, natural and synthetic tanning agents, salts and many toxic metals [2]. In Bangladesh there are more than 220 tannery industries, about 90% of them are engaged in chrome tanning operation [3]. In chrome tanning operation excess amount of chromium is used, 60-70% of chromium is bonded to rawhide and skin, the remaining chromium salts are directly disposed into the environment without any treatment [4]. The toxicity, mobility, and bioavailability of Cr depend fundamentally on its chemical forms, e.g., hexavalent chromium is highly mobile in soil and water systems and toxic on biological systems whereas trace amounts of trivalent chromium is essential for living organisms and less mobile in water and soil systems [5]. However, in aqueous phase trivalent chromium is considered as a serious threat for the environment because it could be oxidized to Cr(VI) in the presence of oxidizers like manganese dioxide [2]. Several experiments suggest that Cr (III) can be accumulated into wheat, rice grains, soybean, sunflower [5, 6].

So if these tannery effluents are directly disposed into a river or a domestic sewage system, they will contaminate surrounding channels, agricultural fields, irrigation fields, surface water and finally will be introduced into the food chain [7, 8].

Over the past few decades, several physical, chemical, and biological methods have been applied for the removal of toxic metals from wastewater. Several methodologies have been used in removing chromium from wastewater. Chemical coagulation can be used to remove substances producing turbidity in water, consisting of clay minerals and proteinous matter but cannot effectively reduce toxic metals [9, 10]. On the other side, membrane methods such as reverse osmosis, nanofiltration, ultrafiltration, and microfiltration can be used to treat wastewater but these methods possess several disadvantages, e.g., incomplete metal removal, expensive equipment setup and monitoring systems required [11-13]. Natural adsorbents have been highly recommended by the researchers to remove heavy metals as these adsorbents can effectively and economically remove toxic metals from wastewater without or with very little modification of the adsorbent. Moreover, natural adsorbents are biodegradable so that after treatment they have no adverse effect on the environment. Several adsorbents have been used in the past like maple sawdust [14], pine species [15], soya coke [16], green algae [17], tea waste [18], plum tree bark [19]. All of these materials show excellent sorbent properties and this

* To whom all correspondence should be sent:
E-mail: didarulislam1992dh@gmail.com

is the main reason to carry out the present study. In this experiment, chitosan (adsorbent) from prawn shells was used in a batch study to find out the optimum conditions for the removal of chromium. Equilibrium adsorption data (dose effect) were modeled using Langmuir and Freundlich isotherm models while pseudo-first-order and pseudo-second-order models (time effect) were used to study the adsorption kinetics. The adsorbent (chitosan) was successfully used under the optimum conditions for the treatment of different operational sections of a tannery effluent.

MATERIALS AND METHODS

Materials

Prawn shells and raw clay for modification were collected from local prawn hatcheries in Satkhira, Bangladesh and Bijoypur, Netrokona, Bangladesh. Sodium hydroxide and potassium dichromate were obtained from LOBA Chemie (India). Hydrochloric acid, acetic acid, sulphuric acid were obtained from Merck, Darmstadt, Germany. All materials were of analytical grade or higher. Chemicals were used as obtained without further purification.

Preparation of chitosan from waste prawn shells

Chitosan was extracted from waste prawn shells according to Taslim *et al.* [20]. First, prawn shells were thoroughly washed with tap water and then boiled in water for 2 h at 60°C temperature. After washing the shells were dried and crushed in a milling machine. Crushed shells were then de-proteinized with 4% (w/w) NaOH in 1:16 ratio (w/w) at 70-90°C for 3 h. Water-insoluble proteins were removed in this stage after neutralization. Dried samples of de-proteinized shells were demineralized with 3N HCl at a ratio of 1:16 (w/w) on stirring for 3 h at 70°C. This demineralization yields chitin. The dried chitin was de-acetylated by heating at 80-100°C with 50% NaOH (w/w) solution at a ratio of 1:20 (w/w) for 4 h. After washing and neutralization chitosan was obtained.

Characterization of chitosan

Fourier transform infrared (FTIR) spectrometry (FT-IR 8400S spectrophotometer Shimadzu Corporation, Japan) was used to analyze the functional groups of chitosan in the diffuse reflectance mode at a resolution of 4 cm⁻¹ in KBr pellets. To determine thermal properties of chitosan TGA and DSC analysis were performed [21]. TGA was conducted in a TGA-50H SHIMADZU thermogravimetric analyzer, Japan from room temperature (30°C) to 600°C at a heating rate of 10°C /min in nitrogen atmosphere with a flow rate

of 10 ml/min on alumina cells. Differential scanning calorimetry (DSC) measurements were performed on a Perkin Elmer DSC7. DSC curves of each film were obtained from the second heating run at a rate of 10°C/min, after the first run of heating up to 190°C and cooling to 25°C at the same rate of 10°C/min, in nitrogen atmosphere, in order to estimate the glass transition temperature [22].

Batch adsorption study

Batch experiments were carried out to evaluate the influence of pH, contact time and adsorbent dose on the removal of chromium from solution. For pH optimization experiments were carried out by adding 40 mg of adsorbents in 100 ml of chromium solution (40 ppm) at a temperature of 30°C on a rotary shaker at 120 rpm for 120 min. The initial pH of the Cr(IV) solution was adjusted to different pH values (2.50, 3.50, 4.00, 4.50, 5.00 and 5.50) by dilute hydrochloric acid and sodium hydroxide using a pH meter (DELTA-320). For determination of the effect of contact time on adsorption, assessments were done with 40 mg of adsorbents in 100 ml of chromium solution (40 ppm) at a temperature of 30°C on a rotary shaker at 120 rpm. The samples were withdrawn from the shaker at predetermined time intervals (30, 60, 90, 120, 150, 180, 210 and 240 min). For dose optimization, 100 ml of 40 ppm stock solution of Cr was taken in a 250 mL conical flask at the optimum pH. Different doses (20, 40, 60, 80, 100, 120, 140, 160 and 180 mg of adsorbent) were added in each of the solutions and agitated at 30°C in a reciprocating shaker at a fixed speed of 120 rpm for 12 min. After adsorption, adsorbents were separated from the solution by centrifugation at 5000 rpm for 10 min. All experiments were replicated and the average results were used in data analysis. The amount of chromium adsorbed per unit adsorbent powder was calculated according to the following equations:

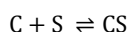
$$\% \text{Removal} = \frac{C_o - C_c}{C_o} \times 100 \quad (1)$$

$$Q_{\max} = \frac{C_o - C_e}{M} \times V \quad (2)$$

Here, Q_{\max} is the adsorption capacity of metal ion adsorbed per gram of adsorbent, C_o and C_e are the initial and final concentration, respectively, M is the mass of the adsorbent (g) and v is the volume of chromium solution taken for the adsorption study (L).

The equilibrium isotherms were experimented in order to get a better insight into the adsorption mechanism. There are many theories relating to adsorption equilibrium. Three isotherm equations were tested in the present research, namely Langmuir and Freundlich.

Langmuir isotherm model is commonly used to describe the relationship between the equilibrium concentration of the adsorbate and the amount adsorbed on the surface of the adsorbent. The surface interaction of chromium with the composite adsorbent can be represented as



where, C and S represent the chromium and the composite surface, respectively, and CS refers to the chromium adsorbed on the adsorbent. This isotherm model was utilized to calculate the maximum adsorption capacity which was obtained by fitting the experimental data to Langmuir isotherm model by assuming that a monolayer is formed at maximum adsorption [23, 24]. The linearized form of Langmuir equation can be expressed as:

$$\frac{1}{q_e} = \frac{1}{K_L q_0} \cdot \frac{1}{C_e} + \frac{1}{q_0} \quad (3)$$

where, C_e is the equilibrium concentration of the metal ion in mg L^{-1} , q_e is the amount of Cr(VI) adsorbed at equilibrium in mg g^{-1} , q_0 is the maximum adsorption capacity in mg g^{-1} , and K_L is a constant (L mg^{-1}) related to the energy of adsorption. The maximum adsorption capacity, q_0 and the constant K_L are obtained from the slope and intercept of the plot of $1/q_e$ against $1/C_e$.

The Freundlich isotherm [25] is a useful model to study the adsorption for dilute solutions. The adsorption on inequivalent adsorption sites is well described by this empirical isotherm. The Freundlich equation takes into account the logarithmic decrease in the energy of adsorption with increasing surface coverage and this is attributed to the surface heterogeneity [25, 26]. The linearized form of this isotherm can be expressed as:

$$\log q_e = \log K_F + \frac{1}{n} \log C_e \quad (4)$$

where, C_e is the equilibrium concentration of the Cr(VI) ion in mg L^{-1} , q_e is the amount of Cr(VI) adsorbed at equilibrium in mg g^{-1} , and K_F and n are the Freundlich constants which indicate the adsorption capacity and the adsorption intensity, respectively. The values of K_F and n were obtained

from the slope and intercept of the logarithmic plot of q_e vs C_e .

Kinetics of adsorption

The kinetic parameters were evaluated using the well-known first-order and pseudo-second-order models [27]. Equations for these models can be described as follows:

$$\log(q_e - q_t) = \log q_e - \frac{k_1 t}{2.303} \quad (5)$$

$$\frac{t}{q_t} = \frac{1}{k_2 q_e^2} + \frac{t}{q_e} \quad (6)$$

where, q_e and q_t refer to the amount of Cr adsorbed at equilibrium and time t with the first- and second-order rate constants k_1 and k_2 , respectively. The slope and intercept obtained from the plots of $\log(q_e - q_t)$ and t/q_t against t give the respective kinetic parameters. a is the initial adsorption rate (mg (g min)^{-1}), and the parameter $1/b$ (mg g^{-1}) is related to the number of sites available for adsorption.

RESULTS AND DISCUSSION

Characteristics of composites

FTIR spectroscopic analysis. FTIR spectra of chitosan showed several bands in the region $4000\text{--}500 \text{ cm}^{-1}$, as seen in Fig. 1. The peak at 3450 cm^{-1} is due to --OH stretching. The C--H stretching (symmetric and asymmetric) vibrations of the polymer backbone are demonstrated through strong peaks at 2900 cm^{-1} and 2850 cm^{-1} . A sharp peak at 1600 cm^{-1} corresponds to aromatic carbon (C=C stretching). Peaks at 1375 cm^{-1} , 1130 cm^{-1} and 1080 cm^{-1} are observed due to asymmetrical C-H bonding of the CH_2 group; $\text{C}_3\text{--O}$ stretching and $\text{C}_6\text{--O}$ stretching overlapped with C=O stretch vibration, respectively. The transmittance bands at 1580 cm^{-1} are due to N--H bonding vibration of chitosan, the peak at 1430 cm^{-1} is due to --C--O stretching of the primary alcoholic group in chitosan. Similar FTIR peaks were also observed in previous studies for chitosan [28, 29].

Thermogravimetric analysis. The thermal stability of chitosan was checked by thermogravimetric analysis (TGA) and results are shown in Figure 2. Thermal decomposition of chitosan exhibits three different stages, within the ranges of $50\text{--}200^\circ\text{C}$, $200\text{--}350^\circ\text{C}$ and $350\text{--}650^\circ\text{C}$. In the first stage, 16% mass loss was associated with the evaporation of water from the surface of the chitosan film. In the second stage, a sudden drop of the weight loss with temperature was observed, due to decomposition of organic and other volatile matters present in the samples [22]. After 350°C only 34% of the mass remained. Further, in the third stage from $350\text{--}650^\circ\text{C}$, a significant mass loss

M. Didarul Islam et al.: Removal of chromium from aqueous solution using chitosan: An experimental study of chitosan was observed. After 650°C only 1% residue was found which was attributed to the presence of minerals.

adsorption of Cr(VI) was observed in weakly acidic medium (2.5-4.5).

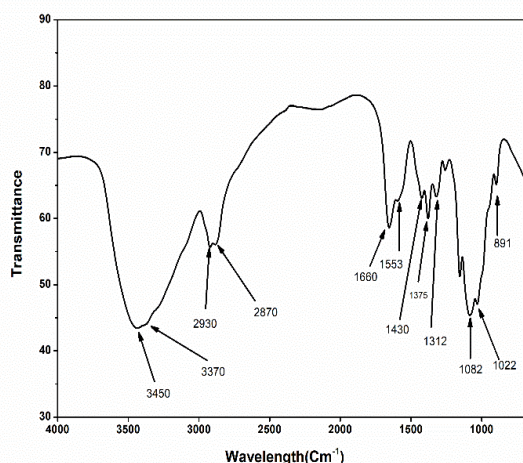


Figure 1. FTIR spectrum of the chitosan film

Differential scanning calorimetry. The DSC thermogram of chitosan within the temperature range of 50 to 400°C at a heating rate of 10°C/min is shown in Figure 3. One endothermic and one exothermic peak were observed. The endothermic peak at 81°C was due to a loss of moisture content in the sample. A sharp exothermic peak at 278°C was observed which is due to the decomposition of the higher content of amine groups.

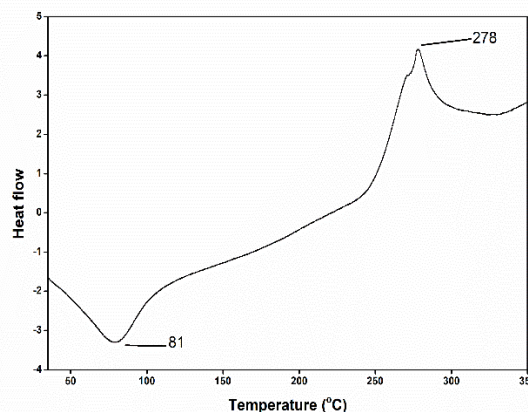


Figure 3. DSC curve of chitosan.

According to Pearson's classification [31], chromium is categorized as a hard acid and chitosan is classified as a hard base. This can be used to explain the variety of complexation reactions. As they are both strong, good interaction between the positively charged protonated amine group of chitosan and the negatively charged bichromate anion can be expected. In acidic medium surface hydroxyl groups of clay can also be protonated and this could serve as electrostatic interaction with bichromate anion either. With the increase in pH, adsorption decreased which could be attributed to the deprotonation of the surface hydroxyl groups [32]. From Figure 5 it can be seen that the optimum pH for chitosan is 3.0 (85.45 mg/g); below and above this pH, adsorption capacity was significantly reduced.

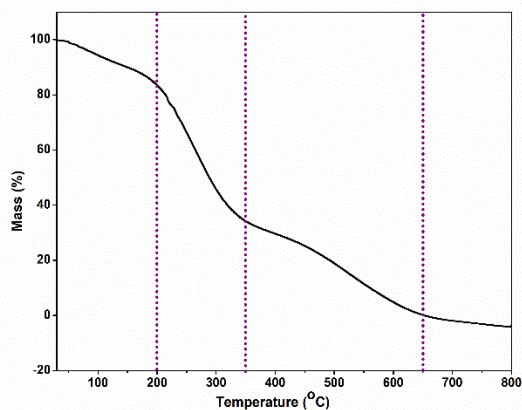


Figure 2. TGA curve of chitosan.

Batch studies

Effect of pH on Cr (VI) adsorption. The optimization of pH is an important factor in the adsorption study. Hexavalent chromium can exist in various forms such as HCrO_4^- , CrO_4^{2-} , and $\text{Cr}_2\text{O}_7^{2-}$ depending on pH and concentration of the aqueous phase. In the pH range 2.5-4.5, Cr(VI) exists in solution primarily as bichromate (HCrO_4^-) anion, whereas the dichromate ($\text{Cr}_2\text{O}_7^{2-}$) anion predominates at lower pH values and higher concentrations [30]. The favorable pH for the

Effect of dose on Cr (VI) adsorption. The adsorption of chromium by chitosan was studied at various adsorbent quantities (20, 40, 60, 80, 100, 120, 140, 160 and 180 mg/100 ml solution) in the test solution keeping chromium concentration 40 ppm at a temperature of 30°C and pH 3 for optimum contact time of 180 min. After 180 min the percentage of adsorbed chromium was calculated. It was found that increasing the dose of adsorbent increased the percentage of chromium removed from the solution which can be attributed to increased adsorbent surface area and availability of a larger number of adsorption sites (Figure 4). However, after 140 mg adsorbent dose chromium removal from the solution was not significant. The adsorption capacity decreased with increase in adsorbent dose. This is due to the low dose, all adsorption sites are exposed and adsorption on the surface is saturated faster, that results in higher adsorption capacity. But at higher adsorption dose, the availability of higher energy sites decreases

with a larger fraction of lower sites occupied as well as adsorption surface area may be overlapped or aggregated at higher dose and less active sites available to chromium [33], produce lower adsorption capacity [34-36]. From Figure 4 it is evident that the optimum dose is 40 to 60 mg. In this range chromium removal percentage and capacity were in optimum condition.

Effect of time on Cr (VI) adsorption. Contact time is an important parameter of adsorption which also reflects adsorption kinetics of an adsorbent for a solution with given concentration and pH values. The batch studies were carried out at 30°C with initial concentration of Cr (VI) of 40 ppm in 100 ml of solution, pH 3 using 40 mg composites at various contact time periods. Figure 5 shows the effect of contact time on the adsorption capacity of the composites for Cr (VI). The results show that adsorption capacity of Cr (VI) increases with increasing contact time from 30 to 240 min and after 180 min the capacity remains constant and attains equilibrium, which indicates that 180 min of contact time is enough for the maximum removal of Cr (VI) ions from aqueous solution under these

experimental conditions. Equilibrium adsorption achieved may be due to the accumulation of Cr (VI) ions on the vacant sites and causes limited mass transfer of the adsorbate from the bulk liquid to the external surface of adsorbent [37].

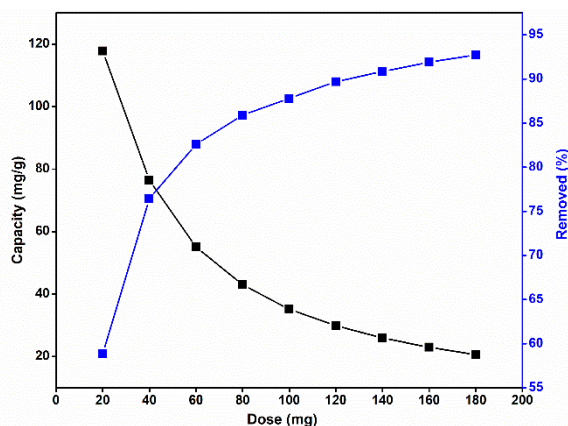


Figure 4. Effect of sorbent dose on chromium adsorption.

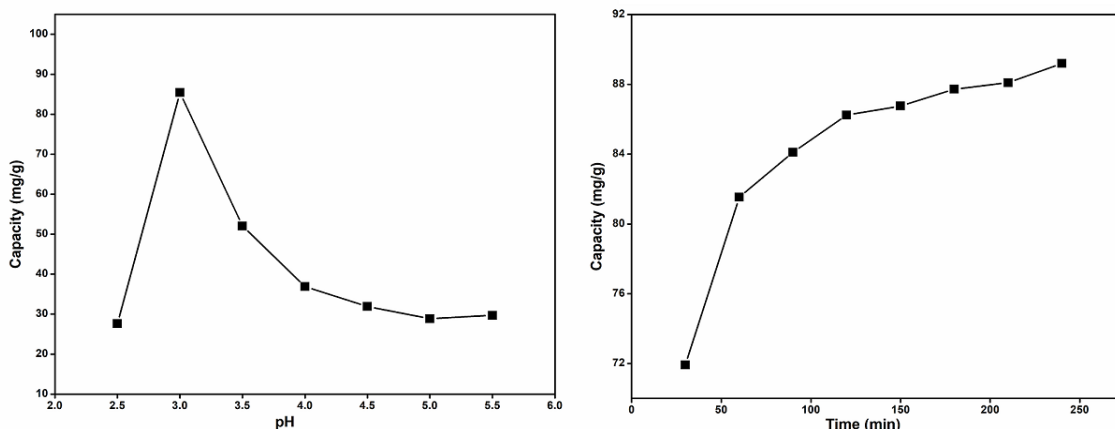


Figure 5. Effect of pH and time on chromium adsorption.

Table 1. Comparison of the isotherm and kinetics constant and calculated and experimental q_e values for chitosan.

Isotherm		Kinetics	
Langmuir		First order	
K_L	0.082	q_e	20.88
R^2	0.9970	K_1	0.01474
		R^2	0.9739
Freundlich		Second order	
n	0.96	q_e	91.74
K_F	6.87	K_2	0.00133
R^2	0.9937	R^2	0.9999

Adsorption isotherm modeling

The data obtained from isotherm studies were tested for their applicability to the two models. Table 1 summarizes the values of all adsorption constants and regression coefficients for each of these isotherms, which were then calculated from

the best-fit lines. According to McKay *et al.* for best fit of Freundlich isotherm the n value should be from 1 to 10 [38, 39]. In this study the n value for the adsorbent was 0.96, which is out of the accepted range. The values of the regression coefficients for Langmuir and Freundlich are 0.9970 and 0.9937, respectively, which implies

that Langmuir adsorption model is the best fit. This observation implies that monolayer adsorption on homogenous surface may co-exist under the applied experimental conditions.

Adsorption kinetics modeling

The pseudo first-order and pseudo-second-order kinetic models were used to obtain the rate constants and equilibrium adsorption capacity of chitosan. The values of pseudo-first order model constants k_1 and q_e were obtained from the slope and intercept of the plots of $\log (q_e - q_t)$ vs t while pseudo-first-order model constants, k_2 , and q_e were calculated from the slope and intercept of the plots of t/q_e vs t . All of these constants and correlation coefficient values are summarized in Table 1. As seen from the table, calculated adsorption capacity and regression coefficient conform that adsorption of chromium onto adsorbent follows a pseudo-second-order kinetic model. The applicability of the pseudo-second-order kinetic model specifies that the adsorption process is chemisorption and the rate-determining step is probably surface adsorption. Similar phenomenon has been experienced for adsorption of chromium on other bio-adsorbents [40-42].

Application of chitosan for the treatment of industrial waste water

In this study chitosan was used to determine the usefulness of chitosan for the removal of

chromium and some other physicochemical properties of waste water. For that purpose, effluent from different operational sections of tannery industry has been collected and the initial and final properties of waste water after the treatment with chitosan were determined. All of these results are summarized in Table 2 and 3. In this experiment, 0.5 g of chitosan was used to treat 250 ml of waste water at a temperature of 30°C and pH 3 with contact time 180 min. After analysis it was found that only chrome tanning and re-tanning waste water contain chromium in high quantities while all other sectional waste waters do not contain any chromium or this level was below detection limit. For that reason, after treatment with chitosan only these two sectional waters were quantified to determine chromium. In this experiment it was found that 83.58 and 90.27 % of chromium was reduced from chrome tanning and re-tanning waste waters, respectively. All other physicochemical parameters such as turbidity (78-84%), conductivity (68-80%), BOD (62-75%), COD (58-75%) and TDS (69-79%) were significantly reduced, which indicates that this adsorbent can be successfully used for the treatment of tannery effluent, as well as domestic waste water.

Table 2. Initial physicochemical parameters of effluents from different chemical operations before treatment

Name of operation	Turbidity (NTU)	Conductivity (μ S/cm)	BOD (mg/L)	COD (mg/L)	TDS (mg/L)	Chromium (mg/L)
Soaking	927	87550	2750	6100	45150	
Liming	1020	137150	4953	14120	67000	
De-liming	921	107000	3750	7710	55150	
Bating	879	89500	2900	5150	45550	
Pickling	793	74100	2150	4340	37550	
Chrome tanning	1123	128100	2450	6130	64500	1723.6
Neutralization	927	104100	3010	7150	52550	
Re-tanning	1050	127500	2750	6150	63500	1038
Dyeing	950	102100	5150	13165	51500	
Fat-liquoring	954	94100	6150	17195	47500	

Table 3. Changes of physicochemical parameters of effluents from different chemical operations after treatment

Name of operation	Turbidity (NTU)	Conductivity (μ S/cm)	BOD (mg/L)	COD (mg/L)	TDS (mg/L)	Chromium (mg/L)
Soaking	151	27500	950	2250	14200	
Liming	201	37100	1810	4250	18500	
De-liming	187	31010	1410	3170	15200	
Bating	177	27550	755	1910	13500	
Pickling	127	19700	527	1650	11550	
Chrome tanning	224	37900	801	2150	19100	283
Neutralization	191	20100	721	1810	11500	
Re-tanning	227	35150	1027	2450	18150	101
Dyeing	163	19510	1520	3710	10500	
Fat-liquoring	174	23010	1810	4150	11710	

CONCLUSION

The removal of chromium from aqueous solution using chitosan was investigated under different experimental conditions in a batch mode. For that purpose, chitosan was successfully prepared from prawn shells and its formation was confirmed by FTIR, TGA and DSC analysis. In this study, results indicate that adsorbent dose, contact time and pH have a high impact on chromium uptake capacity of bioadsorbents. The adsorption follows the Langmuir model that means monolayer coverage of the adsorbate on the outer surface of the adsorbent. The adsorption kinetics followed the pseudo-second-order kinetic model which suggests that the adsorption process is chemisorption and the rate-determining step is probably surface adsorption. This adsorbent was used for the treatment of waste water and it was found that it can remove more than 80% of the chromium (250 ml, >1700 ppm solution). At the same time other physicochemical parameters such as turbidity, conductivity, BOD, COD and TDS were significantly reduced. This investigation implies that chitosan could be a good alternative to expensive chemicals and methods and hence the waste water treatment process (industrial, as well as domestic waste water) can become very economical.

REFERENCES

- M. Doble, A. Kumar, Biotreatment of industrial effluents, Elsevier, 2005.
- A. Benhadji, M.T. Ahmed, R. Maachi, *Desalination*, **277**, 128 (2011).
- M. Chowdhury, M. Mostafa, T.K. Biswas, A.K. Saha, *Water Resources and Industry*, **3**, 11 (2013).
- R. Aravindhnan, B. Madhan, J.R. Rao, B.U. Nair, T. Ramasami, *Environ. Sci. Technol.*, **38**, 300 (2004).
- H. Ma, X. Wang, C. Zhang, *Chemical Speciation & Bioavailability*, **15**, 15 (2003).
- B. Mei, J.D. Puryear, R.J. Newton, *Plant and Soil*, **247**, 223 (2002).
- S. Roy, L. Banna, M. Hossain, H. Rahman, *J. Bangladesh Agril. Univ*, **12**, 285 (2014).
- A.R. M. R. H. Sarker, M. M. Hoque, S. Roy*, M. K. Hossain, *J. Environ. Sci. & Natural Resources*, **8(2)**, 25 (2015).
- G. Qin, M.J. McGuire, N.K. Blute, C. Seidel, L. Fong, *Environ.Sci. Technol.*, **39**, 6321 (2005).
- S. Aber, D. Salari, M. Parsa, *Chem. Eng. J.*, **162**, 127 (2010).
- E. Dialynas, E. Diamadopoulos, *Desalination*, **238**, 302 (2009).
- X. Ren, C. Zhao, S. Du, T. Wang, Z. Luan, J. Wang, D. Hou, *J. Environ. Sci.*, **22**, 1335 (2010).
- M.K. Aroua, F.M. Zuki, N.M. Sulaiman, *J. Hazardous Mater.*, **147**, 752 (2007).
- L.J. Yu, S.S. Shukla, K.L. Dorris, A. Shukla, J. Margrave, *J. Hazardous Mater.*, **100**, 53 (2003).
- J. Randall, V. Garrett, R. Bermann, A. Waiss Jr, *Forest Products J.*, (1974).
- N. Daneshvar, D. Salari, S. Aber, *J. Hazardous Mater*, **94**, 49 (2002).
- E. Malkoc, Y. Nuhoglu, *Fresenius Environ. Bull.*, **12**, 376 (2003).
- E. Malkoc, Y. Nuhoglu, *J. Hazardous Mater.*, **127**, 120 (2005).
- A.R. Netzahuatl-Muñoz, E. Aranda-García, M.d.C. Cristiani-Urbina, B.E. Barragan-Huerta, T.L. Villegas-Garrido, E. Cristiani-Urbina, *Fresenius Environ. Bull.*, **19**, 2911 (2010).
- T.U. Rashid, M.M. Rahman, S. Kabir, S.M. Shamsuddin, M.A. Khan, *Polymer Int.*, **61**, 1302 (2012).
- M.J. Hossana, M. Gafurb, M. Kadirb, M.M. Karima, *Int. J. Eng. Technol.*, 1 (2014).
- K. Sakurai, T. Maegawa, T. Takahashi, *Polymer*, **41**, 7051 (2000).
- I. Langmuir, *J. Amer. Chem. Soc.*, **40**, 1361 (1918).
- V.S. Munagapati, V. Yarramuthi, S.K. Nadavala, S.R. Alla, K. Abburi, *Chem. Eng. J.*, **157**, 357 (2010).
- H. Freundlich, *J. Phys. Chem.*, **57**, 1100 (1906).
- R. Nadeem, M.H. Nasir, M.S. Hanif, *Chem. Eng. J.*, **150**, 40 (2009).
- S.S. Gupta, K.G. Bhattacharyya, *Adv. Colloid Interface Sci.*, **162**, 39 (2011).
- A. Pawlak, M. Mucha, *Thermochim. Acta*, **396**, 153 (2003).
- C. Jung, J. Heo, J. Han, N. Her, S.-J. Lee, J. Oh, J. Ryu, Y. Yoon, *Sep. Purif. Technol.*, **106**, 63 (2013).
- P. Luo, J.-s. Zhang, B. Zhang, J.-h. Wang, Y.-f. Zhao, J.-d. Liu, *Ind. Eng. Chem. Research*, **50**, 10246 (2011).
- R.G. Pearson, *J. Amer. Chem. Soc.*, **85**, 3533 (1963).
- Q. Hu, S. Qiao, F. Haghseresht, M.A. Wilson, G. Lu, *Ind. Eng. Chem. Research*, **45**, 733 (2006).
- H. Lata, V. Garg, R. Gupta, *Dyes and Pigments*, **74**, 653 (2007).
- V.K. Gupta, A. Rastogi, A. Nayak, *J. Colloid Interface Sci.*, **342**, 135 (2010).
- D. Park, Y.-S. Yun, J.M. Park, *Proc. Biochem.*, **40**, 2559 (2005).
- M. Kobya, *Adsorption Sci. Technol.*, **22**, 51 (2004).
- N. Prakash, P. Sudha, N. Renganathan, *Environ. Sci. Pollut. Research*, **19**, 2930 (2012).
- R. Malik, D. Ramteke, S. Wate, *Waste Manag.*, **27**, 1129 (2007).
- G. McKay, *Adsorption*, **4**, 361 (1998).
- C. Namasivayam, M. Sureshkumar, *Bioresource Technol.*, **99**, 2218 (2008).
- H.S. Altundogan, *Proc. Biochem.*, **40**, 1443 (2005).
- R. Elangovan, L. Philip, K. Chandraraj, *J. Hazardous Mater.*, **152**, 100 (2008).

Modeling the separation performance of nanofiltration and reverse osmosis: case study of groundwater desalination (M'Nasra zone Morocco)

M. Bchiti¹, M. Igouzal^{2*}, F. El Azhar¹, H. Oudda¹, A. El Midaoui¹

¹Laboratory of Separation Processes, Department of Chemistry, Faculty of Science, Ibn Tofail University, BP1246 Kenitra, Morocco

¹Interdisciplinary Laboratory for Natural Resources and Environment, Department of Physics, Faculty of Science, Ibn Tofail University, BP1246 Kenitra, Morocco

Received January 21, 2019; Revised, May 7, 2019

Moroccan surface water and groundwater is enduring an increase of salt concentrations which exceed the drinking water standards. To solve this problem, in this study we will use membranes which are a helpful technique to reduce these concentrations and to achieve high water quality within the distribution system. This study is aimed at proposing a model of reverse osmosis experiments conducted in a pilot scale using synthetic water doped with NaCl. Firstly, performances were compared for different types of reverse osmosis membranes. Secondly, a mathematical model was applied on the experimental data. As a detailed characterization of the membranes utilized was not available, a simplified approach for the phenomenon as described in Spiegler-Kedem model was used. This model is based on irreversible thermodynamics and predicts the rejection performance of the system by an estimation of two coefficients: reflexion coefficient and permeability coefficient. The Levenberg-Marquardt's algorithm (LMA) was used which iteratively solves non-linear least-squares problems. Simulations are in good agreement with experimental data and the linear correlation coefficient for the fitted data was greater than 0.85 in all experiments. Application of the model showed that to enhance model predictions, experiments must be conducted in a wider range of pressures, especially those corresponding to lower energy need.

Keywords: Membrane processes, Osmosis, Permeate flux, Reverse salt rejection, Spiegler-Kedem model

INTRODUCTION

In most countries, water resources are scarce and under threat of industrial and urban wastes [1-4]. Wastewater treatment processes are used to treat municipal and industrial wastewater to meet effluent standards before discharging in the natural environment [5-8]. Morocco, like other southern Mediterranean countries, is enduring water shortage and a wide variation in levels of rainfall which is expected to aggravate over the next few years. Population concentrations followed by the industrial and agricultural activities along the coastal zone have led to an increase of drinking water demand along this area. To solve this problem, seawater and groundwater desalination is seen as a useful process. Hence, many desalination plants were built working through reverse osmosis (RO) process. On the other hand, nanofiltration (NF) is widely studied at laboratory and pilot scales. However, its implementation on an industrial scale is not yet well exploited. This technique was only implemented with removing nitrate from the groundwater of Sidi Taibi commune (near Kénitra Town) [9]. Desalination projects are expensive and high energy consuming, so that ready-to-use plants are not always available.

Thus, it is decisive to choose the most appropriate membranes for a given water treatment project [10,11]. First, membrane performances must be studied in a pilot scale, especially where process uncertainties are potentially high, in terms of membranes performance and total operation cost [12,13].

In this study, we are interested in the desalination of M'Nasra's groundwater. This zone has been a subject to many studies. Bouya *et al.* [14] reported that during the last decade, M'Nasra aquifer has been subjected to an anarchic and non-rational groundwater abstraction, leading to an overexploitation of the aquifer, rupture of the hydrodynamic equilibrium, degradation of water quality. They have developed a hydrodynamic model to understand the spatial distribution of permeability and recharge, and have confirmed the nature of M'Nasra aquifer system hydrogeological functioning. Benseddik and Bouabid [15] studied the vulnerability of M'Nasra aquifer water based on three methods used to identify the most vulnerable areas that need a good management. Marouane *et al.* [16] studied the spatio-temporal variability of groundwater nitrate (NO⁻) and pesticide in M'Nasra aquifer during 2012 and found that nitrate concentrations were higher than the critical value of 50 mg L⁻¹. Zouhri [17] reported that marine intrusion and the lithological composition of the

* To whom all correspondence should be sent:
E mail: mohammed.igouzal@uit.ac.ma

saline pre-Rifean nappes, combined with their tectonic structures and their flow towards the Rharb basin (including M'nsara zone), are considered as increasing factors behind the salinity of this area's underground water resources. For drinking water, the maximum acceptable concentration which WHO recommends is 250 mg L⁻¹ for chloride and 200 mg L⁻¹ for sodium [17].

This research is aimed at studying separation experiments by nanofiltration (NF) and reverse osmosis (RO) in a pilot scale laboratory. Measurements were conducted on synthetic groundwater from de M'Nasra zone (Morocco). Different membranes were used and their performances and selectivity towards sodium chloride salt (NaCl) were experimentally compared.

On the other hand, numerous phenomenological and mechanistic models have been proposed to describe solute and solvent transport through porous and dense membranes [18]. These mathematical models are based on conservation principles and include many parameters. Model parameter estimation is achieved by matching model predictions with experimental data. The development of these modeling techniques will successfully lead to a smaller number of experiments and subsequently save time and money in the developmental stage of a given project. For dense membranes, the solution-diffusion model is the most popular. In this model, solutes dissolve at the membrane interface and then diffuse through the membrane along the concentration gradient [19]. Pore-flow models also exist, in which different solutes are separated by size, frictional resistance, and/or charge. Finally, the Kedem-Katchalsky and Spiegler-Kedem (S-K) models employ irreversible thermodynamic arguments to derive solute and solvent transport equations while treating the membrane as a "black box" [20]. Models based on irreversible thermodynamics approach are the easiest to use, especially Spiegler-Kedem model which requires only two parameters for its application. This model is recommended for studies representing first attempts of modeling membranes processes. In addition, it is methodologically true to start with the simplest description of the phenomena under study, and to evaluate the limits of this approximation before investigating more complications. For all these reasons, the use of S-K model is adequate in our case study. Thereafter the capability of Spiegler-Kedem model to predict rejection performance was investigated [9,10].

M'Nasra aquifer belongs to the coastal area of Gharb basin. Geographically, it covers an area of approximately 600 km², and extends to 70 km along

the coastal strip of Kenitra from the south and Moulay Bouselham from the north. It is bordered by Sebou River in the east, and the Atlantic Ocean in the west. This aquifer is the only resource of drinking water which supplies the population of many rural municipalities (Fig. 1) and irrigates various agricultural areas in the region.

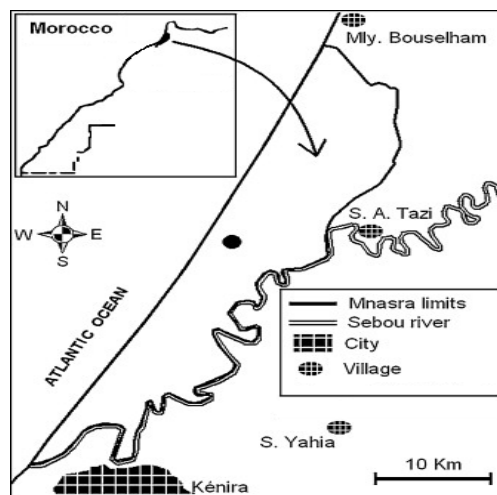


Fig. 1. Situation of the studied area

MATERIALS AND METHODS

Mathematical model

The performances of membranes were measured in terms of salts rejection (R) and permeate flux (J_v). For dilute aqueous mixtures consisting of water and a solute, the selectivity of a membrane toward the mixture is usually expressed in terms of the observed solute rejection coefficient. This parameter is a measure of a membrane's ability to separate the solute from the feed solution, and is defined, as a percentage:

$$R = 100 \frac{C_f - C_p}{C_f} 100 \left(1 - \frac{C_p}{C_f} \right) \quad (1)$$

where C_p and C_f are the solute concentrations in the permeate and feed solution, respectively.

The Spiegler-Kedem (S-K) model, based on irreversible thermodynamics, provides a simple framework for description of solute transport in both RO and NF processes. In this model, the membrane is regarded as a "black-box" that can be characterized in terms of two coefficients: the solute permeability (P_s) and the reflection coefficient (σ). The S-K model considers convective coupling between solute and solvent species. This model has been successfully used to model solute retention in various applications, such as desalination of saline and brackish water, demineralization, etc. For the derivation of the S-K model, the starting point is the assumption that the water flux (J_w) and the solute flux (J_s) are driven

by the forces F_w and F_s , respectively. These generalized forces are due to chemical potential gradients across the membrane:

$$J_w = L_{11}F_w + L_{12}F_s \text{ and } J_s = L_{21}F_w + L_{22}F_s \quad (2)$$

where L_{ij} are phenomenological coefficients.

The chemical potential gradient is caused by a concentration or pressure gradient. So that the final working equations of the nonlinear S-K model are:

$$J_w = L_p \cdot \left(\frac{dP}{dx} - \sigma \frac{d\Pi}{dx} \right)$$

$$\text{and } J_s = P_s \cdot \frac{dC_s}{dx} (1 - \sigma) \cdot C_s \cdot J_w \quad (3)$$

where: J_w ($\text{Kg} \cdot \text{m}^{-2} \cdot \text{s}^{-1}$): water flux; J_s ($\text{Kg} \cdot \text{m}^{-2} \cdot \text{s}^{-1}$): solute flux; L_p ($\text{m} \cdot \text{s}^{-1}$): solvent permeability constant; P (bar): operating pressure; Π (bar): osmotic pressure; x (m): distance across the membrane; C_s : solute concentration inside the membrane; P_s ($\text{m} \cdot \text{s}^{-1}$): solute permeability constant; σ : reflection coefficient.

Solvent transport is due to the pressure gradient across the membrane and solute transport is due to the concentration gradient and convective coupling of the volume flow. Solute transport in RO membranes occurs predominantly *via* diffusion, however, for membranes with larger pores such as NF ones, both convective and diffusive contributions to the solute flux, are important and cannot be ignored [21].

Integration of equation (3) combined with relation (1) and considering the limit conditions of the problem (for $x=0$, $C_s=C_f$ and for $x= \Delta x$, $C_s=C_p$) lead to relation (4):

$$R = 1 - \frac{C_p}{C_f} = \frac{\sigma(1 - F)}{1 - \sigma F} \text{ with } F = \exp\left(-\frac{(1 - \sigma)J_v}{P_s}\right) \quad (4)$$

Table 1. Characteristics of the membranes

Membrane	Surface (m^2)	P_{\max} (bars)	Feed pH range	Max T($^{\circ}\text{C}$)	Material	Manufacturer
BW30LE4040	7.6	41	2-11	45	Polyamide	Filmtec
TMG10	8.0	40	2-11	45	Polyamide	Toray
TM710	8.0	41	3-9	45	Polyamide	Toray
NF90	7.6	40	3-10	45	Polyamide	Filmtec
NF270	7.6	40	3-10	45	Polyamide	Filmtec

Statistical analysis

In this study, a statistical analysis of residual errors was performed based on the Root Mean Square Error (RMSE), the Normalized Root Mean Square Error (NRMSE) and the Nash-Sutcliffe Efficiency (NSE) coefficient.

The RMSE is the distance, on average, of a data point from the fitted line. The NRMSE calculates

where: C_f (kg m^{-3}): solute concentration in the feed solution; C_p (kg m^{-3}): solute concentration in the permeate solution; F (dimensionless): a flow parameter; Δx (m): membrane thickness.

The two transport parameters (σ and P_s) are the main parameters of the model. They are obtained by fitting the experimentally obtained rejection permeation data to the model calculated rejection. The parameter σ is a measure of the degree of membrane semi permeability, i.e. its ability to pass solvent in preference to solute. It characterizes the imperfection of the membrane [21]. The fitted coefficients are then said to represent the values of the transport coefficients for the given feed salt composition. Concentration dependence of these coefficients is assessed by fitting the data for different feed concentrations.

Pilot used

The experiments were performed on an NF/RO pilot plant (E 3039) supplied by TIA Company (Technologies Industrielles Appliquées, France). The pressure applied over the membrane can be varied from 5 to 70 bars by manual valves.

The pilot is equipped with two identical spiral wound modules operating in series. Each module contains one element. The pressure loss is about 2 bars corresponding to 1 bar of each module. Table 1 gives the characteristics of the commercial membranes used.

The experiments were performed at 20°C . Samples of permeate were collected and the water parameters were determined analytically following the standard methods.

the residual variance. The NSE is a normalized statistic that determines the relative magnitude of the residual variance (noise) compared to the measured data variance (information).

RESULTS AND DISCUSSION

RO on synthetic water doped with NaCl

Performances of RO membranes TMG10, TM710 and BW30LE4040 were first compared using synthetic water doped with NaCl at different dilutions as shown in table 2.

For a feed water salinity of 2 g L⁻¹, the influence of pressure on the permeate flux for the different membranes is shown in fig. 2 (a). An increase in applied pressure leads, as is to be expected from equation (4), to an increase in the permeate flux for all three tested membranes. Also, the permeate flux obtained with BW30LE4040 membrane is higher than that attained with other membranes. Fig. 2 (b) shows that the rejection coefficient of Cl⁻ is greater than 0.95 for the three membranes for all applied pressures. Rejection obtained with BW30LE4040

membranes is the lowest, in agreement with the high permeability of this membrane.

Table 2. Characteristics of the synthetic water doped with NaCl.

Salinity (g/l)	pH	Cl ⁻ (ppm)	Na ⁺ (ppm)
2	6.19	789.87	1203.58
4	6.02	1464.37	2482.396
6	6.3	1908.12	3272.22
8	6.44	2440.62	4983.59
10	6.62	3017.5	5641.8

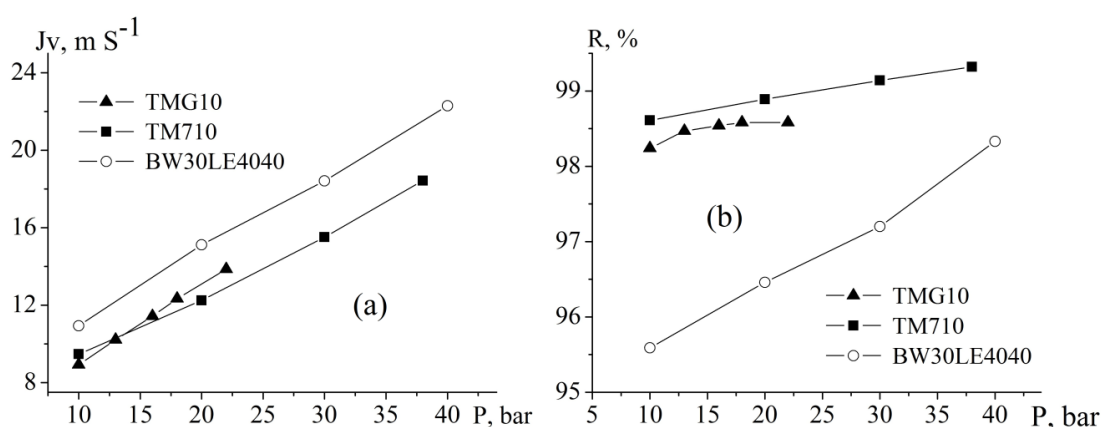


Fig. 2. (a) Variation of permeate flux and (b) rejection coefficient (for Cl⁻) with pressure (for salinity of 2 g L⁻¹)

Fig. 3 shows the permeate flux as a function of pressure at different salinity concentrations (2, 6 and 10 g L⁻¹) for (a) TMG10, (b) TM710 and (c) BW30LE4040, respectively. As salinity concentration increases, permeate flux decreases for all three membranes used. Increasing feed concentration leads to an increase in osmotic pressure and hence permeate flux reduces (see equations 4 and 5).

On the other hand, high rejections are obtained with the three reverse osmosis membranes (greater than 95%) in concordance with manufacturer's specifications.

For all previous experiments, optimal values of coefficients σ and P were mathematically obtained by minimizing the model's cost function which is defined as the sum of the squared differences between predicted and observed values of the rejection coefficient.

Figure 4 shows a plot of the rejection coefficient (Cl⁻, salinity concentration of 10 mg L⁻¹) as a function of the permeate flux for (a) TMG10, (b) TM710 and (c) BW30LE4040. As can be seen, calculations by the S-K model correctly reproduce the experimental data. The correlation coefficients calculated for the membranes TMG10, TM710 and BW30L4040 were equal to 0.93, 0.85 and 0.85, respectively. Table 3 summarizes the values of the parameters σ and Ps for all membranes at different salt concentrations. Increasing feed concentration leads to a decrease of reflection coefficient σ and an increase of permeate coefficient Ps in major cases.

Table 4 shows the results of the statistical analysis as described in material and methods section. The RMES coefficient obtained has a small value, the NRMSE function is smaller than unity and the NSE coefficient is very near to 1. This result demonstrates the good performance of the model and the optimization procedure.

Table 3. σ and P_s estimated by the model (Cl^- , salinity concentrations of 10 mg L^{-1})

Membrane	TM710			TMG10			BW30LE4040		
Salinity (mg/l)	2	6	10	2	6	10	2	6	10
σ	0.979	0.991	0.991	0.955	0.985	0.988	0.991	0.991	0.979
P_s (m/s)	1.10^{-7}	1.10^{-7}	2.10^{-7}	1.10^{-7}	2.10^{-7}	3.10^{-7}	2.10^{-7}	1.510^{-7}	$2.5.10^{-7}$

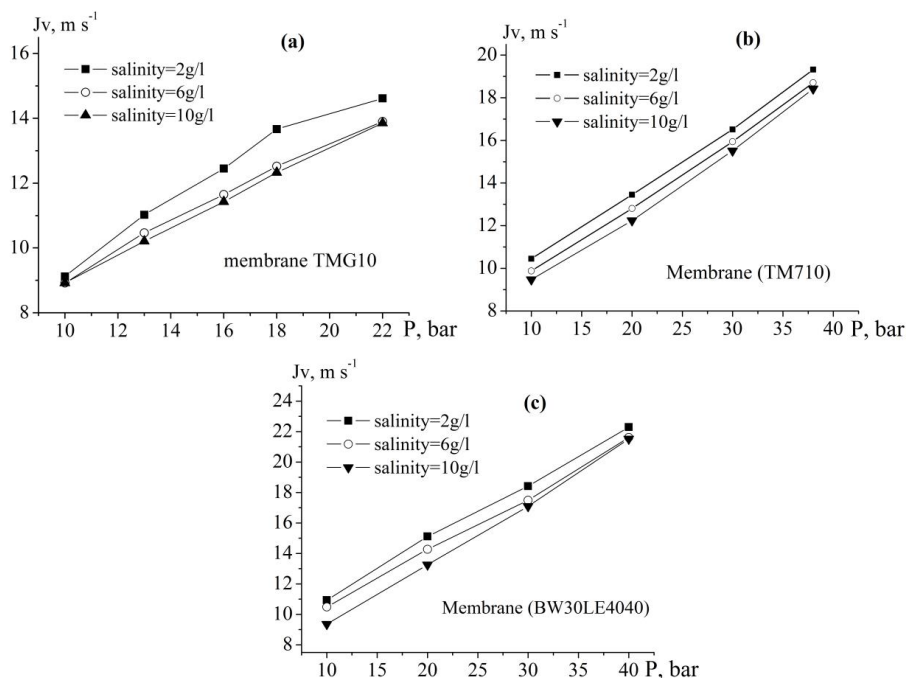


Fig 3. Variation of permeate flux with pressure for three salinity concentrations: (a) TMG10 membrane, (b) TM710 membrane, (c) BW30LE4040 membrane

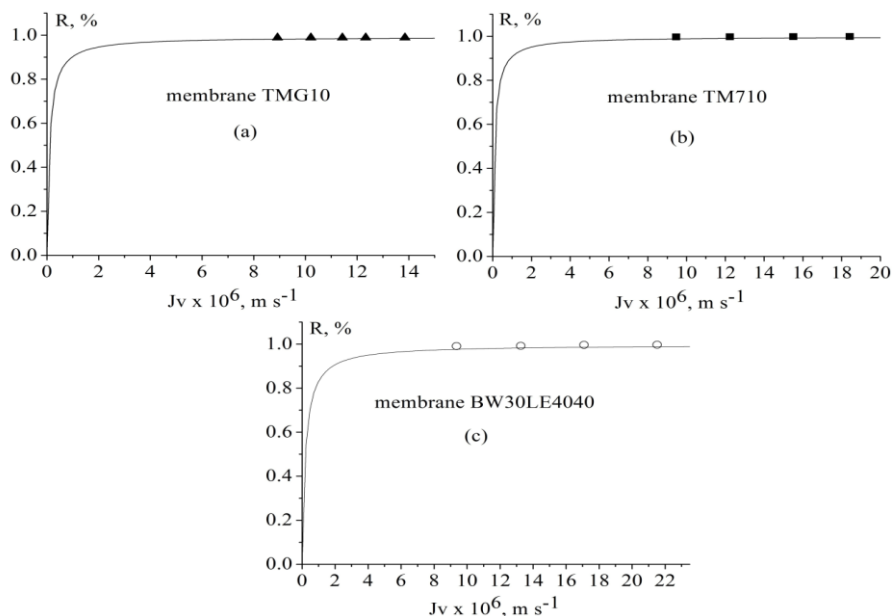


Fig. 4. Comparison between observed and predicted rejection (of Cl^-) for (a) TMG10, (b) TM710 and (c) BW30LE4040 (feed water salinity of 10 g L^{-1})

Table 4. Results of the statistical analysis

Membrane	RMSE (%)	NRMSE(-)	NSE (-)
TMG10	0.026	0.030	0.96
TM710	0.030	0.040	0.98
BW30LE40	0.029	0.060	0.99

Ground water treatment by RO and NF

In the second part of this research, ground water from M’Nasra zone was treated by reverse osmosis using BW30L4040 membrane, and by nanofiltration using NF90 and NF270 membranes. The characteristics of brackish water are shown in Table 5. Figure 5(a) shows the permeate flux as a function of pressure. For all membranes permeate flux increases linearly as pressure increases. The permeate flux obtained with NF membranes is higher than that with the BW30L4040 membrane. NF membranes are more permeable than RO membranes because of the presence of nanoporosity in NF while the RO membrane is dense. Figure 5(b) presents the retention coefficient of Cl⁻ as a function of the applied pressure. The Cl⁻ retention with BW30L4040 membrane is the highest and pressure independent. For NF membranes, there is an increase in retention with increased applied pressure. Also, retention is more important for NF90 membrane than for NF270 membrane.

Application of S-K model leads to reflection coefficients (σ) and solute permeability coefficients (Ps) shown in Table 6.

Table 5. Characteristics of the feed water

Parameters	Brackish water	Moroccan standards	Standards
			World Health Organization
T °C	23	-	25
pH	8.08	6.0 - 9.2	6.5-8.5
TDS (ppm)	2690	< 1000	< 1000
Na ⁺ (ppm)	780.12	100	< 200
Cl ⁻ (ppm)	1325	350 - 750	< 250
Mg ²⁺ (ppm)	87.50	100	< 50
Ca ²⁺ (ppm)	20	< 500	< 270
SO ₄ ²⁻ (ppm)	125.88	200	< 200

Figure 6 shows a plot of the rejection coefficient as a function of the permeate flux. Calculated and experimental rejection coefficients are very close. Correlation coefficients for BW30L4040, NF90 and NF270 were equal to 0.91, 0.85, and 0.85, respectively.

Also, as for synthetic water, statistical indicators (RMES, NRMSE and NSE) for ground water were very satisfactory.

Table 6. Model constants σ and Ps estimated by the model

Membrane	NF90	NF270	BW30L4040
σ	0.925	0.576	0.988
Ps (m/s)	0.14	0.7	0.04

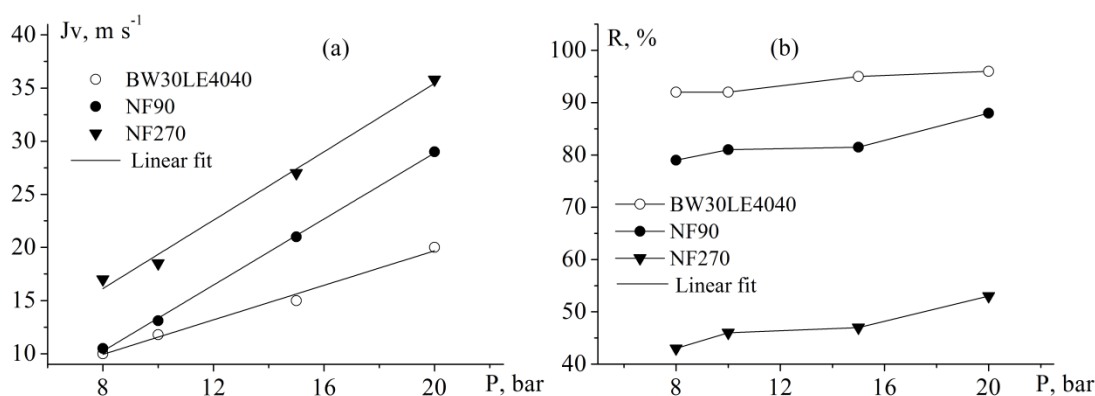


Fig. 5. (a) Variation of permeate flux and (b) rejection coefficient (for Cl⁻) with pressure

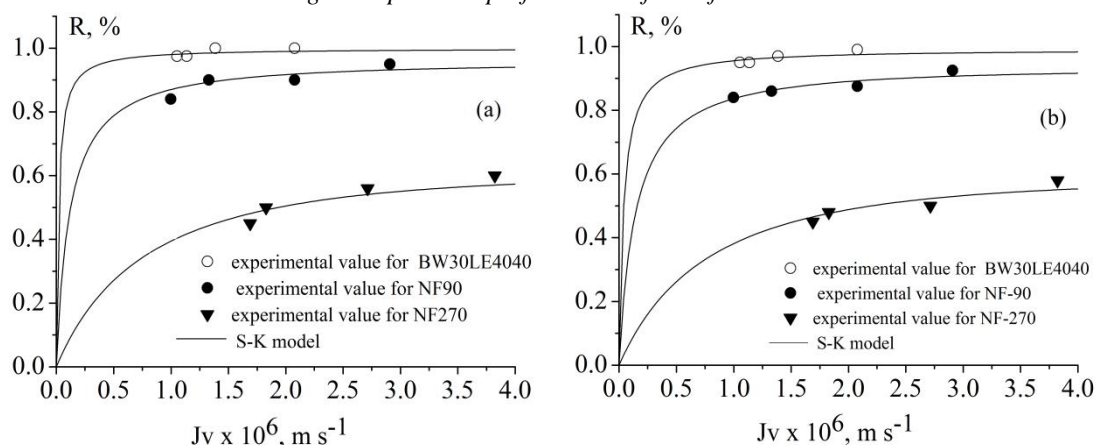


Fig. 6. Comparison between observed and predicted Cl^- and Na^+

CONCLUSION

The aim of this research was to study separation experiments by nanofiltration (NF) and reverse osmosis (RO) in a laboratory pilot scale. Experiments were conducted on synthetic water doped with NaCl and on groundwater from the M'Nasra zone (Morocco). Different sizes of membranes were used (RO and NF membranes) and their performances and selectivities towards sodium chloride salt (NaCl) were experimentally compared.

A first attempt was undertaken to model the separation tests using Spiegler-Kedem model. The simulation results were found to be in good agreement with the experimental data since the coefficient of determination obtained for the fitted data was greater than 0.85 in all experiments. Model results were used to verify the consistency of the experimental measurements in order to improve the procedure. The study has shown that to enhance the output of the model, pilot experiments must be conducted in a wider range of pressures, especially at pressures from 5 to 8 bar which correspond to lower energy consumption. Simulations (models coefficient) remain valid in the range of the concentration and experimental conditions used. Other measurements (made under different conditions) can be used to test the robustness of the model. Also, results of this study are obtained with no information on membranes characteristics. A detailed knowledge of these characteristics can improve the predictability of their filtration performance. Our future development may focus on amelioration of the modeling approach by a better description of the membranes and the transport mechanism occurring inside them.

REFERENCES

1. A. Shokri, *Bulg. Chem. Commun.*, **50**, 27 (2018).
2. A. Shokri, *Int. J. Nano Dimens.*, **7**, 160 (2016).
3. A. Shokri, *Russ. J. Appl. Chem.*, **88**, 2038 (2015).
4. M. Mohadesia, A. Shokri, *Desal. Water Treat.*, **81**, 199 (2017).
5. A. Shokri, A. Hassani, *Russ. J. Appl. Chem.*, **89**, 1985 (2016).
6. A. Shokri, K. Mahanpoor, *Int. J. Ind. Chem.*, **8**, 101, (2017).
7. A. Shokri, *Desal. Water Treat.*, **111**, 173 (2018)
8. A. Shokri, *Desal. Water Treat.*, **58**, 258 (2017).
9. M. Igouzal, F. El Azhar, M. Hafsi, M. Taky, A. Elmidaoui, *Desal. Water Treat.*, **93**, 30 (2017).
10. S. Zarinabadi, *Bulg. Chem. Commun.*, **48**, 112 (2016).
11. A. Shokri, M. Nasiri Shoja, *Bulg. Chem. Commun*, **50**, 1 (2018).
12. N. Zouhri, M. Igouzal, M. Larif, M. Hafsi, M. Taky, A. Elmidaoui, *Desal. Water Treat*, accepted, doi:10.5004/dwt.2018.21410.
13. A. S. M. Tabatabaee Ghomshe, *Bulg. Chem. Commun.*, **48**, 57 (2016).
14. B. Bouya, M. Faouzi, M. Ben Abbou, A. Essahlaoui, M. Bahir, N. Youbi, M A. Hessane, *Comunicações Geológicas*, **98**, 73 (2011).
15. B. Benseddik, E.M. Bouabid, *Arab. J. Earth Sci.*, **3**, 14 (2016).
16. B. Marouane, K. Belhsain, M. Jahdi, S. K. Belhsain, M. Jahdi, S. El Hajjaji, A. Dahchour, S. Dousset, A. Satrallah, *J. Mater. Environ. Sci.*, **5**, 2151 (2014).
17. L. Zouhri, *J. Envir. Hydrol.*, **11**, 1 (2003).
18. J. Wang, D.S. Dlamini, A.K., Mishra, *J. Membrane Sci.*, **454**, 516 (2014).
19. M.F. San Román, E. Bringas, R. Ibañez, I. J. Ortiz, *J. Chem. Technol. Biotechnol.*, **85**, 2 (2010).
20. V. Nikonenko, V. Zabolotsky, C. Larchet, B. Auclair, G. Pourcelly, *Desalination*, **147**, 369 (2002).
21. O. Kedem, K.S. Spiegler, *Desalination*, **1**, 311 (1966).

AUTHOR INDEX

- Abbas Gh., See Hussain et al. 499
- Abreshteh M., Khandan-Barani K., Hassanabadi A., Aspartic acid as an efficient and green catalyst for the one-pot synthesis of 2-amino-4*H*-chromene derivatives under thermal, solvent free conditions 475
- Abu-Nameh E.S.M., See Khanfar et al. 305
- Achimovicova M., See Kostova et al. 437
- Acknowledgement to reviewers for vol. 50 (2018) ... 158
- Afaneh A.T., See Khanfar et al. 305
- Agarwa Sh., See Kamrani et al. 384
- Ahmad A., See Khanfar et al. 305
- Akdut G., Bildik F., Duran H., Tuna A., Şişmanoğlu T., Şenkal B.F., Adsorption of bisphenol A and phenoxyacetic acid onto new polymeric adsorbents 541
- Akgül A., See Sönmez et al. 48
- Akin Polat Z., See Karakus et al. 267
- Akova V.I., See Angelova et al. 342
- Al Bujog M., See Khanfar et al. 305
- Al G.A.M., See Kamrani et al. 384
- Al Khotaba H., See Khanfar et al. 305
- Alagić S.Č., See Dimitrijević et al. 358
- Aleksandrov H.A., See Kolev et al. 552
- Alev B., Tunali S., Yanardag R., Yarat A., Influence of storage time and temperature on activity of urease 159
- Ali A., See Khan et al. 488
- Althagafi I.I., See El-Metwaly et al. 527
- Al-Zahar A.A., See El-Metwaly et al. 527
- Al-Zahrani A.A., See Pasupulety et al. 414
- Anđelković D.H., See Bogdanović et al. 242
- Anđelković T.D., See Bogdanović et al. 242
- Angelova V.R., Akova V.I., Ivanov K.I., Comparative study of the methods for the determination of organic carbon and organic matter in soils, compost and sludge 342
- Anniversary, One hundred years of the founder of chemical engineering in Bulgaria – Prof. Dimiter Elenkov, DSc i
- Anwar J., See Uz-Zaman et al. 332, 337
- Araujo-León J., See Carrera-Lanestosa et al. 80
- Arziani B., See Lekishvili et al. 506
- Ashjari M., Masoud Kandomal S., The effect of plastic waste and elemental sulfur additives on chemical and physical properties of bitumen 312
- Atalay V.E., Determination of the p*K*_a values of some pyridine derivatives by computational methods. 16
- Atanasov V.A., See Kolev et al. 552
- Atanasova M.D., Sasheva P., Yonkova I.M., Doytchinova I.A., Modelling the interaction and prediction of microtubule assembly inhibition of podophyllotoxin and its derivatives by molecular docking. 513
- Atli Ö., See Özşen et al. 200
- Aydogdu S., See Hatipoglu et al. 443
- Azarifar D., Farbodmehr M., Badalkhani O., Jaymand M., Sulfamic acid-functionalized silica-coated magnetite nanoparticles as a recyclable catalyst for the facial synthesis of benzimidazole derivatives 593
- Azimova Sh.S., See Ismailova et al. 73
- Badalkhani O., See Azarifar et al. 593
- Bai Y., See She et al. 96
- Barbakadze Kh., See Lekishvili et al. 506
- Bardarov I., See Chorbadzhiyska et al. 284
- Bayat M., See Hassanpour et al. 185
- Bchiti M., Igouzal M., El Azhar F., Oudda H., El Midaoui A., Modeling the separation performance of nanofiltration and reverse osmosis: case study of groundwater desalination (M'Nasra zone Morocco)..... 622
- Bendjaballah-Lalaoui N., See Rennane et al. 315
- Betancur-Ancona D., See Carrera-Lanestosa et al. 80
- Bildik F., See Akdut et al. 541
- Bogdanova S., See Pereva et al. 326
- Bogdanović D.S., Anđelković D.H., Kostić I.S., Kocić G.M., Anđelković T.D., The effects of temperature and ultrasound on the migration of di-(2-ethylhexyl) phthalate from plastic packaging into dairy products 242
- Bojić A.Lj., See Krstić et al. 394
- Bojinova A., See Kaneva et al. 406
- Bondock S., See El-Metwaly et al. 527
- Bozdogan Konuskan D., See Ozyilmaz et al. 483
- Brostow W., See Lekishvili et al. 506
- Carrera-Lanestosa A., Segura-Campos M., Coral-Martinez T., Ruiz-Ciau D., Araujo-León J., Betancur-Ancona D., Moguel-Ordóñez Y., Development and validation of a chromatographic method to identify and quantify the flavonoids extracted from *S. rebaudiana* Bertoni..... 80
- Chaichi Nosrati A., See Hassanpour et al. 185
- Chakarova V., Monev M., Hydrogen evolution reaction on electroless Ni-P coatings deposited at different pH values 54
- Chamovska D., Porjazoska Kujundziski A., Grchev T., Adsorption of polyacrylamide on activated carbon 521
- Chen J., See She et al. 96
- Chen L., See Zhang et al. 450
- Chitra S., See Mahalakshmi et al. 31
- Chorbadzhiyska E., Bardarov I., Hubenova Y., Mitov M., Modified graphite electrodes as potential cathodic electrocatalysts for microbial electrolysis cells..... 284
- Christov V.Ch., See Ismailov et al. 577
- Chung I.-M., See Mahalakshmi et al. 31
- Civan D., See Hatipoglu et al. 443
- Coral-Martinez T., See Carrera-Lanestosa et al. 80
- Daghighi Asli M., See Jamali Aghbash et al. 146
- Daous M.A., See Pasupulety et al. 414
- Dedeoglu H., See Hatipoglu et al. 443
- Didarul Islam M., Rahaman Sh., Hasan Jiban J., Muhtasim Mahd M., Removal of chromium from

aqueous solution using chitosan: An experimental study.....	615
Dimitrijević S.B., Alagić S.Č., Rajčić-Vujasinović M.M., Dimitrijević S.P., Ivanović A.T., IR/Raman characterization of Au-mercaptoptriazole crystals	358
Dimitrijević S.P., See Dimitrijević et al.	358
Dimitrijević V.D., See Krstić et al.	394
Dimitrov D., See Kaneva et al.	406
Dimitrov D.Z., See Rafailov et al.	219
Dimitrov M.V., See Marchokova et al.	589
Dimitrova M.B., See Vasileva et al.	249
Dong F., See She et al.	96
Dorđević D.M., See Krstić et al.	394
Dorđević M.G., Premović P.I., Iron, manganese, vanadium, copper and zinc of the Cretaceous-Paleogene boundary Fish Clay at the Kirkevig site (Højerup, Stevns Klint, Denmark)	5
Dorđević M.G., See Krstić et al.	394
Doytchinova I.A., See Atanasova et al.	513
Dragicevic N., Krajisnik D., Milic J., Pecarski D., Jugović Z., Hydrophilic gel containing coenzyme Q ₁₀ -loaded liposomes: preparation, characterization and stress stability tests	117
Driss H., See Pasupulety et al.	414
Duran H., See Akdut et al.	541
Dutkova E., See Kostova et al.	431
Duysak O., See Ozyilmaz et al.	483
Ebrahimi A., See Mohammadi Chalanchi et al.	224
Ebrahimi N., Haghghi Asl A., Mottahedin P., Optimization of β-carotene solubility in pressurized hot water using a dynamic method and factorial methodology	279
Ebrahimzadeh M., See Ghaforyan et al.	10
El Azhar F., See Bchiti et al.	622
El Midaoui A., See Bchiti et al.	622
El-Metwaly N.M., Bondock S., Althagafi I.I., Khedr A.M., Al-Zahar A.A., Saad F.A., Investigating the influence of <i>p</i> -substituents upon spectral, thermal, kinetic, molecular modeling and molecular docking characteristics of new synthesized arylazobithiazolylhydrazones.....	527
Elmuradov B.Zh., See Ismailova et al.	73
Erdogan T., On the esterification reaction of phenacyl bromide with benzoic acids: microwave and ultrasound versus conventional heating	134
Erratum	455
Fabian M., See Kostova et al.	431, 437
Fang W.T., See Wu et al.	25
Faraj W., See Khanfar et al.	305
Farbodmehr M., See Azarifar et al.	593
Farkhan M., See Ghaforyan et al.	10
Farshad A., See Parvizi et al.	190
Franco Júnior M.R., Rocha N.R.A.F., Pereira W.A., Merlo N.P., Removal of LAS from water by activated carbon and resins in a continuous process	365
Gecheva G.M., See Gribacheva et al.	256
Ghaffary T., See Ghaforyan et al.	10
Ghaforyan H., Ghaffary T., Mohammadbilankohi S., Hasanpour M., Ebrahimzadeh M., Pincak R., Farkhan M., Effect of ultrasound waves intensity on the removal of Congo red dye from the textile industry wastewater by Fe ₃ O ₄ @TiO ₂ core-shell nanospheres	10
Ghorannevis M., See Hassanpour et al.	185
Gospodinov M.M., See Rafailov et al.	219
Grchev T., See Chamovska et al.	521
Gribacheva N.P., Gecheva G.M., Stefanova V.M., Air pollution monitoring with mosses in Western Rhodopes, Bulgaria	256
Gupta V.K., See Kamrani et al.	384
Haghghi Asl A., See Ebrahimi et al.	279
Hasan Jiban J., See Didarul Islam et al.	615
Hasanpour M., See Ghaforyan et al.	10
Hashemi S., See Hassanpour et al.	185
Hassanabadi A., See Abreshteh et al.	475
Hassanpour S., Bayat M., Chaichi Nosrati A., Ghorannevis M., Hashemi S., The eliminatory effects of cold argon plasma jet on aflatoxin B1 produced by different isolates of <i>Aspergillus section nigri</i>	185
Hatipoglu A., Aydogdu S., Dedeoglu H., Civan D., Toxicity prediction of organophosphorus compounds by QSAR	443
Hayat T., See Imran Khan et al.	180
He Y., See Wu et al.	25
Hemapriya V., See Mahalakshmi et al.	31
Huang H., See She et al.	96
Hubenova Y., See Chorbadzhiyska et al.	284
Hussain Sh., Abbas Gh., Shahid M., Mass spectroscopic and biological activity investigations of bis(triorganotin(iv)) carboxylates with acetylene dicarboxylic acid.....	499
Igouzal M., See Bchiti et al.	622
Ijaz Khan M., See Imran Khan et al.	180
Iliev I.A., See Vasileva et al.	249
Iliev I.I., Calibration of a system for air-borne gamma spectrometry survey and mapping implementation	608
Imran Khan M., Hayat T., Ijaz Khan M., Yasmeeen T., Thermal properties and time dependent flow behavior of viscous fluid	180
In memoriam, for Prof. Lubomir Boyadzhiev.....	303
Instruction to the authors.....	159, 289, 456, 639
Ismailov I.E., Ivanov I.K., Christov V.Ch., Trifunctionalized allenes. Part II. A practical regioselective synthesis of 4-phosphorylated β-hydroxyallene-carboxylates	577
Ismailova D.S., Ziyaev A.A., Sasmakov S.A., Makhmudov U.S., Khasanov Sh.Sh., Azimova Sh.S., Elmuradov B.Zh., Synthesis and biological activity of 2-alkylthio-5-(4- <i>N</i> -acetyl(<i>N</i> -chloroacetyl)aminophenyl)-1,3,4-oxadiazoles.....	73
Ivanov I.G., See Papanov et al.	113, 426
Ivanov I.K., See Ismailov et al.	577
Ivanov I.P., See Vasileva et al.	249
Ivanov K.I., See Angelova et al.	342
Ivanov S., See Stamenković et al.	372

Ivanova G., Stoyanova-Ivanova A., Kovacheva D., Stoyanova A., Improvement of the electrochemical properties of Ni-Zn rechargeable batteries by adding B(Pb)SrCaCuO conducting ceramics.....	66	Komorsky-Lovrić Š., Lovrić M., Theory of staircase cyclic voltammetry of two electrode reactions coupled by a chemical reaction.....	348
Ivanova St.D., See Papanov et al.....	426	Kostić I.S., See Bogdanović et al.....	242
Ivanović A.T., See Dimitrijević et al.....	358	Kostova N.G., Achimovicova M., Fabian M., Photocatalytic behavior of ZnSe-TiO ₂ composite for degradation of methyl orange dye under visible light irradiation.....	437
Jamali Aghbash B., Manoochehri M., Daghighi Asli M., Cadmium(II) organometallic complex with 4-chloro-N ((pyridine-2 yl) methylene) benzene amine: synthesis, spectroscopy and antibacterial evaluation.....	146	Kostova N.G., Fabian M., Dutkova E., Mechanochemically synthesized N-doped ZnO for photodegradation of ciprofloxacin.....	431
Janjušević Z.V., See Sokić et al.....	457	Kotian S.Y., see Vinaya et al.....	479
Jaymand M., See Azarifar et al.....	593	Kovacheva D., See Ivanova et al.....	66
Jugović Z., See Dragicevic et al.....	117	Krajisnik D., See Dragicevic et al.....	117
Kadnor V.A., Shelke S.N., Synthesis and biological evaluation of novel carbazole chalcones and corresponding 1,5-benzothiazepine derivatives.....	234	Krstić N.S., Stanković M.N., Đorđević D.M., Dimitrijević V.D., Marinković M., Đorđević M.G., Bojić A.Lj., Characterization of raw and chemically activated natural zeolite as a potential sorbent for heavy metal ions from waste water.....	394
Kamrani M.-S., Seifpanahi-Shabani K., Seyed-Hakimi A., Al G.A.M., Agarwa Sh., Gupta V.K., Degradation of cyanide from gold processing effluent by H ₂ O ₂ , NaClO and Ca(ClO) ₂ combined with sequential catalytic process.....	384	Kumar B., Seth G.S., Nandkeolyar R., Regression model and analysis of MHD mixed convective stagnation point nanofluid flow: SLM and SRM approach.....	557
Kaneva N., Bojinova A., Papazova K., Dimitrov D., Photocatalytic degradation of the pharmaceuticals Paracetamol and Chloramphenicol by Ln-modified ZnO photocatalysts.....	406	Kumar R., See Seth et al.....	168
Kanwal F., Rehman R., Warraich H.A., Synthesis of novel polyaniline composites with <i>Eriobotrya japonica</i> leaves for removal of Methyl red dye from wastewater.....	589	Le P.T.Q., Phytochemical screening and antimicrobial activity of extracts of <i>Cassia alata</i> L. leaves and seeds.....	378
Karahan M., See Karakus et al.....	267	Lei J., See She et al.....	96
Karakus G., Akin Polat Z., Karahan M., Design, synthesis, structural characterization and cell cytotoxicity of new derivative poly(maleic anhydride-co-vinyl acetate)/miltefosine polymer/drug conjugate.....	267	Lekishvili G., See Lekishvili et al.....	506
Kavrakovski Z.S., See Simonovska et al.....	103	Lekishvili N., Barbakadze Kh., Arziani B., Lekishvili G., Brostow W., Antibiocorrosive coatings based on antimicrobial polymer hybrid composites.....	506
Khalil M., See Khanfar et al.....	305	Lokanatha Rai K.M., See Vinaya et al.....	479
Khan I., Ur Rahman N., Ali A., Saeed Kh., Adsorption of cobalt onto activated charcoal and its utilization for decolorization of bromocresol green dye.....	488	Lončar B.Lj., See Sokić et al.....	457
Khandan-Barani K., See Abreshteh et al.....	475	Lovrić M., See Komorsky-Lovrić et al.....	348
Khanfar M.F., Abu-Nameh E.S.M., Afaneh A.T., Saket M.M., Ahmad A., Faraj W., Khalil M., Al Khotaba H., Al Bujog M., Voltammetric detection of hydrochlorothiazide at molybdenum oxide modified screen printed electrodes.....	305	Lozanov V.S., See Vasileva et al.....	249
Khanlarkhani A., See Parvizi et al.....	190	Mahalakshmi D., Unnisa C.B.N., Hemapriya V., Subramaniam E.P., Roopan S.M., Chitra S., Chung I.-M., Kim S.-H., Prabakaran M., Anticorrosive potential of ethanol extract of <i>Delonix elata</i> for mild steel in 0.5 M H ₂ SO ₄ - a green approach.....	31
Khasanov Sh.Sh., See Ismailova et al.....	73	Makhmudov U.S., See Ismailova et al.....	73
Khedr A.M., See El-Metwaly et al.....	527	Manoochehri M., See Jamali Aghbash et al.....	146
Kim S.-H., See Mahalakshmi et al.....	31	Marchokova N.I., Petkova V.B., Dimitrov M.V., UV-spectrophotometric approach in comparative studies of Gliclazide modified-release tablets.....	589
Kim Y.M., See Seo et al.....	261	Marinković M., See Krstić et al.....	394
Kiran İ., See Özşen et al.....	200	Marinova V., See Rafailov et al.....	219
Knez Ž.F., See Simonovska et al.....	103	Marković B.R., See Sokić et al.....	457
Kocić G.M., See Bogdanović et al.....	242	Marković I., See Stamenković et al.....	372
Kolev S.K., Atanasov V.A., Aleksandrov H.A., Popov V.N., Milenov T.I., Semiconducting graphene.....	552	Masoud Kandomal S., See Ashjari et al.....	312
Kolev Ts., See Petrova et al.....	88	Merlo N.P., See Franco Júnior et al.....	365
		Mikhova B.P., See Simonovska et al.....	103
		Milenov T.I., See Kolev et al.....	552
		Milic J., See Dragicevic et al.....	117
		Mitev V.I., See Vasileva et al.....	249
		Mitov M., See Chorbadzhiyska et al.....	284
		Mladenović J.D., See Pavlović et al.....	400
		Mladenović J.D., See Zdravković et al.....	601
		Moguel-Ordóñez Y., See Carrera-Lanestosa et al.....	80

Mohammadi Chalanchi S., Ebrahimi A., Nowroozi A., Theoretical insight to intermolecular hydrogen bond interactions between methyl <i>N</i> -(2-pyridyl) carbamate and acetic acid: substituent effects, cooperativity and energy decomposition analysis.....	224	Pereira W.A., See Franco Júnior et al.	365
Mohammadibilankohi S., See Ghaforyan et al.	10	Pereva S.M., Sarafska Ts.P., Petrov V., Spassova M., Bogdanova S., Spassov T., Ibuprofen/ β -CD complexation by controlled annealing of their mechanical mixture.....	326
Momchilova S.M., See Simonovska et al.	103	Petkova Ek.G., See Papanov et al.	113, 426
Moravčević Đ.Z., See Pavlović et al.	400	Petkova K., See Petrova et al.	88
Mottahedin P., See Ebrahimi et al.	279	Petkova V.B., See Marchokova et al.	589
Muhtasim Mahd M., See Didarul Islam et al.	615	Petrov L.A., See Pasupulety et al.	414
Monev M., See Chakarova et al.	54	Petrov V., See Pereva et al.	326
Nagalakshmi K.V., Shyamala P., Kinetics of oxidation of [Fe(phen) ₃] ²⁺ by persulphate: catalysis in the water pools of CTAB reverse micelles	494	Petrova D., Petkova K., Saltirov I., Kolev Ts., Application of vibrational spectroscopy and XRD analysis for investigation of calcium oxalate kidney stones	88
Nandkeolyar R., See Kumar et al.	557	Pezo L.L., See Sokić et al.	457
Nosal-Wiercinska A., See Sadikoglu et al.	125	Pincak R., See Ghaforyan et al.	10
Nowroozi A., See Mohammadi Chalanchi et al.	224	Popov D.I., See Papanov et al.	426
Odović J.V., In silico investigation of the relation between calcium channel blockers' molecular descriptors and oral bioavailability data.....	60	Popov V.N., See Kolev et al.	552
Oudda H., See Bchiti et al.	622	Porjazoska Kujundziski A., See Chamovska et al.	521
Özden Ö., See Sönmez et al.	212	Poštić D.Ž., See Pavlović et al.	400
Özşen Ö., Atli Ö., Kiran İ., Biotransformation of oleic acid and antimicrobial and anticancer activities of its biotransformation extracts.....	200	Prabakaran M., See Mahalakshmi et al.	31
Ozyilmaz A., Duysak O., Bozdogan Konuskan D., Proximate (lipid, moisture, ash) levels and fatty acid profiles in edible parts of common cuttlefish (<i>Sepia officinalis</i> , L., 1758) from different geographical areas	483	Premović P.I., See Đorđević et al.	5
Paliulis D., Extraction of zinc and copper from a contaminated soil by using organic acids.....	38	Primožić M.J., See Simonovska et al.	103
Palizdar Y., See Parvizi et al.	190	Radulescu A.V., See Radulescu et al.	419
Papanov S.I., Petkova Ek.G., Ivanov I.G., Polyphenols content and antioxidant activity of various pomegranate juices.....	113	Radulescu I., Radulescu A.V., Study of degradation phenomenon for transmission lubricants	419
Papanov S.I., Petkova Ek.G., Ivanov I.G., Ivanova St.D., Popov D.I., Analysis of the changes in the main characteristics and antioxidant properties in raspberries of "Rubin" variety depending on the altitude.....	426	Rafailov P.M., Todorov R., Marinova V., Dimitrov D.Z., Gospodinov M.M., Optical spectroscopic study of Ru- and Rh-DOPED Bi ₁₂ TiO ₂₀ crystals.....	219
Papazova K., See Kaneva et al.	406	Rafajlovska V.G., See Simonovska et al.	103
Parvizi B., Khanlarkhani A., Palizdar Y., Farshad A., Comparison of ANFIS and ANN modeling for predicting the behavior of a catalytic methane reformer.....	190	Rahaman Sh., See Didarul Islam et al.	615
Pasupulety N., Driss H., Al-Zahrani A.A., Daous M.A., Petrov L.A., On the role of texture and physicochemical characteristics on adsorption capacity of granular activated carbon.....	414	Rajčić-Vujanović M.M., See Dimitrijević et al.	358
Patarić A.S., See Sokić et al.	457	Rehman R., See Kanwal et al.	589
Pavlović N.V., Mladenović J.D., Zdravković N.M., Moravčević Đ.Z., Poštić D.Ž., Zdravković J.M., Effect of tomato juice storage on vitamin C and phenolic compounds and their stability over one-year period	400	Rehman R., See Uz-Zaman et al.	332, 337
Pavlović N.V., See Zdravković et al.	601	Rehman R., Tanveer T., Spectrophotometric determination of significant minerals in milk samples found in Lahore (Pakistan) for ensuring food safety	206
Pecarski D., See Dragicevic et al.	117	Ren D., See She et al.	96
		Rennane S., Bendjaballah-Lalaoui N., Trari M., Comparative removal of naphthalene by adsorption on different sand/bentonite mixtures	315
		Rocha N.R.A.F., See Franco Júnior et al.	365
		Roopan S.M., See Mahalakshmi et al.	31
		Ruiz-Ciau D., See Carrera-Lanestosa et al.	80
		Saad F.A., See El-Metwaly et al.	527
		Sadikoglu M., Soylu U.I., Yilmaz S., Selvi B., Yildiz Seckin H., Nosal-Wiercinska A., Electrocatalytic oxidation of moxifloxacin hydrochloride on modified glassy carbon surface and determination in Avelox tablets.....	125
		Saeed Kh., See Khan et al.	488
		Saket M.M., See Khanfar et al.	305
		Saltirov I., See Petrova et al.	88
		Sapundzhi F.I., Modelling and optimization of the structure-activity relationship by using surface fitting methods.....	569
		Sarafska Ts.P., See Pereva et al.	326
		Sasheva P., See Atanasova et al.	513

Sasmakov S.A., See Ismailova et al.....	73	Trari M., See Rennane et al.....	315
Segura-Campos M., See Carrera-Lanestosa et al.....	80	Tripathi R., See Seth et al.....	168
Seifpanahi-Shabani K., See Kamrani et al.....	384	Tuna A., See Akdut et al.	541
Selvi B., See Sadikoglu et al.....	125	Tunali S., See Alev et al.....	159
Şenkal B.F., See Akdut et al.	541	Turkyilmaz B., Yanardag R., Protecting effect of vitamin U against amiodarone-induced hepatic damage via its antioxidative activity	20
Seo S.B., Kim Y.M., Optimization of high ultrasound- assisted extraction (INEFU) of active components from natural materials by response HPLC-PDA analysis.....	261	Unnisa C.B.N., See Mahalakshmi et al.	31
Seth G.S., Kumar R., Tripathi R., Thermo-diffusion effects on magnetohydrodynamic natural convection flow of a chemically reactive Brinkman type nanofluid in a porous medium.....	168	Ur Rahman N., See Khan et al.	488
Seth G.S., See Kumar et al.....	557	Uz-Zaman W., Rehman R., Anwar J., Zafar J., A novel approach to analyze total amino acids contents of food samples by computational image scanning densitometry	332
Seyed-Hakimi A., See Kamrani et al.	384	Uz-Zaman W., Rehman R., Anwar J., Zafar J., Rapid photo-catalytic degradation of methylene blue, tartrazine and brilliant green dyes by high flux UV irradiation photolysis reactor	337
Shahid M., See Hussain et al.	499	Vasileva A.M., Iliev I.A., Lozanov V.S., Dimitrova M.B., Mitev V.I., Ivanov I.P., In vitro study on the antitumor activity of <i>Tanacetum vulgare</i> L. Extracts	249
She W., Chen J., Huang H., Zhu H., Lei J., Ren D., Bai Y., Dong F., Yang F., Experimental study on coalbed methane (CBM) displacement by mixed carbon dioxide and nitrogen.....	96	Vinaya, Kotian S.Y., Lokanatha Rai K.M., Reduction of nitro compounds using copper as catalyst in dioxolane medium	479
Shelke S.N., See Kadnor et al.....	234	Vrabic Brodnjak U., Experimental investigation of moisture and tensile properties of shellac andchitosan films for packaging applications.....	152
Shyamala P., See Nagalakshmi et al.....	494	Vragolović Bošković N.M., See Zdravković et al.....	601
Simonovska J.M., Yancheva D.Y., Mikhova B.P., Momchilova S.M., Knez Ž.F., Primožić M.J., Kavrakovski Z.S., Rafajlovska V.G., Characterization of extracts from red hot pepper (<i>Capsicum annum</i> L.).....	103	Wang Y.S., See Wu et al.	25
Sinirkaya M., Effect of ultrasound on the dissolution of Mardin-Mazıdađı (Turkey) phosphate ore in dilute H ₃ PO ₄ solution	164	Warraich H.A., See Kanwal et al.	589
Şişmanođlu T., See Akdut et al.....	541	Wen Y., See Zhang et al.....	450
Sokić M.D., Marković B.R., Pezo L.L., Stanković S.B., Patrić A.S., Janjušević Z.V., Lončar B.Lj., Copper leaching from chalcopyrite concentrate by sodium nitrate in sulphuric acid solution – chemometric approach.....	457	Wu N.N., He Y., Tan Y.C., Wang Y.S., Fang W.T., Degradation of sulfonamides in aqueous solution by an electro/Fe ²⁺ /peroxydisulfate process.....	25
Sönmez S., Özden Ö., The influence of pigment proportions and calendering of coated paperboards on dot gain.....	212	Yanardag R., See Alev et al.	159
Sönmez S., Yıldız Z., Akgül A., The effects of epoxyarylate coating on printability of bio/synthetic-based fabrics in a thermal transfer printing system.....	48	Yanardag R., See Turkeyilmaz et al.....	20
Soylu U.I., See Sadikoglu et al.	125	Yancheva D.Y., See Simonovska et al.	103
Spasov T., See Pereva et al.	326	Yang F., See She et al.	96
Spasova M., See Pereva et al.....	326	Yarat A., See Alev et al.....	159
Stamenković U., Ivanov S., Marković I., The influence of isochronal aging on the mechanical and thermophysical properties of the EN AW-6060 aluminum alloy	372	Yasmeen T., See Imran Khan et al.....	180
Stanković M.N., See Krstić et al.....	394	Yildiz Seckin H., See Sadikoglu et al.	125
Stanković S.B., See Sokić et al.....	457	Yıldız Z., See Sönmez et al.	48
Stefanova V.M., See Gribacheva et al.	256	Yilmaz S., See Sadikoglu et al.	125
Stoyanova A., See Ivanova et al.	66	Yonkova I.M., See Atanasova et al.	513
Stoyanova-Ivanova A., See Ivanova et al.	66	Zafar J., See Uz-Zaman et al.	332, 337
Subramaniam E.P., See Mahalakshmi et al.	31	Zdravković J.M., Pavlović N.V., Mladenović J.D., Vragolović Bošković N.M., Zdravković N.M., Effects of tomato processing on carotenoids antioxidant activity and stability during one-year storage	601
Tan Y.C., See Wu et al.	25	Zdravković J.M., See Pavlović et al.....	400
Tanveer T., See Rehman et al.....	206	Zdravković N.M., See Pavlović et al.....	400
Todorov R., See Rafailov et al.....	219	Zdravković N.M., See Zdravković et al.	601
		Zhang J., Wen Y., Chen L., Study on fatigue properties of basic magnesium sulfate cement reinforced concrete beams based on response surface methodology.....	450
		Zhu H., See She et al.	96
		Ziyaev A.A., See Ismailova et al.....	73

SUBJECT INDEX

[2,3]-sigmatropic rearrangement	577	calcium channel blockers	60
1,4-benzothiazepine	234	calendering	212
¹ H-NMR.....	267	calibration method.....	608
1-year storage	601	cancer cell line.....	249
2-alkylthio-5-(4- <i>N</i> -acetyl(<i>N</i> -chloroacetyl)aminophenyl) -1,3,4-oxadiazoles	73	capsaicinoids	103
2-Amino-4 <i>H</i> -chromenes	475	<i>Capsicum annuum</i> L.	103
³¹ P-NMR.....	267	carbamate	224
4,6-dimethyl dibenzothiophene	414	carbazole	234
4-aminobenzene sulfonic acid	125	carbomer gel.....	117
4-phosphorylated 6-hydroxyhepta-2,3-dienoates.....	577	carbon dioxide.....	96
acetic acid	35	<i>Cassia alata</i> L.	378
acidity	60	catalytic reforming	190
activated carbon.....	365, 488, 521	cavitation	164
activation	394	cell viability.....	249
adsorbent.....	414	<i>Centella asiatica</i>	261
adsorption	315, 365, 488, 521, 541, 581, 615	certified samples.....	342
aflatoxins	185	chalcopyrite.....	457
aging	372	chemical properties	312
airborne.....	608	chitosan	615
aluminum alloys	372	<i>Chloramphenicol</i>	406
amino acids	332	citric acid.....	35
amiodarone	20	<i>Citrus madurensis</i>	261
anthocyanins	113, 426	coalbed methane (CBM)	96
antibacterial	499	coating.....	212, 506
antibacterial activity.....	73, 146, 378	cobalt.....	488
antifungal.....	499	coenzyme Q ₁₀	117
antifungal activity	73	colchicine binding site.....	513
antimalarial activity	234	cold plasma jet.....	185
antimicrobial.....	506	computational chemistry	134
antimicrobial activity.....	200, 234	computer modelling	569
antioxidant	378	congo red.....	10
antioxidant activity	113, 426	continuous process	365
antioxidative activity	601	copper.....	35, 457, 479
antitumor activity.....	249	core-shell nanospheres	10
aromatic nitro compounds	479	correlation	279
arsenic trioxide	506	Cretaceous–Paleogene boundary.....	5
aspartic acid.....	475	crystal growth.....	219
<i>Aspergillus nigr</i>	185	crystal structure	73
atmospheric deposition	256	cyanide degradation.....	384
atomic absorption spectrometry.....	206	cyclic voltammetry.....	348
B(Pb)SrCaCuO conducting ceramics	66	cytotoxic activity	200, 267
B3LYP	16	decolorization.....	488
band gap.....	552	degradation.....	337, 419
bentonite	315	<i>Delonix elata</i>	31
benzimidazoles	593	densitometry.....	332
BET.....	394	density functional theory (DFT).....	16, 305, 443
Bi ₁₂ TiO ₂₀	219	DHA	483
biotransformation.....	200	dibenzothiophene	414
bisphenol A.....	541	dielectric constant.....	279
bithiazolyhydrazones	527	different conditions	400
bitumen	312	dioxolane.....	479
BMSC	450	displacement experiment.....	96
brilliant green.....	337	dissolution kinetics	164
Brinkman type nanofluid	168	docking.....	569
bromocresol green	488	doping.....	219, 431
Brownian and thermophoretic diffusions.....	557	dot gain.....	212
cadmium (II) complexes	146	drug release	589
		dye.....	437

ECE mechanism	348	IR	103
EIMS.....	499	IR spectroscopy	358
ejecta layer	5	isotherm.....	615
electrocatalytic ability.....	125	<i>Kerria Lacca</i>	152
electrochemical deposition	305	kidney stones	88
electrochemical properties	66	kinetic models	589
electrochemistry.....	25	kinetic study	527
electroless deposition.....	54	kinetics	494, 615
electropolymerization	125	<i>Laminaria Japonica</i>	261
ELISA.....	185	Langmuir isotherm	521
EN AW-6060.....	372	leachability	242
EPA.....	483	leaching	457
epoxyacrylate coating	48	ligand-receptor interaction	569
<i>Eriobotrya japonica</i> leaves.....	581	lipophilicity	60
essential metals	206	liposome	117
esterification	134	liver	20
extract	378	localized molecular orbital energy decomposition analysis (LMO-EDA)	224
extraction	35	lubricant	419
factorial methodology.....	279	lycopene	601
fatigue property.....	450	M06-2X.....	16
fatty acid	483	maleic anhydride-co-vinyl acetate copolymer conjugation	267
Fe ²⁺	25	malononitrile	475
Fe ₃ O ₄ @TiO ₂	10	mathematical modelling	457
ferroin	494	mechanochemistry.....	431, 437
FET	552	Mediterranean	483
films	152	melting method.....	326
filtration	365	membrane processes.....	622
flame emission spectroscopy	206	metal complexes.....	146
flavonoids	80	methods	342
FTIR	88, 267, 394	methyl orange.....	437
gamma-mapping	608	methyl red dye.....	581
gas chromatography - mass spectrometry (GC-MS)	31, 242	methylene blue	337
Gaussian 09 software.....	527	MHD	180
Gliclazide.....	589	MIC	378
gold processing effluents treatment	384	micro level.....	332
gold-mercaptoptriazole (Au-MT)	358	microbial electrolysis cell.....	284
granular activated carbon.....	414	microscopy	419
graphen	552	microtubule inhibition	513
green catalyst	475	microwave chemistry	134
green chemistry.....	593	milk samples.....	206, 242
green coffee beans	261	miltefosine.....	267
heat absorption.....	168	minimum inhibitory concentration	200
heat treatment	372	modeling.....	190, 513
heavy metal sorption.....	394	modified glassy carbon electrode.....	125
hemolytic	499	modified graphite electrodes	284
heterocycles	593	modified-release tablets.....	589
HPLC	80, 261	molecular descriptors	443
hydrochlorothiazide	305	molecular docking	513, 527
hydrogen bond	224	molybdenum oxide.....	305
hydrogen evolution reaction	54	moxifloxacin hydrochloride	125
hydrogen production.....	284	multi-component reactions	475
ibuprofen.....	326	mu-opioid receptor	569
ICH	80	NAA	256
ICP-MS	256	NaI(Tl)	608
ICP-OES	256	nanocatalyst.....	593
inclusion complex.....	326	nanoparticles	10
INEFU	261	naphthalene	315
influence of working parameters	457	natural convection	168
inhibitive action	31		

natural materials	261	raspberry.....	426
neural network	190	rat	20
neuro-fuzzy	190	reaction kinetics	25
Ni-P coatings	54	red hot pepper.....	103
nitrogen.....	96	regression model	557
nitrophthalic acid	479	reinforced concrete.....	450
Ni-Zn rechargeable batteries.....	66	resins	365
NMR.....	103	response surface method	384
non-linear kinetic modeling.....	384	response surface methodology	450, 569
offset.....	212	reverse micelles.....	494
oleic acid.....	200	reverse salt rejection.....	622
optical spectroscopy.....	219	rheology	117, 419
oral bioavailability.....	60	salmon sperm	499
organic acids.....	35	sand/bentonite mixture	315
organic carbon	342	Schiff base.....	146
organic matter	342	screen-printed electrodes.....	305
osmosis	622	SEC	267
oxidation	494	secondary resources.....	506
oxidation process	384	SEM	54
packaging.....	152	SEM-EDX	394
<i>Paracetamol</i>	406	SEM-EDX-AFM.....	31
permeate flux	622	<i>Sepia officinalis</i>	483
peroxydisulfate	25	silicon carbide	552
persulphate.....	494	SLM (successive linearization method)	557
pesticide.....	541	smectite	5
phenacyl benzoates	134	soil.....	35
phenol	113, 400, 414, 426	solubility.....	279
phenolic compounds.....	249	solvent effect	443
phenoxyacetic acid.....	541	solvent-free.....	475
phosphate rock.....	164	sonochemistry	134
phosphoric acid.....	164	spectrometry.....	608
photocatalysis	431, 437	Spiegler-Kedem model.....	622
photocatalytic degradation.....	406	SRM (spectral relaxation method)	557
photoluminescence	431	stability.....	117
photolysis.....	337	<i>Stevia rebaudiana</i>	80
phthalate.....	242	storage	400
physical properties.....	312	storage temperature	159
pigment	212	storage time	159
pK _a	16	substituent effects.....	224
plastic waste.....	312	sulfamethoxazole.....	25
podophyllotoxin.....	513	sulfonated magnetic nanoparticles	593
polyacrylamide	521	sulfur	312
polyaniline composite.....	581	synergistic effect	96
polymeric resin	541	synthesis.....	358, 577
pomegranate.....	113	<i>Tanacetum vulgare</i> L.	249
powder milk.....	206	tartaric acid.....	35
pressurized hot water	279	tartrazine.....	337
print gloss	48	tensile properties	152
properties	506	TGA	394
protection of hydroxy group	577	theory	348
pyrazoline	234	thermal properties.....	372
pyridine.....	16	thermal radiation	180
QSAR	569	thermal transfer printing.....	48
quantitative relationships.....	513	thickness.....	152
radioactive pollution	608	time-dependent flow.....	180
Raman analysis.....	219	tomato juice.....	400, 601
Raman spectroscopy.....	358	toxic metals	206
ramped surface concentration	168	toxicity	20, 443
ramped temperature	168	trace elements.....	256
rare earth.....	406	trace metals.....	5

triacylglycerols	103	voltammetry	125
TVI	212	water pools	494
ultrasound	164	water treatment.....	10
ultrasound waves	10	water vapour permeability.....	152
ultrasound-promoted.....	593	WB97XD	16
urease activity	159	X-ray analysis.....	73
validation	80	XRD	54, 88, 394
variable sheet thickness	180	zinc oxide (ZnO)	406, 431
vibrational assignment	88	zink.....	35
viscosimetry.....	521	Zlatokop zeolite.....	394
viscous and Joule dissipations	557	Zn-electrode	66
viscous liquid.....	180	ZnSe	437
visible light	431	β -carotene.....	279, 601
vitamin C	400	β -cyclodextrin	326
vitamin U	20		

Instructions about Preparation of Manuscripts

General remarks: Manuscripts are submitted in English by e-mail. The text must be typed on A4 format paper using Times New Roman font size 11, normal character spacing. The manuscript should not exceed 15 pages (about 3500 words), including photographs, tables, drawings, formulae, etc. Authors are requested to use margins of 2 cm on all sides.

Manuscripts should be subdivided into labelled sections, e.g. **Introduction, Experimental, Results and Discussion**, etc. **The title page** comprises headline, author's names and affiliations, abstract and key words. Attention is drawn to the following:

a) **The title** of the manuscript should reflect concisely the purpose and findings of the work. Abbreviations, symbols, chemical formulas, references and footnotes should be avoided. If indispensable, abbreviations and formulas should be given in parentheses immediately after the respective full form.

b) **The author's** first and middle name initials and family name in full should be given, followed by the address (or addresses) of the contributing laboratory (laboratories). **The affiliation** of the author(s) should be listed in detail by numbers (no abbreviations!). The author to whom correspondence and/or inquiries should be sent should be indicated by asterisk (*) with e-mail address.

The abstract should be self-explanatory and intelligible without any references to the text and containing not more than 250 words. It should be followed by key words (not more than six).

References should be numbered sequentially in the order, in which they are cited in the text. The numbers in the text should be enclosed in brackets [2], [5, 6], [9–12], etc., set on the text line. References are to be listed in numerical order on a separate sheet. All references are to be given in Latin letters. The names of the authors are given without inversion. Titles of journals must be abbreviated according to Chemical Abstracts and given in italics, the volume is typed in bold, the initial page is given and the year in parentheses. Attention is drawn to the following conventions: a) The names of all authors of a certain publication should be given. The use of "et al." in the list of references is not acceptable. b) Only the initials of the first and middle names should be given. In the manuscripts, the reference to author(s) of cited works should be made without giving initials, e.g. "Bush and Smith [7] pioneered...". If the reference carries the names of three or more authors it should be quoted as "Bush et al. [7]", if Bush is the first author, or as "Bush and co-workers [7]", if Bush is the senior author.

Footnotes should be reduced to a minimum. Each footnote should be typed double-spaced at the bottom of the page, on which its subject is first mentioned. **Tables** are numbered with Arabic numerals on the left-hand top. Each table should be referred to in the text. Column headings should be as short as possible but they must define units unambiguously. The units are to be separated from the preceding symbols by a comma or brackets. Note: The following format should be used when figures, equations, etc. are referred to the text (followed by the respective numbers): Fig., Eqns., Table, Scheme.

Schemes and figures. Each manuscript should contain or be accompanied by the respective illustrative material as well as by the respective figure captions in a separate file (sheet). As far as presentation of units is concerned, SI units are to be used. However, some non-SI units are also acceptable, such as °C, ml, l, etc. The author(s) name(s), the title of the manuscript, the number of drawings, photographs, diagrams, etc., should be written in black pencil on the back of the illustrative material (hard copies) in accordance with the list enclosed. Avoid using more than 6 (12 for reviews, respectively) figures in the manuscript. Since most of the illustrative materials are to be presented as 8-cm wide pictures, attention should be paid that all axis titles, numerals, legend(s) and texts are legible.

The authors are required to submit the text with a list of three individuals and their e-mail addresses that can be considered by the Editors as potential reviewers. Please, note that the reviewers should be outside the authors' own institution or organization. The Editorial Board of the journal is not obliged to accept these proposals.

The authors are asked to submit **the final text** (after the manuscript has been accepted for publication) in electronic form by e-mail. The main text, list of references, tables and figure captions should be saved in separate files (as *.rtf or *.doc) with clearly identifiable file names. It is essential that the name and version of the word-processing program and the format of the text files is clearly indicated. It is recommended that the pictures are presented in *.tif, *.jpg, *.cdr or *.bmp format.

The equations are written using "Equation Editor" and chemical reaction schemes are written using ISIS Draw or ChemDraw programme.

EXAMPLES FOR PRESENTATION OF REFERENCES

REFERENCES

1. D. S. Newsome, *Catal. Rev.–Sci. Eng.*, **21**, 275 (1980).
2. C.-H. Lin, C.-Y. Hsu, *J. Chem. Soc. Chem. Commun.*, 1479 (1992).
3. R. G. Parr, W. Yang, *Density Functional Theory of Atoms and Molecules*, Oxford Univ. Press, New York, 1989.
4. V. Ponec, G. C. Bond, *Catalysis by Metals and Alloys (Stud. Surf. Sci. Catal., vol. 95)*, Elsevier, Amsterdam, 1995.
5. G. Kadinov, S. Todorova, A. Palazov, in: *New Frontiers in Catalysis (Proc. 10th Int. Congr. Catal., Budapest, (1992)*, L. Guzzi, F. Solymosi, P. Tetenyi (eds.), Akademiai Kiado, Budapest, 1993, Part C, p. 2817.
6. G. L. C. Maire, F. Garin, in: *Catalysis. Science and Technology*, J. R. Anderson, M. Boudart (eds), vol. 6, SpringerVerlag, Berlin, 1984, p. 161.
7. D. Pocknell, *GB Patent 2 207 355* (1949).
8. G. Angelov, PhD Thesis, UCTM, Sofia, 2001, pp. 121-126.
- 9 JCPDS International Center for Diffraction Data, Power Diffraction File, Swarthmore, PA, 1991.
10. CA **127**, 184 762q (1998).
11. P. Hou, H. Wise, *J. Catal.*, in press.
12. M. Sinev, private communication.
13. <http://www.chemweb.com/alchem/articles/1051611477211.html>.

Texts with references which do not match these requirements will not be considered for publication!!!

Anniversary, One hundred years of the founder of chemical engineering in Bulgaria – Prof. Dimiter Elenkov, DSc.....	473
M. Abreshteh, K. Khandan-Barani, A. Hassanabadi, Aspartic acid as an efficient and green catalyst for the one-pot synthesis of 2-amino-4H-chromene derivatives under thermal, solvent free conditions.....	475
Vinaya, S.Y. Kotian, K.M. Lokanatha Rai, Reduction of nitro compounds using copper as catalyst in dioxolane medium.....	479
A. Ozyilmaz, O. Duysak, D. Bozdogan Konuskan, Proximate (lipid, moisture, ash) levels and fatty acid profiles in edible parts of common cuttlefish (<i>Sepia officinalis</i> , L., 1758) from different geographical areas.....	483
I. Khan, N. Ur Rahman, A. Ali, K. Saeed, Adsorption of cobalt onto activated charcoal and its utilization for decolorization of bromocresol green dyeI.	488
K.V. Nagalakshmi, P. Shyamala, Kinetics of oxidation of $[\text{Fe}(\text{phen})_3]^{+2}$ by persulphate: catalysis in the water pools of CTAB reverse micelles.....	494
Sh. Hussain, Gh. Abbas, Mu. Shahid, Mass spectroscopic and biological activity investigations of bis(triorganotin(IV)) carboxylates with acetylene dicarboxylic acid.....	499
N. Lekishvili, Kh. Barbakadze, B. Arziani, G. Lekishvili, W. Brostow, Antibiocorrosive coatings based on antimicrobial polymer hybrid composites.....	506
M.D. Atanasova, P. Sasheva, I.M. Yonkova, I.A. Doytchinova, Modelling the interaction and prediction of microtubule assembly inhibition of podophyllotoxin and its derivatives by molecular docking.....	513
D. Chamovska, A. Porjazoska Kujundziski, Adsorption of polyacrylamide on activated carbon.....	521
N.M. El-Metwaly, S. Bondock, I.I. Althagafi, A.M. Khedr, A.A. Al-Zahhar, F A. Saad, Investigating the influence of <i>p</i> -substituents upon spectral, thermal, kinetic, molecular modeling and molecular docking characteristics of new synthesized arylazobithiazolyhydrazones.....	527
G. Akdut, F. Bildik, H. Duran, A. Tuna, T. Şişmanoğlu, B. F. Şenkal, Adsorption of bisphenol A and phenoxyacetic acid onto new polymeric adsorbents.....	541
S.K. Kolev, V.A. Atanasov, H.A. Aleksandrov, V.N. Popov, T.I. Milenov, Semiconducting graphene.....	552
B. Kumar, G.S. Seth, R. Nandkeolyar, Regression model and analysis of MHD mixed convective stagnation point nanofluid flow: SLM and SRM approach	557
F.I. Sapundzhi, Computer modelling and optimization of the structure-activity relationship by using surface fitting methods.....	569
E. Ismailov, I.K. Ivanov, V.Ch. Christov, Trifunctionalized allenes. Part II. A practical regioselective synthesis of 4-phosphorylated β -hydroxyallene-carboxylates.....	580
F. Kanwal, R. Rehman, H.A. Warraich, Synthesis of novel polyaniline composites with <i>Eriobotrya japonica</i> leaves for removal of Methyl Red dye from wastewater.....	586
N.I. Marchokova, V.B. Petkova, M.V. Dimitrov, UV-spectrophotometric approach in comparative studies of Gliclazide modified-release tablets.....	592
D. Azarifar, M. Farbodmehr, O. Badalkhani, M. Jaymand, Sulfamic acid-functionalized silica-coated magnetite nanoparticles as a recyclable catalyst for the facial synthesis of benzimidazole derivatives.....	596
J.M. Zdravković, N.V. Pavlović, J.D. Mladenović, N.M. Vragolović Bošković, N.M. Zdravković, Effects of tomato processing on carotenoids antioxidant activity and stability during one-year storage.....	604
I.I. Iliev, Calibration of a system for air-borne gamma spectrometry survey and mapping implementation.....	611
M. Didarul Islam, Sh. Rahaman, J.H. Jiban, M.M. Mahdi, Removal of chromium from aqueous solution using chitosan: An experimental study.....	618
M. Bchiti, M. Igouzal, F. El Azhar, H. Oudda, A. El Midaoui, Modeling the separation performance of nanofiltration and reverse osmosis: case study of groundwater desalination (M'Nasra zone Morocco).....	625
Author index	632
Subject index	637
Instruction to the authors.....	641